EQUIVALENT LINEARIZED ANALYTICAL MODELS FOR THE MODULAR MULTILEVEL CONVERTER

Cleiton Magalhães Freitas

Tese de Doutorado apresentada ao Programa de Pós-graduação em Engenharia Elétrica, COPPE, da Universidade Federal do Rio de Janeiro, como parte dos requisitos necessários à obtenção do título de Doutor em Engenharia Elétrica.

Orientador: Edson Hirokazu Watanabe

Rio de Janeiro
June 2020

EQUIVALENT LINEARIZED ANALYTICAL MODELS FOR THE MODULAR MULTILEVEL CONVERTER

Cleiton Magalhães Freitas

TESE SUBMETIDA AO CORPO DOCENTE DO INSTITUTO ALBERTO LUIZ COIMBRA DE PÓS-GRADUAÇÃO E PESQUISA DE ENGENHARIA DA UNIVERSIDADE FEDERAL DO RIO DE JANEIRO COMO PARTE DOS REQUISITOS NECESSÁRIOS PARA A OBTENÇÃO DO GRAU DE DOUTOR EM CIÊNCIAS EM ENGENHARIA ELÉTRICA.

Orientador: Edson Hirokazu Watanabe

Aprovada por: Prof. Edson Hirokazu Watanabe
Prof. Luís Guilherme Barbosa Rolim
Prof. Tatiana Mariano Lessa
Prof. Luís Fernando Corrêa Monteiro
Prof. Pedro Gomes Barbosa
Prof. José Antenor Pomilio

RIO DE JANEIRO, RJ – BRASIL
JUNE 2020

Freitas, Cleiton Magalhães

Equivalent Linearized Analytical Models for the Modular Multilevel Converter/Cleiton Magalhães Freitas. – Rio de Janeiro: UFRJ/COPPE, 2020.

XXVIII, 186 p.: il.; 29, 7cm.

Orientador: Edson Hirokazu Watanabe

Tese (doutorado) – UFRJ/COPPE/Programa de Engenharia Elétrica, 2020.

List of References: p. 153 – 168.

1. Modular Multilevel Converter. 2. Grid-forming converter. 3. Grid-connected converter. 4. Analytical model. 5. Norton-equivalent model. 6. Thévenin-equivalent model. I. Watanabe, Edson Hirokazu. II. Universidade Federal do Rio de Janeiro, COPPE, Programa de Engenharia Elétrica. III. Título.

All models are wrong, but some are useful.

George E. P. Box

Acknowledgments

This work is the major achievement of several years dedicated to learning Electrical Engineering. Every single hour back on the undergrad course in Rio de Janeiro State University (UERJ), somehow, contributed to it. Every single moment back on the master-degree course, also in UERJ, has its mark on it. And of course, every single day in the Electrical Engineering program of COPPE/Federal University of Rio de Janeiro has its effect on this work. But, if weren't for the support of my Mother, Rita Maria Magalhães Freitas, none of this would be possible. She was the person who taught me and my brother that learning is not something to be taken for granted. On the contrary, she taught us that learning and studying were the only paths for succeeding, especially when you do not belong to the upper layers of society. So, I could say that this thesis also contains her mark, just like the sun, the moon, the stars bear the seal of the main character in Black Sabbath's N.I.B. I have also to highlight the importance of my grandmother, Francisca Rita Magalhães, aka second mother, who also employed great effort in our (my brother's and mine) upbringing. Certainly, without her support, I would have not been able to get to this point in my career.

Furthermore, I also thank my supervisor, Professor Edson H. Watanabe, for all the support and insightful questionings he provided to me in these last five years. I also thank a friend and colleague of mine at Rio de Janeiro State University, Professor Luís Fernando Corrêa Monteiro, for all the support in the process of pursuing my doctoral degree. Last, but not least, I thank the volunteers behind the CoppeTeX project, once this thesis was written with their LaTeX template.

Resumo da Tese apresentada à COPPE/UFRJ como parte dos requisitos necessários para a obtenção do grau de Doutor em Ciências (D.Sc.)

MODELOS ANALÍTICOS EQUIVALENTES LINEARIZADOS PARA CONVERSOR MULTINÍVEL MODULAR

Cleiton Magalhães Freitas

June/2020

Orientador: Edson Hirokazu Watanabe

Programa: Engenharia Elétrica

O Conversor Multinível Modular (MMC) vem desempenhando um papel importante na modernização dos sistemas de potência como um componente de HVDCs, FACTs e em muitas outras aplicações. Devido à sua topologia, o MMC apresenta um comportamento singular, mesmo em relação a outros conversores multiníveis cc/ca, exigindo o desenvolvimento de modelos matemáticos para representá-lo em diferentes análises. Grande destaque tem sido dado ao desenvolvimento de modelos analíticos que além de reduzirem o custo computacional em simulações, também permitem analisar a estabilidade do conversor e auxiliam no desenvolvimento de técnicas de controle. Tendo em vista este contexto, esta tese tem como objetivo propor modelos linearizados no domínio da frequência para o MMC, considerando diferentes modos de controle e implementações. Particularmente, os modelos para o MMC controlado por laço duplo de corrente / tensão em referenciais estáticos e síncronos constituem as principais contribuições deste trabalho devido ao grau de novidade deste modo de controle para conversores de alta potência e alta tensão. É mostrado que os modelos desenvolvidos descrevem com precisão o comportamento dinâmico do conversor, sendo adequados para análises transitórias e de estabilidade. Também são apresentados na tese ações de controle para melhorar o desempenho do MMC operando em condições distorcidas, entre as quais está o uso de controladores feed-forward para produzir admitâncias e impedâncias virtuais. Nesse sentido, os controladores feed-forward são derivados e os modelos analíticos atualizados para incluir esses elementos virtuais.

Abstract of Thesis presented to COPPE/UFRJ as a partial fulfillment of the requirements for the degree of Doctor of Science (D.Sc.)

EQUIVALENT LINEARIZED ANALYTICAL MODELS FOR THE MODULAR MULTILEVEL CONVERTER

Cleiton Magalhães Freitas

June/2020

Advisor: Edson Hirokazu Watanabe

Department: Electrical Engineering

The Modular Multilevel Converter (MMC) has been playing an important role in power system modernization as a component of voltage-source HVDCs, FACTs and in plenty of other applications. Due to its topology, the MMC presents distinguishable behavior, even from the other multilevel ac/dc converters, requiring the development of mathematical models for representing it in different analysis domain. The state-of-art front, indeed, concerns the development of analytical models which could not only speed up simulations but also allow accessing the stability of the converter and aid the development of control techniques. In view of that, this thesis is focused on proposing linearized frequency-domain models for the MMC considering different control modes and implementations. Particularly, the models for the double-loop current/voltage controlled MMC in natural and in synchronous reference frames constitute the major contributions of this work due to the novelty of this control mode for high-voltage high-power converters. It is shown that the derived models accurately describe the dynamic behavior of the converter, being then suitable for transient and stability analysis. It is also presented in the thesis control actions for improving the performance of the MMC operating in distorted conditions, among which, the use of feed-forward controllers to produce virtual admittances and impedances. In this regard, the feed-forward controllers are derived and the analytical models updated to account these virtual elements.

Table of Contents

List of Figures

List of Tables

List of Acronyms

FACTS Flexible AC Transmission System, p. 1

FPGA Field Programmable Gate Array, p. 1

HVDC High Voltage Direct Current, p. 1

LCC Line-Commuted Converter, p. 7

MMC Modular Multilevel Converter, p. 1

NLC Nearest Level Control (one of the modulation approaches for the MMC), p. 12

NRF Natural Reference Frame, p. 5

PD-PWM Phase Disposition PWM (another modulation technique for MMC), p. 15

SM Submodule, p. 10

SRF Synchronous Reference Frame, p. 5

THD Total harmonic distortion, p. 12

VSC-HVDC VSC-based HVDC, p. 3

VSC Voltage source converter, p. 3

List of Symbols

N	Number of SM per arm, p. 10
k	A certain phase, **a**, **b** or **c**, of the system, p. 10
p	if it appears superscript o subscript in a variable, It is related to an upper arm of the MMC, p. 10
n	if it appears superscript o subscript in a variable, It is related to an lower arm of the MMC, p. 10
SM_{ij}^{k}	A certain SM in the upper, if **i=p**, or lower, if **i=n**, arm of the phase k, p. 10
L	Coupling reactor of each of the arms of the MMC, p. 10
R	Equivalent resistance of each of the arms of the MMC, p. 10
L_f	Equivalent inductance linking the MMC output to the main bus, p. 10
R_f	Equivalent resistance linking the MMC output to the main bus, p. 10
C	Capacitance of the SM capacitor, p. 10
e_c^a, e_c^b, e_c^c	MMC produced ac voltages in phases **a**, **b** and **c**, p. 11
i_c^a, i_c^b, i_c^c	MMC output ac currents in phases **a**, **b** and **c**, p. 11
v_o^a, v_o^b, v_o^c	MMC output ac currents in phases **a**, **b** and **c**, p. 11
v_{dc}	DC-bus voltage, p. 11
v_{ac}^{ijk}	AC terminal voltage of a certain SM: **i** can be **p** or **n**; **j** is the number of the SM; **k** is the phase, p. 11
v_{dc}^{ijk}	DC voltage of a certain SM: **i** can be **p** or **n**; **j** is the number of the SM; **k** is the phase, p. 11
i_c^k	Output current of the phase **k**, p. 12

i_{cp}^{k} Upper-arm current of the phase **k**, p. 12

i_{cn}^{k} Lower-arm current of the phase **k**, p. 12

Q_{+} The upper switch of a SM, p. 15

Q_{-} The lower switch of a SM, p. 15

v_{RL} AC voltage across the RL net of a arm of the MMC, p. 20

$\sum_{inserted} v_{dc}^{pja}$ Sum of the dc voltages inserted in the upper arm of phase **a** in a certain time instant, p. 20

$\sum_{inserted} v_{dc}^{nja}$ Sum of the dc voltages inserted in the lower arm of phase **a** in a certain time instant, p. 20

P Active power, p. 21

M_{i}^{k} Number of inserted SMs in a certain time instant in the arm **i** of the phase **k**, p. 22

m_{i}^{k} Percent of SMs in a certain time instant in the arm **i** of the phase **k**, p. 22

m_{p}^{k} Insertion index of the upper arm of the phase **k**, p. 23

m_{n}^{k} Insertion index of the lower arm of the phase **k**, p. 23

e_{c}^{k*} Reference signal for the produced voltage of the phase **k**, p. 24

e_{cir}^{k*} Reference signal for mitigating the second-harmonic component of the phase **k**, p. 24

v_{ac}^{pk} Equivalent ac voltage of the SMs of the upper arm of the phase **k**, p. 30

v_{ac}^{nk} Equivalent ac voltage of the SMs of the lower arm of the phase **k**, p. 30

v_{dc}^{pk} Equivalent dc voltage of the SMs of the upper arm of the phase **k**, p. 31

v_{dc}^{nk} Equivalent dc voltage of the SMs of the lower arm of the phase **k**, p. 31

v_{dc}^{ik} Equivalent dc voltage of the upper, if i = p, or lower, if i = n, arm of the phase **k**, p. 32

m_{i}^{k} Insertion index of the upper, if i = p, or lower, if i = n, arm of the phase **k**, p. 32

i_{ci}^{k} Current of the upper, if i = p, or lower, if i = n, arm of the phase **k**, p. 32

i_{dc}^{pk} Equivalent dc current of the upper arm of the phase **k**, p. 33

i_{dc}^{nk} Equivalent dc current of the lower arm of the phase **k**, p. 33

C_{eq} Equivalent capacitor of the SMs, p. 33

$v_{dc}^{\Sigma k}$ Sum of the equivalent dc voltages of an arm of the phase **k** , p. 40

$v_{dc}^{\Delta k}$ Difference of the equivalent dc voltages of an arm of the phase **k** , p. 40

$v_{o,ss}^{k}$ Instantaneous steady-state value of the phase **k** of the main-bus voltage, p. 41

V_{ss} Steady-state RMS value of the main-bus voltage, p. 41

ϕ_k Phase displacement between the phases of the system, p. 41

$i_{c,ss}^{k}$ Instantaneous steady-state value of the phase **k** of the output ac current, p. 41

I_{ss} Steady-state RMS value of the output ac current, p. 41

ϕ_i Phase displacement between the output current and main-bus voltage, p. 41

S_{ss} Complex power produced by the MMC in steady-state, p. 41

P_{ss} Active power produced by the MMC in steady-state, p. 41

Q_{ss} Reactive power produced by the MMC in steady-state, p. 41

$e_{c,ss}^{k}$ Instantaneous steady-state value of the phase **k** of the output voltage, p. 42

$\overline{v_{dc}^{kn}}$ Average value over a fundamental-frequency spam of v_{dc}^{kn} , p. 42

$\overline{v_{dc}^{kp}}$ Average value over a fundamental-frequency spam of v_{dc}^{kp} , p. 42

V_{dcss} Steady-state value of the dc voltage v_{dc} , p. 42

E_{ss}^{s*} Sine projection of the steady-state value of the amplitude of the output voltage e_c^k, p. 42

E_{ss}^{c*} Cosine projection of the steady-state value of the amplitude of the output voltage e_c^k, p. 42

E^*_{ss} Steady-state value of the amplitude of the output voltage e^k_c, p. 42

γ_e Steady-state phase displacement between the output voltage e^k_c and the main-bus voltage v^k_o, p. 42

$m^k_{p,ss}$ Steady-state instantaneous value of m^k_p, p. 43

$m^k_{n,ss}$ Steady-state instantaneous value of m^k_n, p. 43

$i^k_{cir,ss}$ Instantaneous steady-state value of the phase **k** of the circulating current i^k_{cir}, p. 43

$\bar{i}^k_{cir,ss}$ Steady-state dc component of the circulating current i^k_{cir}, p. 43

$v^{na}_{dc,ss}$ Steady-state instantaneous value of v^{na}_{dc}, p. 44

$v^{pa}_{dc,ss}$ Steady-state instantaneous value of v^{pa}_{dc}, p. 44

$V^{pa}_{dc_{ic}}$ Steady-state cosine-projection of the amplitude of the ith-order harmonic component of v^{pa}_{dc}, p. 44

$V^{pa}_{dc_{is}}$ Steady-state sine-projection of the amplitude of the ith-order harmonic component of v^{pa}_{dc}, p. 44

$V^{na}_{dc_{ic}}$ Steady-state cosine-projection of the amplitude of the ith-order harmonic component of v^{na}_{dc}, p. 44

$V^{na}_{dc_{is}}$ Steady-state sine-projection of the amplitude of the ith-order harmonic component of v^{na}_{dc}, p. 44

$I_{cir_{is}}$ Steady-state sine-projection of the amplitude of the ith-order harmonic component of i^k_{cir}, p. 44

$I_{cir_{ic}}$ Steady-state cosine-projection of the amplitude of the ith-order harmonic component of i^k_{cir}, p. 44

$\mathbf{X}_{ss}$ Column vector with the amplitude of the harmonic components of i_{cir}, v^{pk}_{dc} and v^{nk}_{dc} in steady state, p. 44

$\mathbf{A}_{ss}$ 22×22 coefficient matrix which describes i_{cir}, v^{pk}_{dc} and v^{nk}_{dc} in steady state, p. 44

$\mathbf{B}_{ss}$ 22×22 constant column vector which describes i_{cir}, v^{pk}_{dc} and v^{nk}_{dc} in steady state, p. 44

$\tilde{i}^k_{cir}$ Small-signal representation of i^k_{cir}, p. 49

$\tilde{i}_c^k$	Small-signal representation of i_c^k, p. 49
$\tilde{e}_c^{k*}$	Small-signal representation of e_c^{k*}, p. 49
$\tilde{v}_o^k$	Small-signal representation of v_o^k, p. 49
$\tilde{e}_{cir}^{k*}$	Small-signal representation of e_{cir}^{k*}, p. 49
$\tilde{v}_{dc}^{\Delta k}$	Small-signal representation of $v_{dc}^{\Delta k}$, p. 49
$\tilde{v}_{dc}^{\Sigma k}$	Small-signal representation of $v_{dc}^{\Sigma k}$, p. 49
e_{c0}^{k*}	Equilibrium point considered for e_c^{k*}, p. 49
e_{cir0}^{k*}	Equilibrium point considered for e_{cir}^{k*}, p. 49
i_{cir0}^k	Equilibrium point considered for i_{cir}^k, p. 49
i_{c0}^k	Equilibrium point considered for i_c^k, p. 49
$v_{dc0}^{k\Sigma}$	Equilibrium point considered for $v_{dc}^{k\Sigma}$, p. 49
$v_{dc0}^{k\Delta}$	Equilibrium point considered for $v_{dc}^{k\Delta}$, p. 49
$\tilde{I}_{cir}^k$	Laplace-domain representation of $\tilde{i}_{cir}^k$, p. 53
$\tilde{I}_c^k$	Laplace-domain representation of $\tilde{i}_c^k$, p. 53
$\tilde{E}_c^{k*}$	Laplace-domain representation of $\tilde{e}_c^{k*}$, p. 53
$\tilde{V}_o^k$	Laplace-domain representation of $\tilde{v}_o^k$, p. 53
$\tilde{E}_{cir}^{k*}$	Laplace-domain representation of $\tilde{e}_{cir}^{k*}$, p. 53
$\tilde{V}_{dc}^{\Delta k}$	Laplace-domain representation of $\tilde{v}_{dc}^{\Delta k}$, p. 53
$\tilde{V}_{dc}^{\Sigma k}$	Laplace-domain representation of $\tilde{v}_{dc}^{\Sigma k}$, p. 53
Z	Arm impedance, p. 53
Z_f	Output impedance, p. 53
C_{cir}	Controller used for mitigating the circulating current, p. 54
k_r^{cir}	Resonant gain of the controller used for mitigating the circulating current, p. 54
Y_{dc}	Equivalent admittance of the dc side of the MMC in NRF, p. 55
C_i	Controller used in current loop of the MMC, p. 57

k_r^i Resonant gain of the controller used in current loop of the MMC in NRF, p. 57

k_p^i Proportional gain of the controller used in current loop of the MMC in NRF, p. 57

Y_{ac} Norton-equivalent admittance of the current-controlled MMC in NRF, p. 57

C_i^{cl} Closed-loop gain of the current-controlled MMC in NRF, p. 57

C_v^{sl} Controller used in voltage loop of the single-loop voltage-controlled MMC, p. 59

$k_r^{v,sl}$ Resonant gain of the controller used in voltage loop of the single-loop voltage-controlled MMC, p. 59

$k_p^{v,sl}$ Proportional gain of the controller used in voltage loop of the single-loop voltage-controlled MMC, p. 59

Z_{ac}^{sl} Series impedance of the single-loop voltage-controlled MMC in NRF without considering the capacitor bank, p. 60

$G_{v,cl}^{sl}$ Closed-loop gain of the single-loop voltage-controlled MMC in NRF without considering the capacitor bank, p. 60

Z_{th}^{sl} Thévenin-equivalent impedance of the single-loop voltage-controlled MMC in NRF, p. 61

G_{th}^{sl} Thévenin-equivalent gain of the single-loop voltage-controlled MMC in NRF, p. 61

C_v^{dl} Controller used in voltage loop of the double-loop current/voltage-controlled MMC, p. 62

$k_r^{v,dl}$ Resonant gain of the controller used in voltage loop of the double-loop current/voltage-controlled MMC, p. 62

$k_p^{v,dl}$ Proportional gain of the controller used in voltage loop of the double-loop current/voltage-controlled MMC, p. 62

Z_{ac}^{dl} Series impedance of the double-loop current/voltage-controlled MMC in NRF without considering the capacitor bank, p. 63

$G_{v,cl}^{dl}$ Closed-loop gain of the double-loop current/voltage-controlled MMC in NRF without considering the capacitor bank, p. 63

Z_{th}^{v} Thévenin-equivalent impedance of the double-loop current/voltage-controlled MMC in NRF, p. 63

G_{th}^{dl} Thévenin-equivalent gain of the double-loop current/voltage-controlled MMC in NRF, p. 63

$\tilde{\mathbf{v}}_{dc}^{abc\Sigma}$ Column vector containing the components $\tilde{V}_{dc}^{\Sigma a}(t)$, $\tilde{V}_{dc}^{\Sigma b}(t)$ and $\tilde{V}_{dc}^{\Sigma c}(t)$, p. 66

$\tilde{\mathbf{v}}_{dc}^{abc\Delta}$ Column vector containing the components $\tilde{V}_{dc}^{\Delta a}(t)$, $\tilde{V}_{dc}^{\Delta b}(t)$ and $\tilde{V}_{dc}^{\Delta c}(t)$, p. 66

$\tilde{\mathbf{i}}_{cir}^{abc}$ Column vector containing the components $\tilde{i}_{cir}^{a}(t)$, $\tilde{i}_{cir}^{b}(t)$ and $\tilde{i}_{cir}^{c}(t)$, p. 66

$\tilde{\mathbf{i}}_{c}^{abc}$ Column vector containing the components $\tilde{i}_{c}^{a}(t)$, $\tilde{i}_{c}^{b}(t)$ and $\tilde{i}_{c}^{c}(t)$, p. 66

$\tilde{\mathbf{v}}_{o}^{abc}$ Column vector containing the components $\tilde{v}_{o}^{a}(t)$, $\tilde{v}_{o}^{b}(t)$ and $\tilde{v}_{o}^{c}(t)$, p. 66

$\tilde{\mathbf{v}}_{dc}^{abc}$ Column vector containing three components equal to $\tilde{V}_{dc}(t)$, p. 66

$\tilde{\mathbf{e}}_{cir}^{abc*}$ Column vector containing the components $\tilde{e}_{cir}^{a*}(t)$, $\tilde{e}_{cir}^{b*}(t)$ and $\tilde{e}_{cir}^{c*}(t)$, p. 66

$\tilde{\mathbf{e}}_{c}^{abc*}$ Column vector containing the components $\tilde{e}_{c}^{a*}(t)$, $\tilde{e}_{c}^{b*}(t)$ and $\tilde{e}_{c}^{c*}(t)$, p. 66

$\mathbf{T}_{dq0}$ Frame transformations, p. 66

θ Electrical angle, p. 66

$\mathbf{\Omega}$ SRF coupling matrix, p. 67

$\tilde{\mathbf{V}}_{dc}^{2dq0\Sigma}$ Column vector containing the components $\tilde{V}_{dc}^{\Sigma d}(s)$, $\tilde{V}_{dc}^{\Sigma q}(s)$ and $\tilde{V}_{dc}^{\Sigma 0}(s)$, p. 67

$\tilde{\mathbf{V}}_{dc}^{dq0\Delta}$ Column vector containing the components $\tilde{V}_{dc}^{\Delta d}(s)$, $\tilde{V}_{dc}^{\Delta q}(s)$ and $\tilde{V}_{dc}^{\Delta 0}(s)$, p. 67

$\tilde{\mathbf{I}}_{cir}^{2dq0}$ Column vector containing the components $\tilde{I}_{cir}^{d}(s)$, $\tilde{I}_{cir}^{q}(s)$ and $\tilde{I}_{cir}^{0}(s)$, p. 67

$\tilde{\mathbf{I}}_{c}^{dq0}$ Column vector containing the components $\tilde{I}_{c}^{d}(s)$, $\tilde{I}_{c}^{q}(s)$ and $\tilde{I}_{c}^{0}(s)$, p. 67

$\tilde{\mathbf{V}}_{o}^{dq0}$ Column vector containing the components $\tilde{V}_{o}^{d}(s)$, $\tilde{V}_{o}^{q}(s)$ and $\tilde{V}_{o}^{0}(s)$, p. 67

$\tilde{\mathbf{V}}_{dc}^{2dq0}$ Column vector containing the components equal to 0, 0 and $\tilde{V}_{dc}(s)$, p. 67

$\tilde{\mathbf{E}}_{cir}^{2dq0*}$ Column vector containing the components $\tilde{E}_{cir}^{d*}(s)$, $\tilde{E}_{cir}^{q*}(s)$ and $\tilde{E}_{cir}^{0*}(s)$, p. 67

$\tilde{\mathbf{E}}_{c}^{dq0*}$ Column vector containing the components $\tilde{E}_{c}^{d*}(s)$, $\tilde{E}_{c}^{q*}(s)$ and $\tilde{E}_{c}^{0*}(s)$, p. 67

$\mathbf{s}_{dq}$ SRF complex-frequency matrix, p. 67

$\mathbf{s}_{2dq}$ D-SRF complex-frequency matrix, p. 67

$\mathbf{C}_{cir}^{2dq0}$ Transfer matrix for the circulating-current mitigation controller in SRF, p. 68

k_i^{icir} Integral gain for the circulating-current mitigation controller in SRF, p. 69

$\mathbf{Y}_{dc}^{2dq0}$ Admittance matrix representing the dc side of the MMC in SRF, p. 69

$\mathbf{\Gamma}_{cir}$ One of the matrix-components of $\mathbf{Y}_{dc}^{2dq0}$, p. 69

$\mathbf{C}_{i}^{dq0}$ Transfer matrix for the output-current controller in SRF, p. 71

$\mathbf{D}_{i}^{dq}$ Decoupling factor used in the output-current controller in SRF, p. 71

k_i^{i} Integral gain for the output-current controller in SRF, p. 71

$\mathbf{Y}_{ac}^{dq0}$ Norton-equivalent admittance matrix for the current controlled MMC in SRF, p. 72

$\mathbf{\Gamma}_{i}$ One of the matrix-components of $\mathbf{Y}_{ac}^{dq0}$, p. 72

$\mathbf{C}_{v,sl}^{dq0}$ Transfer matrix of the controller used in the single-loop voltage controlled MMC in SRF, p. 74

$k_i^{v,sl}$ Integral gains of the controller used in the single-loop voltage controlled MMC in SRF, p. 74

$\mathbf{Z}_{dq}$ SRF representation of the arm impedance of the MMC, p. 74

$\mathbf{Z}_{fdq}$ SRF representation of the output impedance of the MMC, p. 74

$\mathbf{\Gamma}_{v,in}^{sl}$ Auxiliary matrix used in $\mathbf{Z}_{sl,th}^{dq0}$ and $\mathbf{G}_{sl,th}^{dq0}$, p. 75

$\mathbf{G}_{v,sl,cl}^{dq0}$ Closed-loop voltage gain matrix of the SRF single-loop voltage-controlled MMC without considering the capacitor bank, p. 76

$\mathbf{Z}_{in}^{sl}$ Inner impedance matrix of the SRF single-loop voltage-controlled MMC without considering the capacitor bank, p. 76

$\mathbf{Z}_{sl,th}^{dq0}$ Thévenin-equivalent impedance matrix of the SRF single-loop voltage-controlled MMC, p. 76

$\mathbf{G}_{sl,th}^{dq0}$ Thévenin-equivalent voltage gain matrix of the SRF single-loop voltage-controlled MMC, p. 76

$G_{v,sl}$ Transfer matrix of the controller used in the double-loop current/voltage controlled MMC in SRF, p. 80

$k_i^{v,dl}$ Integral gains of the controller used in the double-loop current/voltage controlled MMC in SRF, p. 80

$\mathbf{Z}_{in}^{dl}$ Inner impedance matrix of the SRF double-loop current/voltage-controlled MMC without considering the capacitor bank, p. 80

$\mathbf{Z}_{dl,th}^{dq0}$ Thévenin-equivalent impedance matrix of the SRF double-loop current/voltage-controlled MMC, p. 80

$\mathbf{G}_{dl,th}^{dq0}$ Thévenin-equivalent voltage gain matrix of the SRF double-loop current/voltage-controlled MMC, p. 80

$\varepsilon_{cp}\{\bullet\}$ Computational error, p. 89

F^k A generic variable in NRF, p. 108

F^{k*} A generic reference signal in NRF, p. 108

U^{k*} A generic control signal in NRF, p. 108

k_{r5} Gain of the fifth-order resonant controller in NRF, p. 108

k_{r7} Gain of the seventh-order resonant controller in NRF, p. 108

F^{dq} A generic variable in SRF, p. 111

F^{dq*} A generic reference signal in SRF, p. 111

U^{dq*} A generic control signal in SRF, p. 111

k_r Gain of the sixth-order resonant controller in SRF, p. 111

Λ_i^{abc} Feed-forward factor of the NRF current-controlled MMC, p. 115

Y_{vir} Virtual admittance of the NRF current-controlled MMC, p. 116

$\Lambda_{v,sl}^{abc}$ Feed-forward factor of the NRF single-loop voltage-controlled MMC, p. 117

Z_{vir}^{sl}	Virtual impedance of the NRF single-loop voltage-controlled MMC, p. 118
$\Lambda_{v,dl}^{abc}$	Feed-forward factor of the NRF double-loop current/voltage-controlled MMC, p. 119
Z_{vir}^{dl}	Virtual impedance of the NRF double-loop current/voltage-controlled MMC, p. 120
$\boldsymbol{\Lambda}_{i}^{dqo}$	Feed-forward factor matrix of the SRF current-controlled MMC, p. 122
$\mathbf{Y}_{vir}$	Virtual admittance matrix of the SRF current-controlled MMC, p. 122
$\boldsymbol{\Lambda}_{v,sl}^{dqo}$	Feed-forward factor matrix of the SRF single-loop voltage-controlled MMC, p. 123
$\mathbf{Z}_{vir}^{sl,dqo}$	Virtual impedance matrix of the SRF single-loop voltage-controlled MMC, p. 124
$\boldsymbol{\Lambda}_{v,dl}^{dqo}$	Feed-forward factor matrix of the SRF double-loop current/voltage-controlled MMC, p. 126
$\mathbf{Z}_{vir}^{dl,dqo}$	Virtual impedance matrix of the SRF double-loop current/voltage-controlled MMC, p. 126
$\boldsymbol{\Gamma}_{vir}^{dl,dqo}$	Matrix part of the Virtual impedance matrix of the SRF double-loop current/voltage-controlled MMC, p. 126

Chapter 1

Introduction

In views of the increasing number of power-electronics-based systems widespread throughout the generation, transmission, and distribution, it stands to reason that the next-generation power grid is inherently linked to power electronic devices [1]. Some application in which this devices play an important role include photovoltaic-[2–6] and wind-based generation systems [7–9]; High Voltage Direct Current (HVDC) transmission [10, 11] and Flexible AC Transmission System (FACTS) [12, 13]; motor drive [14], transportation electrification [15, 16]; energy storage systems [17, 18]; microgrids [19, 20] and etc. Different types of power-electronic converters are present in this scenario, among them, the Modular Multilevel Converter (MMC) stands out. This converter was firstly considered for applications in HVDC and FACTS [21]; however, its low-distorted ac voltages and reduced switching losses compared to others topologies pave the way for using MMC in a variety of applications ranging from motor drive [22, 23] to the integration of renewable sources to the power system [24, 25].

One segment which is gathering a great deal of attention concerning the MMC is the development of mathematical models for representing the converter in different analysis. One of the possible focuses in this regard are the models for speeding up simulations and even representing the MMC in real-time digital simulators. One example in this context is the work of LIN and DINAVAHI [26] in which the authors provided a transistor-level model for an MMC. The great challenge of the authors was to represent the MMC, together with the model of an induction machine, which would be driven by the converter, to guarantee the implementation in an FPGA-based[1]real-time simulator. The same idea of representing the MMC in real-time simulators are also found in the works of OULD-BACHIR *et al.* [27], SHEN and DINAVAHI [28], LI and BÉLANGER [29], and ASHOURLOO *et al.* [30].

[1]FPGA - Field Programmable Gate Array - is a device in which its hardware is configurable by software.

1.1 State of the art

This section aims at presenting a brief, yet representative, literature review on analytical models for the MMC. When it comes to analytical models, it is commonly found in the literature both time- and frequency-domain approaches. Considering steady-state time-domain models, for instance, ILVES *et al.* [31] developed a steady-state analytical model for representing the interaction between the harmonic components produced by the MMC in the time domain. Meanwhile, SHI *et al.* [32] modeled the influence of unbalanced grid voltages into the ac-side second-order harmonic voltages of the converter, still considering the steady-state condition. Also, ZHAO *et al.* [33] proposed a mathematical model to describe the relationship between the harmonic components on the ac side - coming by either non-linear loads distorted voltages depending on whether the MMC is under voltage or current control - and the harmonic components generated by the MMC.

Some examples considering the dynamics of the MMC in time-domain include the work of PERALTA *et al.* [34]. They presented the model for an MMC-based $\pm 320kV$ HVDC linking France and Spain but did not consider the dynamics of the dc voltages of the submodules and did not included in the model the control loops of the converters. WANG *et al.* [35], on the other hand, proposed a state-space model based on switching functions which included the dynamics of the dc voltages of the MMC. Also, their proposed model allowed the development of a new technique for balancing the dc voltages of the submodules. HARNEFORS *et al.* [36] presented a mathematical model that contemplates the internal dynamics of the converter, that is, the dynamics of the sub-module capacitors and the effects caused by the circulating currents. The only simplification used was to consider an equivalent capacitor for each arm of the converter, instead of considering each capacitor of each submodule. JAMSHIDIFAR and JOVCIC [37] presented a group of state-space models for representing the MMC dynamics in the synchronous reference frame. In a nutshell, each model is distinguished by its order, making each one suitable for a specific type of simulation. ZHOU *et al.* [38] modeled a current-controlled MMC and analyzed how the PLL and the short-circuit ratio of the power grid affect the performance of a voltage-source-converter-based HVDC (VSC-HVDC). MEHRASA *et al.* [39] considered different VSC-HVDC, in this case with current-controlled MMCs on both sides. The steady-state analytic model was incorporated in a novel current controller and the dynamic model was used for stability analysis. In common to all these papers is the fact that the MMC was always considered under output current control.

Still considering time-domain dynamic models, some researchers focused their work on developing reduced-order models which could curb the computation burden of representing the MMC in large system simulations. Some examples include the papers of LEON and AMODEO [40], HAO *et al.* [41], ZHU *et al.* [42]. Last, yet not least, papers such as those from WANG *et al.* [43], XIAO *et al.* [44], TRINH *et al.* [45], aim at representing the dynamics of the MMC in time-domain Electromechanical Transient analysis.

As for frequency-domain models, some examples include the references [46–51]. YANG *et al.* [46], for instance, presented an SRF average model of the MMC from which it was possible to obtain both the equivalent ac- and dc-side impedances of the converter. SUN and LIU [47], on the other hand, proposed a linear model for the MMC based on positive- and negative-sequence impedances for a series of different harmonic components. In the first step, the authors derived the average value model of the converter considering the circulating currents but disregarding the dynamics of the dc voltages. It is important to comment that, although the dynamics of the capacitors were ignored, their oscillating voltage components were not. In a second step, the authors decomposed the model obtained into components related to different frequencies using the complex notation of the Fourier series. KHAZAEI *et al.* [48] also worked on determining the equivalent impedances of the MMC. Nonetheless, their primary aim was to verify the interaction of the converter with a weak power grid. LIU *et al.* [49], presented a frequency-domain model (in addition to a time-domain model, to be more precise) considering asymmetric arm parameters and used it to design a controller that tackles the influence of asymmetry on the performance of the converter. WANG *et al.* [50] also considered a current-controlled, grid-connected MMC, but instead of basing their work in the typical average modeling approach onto which the set of submodules of an arm is represented as a single equivalent source, they represented the dynamics of each of the dc capacitors in the model. MA *et al.* [51], on the other hand, proposed an equivalent model in which the ac-side of the MMC is modeled as a two-level voltage source converter, whereas the dc-side dynamics is mimicked by an equivalent dc/dc converter. This approach allowed their model to verify the influence of the dc-side voltage oscillations in both the dc- and ac-side of the MMC. Once more, all the papers mentioned in this paragraph considered the MMC strictly under current control.

As far as it was possible to verify, only the references [52–55] deal with the modeling of an MMC under voltage control. BESSEGATO *et al.* [52] provided models for the voltage- and current-controlled MMC, though, the voltage control was implemented in an open-loop approach. Their objective was to analyze the ac equivalent admittance of the MMC for different control modes and different implementations, i.e., Natural Reference Frame (NRF) or Synchronous Reference Frame (SRF). Finding the AC-side admittance of the MMC was also the work addressed by BEZA *et al.* [54], considering both the MMC under current and open-loop voltage control.

LYU *et al.* [53], on the other hand, focused they work into analyzing the stability of the interaction between the grid-forming MMC of a VSC-HVDC and the wind farm. For this matter, they presented the Thévenin-equivalent model of the MMC controlled in the natural reference frame with proportional-resonant controllers. Among the papers addressing the MMC under voltage control, [55] is the only one that consider a double loop, i.e., an outer voltage-control loop in cascade with an inner current-control loop. Although their primary focus was not to provide an analytical model, they derived a frequency-domain model relating the ac and dc powers and the energy stored internally. Their frequency-domain model, nonetheless, is not suitable for analyzing the relationship between ac voltages and currents.

1.2 Alignment of the thesis with the current state-of-art research

Given the contextualization in the previous section, this work aims at contributing with the development of analytical models for the MMC controlled in both Natural and Synchronous Reference Frame (NRF and SRF), as the two control/modeling approaches are equally common in the literature. In other words, this thesis provides a set of frequency-domain linearized models for representing the MMC in electromagnetic transient analyses, especially when the MMC is controlled as a grid-forming converter with a double control loop. The author did not find this kind of model in the literature. Primarily, the models are focused on representing the MMC for high-voltage, high-power applications, such as VSC-HVDC and FACTS, where the number of submodules is high enough that the effects of switching frequency (e.g. harmonics) are negligible. As for the operation mode, three different cases encompassing both current and voltage control were considered throughout this work. In the first mode, which is presented in Figure 1.1a, the MMC is under current control either driving a load or connected to the power grid. Notice that e_c is the MMC output ac-side voltage, i_c is the output current, and i_c^* is its reference. Besides that, Z_g, Z_f, and Z_o are, respectively, the grid-equivalent, MMC grid-coupling, and load impedances, and G_i is the current controller. Although the proposed models are suitable for both situations, the results presented were obtained for the MMC as a grid-tied converter. In the control modes highlighted in Figures 1.1b and 1.1c, the MMC acts as a grid-forming converter [56] which, in turn, is a typical configuration used in VSC-HVDC linking offshore wind power plants to the onshore grid [57–61]. In these cases, v_o and v_o^* are the ac bus voltage and its reference signal, and G_v the voltage controller. The control mode in Figure 1.1b may be referred to as single-loop voltage control as it presents only the voltage control loop. The control

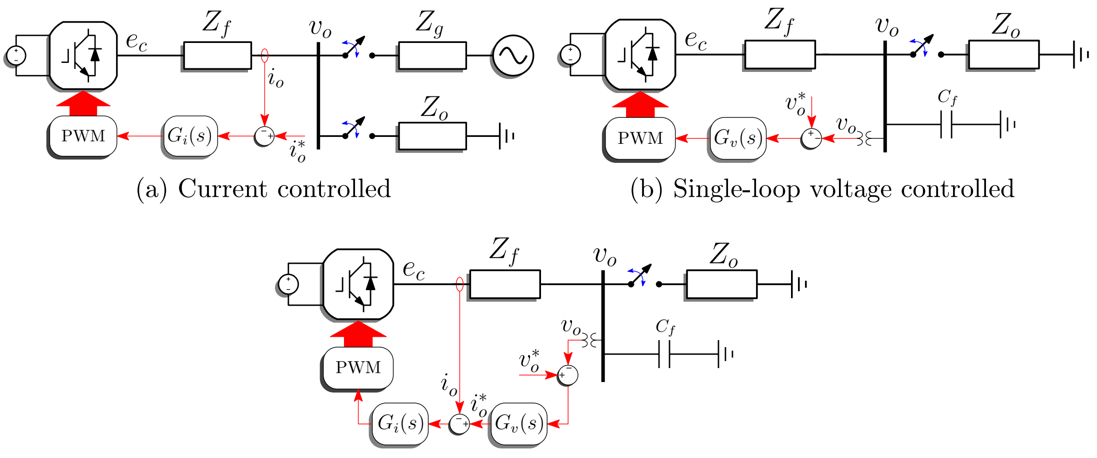

(a) Current controlled (b) Single-loop voltage controlled

(c) Double-loop current/voltage controlled

Figure 1.1: Generic control strategies for voltage source converters

mode in Figure 1.1c, on the other hand, is referred to as double-loop voltage control, once the system presents an inner current loop in addition to the voltage loop. In both cases, a capacitor bank is included as part of the scenario, provided that some MMC-based grid-forming inverters presented in the literature follow this structure. Nevertheless, the models obtained in this work can be easily reduced for the cases where no capacitor bank is used by making $C_f = 0$.

Among the outcomes of this thesis, the Thévenin-equivalent model for the double-loop NRF voltage-controlled MMC in Section 4.1 constitutes a contribution to the body of knowledge. In a nutshell, it goes along the lines of the researches in LYU *et al.* [53] and [54], nonetheless, it was considered here the MMC under double-loop current/voltage control. In this regard, the results of Sections 4.1.3, 4.1.5 and 5.1.1 compiled together with some contents of Chapter 5 (Section 5.3) into the paper *A linearized small-signal Thévenin-equivalent model of a voltage-controlled modular multilevel converter* [62], written within the context of this doctoral research, which was published by *Electric Power Systems Research* in early 2020. Also, it was not found in literature papers providing models for the double-loop voltage-controlled MMC in SRF. To be fair, reference [55] follows these lines, yet, as previously explained, their frequency-domain model is not suitable for analyzing the relationship between ac voltages and currents. To fill this gap, the thesis also provides a Thévenin-equivalent model for the MMC under double-loop current/voltage control in SRF. Section 1.5 presents a list of contributions of this Thesis.

One last point must be clarified before continuing the discussions on motivations and contributions of the thesis. This thesis was focused on the models which represent the fastest dynamics of MMC-based power-electronics systems. That is, this model cover phenomena in which time constants are in the order of milliseconds, such as it is discussed in [63]. Because of that, outer control loops like the ones used for controlling dc-voltage and power, very common in HVDC and FACTS devices, are not addressed in this thesis. These later control loops present slower dynamics and do necessitate different modeling approaches considering different time scales.

1.3 Motivation

As previously explained, there is a growing number of power electronic-based systems, and the MMC plays an important role in this scenario. Take for instance the case of HVDC links, where the MMC is becoming widely used in new projects [11]. Two-level converters were considered in this segment at its very beginning, with the example of the $\pm 80kV$, 3×65MVA DIRECTLINK project [64], and later on, three-level Neutral-Point Clamped (NPC) converters, which is the case of the $138kV$, $150MW$ Eagle Pass link [65]. However, to operate at high-voltage levels, these topologies rely on IGBT stacks [66], which require more complex driving systems [67] and present higher switching losses than MMC [68]. Besides that, MMC presents easier voltage scalability and lower total harmonic distortion (THD)[69]. Concerning MMC-based projects, we have the examples of the 1GW $\pm 320kV$ HVDC between France and Spain [70], the 1.4GW, $\pm 525kV$ link between Germany and Norway, and several cases of interconnection between offshore wind power plants and the continent grid [71]. This last example is understood as one of the most promising fields in a short-term point of view, once wind power plants are popping out everywhere. Just to have a glimpse of the scenario, consider the case of the Brazil where wind generation skyrocketed in the last decade, reaching the level of almost 15GW of installed capacity, nearly 10% of the total capacity of the Brazilian power system [72, 73]. Also, despite the fact there is no offshore wind power plant in Brazil yet, three projects are undergoing environmental-licensing procedures [74] and it is estimated a potential of 700GW for offshore wind generation in Brazil [75]. Of course, it is not possible to predict how many MMC-HVDC are going to be commissioned in this scenario, but stands to reason that they should be considered or all the potential would not be unlocked[2]. Static synchronous compensator (STATCOM) [76–79] is another application in which MMC is making its way through, especially with companies such as ABB, GE, and Siemens employing this technology in their newer products, say it, SVC LIGHT [80, 81], GE's STATCOM [82, 83] and SVC PLUS [84, 85].

Considering the scenario described in the previous paragraph and all the bibliography review presented at the beginning of the chapter, it is possible to point out that grid-forming MMC-based converters may play an important role in the inte-

[2]HVDC becomes more economically suitable than HVAC for offshore energy transmission for distances over 50km off the coast [11].

gration of wind power plants to the power system. Thus, the necessity of developing mathematical, especially analytical, models for representing the MMC increases as well, given the novelty of these new systems in comparison to other high-power high-voltage power-electronic solutions, e.g. line-commuted converter (LCC) HVDC. Among the objectives of these models, providing faster time-domain simulations and using for stability analysis stood out.

Still in this subject, it is important to reassure that it lacks in the literature the addressing of analytical models considering the grid-forming MMC under double-loop current/voltage control. This control approach, presented in [55] and [62], is very useful because it allows limiting the current in case an ac fault occurs in the system. It is also not found in literature analysis showing how the control settings interfere with the frequency-domain behaviour of the MMC when controlled as a grid-forming converter with double control loop. Notice that, this kind of study is important because it could highlight important aspects to be considered when planing the use of MMC in different scenarios.

1.4 Objectives

The main objective of thesis is to develop analytical models for representing the grid-forming (voltage controlled) MMC in different referential frames when it is under double-loop voltage control, i.e, its control system comprises an outer voltage control loop and an inner current control loop. Along with the development of these models, it is also at the aim of the thesis to derive the equivalent models for the MMC under current control and single-loop voltage control. Last, yet not least, it was also an objective of the thesis to present techniques such as the of multiple-resonant loops and virtual elements to shaping the equivalent impedance of the MMC and provide it with immunity to distorted currents.

1.5 Contributions of the thesis

The major contributions of the thesis were the development of analytical models for the MMC under double-loop current/voltage control either in NRF [62] or SRF. Following it is presented a list with other contributions of the thesis:

- Deriving and use of an analytical steady-state model to evaluate the influence of active and reactive power into the harmonic components of the dc voltages and the circulating currents;

- Analysis of the influence of the control settings in the equivalent impedances and admittances of the converter;

- Analysis of the effect of multiple resonant control loops in the characteristic of the equivalent admittance and impedance when the MMC is controlled in NRF;

- Analysis of the effect of proportional-integral-resonant controllers in the characteristic of the equivalent admittance and impedance when the MMC is controlled in SRF;

- Development of feed-forward control loops to provide the MMC with immunity to distorted voltages, when it is in grid-connected mode, or distorted currents, when it is acting as a grid-forming converter;

- Derivation of the models for the virtual elements (admittance and impedance) created by the feed-forward control loops;

- Stability analysis of a power-electronic-based system comprised of two MMCs, one as a grid-forming converter and other as a current-controlled converter.

1.6 Publication

FREITAS, C. M., WATANABE, E. H., MONTEIRO, L. F. C. "A linearized small-signal Thévenin-equivalent model of a voltage-controlled modular multilevel converter", *Electric Power Systems Research*, v. 182, pp. 106231, 2020. ISSN: 0378-7796. doi:10.106/j.epsr.2020.106231.

1.7 Some preliminary definitions

Before starting the thesis, it is necessary to define some expressions that are massively used throughout the manuscript:

- **Switching-level model**: This is the full simulation model of the MMC. In this case, each one of the half-bridge submodules (SM) is implemented in the simulation and the circuit also includes a PWM-based modulator and control algorithms for balancing the dc voltages of each SM (and, of course, all the other control loops). This model was implemented in PSCAD due to its capability of simulating large systems in a feasible time. Chapter 2 presents the details of this model.

- **Averaged model**: In this model, the set of SMs of the MMC are substituted by equivalent sources that represent the low-frequency behavior of them. Notice that in this context, low-frequency means all the spectrum bellow the switching frequency. In other words, this model encompasses the fundamental and harmonic components, yet not the switching effects of the circuit. It is important to have in mind that non-linear effects inherent to the MMC are still present in this model and because of that, interchangeably, this model is called "non-linear model" or "non-linear, time-domain model" in several parts of the text. This model was implemented in PSIM due to its simplicity when dealing with small systems. Chapter 3 presents an in-deep analysis of this model.

- **Non-linear model**: Also called "Non-linear, time-domain model", is the Averaged model described in the previous bullet.

1.8 Summary of the thesis

The thesis is organized into six chapters, including the introduction. Chapter 2 presents a brief discussion on the modular multilevel converter regarding its structure, operating principles, modulation, and inherent characteristics. It is also presented in this chapter some preliminary simulation results using a detailed PSCAD model for the MMC considered throughout this work. Chapter 3, on the other hand, showcases the standard average model for the MMC and the analytical steady-state solution for the MMC. Still in the chapter, some simulation results are presented for comparing the averaged (also named the non-linear model in this thesis) with the detailed PSCAD models. The steady-state solution, on the other hand, is used to analyze the influence of active and reactive powers into the harmonic components of the dc voltages and the circulating currents of the MMC. In Chapter 4 are presented the linearized frequency-domain models for the different control modes of the MMC. The first part of the chapter is focused on natural reference frame models, where the control loops comprise resonant controllers, and the second part is focused on synchronous reference frame models, where the control loops present PI controllers in dq frame. In the sequence, Chapter 5 is focused on showing how the control settings affect the performance of the MMC when it comes to the presence of harmonic content in the power system and on presenting strategies for providing the MMC with immunity to the harmonic content of the system. The major point of this chapter was to propose feed-forward actions to cope with the issues caused by the harmonic components and to derive the analytical models to represent these actions. Finally, the conclusions are drawn in Chapter 6.

Chapter 2

Modular Multilevel Converter

This chapter presents a brief summary on the modular multilevel converter (MMC), considering its general topology and working principle. It is included in this summary a brief discussion on modulation techniques and explanations on the main issues of this topology, i.e. dc-voltage balancing and circulating currents, and the way it is possible to cope with them. It is also in the scope of this chapter to introduce the concepts of insertion indices, which are used in the following chapters as the modulation signals of the converter. Finally, some preliminary simulation results considering a 20-submodules-per-arm three-phase MMC are presented.

2.1 Topology of the MMC

Figure 2.1a presents the basic topology of the MMC in which each of the submodules (SM) is formed by an IGBT half-bridge and an electrolytic capacitor, as shown in Figure 2.1b[1]. Each leg of the converter has $2N$ submodules, where N is the number of submodules per arm. For reference purposes, each of the submodules was named SM_{ij}^{k}, where i indicates whether the modules belong to an upper arm, p, or lower n; j is the position of the module within the arm and k the phase in which the module belongs. Still in the figure, C is the electrolytic capacitor of each SM, L indicates the coupling reactors used in each arm of a leg. These reactors are used for the purpose of limiting current surges, short circuit current and high frequency current components in the converter [34], [86]. The resistance R represents the equivalent resistance of each of the converter arms and L_f and R_f are the external inductance and resistance of the converter used, depending on the application, for coupling with the grid or the load.

Still in Figure 2.1a, the voltages e_c^a, e_c^b and e_c^c are the produced ac voltages by the MMC, whereas v_o^a, v_o^b and v_o^c are the main-bus voltages. The same way, the ac

[1] it is also possible to have other configurations of SM based on full bridges. More information on this matter can be find in [87].

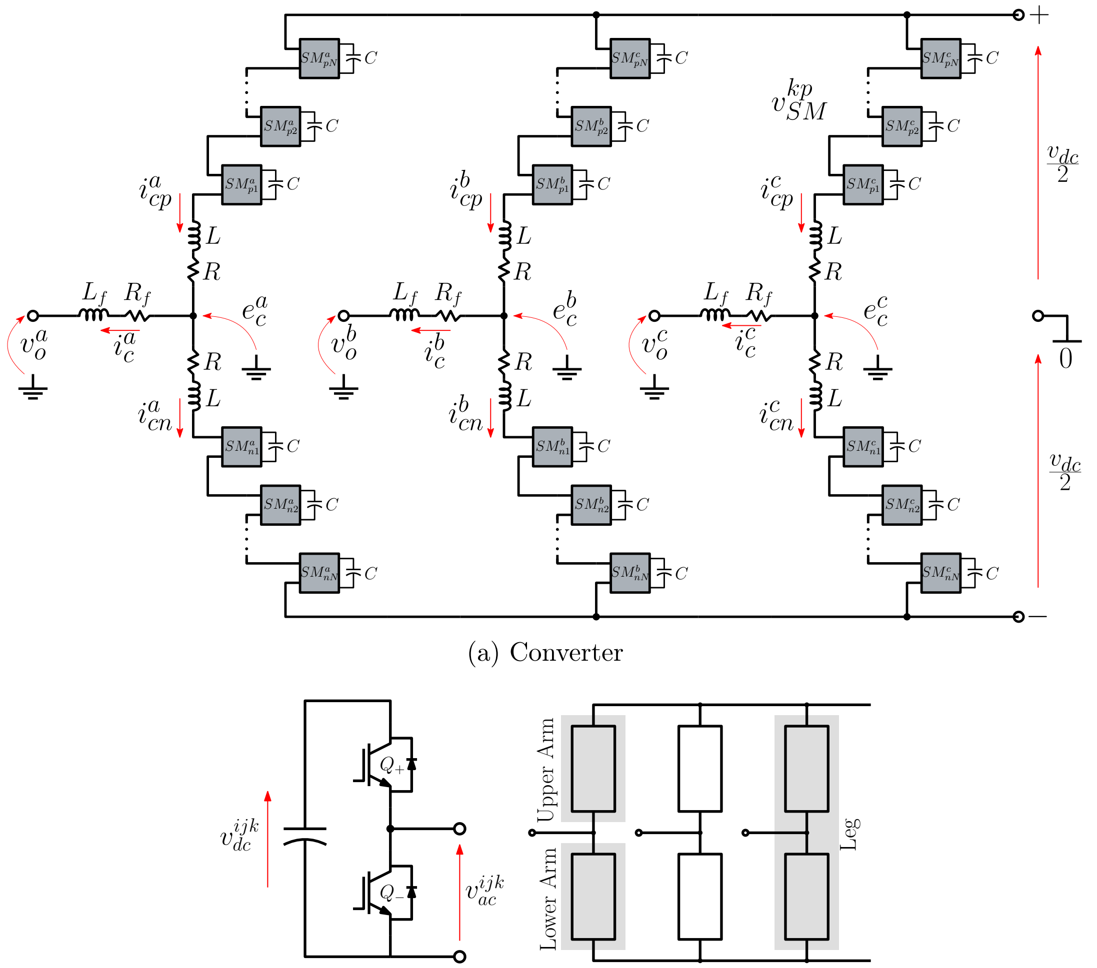

(a) Converter

(b) Submodule

(c) Definitions

Figure 2.1: Modular Multilevel Converter

currents i_c^a, i_c^b and i_c^c are the MMC output currents. The subscript p in i_{cp} and n in i_{cn} indicates that these are currents flowing through the upper and lower arms of a certain phase of the MMC. In all these cases, the superscript indicates the phase which each one of the variables belongs. Finally, v_{dc} is the dc-bus voltage of the MMC. It is important to notice that the ac voltages are measured considering the main ground bus as reference. In ideal condition, where the dc voltages and ac currents of the SM are balanced, there is no potential difference between the main bus ground and the middle point of the dc bus, labeled as 0 in Figure 2.1a.

The operation of the converter is simple, each of the SM has two possible states, ON and OFF. Depending on the signal level that each SM receives for the Q_+ and Q_- transistors, high or low, the dc voltage of that SM is or is not inserted in the ac-side circuit. Thus, the ac side of a certain SM, v_{ac}^{ijk} [2], can assume either v_{dc}^{ijk} or 0 depending on the firing signals. Consequently, the voltage produced on the AC side of the MMC depends on how many SM of each phase are inserted.

[2]Throughout this chapter, the superscript ijk indicates that the variable corresponds to the arm i (it can be either p for the upper or n for the lower arm of a certain phase), SM number j

The current flowing in each phase can be divided into two components as follows:

$$i_c^k(t) = i_{cp}^k(t) - i_{cn}^k(t), \tag{2.1}$$

where $i_{cp}^k(t)$ e $i_{cn}^k(t)$ are, respectively, the currents flowing through upper and lower arms of the phase k $(k = a,\ b,\ c)$ of the MMC.

In addition, it is possible to write the following net-equation following the loop through the upper arm to the middle point, 0, of the dc bus[3]:

$$e_c^k(t) = \frac{v_{dc}}{2} - \sum_{j=1}^{N} v_{ac}^{pjk}(t) - L\frac{di_{cp}^k(t)}{dt} - Ri_{cp}^k(t). \tag{2.2}$$

Similarly, considering the net-equation through the lower arm, we can write:

$$e_c^k(t) = -\frac{v_{dc}}{2} + \sum_{j=1}^{N} v_{ac}^{njk}(t) + L\frac{di_{cn}^k(t)}{dt} + Ri_{cn}^k(t). \tag{2.3}$$

Combining (2.2) and (2.3), it is possible to obtain the equation which describes the produced voltages $e_c^k(t)$ which are independent of dc-link voltage:

$$e_c^k(t) = \frac{1}{2}\sum_{j=1}^{N} v_{ac}^{njk}(t) - \frac{1}{2}\sum_{j=1}^{N} v_{ac}^{pjk}(t) - \frac{R}{2}i_c^k(t) - \frac{L}{2}\frac{di_c^k(t)}{dt} \tag{2.4}$$

The charts in Figure 2.2 illustrate the effect of the number of SMs per arm on the produced voltage $e_c^a(t)$. They were obtained from (2.5) considering both $N+1$ and $2N+1$ Nearest Level Control (NLC) [88] modulation approach. It is possible to observe that the increase in the number of submodules provides an output voltage with lower harmonic distortion, intuitively reducing the amplitude of the switching-frequency harmonic components. This feature, especially when the number of SM exceeds 20, exempts MMC from the use of high-frequency filters. This feature also allows the SMs to be switched with frequencies considerable lower than the frequency which a similar two-level converter would be driven, reducing the switching losses without increasing the total harmonic distortion (THD) of the produced voltages and currents.

---

and phase k $(k = a,\ b,\ c)$.

[3] As previously explained, it was considered the voltage between the ground of the ac main bus and the middle point of the dc bus is null.

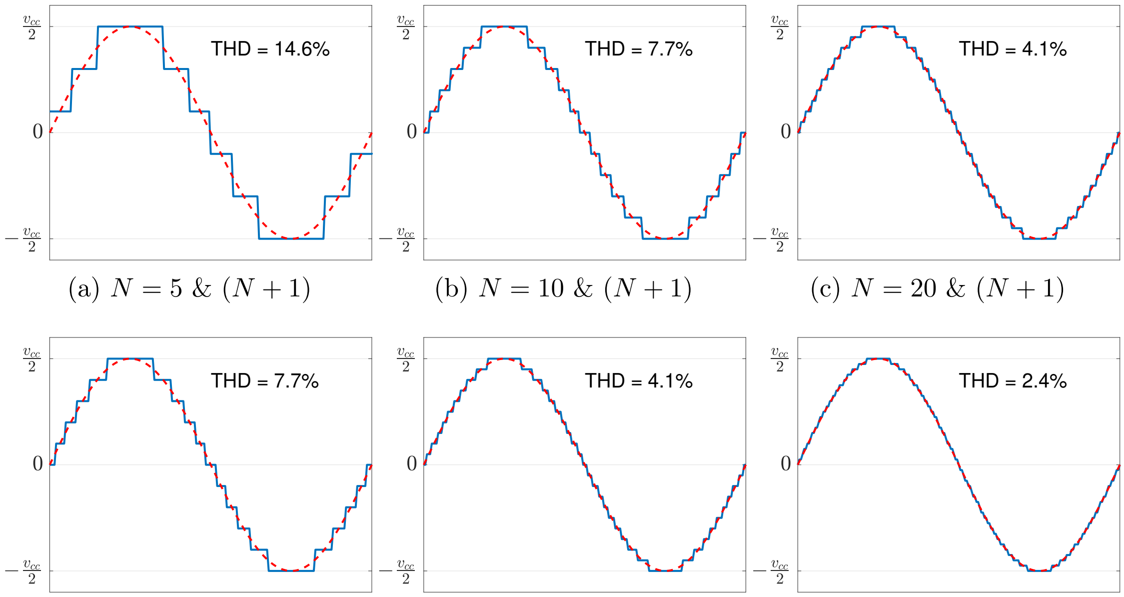

(a) $N = 5$ & $(N + 1)$ (b) $N = 10$ & $(N + 1)$ (c) $N = 20$ & $(N + 1)$

(d) $N = 5$ & $(2N + 1)$ (e) $N = 10$ & $(2N + 1)$ (f) $N = 20$ & $(2N + 1)$

Figure 2.2: Voltage produced by the MMC considering $N + 1$ and $2N + 1$ NLC modulation approaches. In this case is only presented the voltage at phase **a**.

2.2 Modulation Techniques

In this section a few MMC modulation techniques are presented in order to inform the reader how this PSCAD/EMTDC simulations used in the work were implemented. It was not taken into consideration how the modulation signals are obtained because it will be focused in Section 2.5[4].

In general, the modulation techniques for the MMC can be sorted in two main groups: carrier disposition and phase-shifted carrier. More details on these and other modulation approaches can be found in [89]. From hereafter, this section is focused in the carrier disposition approach once the modulation scheme used in the PSCAD/EMTDC belongs to this group.

The graphs in Figure 2.2, for example, were draw considering NLC modulation which is closer to the carrier disposition techniques. To better understand this technique which is the basis for other more advanced, we can refer to Figure 2.3. It is possible see a reference sinusoidal signal and a set of dashed horizontal lines indicated by *Levels* 1-4 in the upper part of the figure. In this case, the sinusoid is the modulating signal, while the dashed lines play the role of the modulation carriers of each one of the SMs (it is considered $N = 4$ for this example). The firing pulses of a given SM, shown at the bottom of the figure, are high when the reference signal is greater than its respective carrier and vice versa. It is important to notice that in

[4]To be in accordance of the literature, the modulation signals of the MMC is going to be called insertion indices in this work.

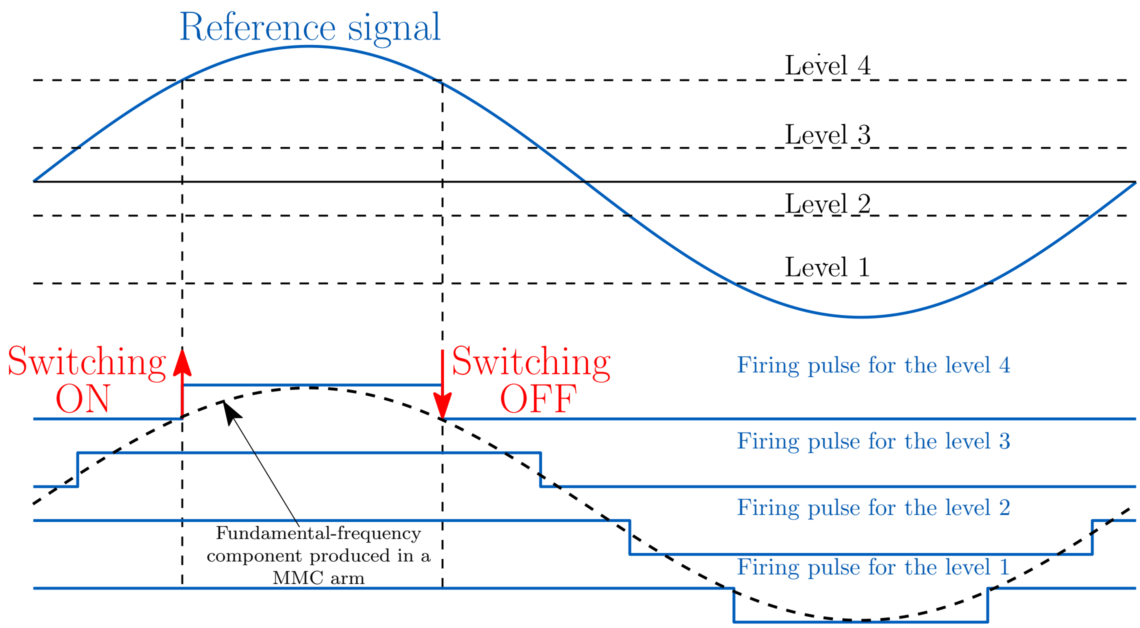

Figure 2.3: Firing signals of the MMC considering the NLC modulation technique. In this case, it was considered a four-SM-per-arm MMC. The upper chart shows the modulation signal and the levels. The lower chart shows the the firing pulses and the equivalent fundamental component of their sum.

this modulation approach each SM and consequently each IGBT is only switched on and off one time during the fundamental cycle of the output voltage. This feature is highlighted in the firing pulse of the level-4 SM in Figure 2.3. Another interesting feature to notice is that by adding the pulses of the SMs it is possible to obtain a signal with a shape similar to the equivalent voltage produced in the arm. Thus, the dashed sinusoidal signal in the lower portion of the figure is equivalent to a fundamental component produced in the analyzed arm.

A variation of the NLC approach is called Phase Disposition pulse width modulation (PD-PWM) and it belongs to the group of carrier disposition techniques. The difference between these techniques is that PD-PWM uses triangular carriers instead of level signals, as shown in the diagrams in Figure 2.4. As with NLC modulation, PD-PWM modulation can produce either $N+1$ or $2N+1$ levels, depending on the driving scheme used. For instance, to produce $N+1$ levels it is used N triangular carriers arranged as in Figure 2.4a. In this case, the results of the comparison between the modulating signal with the carriers are used to drive the upper-arm SMs, whereas the lower-arm SMs are driven by the complementary signals. PD-PWM modulation with $2N+1$ levels is performed according to the diagram in Figure 2.4b. In this case, two modulation signals and N carriers are used to generate $2N$ firing signals. The firing pulses generated by one modulation signal are directed to the upper arm SMs and the others to the lower SMs. It is important to mention that in both cases the pulses produced by the modulator are intended to drive the upper transistors, Q_+, from each of the modules[5]. Because it is a voltage source converter, the lower switches of the SMs are driven by complementary firing signals so as to prevent a short circuit in the dc voltage.

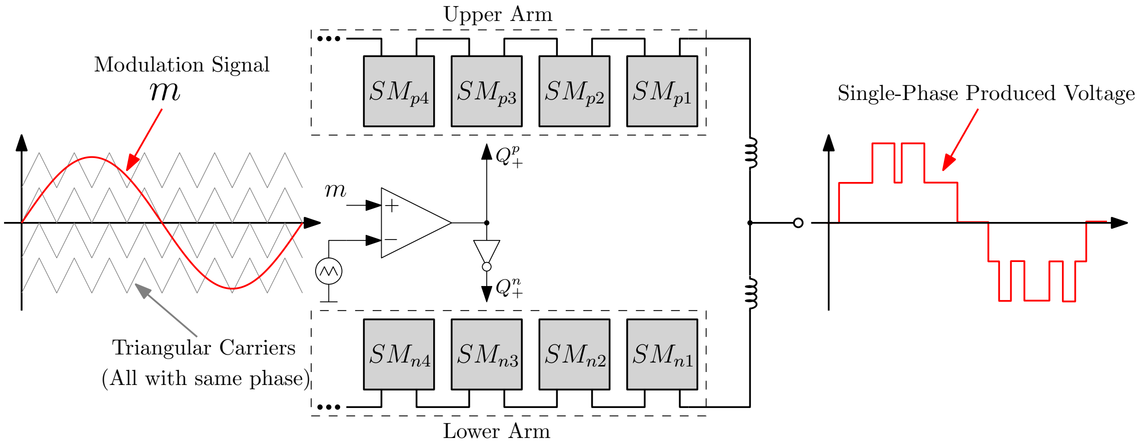

(a) $N + 1$ Levels

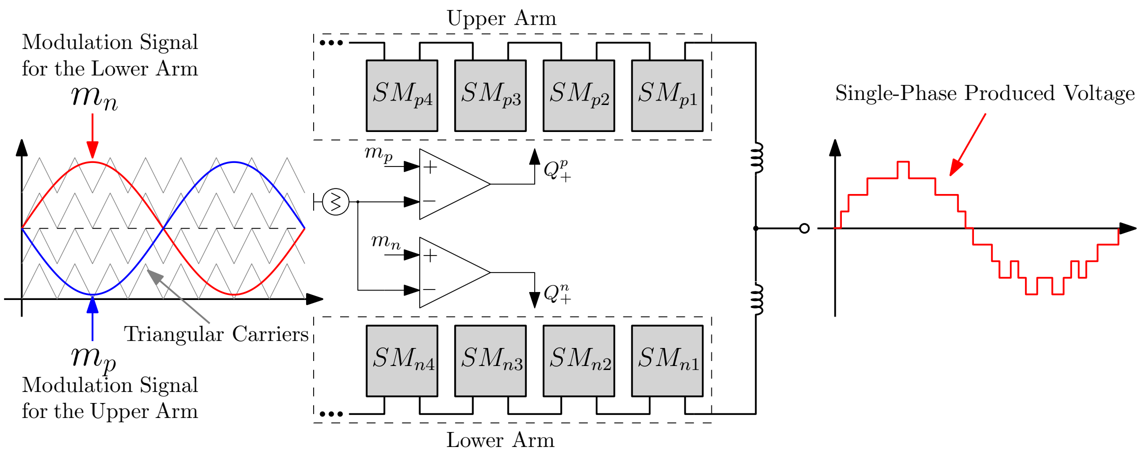

(b) $2N + 1$ Levels

Figure 2.4: Examples of $N + 1$ and $2N + 1$ PD-PWM schemes. In this case it was considered a four-SM-per-arm MMC to simplify the diagrams.

It is important to mention that the produced voltage is not affected by the order in which the firing pulses are linked to the SMs. In other words, the MMC produces the same voltage independently of which SM in a arm a certain firing signal drives. This fact is used to provide the balancing of the dc voltages of the SMs.

2.3 Balancing of the dc voltages of the SMs

As the MMC is driven, the capacitor voltages of the SMs start to change. Depending on the operating condition, certain modules may be driven by high pulses longer than others and this generates unbalance between the dc voltages of the modules.

[5]It is also possible to implement the $2N + 1$ PD-PWM considering a single modulation signals and $2N$ triangular carriers.

This condition is better illustrated by Figure 2.5, which corresponds to a generic five-SM-per-arm MMC driven to deliver 60Hz voltage to a resistive load. In this case, the converter does not have a SM dc-voltage balancing system and therefore its voltages are not kept with the same average value. In fact, it is easily observed that the dc voltages of some SMs increase uncontrollably, while in others SMs the opposite process occurs. This unbalance between the dc voltages affects the quality of the voltages produced on the ac side and may cause harmonic distortion or imbalance or even undesired dc components in the ac side. Besides that, in the worst scenario, the IGBTs of the SMs with the highest voltages would be submitted to prohibitive voltages, canceling the ability of the MMC of handling high voltages. For this reason the MMC driver must comprise dc-voltage balancing system along with the modulator.

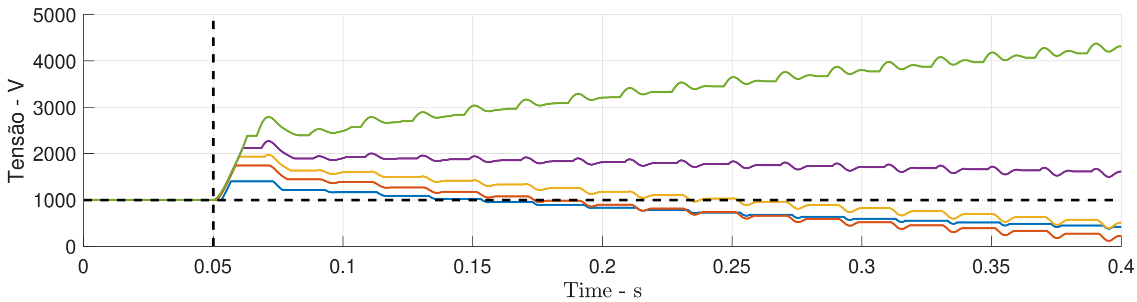

Figure 2.5: Typical dc voltage imbalance observed when the MMC does not have a voltage balancing system.

To understand the dc voltage balancing technique it is firstly necessary to understand the states each SM undergoes during the operation. Basically, the SM have four possible states as illustrated in Figure 2.6. In the first state, Figure 2.6a, the current i in the arm in which the SM is located flows upwards and Q_+ is ON. In this case, it is possible to observe that the current flows through the SM capacitor discharging it. In the second state, Figure 2.6a, the arm current is in the same direction, however Q_+ is OFF. According to the figure, the current flows through the Q_- diode, not interfering with the state of charge of the capacitor. In the other two conditions, Figures 2.6c and 2.6d, the current flows in the opposite direction, i.e. in the downward direction of the arm. Therefore, when Q_- is OFF the current flows through Q_+ diode into the capacitor, charging it, otherwise, the current flows through Q_-, thus bypassing the capacitor. Table 2.1 summarizes the explanation of this paragraph.

In views of the conditions explained in the previous paragraph, the voltage balancing module must simply direct the PWM pulses to the SMs so that the less charged capacitors are subjected to the recharge condition for a longer period of time, while those with the highest voltages are subjected to longer discharge conditions [69, 90].

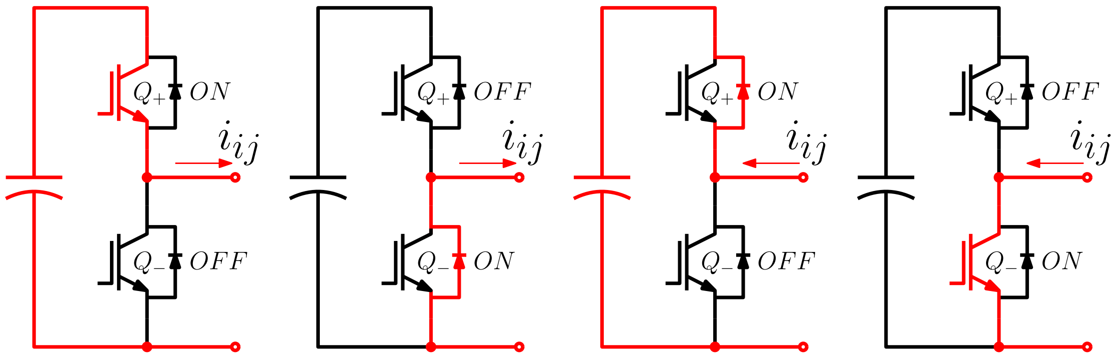

(a) i_{ij} upward and Q_+ ON (capacitor discharging)

(b) i_{ij} upward and Q_+ OFF (bypass)

(c) i_{ij} downward and Q_+ ON (capacitor charging)

(d) i_{ij} downward and Q_+ OFF (bypass)

Figure 2.6: Possible states of a SM during the operation.

This directioning is performed separately for each of the six arms of the converter so as to keep all the dc voltages balanced. Considering Q_+ enabled, according to Table 2.1, there will be capacitor recharge when $i_{ij} > 0$ and discharge when $i_{ij} < 0$, where i_{ij} is the current flowing through a given arm of the MMC. It is important to notice that the Q_+ switches are directly triggered by the PWM pulses and these tend to have a longer duty cycle when generated by comparing the reference signal with lower-level carriers, as seen in Figure 2.3. Consequently, the greater the PWM duty cycle is, the longer a given SM will be subject to the Q_+ enabled condition. It is also known that the produced ac voltage depends only on how many SM are inserted at a given time, yet not depending on which SM is inserted. Thus, as highlighted in the end of the previous section, it is possible to direct the PWM pulses as desired and the dc-voltage balancing system can be implemented as shown in Figure 2.7. Notice that, once the dc voltages are measured, the sorting algorithm provides a list (sorted voltages) indicating the capacitor in a crescent order of voltage. This result is used to determine at each balancing period which capacitor must preferentially be under recharge or discharge condition. Summarizing, the PWM signal which provide longer recharging states are directed to the SMs in which the capacitors have lowest voltages and the opposite with the PWM signal which provide longer discharge periods.

Table 2.1: States in which the SM capacitor undergoes during operation.

State of Q_+	**State of Q_-**	**Upward Current**	**Downward Current**
ON	OFF	Capacitor Discharging	Capacitor Recharging
OFF	ON	Capacitor Bypassed	Capacitor Bypassed

It is important to mention that the presented voltage balancing strategy is res-

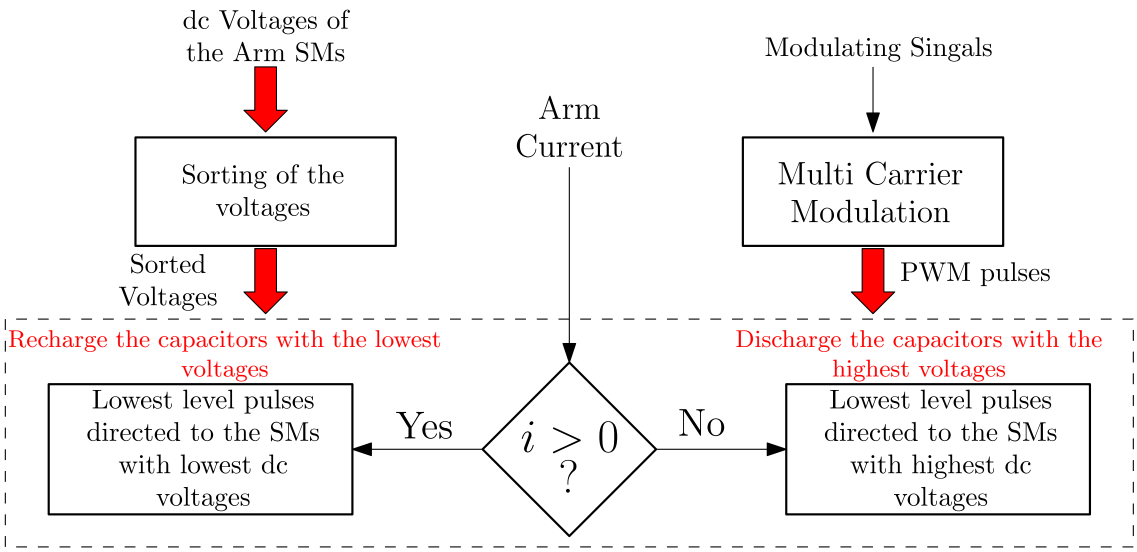

Figure 2.7: SM dc voltage balancing scheme used in this work.

ponsible to keep the average values of the dc voltages of each SM approximately at the same level. In fact, neglecting the resistive losses in the arms, the average values of the dc voltages under the balance approach may converge to V_{dc}/N. Nonetheless, their instantaneous values might not be equal due to inherent oscillating components. The effect of these components is better explained in the next section. To evaluate the effectiveness of the balancing strategy, the algorithm was used to balance the voltages of a $150kV$-dc voltage with 20 SM per arm, and the dc voltages of some of the SMs of the MMC are shown in Figure 2.8. It was chosen not to show

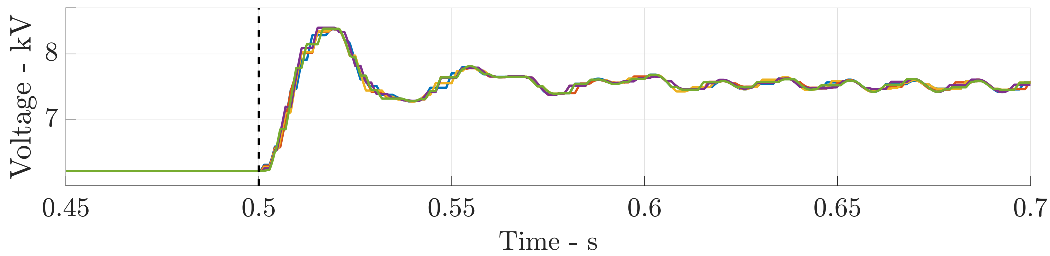

(a) Dc voltages

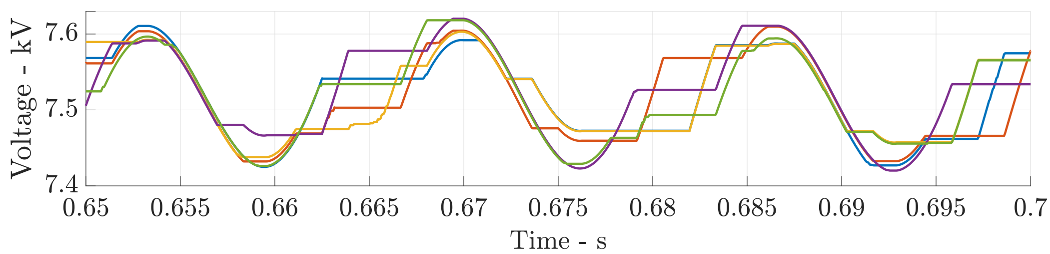

(b) Zoomed dc voltages

Figure 2.8: Time simulation showing how balanced are the SM dc voltages.

all the voltages in favor of a better distinction between the signal in the graph, but all the voltages presented a similar pattern. At $t = 0.5$ the MMC starts to be driven and differently from the case presented in Figure 2.5, the voltages are kept balanced around the average point. Notice in the zoomed graph in Figure 2.8b that balancing strategy makes each SM alternates between the bypassed condition, where the SM dc voltage remains constant, and the condition when the capacitor as either charged or discharged.

2.4 Circulating currents

To help understand the mechanism behind circulating currents, the phase **a** of the MMC is zoomed in Figure 2.9. In this case, just for the sake of the didactic, it is considered a time instant in which the second SM of the upper arm is in capacitor discharge condition. This was randomly chosen, and the explanation which is about to be developed is valid for any condition of the MMC.

Differently from a two-level converter, the legs of the MMC are not connected through a single dc bus. In fact, each of the phases of the MMC has two dc buses which are not coupled with the other phases. These buses, indeed, are formed by the electrolytic capacitors of the upper- and -lower arm SMs and play an important role in the inherent characteristic of the MMC. This decoupling between the buses makes the MMC behaves as three independent single-phase converters rather than a three-phase converter. In a single-phase converter [91], the instantaneous real power presents an oscillation component at the frequency of the second harmonic and so does the voltages of the dc buses. It is important to mention here that, because of the insertion of SM capacitors on the ac side of the MMC (this process is better explained in Section 2.5), these dc buses also comprise a fundamental-frequency oscillating component with amplitude greater than the second-order harmonic, as will be noticed in the simulation results later on. Once this fundamental-order component does not contribute to the circulating current, it is not considered in the analysis presented in this section. Thus, in steady-state condition of the dc voltages of the SMs can be represented by:

$$v_{dc}^{ijk}(t) = \frac{V_{dc}}{N} + \tilde{v}_{dc}^{ijk}(t) \tag{2.5}$$

where $\tilde{v}_{dc}^{ijk}$ is the oscillating component present in the dc voltages and V_{dc} is the average dc voltage.

Having concluded that the SM dc voltages comprise both dc and oscillating components, it is possible to explain its implications. As seen in Figure 2.9, the dc capacitors are inserted in the ac side of the converter so as to produce the desired ac voltage. Thus, it is possible to write the following net-equation:

$$V_{dc} - \sum_{inserted} v_{dc}^{pja}(t) - 2v_{RL}(t) - \sum_{inserted} v_{dc}^{nja}(t) = 0, \tag{2.6}$$

where v_{RL} is the voltage drop across the two arms RL circuits and $\sum_{inserted}$ counts only the dc voltages inserted in a certain time instant.

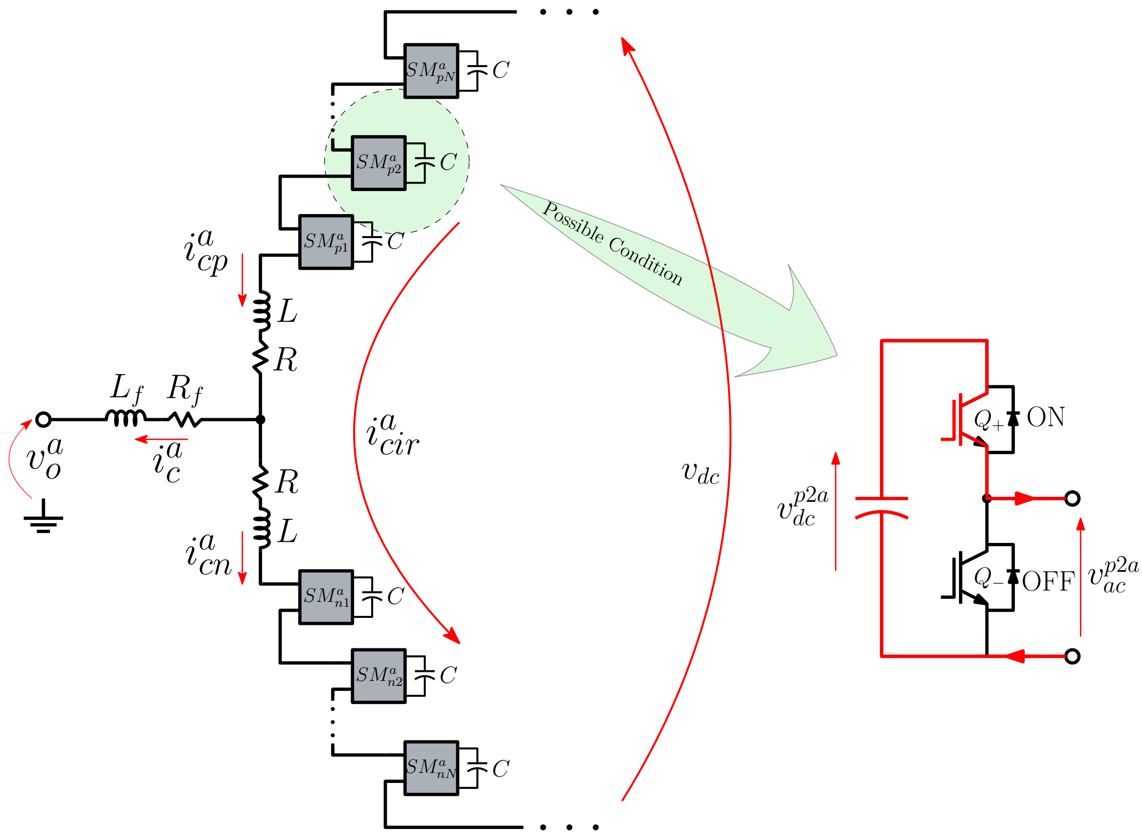

Figure 2.9: Circulating current: phase **a** of the MMC in a certain time instant. This figure is presented only to support the explanation of the circulating current.

Considering first that V_{dc} is constant, it is possible to realize that the oscillation components v_{dc}^{pja} and v_{dc}^{pja} are inserted in the ac side of the converter. Consequently, (2.6) indicates that v_{RL} comprises harmonic components corresponding to $\tilde{v}_{dc}^{ijk}$, such as the second harmonic component. The only way v_{RL} could present a harmonic component in the frequency of the oscillating component of $\tilde{v}_{dc}^{ijk}$ is having a current with this component flowing through the leg of the converter. This current is called circulating current and it is represented by i_{cir}^{k} in Figure 2.9 and throughout this work. This current circulates between the three legs and does not appear in the ac or dc sides of the MMC.

It is important to notice that the displacements of the oscillating components of the instantaneous real power of different phases are different, and so are the oscillating components of the dc voltages of the SM of different phases. As a consequence, even if v_{dc} were constant the circulating current probably would exist because the equivalent dc voltages of different phases are instantaneously different [90] among them. The previous paragraphs lead to the conclusion that the magnitude of the circulating current depends firstly on the power produced by the converter and secondly on the passive components, R, L and C, to be more specific. Indeed, the greater the produced power, the greater the oscillating component of the instantaneous power which is the primary cause of the circulating current. Also, the greater the SM capacitance C, the smaller the oscillating components of the dc voltages and, consequently, the smaller the circulating current. The same is valid for the coupling reactor L and the equivalent arm resistance R.

The presented discussion points out that i^k_{cir} presents mainly a second-harmonic component. To be more precise, it comprises a dc and other harmonic components as well. It is easy to notice, following the same approach of this discussion, that if the dc voltages contain other oscillating components, so do the circulating currents. Apart from that, i^k_{cir} also presents a dc component which is responsible for the energy balance of the converter so that:

$$\frac{1}{2\pi}\int_0^{2\pi} i^a_{cir} v_{dc}\, d\omega t + \frac{1}{2\pi}\int_0^{2\pi} i^b_{cir} v_{dc}\, d\omega t + \frac{1}{2\pi}\int_0^{2\pi} i^c_{cir} v_{dc}\, d\omega t = P, \tag{2.7}$$

where P is the active power produced by the MMC.

Here it is important to understand that, differently of the dc component, the second-harmonic component of i^k_{cir} is an undesired component. It, in a first analysis, causes losses and because of that it is common to apply specific techniques to mitigate it. Passive and active strategies are used in this regard [92–94], yet they are not analyzed in this chapter. Later on this work, the active strategies considered to mitigate the second harmonic are better explained.

Finally, it is possible to correlate this circulating current with i^k_{cp}, i^k_{cn} and i^k_c as follows [47, 53]:

$$\begin{aligned} i^k_{cp}(t) &= i^k_{cir}(t) + \tfrac{1}{2} i^k_c(t) \\ i^k_{cn}(t) &= i^k_{cir}(t) - \tfrac{1}{2} i^k_c(t) \end{aligned} \tag{2.8}$$

2.5 Insertion Indices

Before presenting the definition of the insertion indices it is necessary to better explain the insertion principle itself. As mentioned in the last section, depending on the firing pulses some SMs can have their dc capacitors inserted in the ac side of the converter or bypassed. Figure 2.10 presents a diagram with three SMs which exemplifies this idea. In this diagram, the current is flowing from the right to the left and the capacitors of the first and the third SMs are being inserted in the ac side.

Notice that in this time instant the total ac voltage is $v_{dc}^{p3a} + v_{dc}^{p1a}$ and, assuming that the voltage balancing system is working, this values is equal to $2V_{dc}/3$. Of course this condition changes over time so that the produced ac voltages assume a sinusoidal shape.

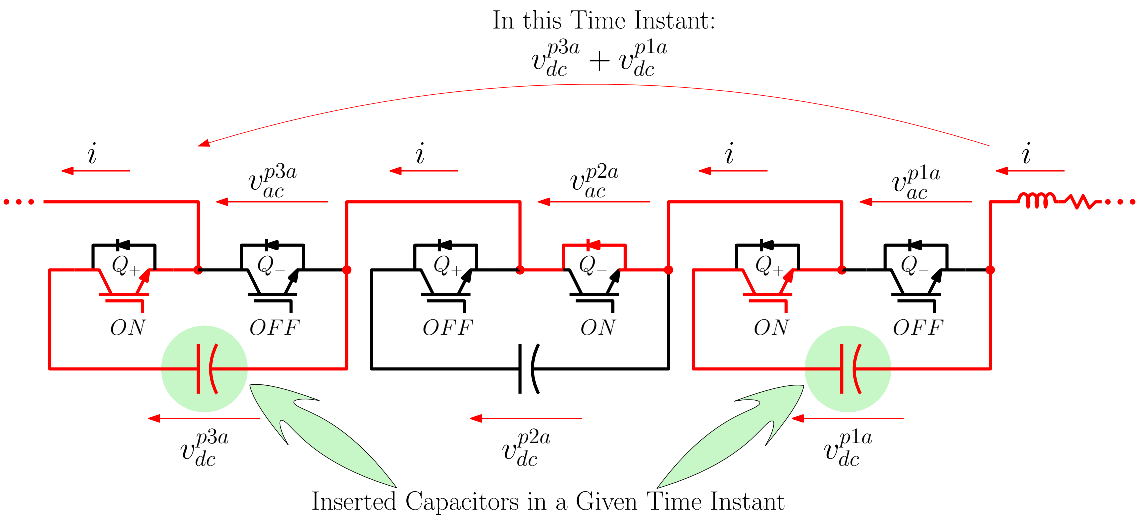

Figure 2.10: Diagram exemplifying the capacitor insertion.

The idea presented in the last paragraph can be extended to a generic MMC with N SMs per arm. In this case, the produced voltage in phase k by the set of SMs is given by:

$$\sum_{j=1}^{N} v_{ac}^{ijk}(t) = \sum_{inserted} v_{dc}^{ijk}(t) \approx M_i^k(t)\frac{V_{dc}}{N}, \tag{2.9}$$

where M_i^k is an integer number within the interval $[1,\ N]$ representing the number of inserted submodules in the arm j of the phase k in a given time instant. The plot of this integer variable, that is going to be called the discrete insertion index, assumes a shape similar to the voltage waveform observed in Figure 2.2 when considering a time window sprawling a fundamental-frequency cycle, yet assuming only positive integer values.

Still using Figure 2.6 for means of comparison of M_i^k, it is possible to state that for MMCs with $N \geq 20$ the difference between a discrete signal as M_i^k to a continuous one, over a fundamental cycle, is barely noticeably[6]. Thus, it is possible to substitute this integer variable, M_i^k, by its continuous-time, percent-based version:

$$m_i^k(t) = \frac{1}{N} M_i^k(t). \tag{2.10}$$

[6]It is analyzed in [95, Chapter 4] that with twenty levels, the produced voltage of the MMC stays under a 5% THD threshold, which is a level of distortion barely distinguished visually. With $N = 20$, it is possible to produce either 21 or 41 levels, depending on the modulation technique used.

These last variables, m_p^k and m_n^k, are called the insertion indices of the upper and lower arms of the phase **k** of the MMC.

As defined in [36] and [96], the insertion indices are computed so as to allow controlling the produced ac voltage, e_c^k, as well as mitigating undesired components of the circulating current. Note that, based on Figure 2.1b, the following net-equations can be written:

$$\frac{v_{dc}}{2} - m_p^k \sum_{j=1}^{N} v_{dc}^{pk}(t) - v_{RL}^{kp} = e_c^k, \tag{2.11}$$

$$-\frac{v_{dc}}{2} + m_n^k \sum_{j=1}^{N} v_{dc}^{nk}(t) + v_{RL}^{kn} = e_c^k. \tag{2.12}$$

It is important to notice in (2.11) and (2.12) that:

$$m_p^k \sum_{j=1}^{N} v_{dc}^{pjk}(t) \approx \sum_{inserted} v_{dc}^{pjk}(t), \tag{2.13}$$

$$m_n^k \sum_{j=1}^{N} v_{dc}^{njk}(t) \approx \sum_{inserted} v_{dc}^{njk}(t), \tag{2.14}$$

and that this result is valid when the dc voltages of the SMs are properly balanced.

One more approximation, explained in [36], can be embraced so that the determining of m_p^k and m_n^k could be simplified:

$$\sum_{j=1}^{N} v_{dc}^{pjk}(t) = \sum_{j=1}^{N} v_{dc}^{njk}(t) = V_{dc}. \tag{2.15}$$

Here it is important to mention that, although the second-harmonic component is excluded from the dc voltages the voltage drop v_{RL}^k will be kept so as to allow including a second-harmonic mitigation signal later on. Continuing, it is possible to obtain the following results from (2.13) and (2.14):

$$m_p^k(t) = \frac{V_{dc} - 2e_c^k(t) - 2v_{RL}^{pk}(t)}{2V_{dc}}, \tag{2.16}$$

$$m_n^k(t) = \frac{V_{dc} + 2e_c^k(t) - 2v_{RL}^{nk}(t)}{2V_{dc}}. \tag{2.17}$$

Making $e_c^{k*} = 2e_c^k/v_{dc}$ and $e_{cir}^{k*} = 2e_{cir}^k/v_{dc}$ it is possible to reach the final version of the insertion indices:

$$m_p^k(t) = \frac{1 - e_c^{k*}(t) - e_{cir}^{k*}(t)}{2}, \tag{2.18}$$

$$m_n^k(t) = \frac{1 + e_c^{k*}(t) - e_{cir}^{k*}(t)}{2}, \tag{2.19}$$

where e_c^{k*} is a normalized signal which is responsible for controlling the produced voltage of the MMC and e_{cir}^{k*} is also a normalized signal, yet with the objective of mitigating the second-harmonic component of the circulating current. Details on how these signals are computed are better explained in Sections 4.1 and 4.2.

It is worthwhile noticing that these indices are for the MMC what the modulation signals are for a regular two-level converter and, in fact, they represent how many SM are due to be inserted or bypassed during a specific time instant.

2.6 Preliminary simulations of the MMC

This sections aims at presenting some time-domain simulation results of the MMC considered throughout this work. In this case, it is considered a switching-level model, i.e., a model encompassing PWM-driven half-bridge SMs and the modulating and voltage balancing systems explained in Sections 2.2 and 2.3. This model was implemented in PSCAD/EMTDC considering the parameters presented in Table 2.2. Despite the fact that MMCs with the rated power and number of levels of this work are generally driven by under-$1kHz$ PWM signals, it was chosen the switching frequency of $4.8kHz$ so as to reduce the harmonic components of the circulating current and allow a better visualization of the major components.

Table 2.2: Parameters considered throughout this work.

Symbol	**Parameter**	**Value**	**Symbol**	**Parameter**	**Value**
V_{o0}	Rated line voltage	$69kV$	S_0	Rated power	$100MVA$
V_{dc0}	Rated dc voltage	$150kV$[7]	I_{dc0}	Rated dc Current	$666A$
f_1	Rated frequency	$60Hz$	ω_1	Rated Angular Frequency	$120\pi rad/s$
I_{c0}	Rated ac current	$838A$	R	Arm resistance	1Ω
R_f	Coupling resistance	1Ω	L	Arm inductance	$19mH$
L_f	Coupling inductance	$20mH$	N	Number of sub-modules per arm	20
C_f	Capacitor bank	$20\mu F$	C	Capacitance per sub-module	$9000\mu F$

As for the controlling system, it was decided to present here only open-loop results where the MMC is fed by a rated dc voltage source V_{dc} and supply ac voltage for a resistive load as in Figure 2.11. The amplitude of e_c^k was set to 0.75 and it was also decided not to include any circulating current mitigation approach so as to allow the visualization of the basic MMC characteristic. Last, but not least, all the results are presented in p.u., considering the rated values presented in Table 2.2, in order to facilitate the understanding of them. In this regard, it is important to mention that the rated dc current was used as basis for the circulating currents once they also present dc components.

[7]The dc voltage was chosen so that it overpass with a certain margin the minimum voltage (twice the peak of the single-phase ac voltage) for the converter to be fully controllable.

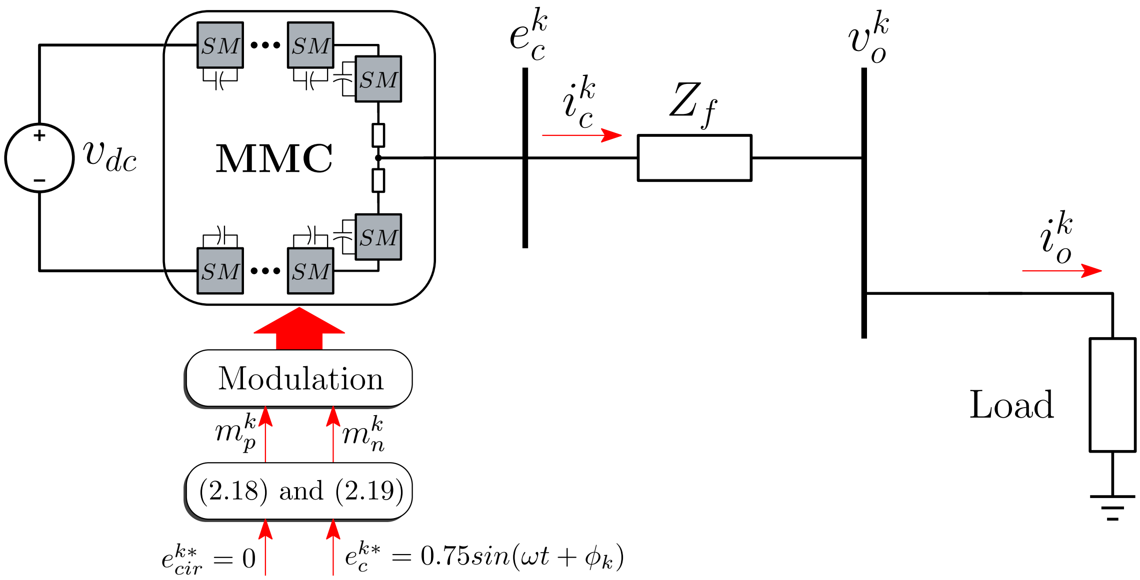

Figure 2.11: Schematic of the system used in the open-loop simulation.

The signals e_c^{k*} were kept null until $0.1s$ in order to let the SM capacitors be pre-charged by the dc source. The main results are presented in Figure 2.12.

As mentioned, produced voltages e_c^k and output currents i_c^k converge to near their rated values in about a fundamental cycle, as it is visualized in Figures 2.12a and 2.12b. The circulating current, on the other hand, undergoes a severe transient condition before reaching its steady-state condition. It is also possible to notice in Figure 2.12c the dc level predicted in Section 2.4. In Figures 2.12d and 2.12e it is possible to observe the dynamics of the SM capacitors dc voltages. Each one of the graphs presents the dc voltages of all forty SMs of the phase **a**. Notice that, differently from the results in Figure 2.5, the average values of all SM capacitor dc voltages converge to approximately the same value, $0.05p.u.$. This achievement is obtained by the voltage balancing system presented in Section 2.3.

The graphs in Figures 2.13, 2.14 and 2.15 zoom in some steady-state details overshadowed in Figure 2.12. For instance, the voltage levels of e_c^k are highlighted in Figures 2.13. As highlighted in Table 2.3 these voltages presented THD of 2.63% and their fundamental component present value of $0.97p.u.$ It was also noticed a small dc component in these voltages, $0.0001p.u.$ to be more precise, that is caused by a small difference in the balancing of upper and lower SM voltages. It was not presented any zoomed graph of i_c^k because it does not present any relevant point to be highlighted other than the ones visualized in 2.12b. Due to the reactors present in the circuit, these currents presented in steady state a THD of 0.23%, also presented in the Table 2.3.

A zoom in the steady-state condition of the circulating current is presented in Figure 2.14. Is is observed that neglecting the $0.3066p.u.$ dc component, the

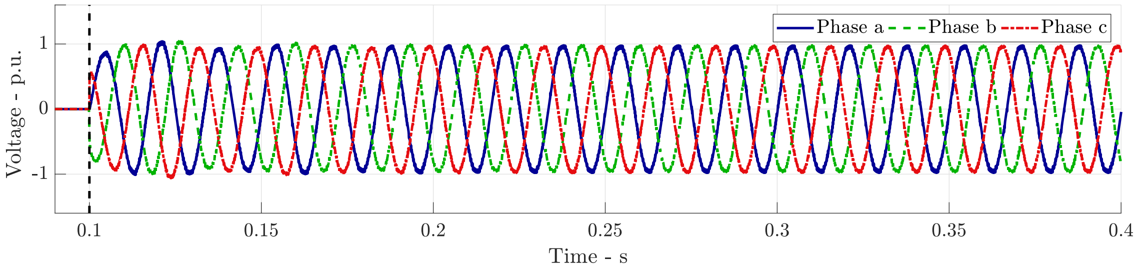

(a) Produced voltage e_c^k

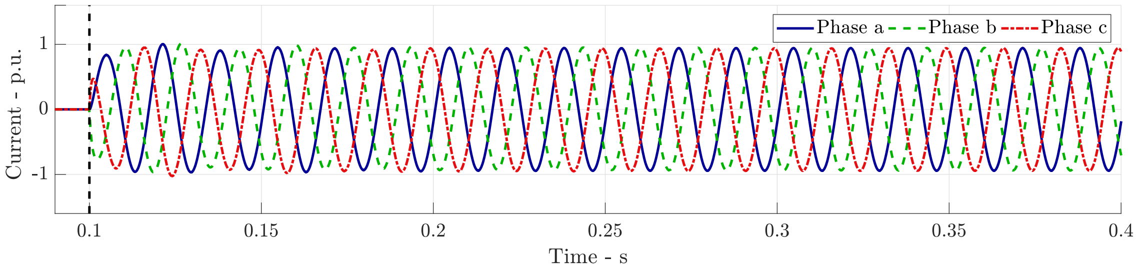

(b) Output current i_c^k

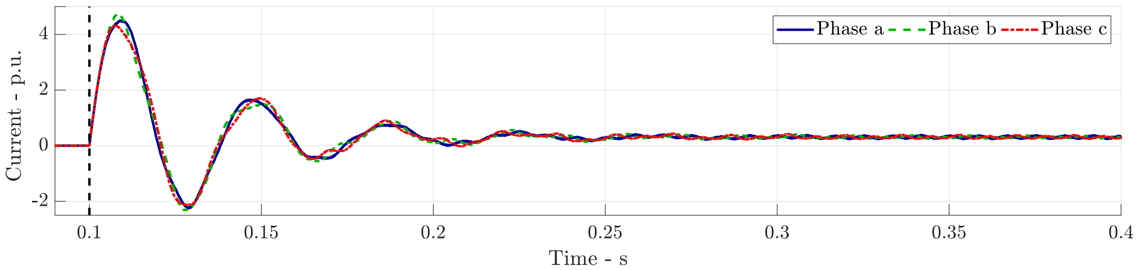

(c) Circulating current i_{cir}^k

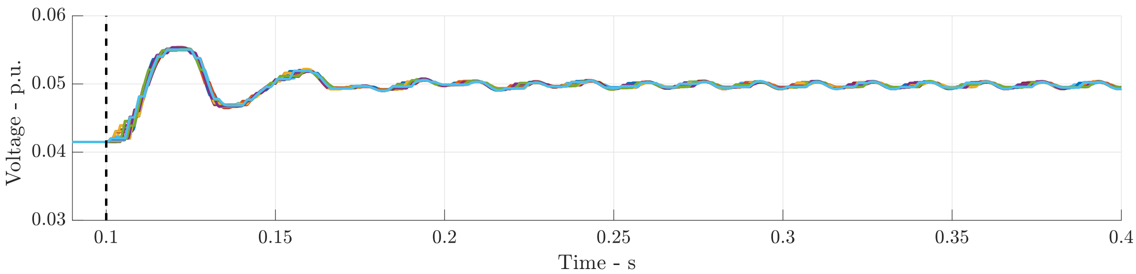

(d) Upper-arm SM capacitor dc voltages v_{dc}^{pja}, for $j = 1,\ 2,\ \cdots,\ N$

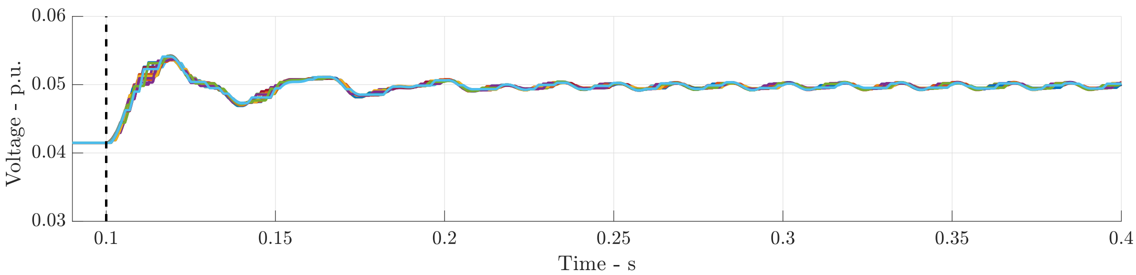

(e) Lower-arm SM capacitor dc voltages v_{dc}^{nja}, for $j = 1,\ 2,\ \cdots,\ N$

Figure 2.12: Simulation results of an open loop MMC obtained from a switch-level model in PSCAD/EMTDC.

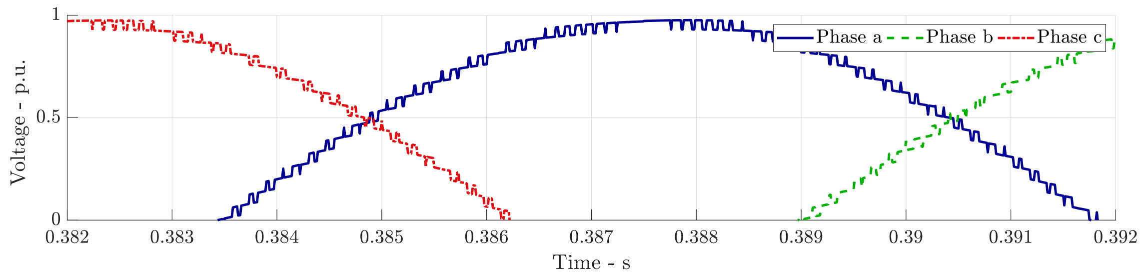

Figure 2.13: Simulation results of an open loop MMC obtained from a switch-level model in PSCAD/EMTDC: Zoom in e_c^k

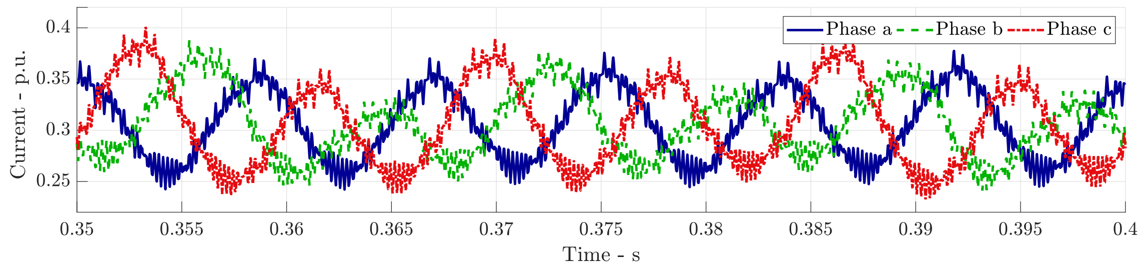

Figure 2.14: Simulation results of an open loop MMC obtained from a switch-level model in PSCAD/EMTDC: Zoom in i_{cir}^k

major component is the second harmonic, in this case with $0.0449p.u.$. It is also present in these currents a fundamental-frequency component of $0.0032p.u.$ caused by imbalance mentioned in the last paragraph. It was not noted in the presented case any other significant harmonic component in these currents. In fact, to be more precise, these signals present other even-order harmonic components, yet they did not reach to four-digit precision adopted for the results in Table 2.3.

Figure 2.15 presents a zoom in all the dc voltages of the phase **a** of the MMC. It is possible to observe with more details their oscillating components and the effect of the voltage balancing system. To keep up with the four-digit approach, Table 2.3 presents the main components of the equivalent dc voltages, i.e., the sum of the upper and the sum of lower dc voltages. Then, it is noted that these equivalent voltages present dc, fundamental and second-harmonic components. The fundamental components of the upper and lower arms are complementary, which means that their sum ideally would be zero. In this case, a small difference of about

Table 2.3: Harmonic components of the variables obtained from a switch-level model in PSCAD/EMTDC.

Variable	Symbol	dc	1st	2nd	3rd	4th	THD
Produced Voltage	e_c^k	0.0001	0.9729	0.0000	0.0012	0.0004	2.63%
Output Current	i_c^k	0.0001	0.9418	0.0000	0.0011	0.0001	0.23%
Circulating Current	i_{cir}^k	0.3066	0.0032	0.0449	0.0000	0.0000	–
Sum of upper-arm SM voltage	$\sum v_{dc}^{pjk}$	0.9959	0.0083	0.0023	0.0000	0.0000	–
Sum of lower-arm SM voltage	$\sum v_{dc}^{njk}$	0.9957	0.0082	0.0023	0.0000	0.0000	–

$0.0001p.u.$ is notices and this difference caused the fundamental component in the circulating current.

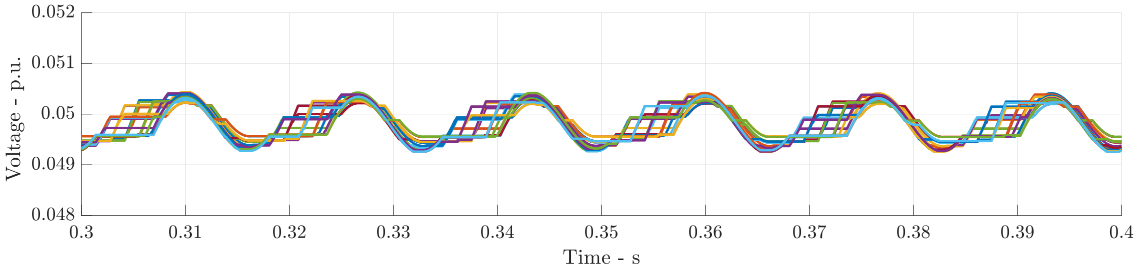

(a) Upper-arm SM capacitor dc voltages v_{dc}^{pja}, for $j = 1,\ 2,\ \cdots,\ N$

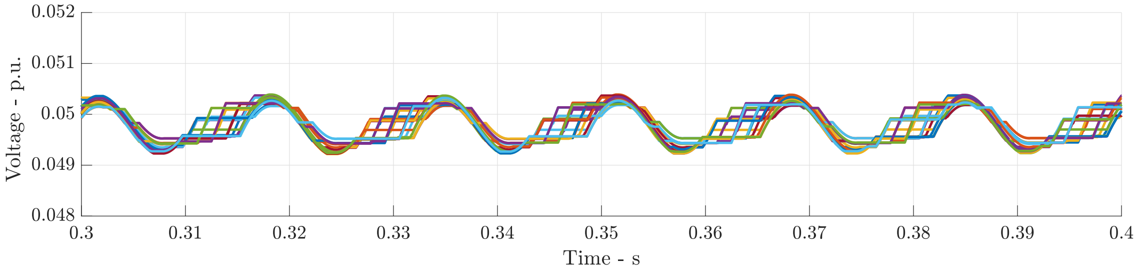

(b) Lower-arm SM capacitor dc voltages v_{dc}^{nja}, for $j = 1,\ 2,\ \cdots,\ N$

Figure 2.15: Simulation results of an open loop MMC obtained from a switch-level model in PSCAD/EMTDC: Zoom in v_{dc}^{ijk}

2.7 Partial conclusions

This chapter presented an overview of the MMC with focus on its working principle, the modulating and voltage balancing techniques used in the switching-level simulations presented in this work. It was shown that the dc voltage is not uniformly divided among the dc-side capacitors unless a voltage-balancing algorithm is combined with the modulation scheme. This algorithm is based on the inherent redundancy of the MMC, which makes it possible to produce a certain ac voltage by different combinations of inserted SMs. This algorithm chooses the combination which best fits on the purpose of keeping the dc voltages balanced, i.e., the combination that submits, whenever possible, the lowest-voltage capacitors to a rechanging condition and the opposite for the ones with highest voltages. It was also shown that the MMC presents an inherent undesired component circulating through the arms without contributing to the output current of the converter. These components are majored in the second-harmonic component, although it is also possible to find other even-order harmonic components. The PSCAD/EMTDC simulation results showed that the harmonic distortions of the voltage and current produced are as small as 2.6% and 0.2%, respectively, although some differences between the dc voltages could cause small dc components in these variables.

Chapter 3

State-space average and steady-state models of the MMC

The objective of this chapter is to present a time-domain analytical model for the MMC considering the dynamics of the circulating currents and the equivalent dc voltages, yet letting apart the control loops. The quintessence of the model presented in this section is the average modeling technique, in which the dynamics of switching-frequency components are neglected in face of the main components of the variables of the converter. Despite the fact the averaging approach clear out the switching-frequency components, the model developed remains non-linear due to the inherent characteristics of the MMC, hence, the definition non-linear, time-domain model might be used throughout this work to refer to this model. Still in this chapter, some simulations were carried out, and their results compared to the results obtained with the switching-level model, to show that the non-linear, time-domain model accurately describes the behavior of the MMC. After that, the non-linear state-space model was used to derive an analytical steady-state solution for the variables of the MMC. This result allowed analyzing the influence of active and reactive power in the harmonic components of the variables of the MMC. Towards the end of the chapter, the state-space model is presented and then linearized, and this new version becomes the starting point for the development of the models in Sections 4.1 and 4.2.

3.1 Average-value modeling of the MMC

Before presenting how the average-value modeling approach is applied to the MMC, it is quite important show its working principle. For this matter, Figure 3.1 was prepared showing an simple one-SM-per-arm MMC and its time-domain variables, current and voltage. Notice that, the choice of this configuration rather than the 20-SM-per-arm used in the work intends only to simplify and generalize the explanation.

The average-value modeling approach consists on considering only the average values of the variables over a switching period. This is represented in the graph at the left side of the figure. It is possible to observe that the ac variables assume a staircase-like pattern with a clear dominant sinusoidal component. The number of steps in these variables depends on the ratio between the frequencies of the analyzed signals and the frequency of the modulation carrier. This ratio was made small (10 times) in the figure so as to improve the visualization, yet in real converters it can reach values as huge as hundreds or thousands. Thus, the staircase-like signals can be approximated to continuous signals such as presented in the rightest part of the graphs in the figure. In general, the continuous approximation is used to represent the average behavior of power electronic converters. It is important to mention that the average-value modeling can be applied to ac and dc variables alike[97–100].

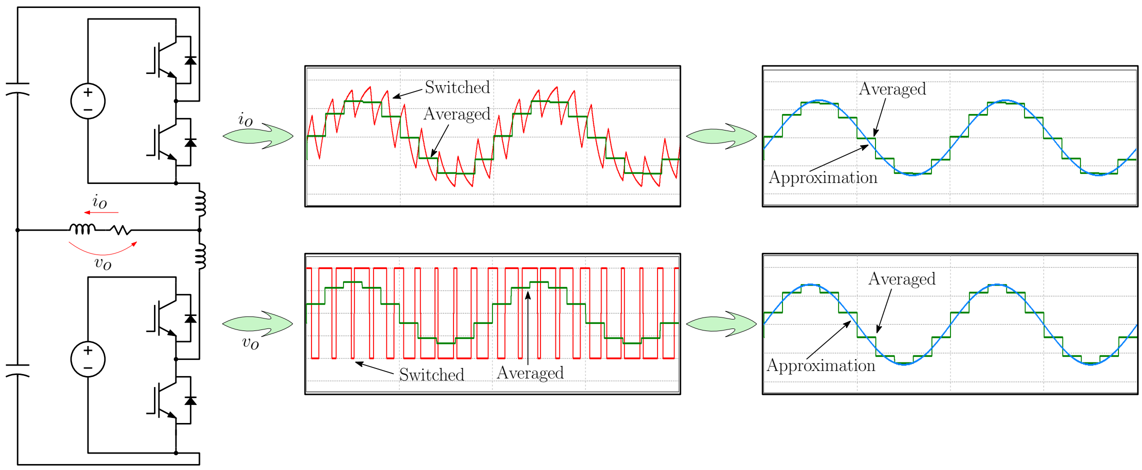

Figure 3.1: Average modeling principle. One SM per arm is used to facilitate the explanation.

Some of the results presented in Section 2.5 are quite useful for this chapter and they might be reproduced here. Firstly, the diagram of the Figure 2.10 was adapted and presented in the Figure 3.2 so as to help understanding the average-value modeling of the MMC. Notice in the figure that at given time instant a certain amount of capacitors are inserted in the ac side of the arm. The equivalent voltage produced by the set of SMs of a certain arm, v_{ac}^{ik}, then, can be described by:

$$v_{ac}^{pk}(t) = m_p^k(t) \sum_{j=1}^{N} v_{dc}^{pjk}(t) \approx \sum_{inserted} v_{dc}^{pjk}(t), \tag{3.1}$$

$$v_{ac}^{nk}(t) = m_n^k(t) \sum_{j=1}^{N} v_{dc}^{njk}(t) \approx \sum_{inserted} v_{dc}^{njk}(t), \tag{3.2}$$

as previously presented in (2.13) and (2.14).

The state-space modeling is only presented in the next section, but right here it is

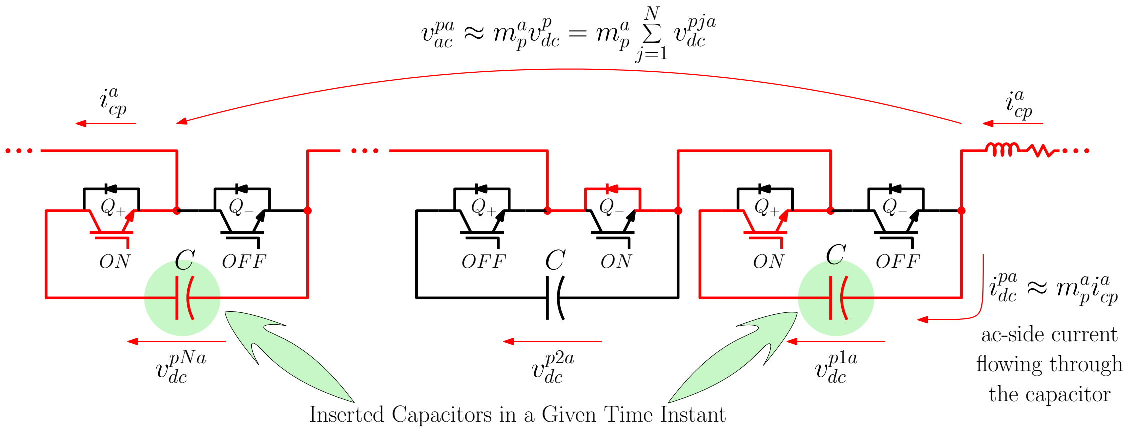

Figure 3.2: Diagram exemplifying the capacitor insertion in the average-value modeling context. It was considered the upper arm of phase **a** of a generic N-SM-per-arm MMC.

possible to conclude that the greater the number of capacitors the large the number of state equations to represent the MMC. For this reason, instead of considering all the dc voltages of an arm, they might be combined into one equivalent dc voltage. Thus, from this point on, the sums $\sum v_{dc}^{pjk}$ and $\sum v_{dc}^{njk}$ are defined as state variables of the MMC and represented by v_{dc}^{pk} and v_{dc}^{pn} as follows:

$$v_{dc}^{pk}(t) = \sum_{j=1}^{N} v_{dc}^{pjk}(t), \tag{3.3}$$

$$v_{dc}^{nk}(t) = \sum_{j=1}^{N} v_{dc}^{njk}(t). \tag{3.4}$$

Combining the results presented in (3.3) and (3.4) with the results in (3.1) and (3.2) it is possible to find the following relationship between the equivalent dc and ac voltages of the SMs of an arm:

$$v_{ac}^{pk}(t) = m_p^k(t) v_{dc}^{pk}(t), \tag{3.5}$$

$$v_{ac}^{nk}(t) = m_n^k(t) v_{dc}^{nk}(t). \tag{3.6}$$

Notice that, as the time-continuous variables $m_p^k(t)$ and $m_n^k(t)$ are used instead of the staircase-like M_p^k and M_n^k, these equations represent the average-value representation of the set of SMs of the arms of the MMC.

Other aspect that must be highlighted is that once v_{dc}^{pk} and v_{dc}^{pn} are state variables, they have to represent the voltage across an energy-storage element, in this case, an equivalent capacitor C_{eq}. To determine this equivalent capacitor and how it interacts with the circuit it is necessary to analyze Figure 3.2 once more. Observe that in a given time instant a certain number of capacitors C are connected in series[1]. In fact, this number is equal to M_i^k, where the index i can assume either p or n depending on the arm this insertion index control. A possible approach here would be replacing the SMs of the arms by capacitance-variable capacitors, i.e., making $C_{eq} = C/M_i^k \approx C/(Nm_i^k)$. This approach would require some adaptations in the capacitor voltage-current relationship and because of that it is not being used. Instead, the common approach used to solve this problem is using voltage and current sources to represent the set of SMs of arm [47, 101], as is presented in Figure 3.3. In this diagram the ac side of a group of SMs is represented by a controlled voltage source which implements either (3.5) or (3.6) depending if the SMs are located in the upper o lower arm of the phase **k**. Notice that, when it comes to the voltage produced in the ac side, this approach leads to the same result of using capacitance-variable capacitors. It is also important to notice that, were the capacitance-variable-capacitor approach used, the current flowing through this capacitor would be either i_{cp}^k or i_{cn}^k. Then:

$$\frac{dv_{dc}^{ik}}{dt}(t) = \frac{1}{C_{eq}} i_{ci}^k(t) = \frac{Nm_i^k(t)}{C} i_{ci}^k(t) = \frac{1}{C/N}\ m_i^k(t) i_{ci}^k(t). \tag{3.7}$$

From (3.7) it is possible to conclude that the effect of the capacitance-variable capacitor can be mimicked by a constant-capacitance capacitor so that:

$$C_{eq} = \frac{C}{N}. \tag{3.8}$$

The current which flow through this capacitor, now, depends on the arm current and the insertion index associated to that arm. For this reason, the capacitor in

[1]In the time instant in which Figure 3.2 was captured, the capacitors of the SM_{p1} and SM_{pN} are connected in series. The capacitor of SM_{p2}, though, is bypassed.

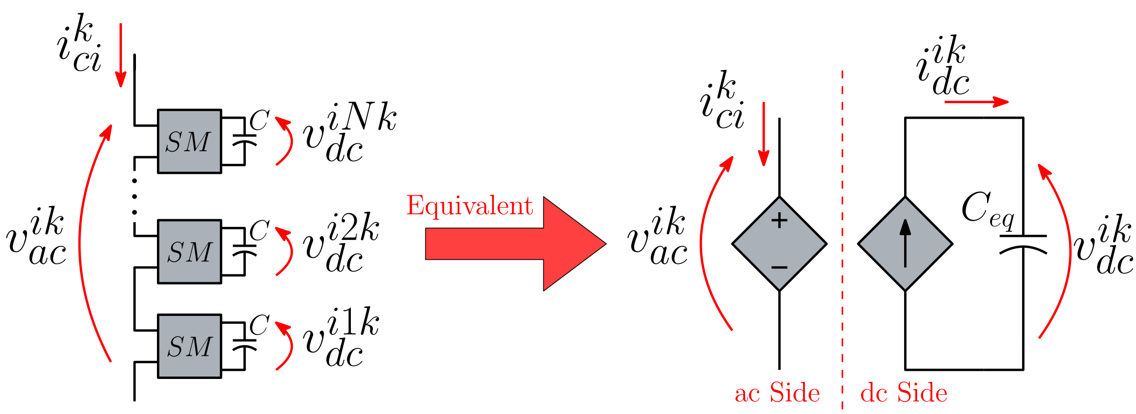

Figure 3.3: Average-value equivalent model of a group of SM in an arm of the MMC. The superscript i can either be p or n depending whether the SM are located in the upper or lower arm. The superscript k indicates the phase (a, b or c).

Figure 3.3 is connected to a current source which precisely produces this dc current as follows:

$$i_{dc}^{pk}(t) = m_p^k(t) i_{cp}^k(t), \tag{3.9}$$

$$i_{dc}^{nk}(t) = m_n^k(t) i_{cn}^k(t). \tag{3.10}$$

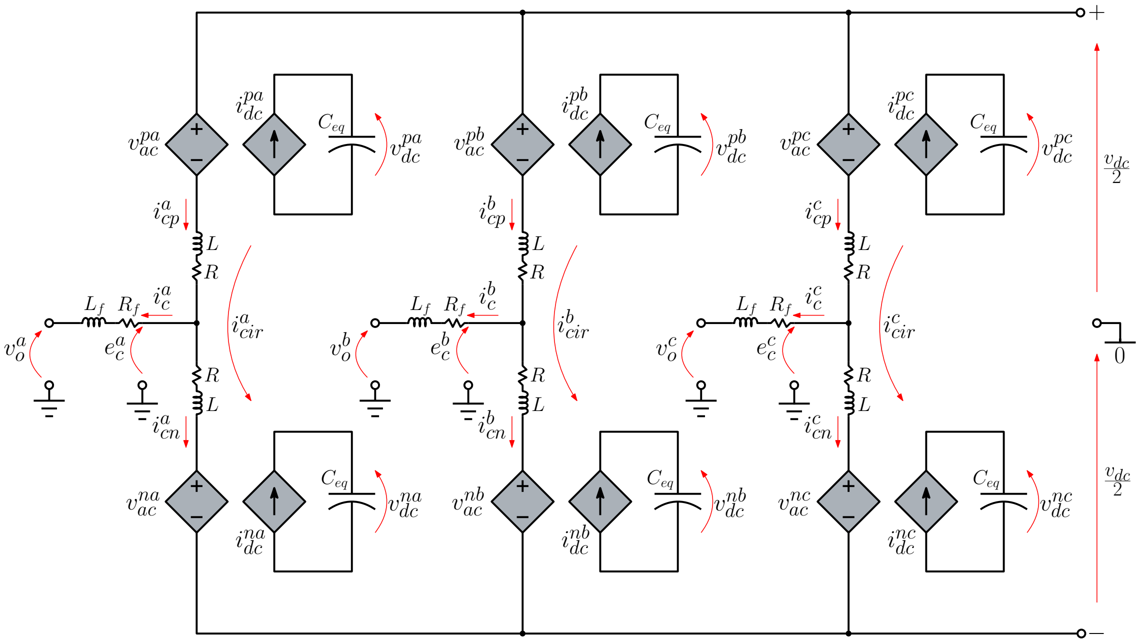

Figure 3.4: Circuit representation of the average-value model of the MMC.

Replacing all the SMs of each arm by the equivalent representation shown in Figure 3.3 it is finally possible to reach average-value model of the MMC presented in Figure 3.4. Throughout this text, this model may either be called average-value model or non-linear, time-domain model.

3.2 Comparison between the analytical non-linear model and the PSCAD model

In order to validate the non-linear, time-domain model presented in the last section, some simulations were carried out and the results compared with the results obtained with the switching-level model of the Chapter 2. Some points must be explained beforehand. First of all, in the switching-level model the SM capacitors are initially charged even before the MMC is enabled because of the diodes of the switches. As this effect is not encompassed by the average-value model, it was decided setting initial dc voltages in the capacitors corresponding to this pre-charge. As already mentioned in Chapter 2, the switching-level model was simulated in PSCAD/EMTDC and due to numeric convergence aspects the resistance of the switches

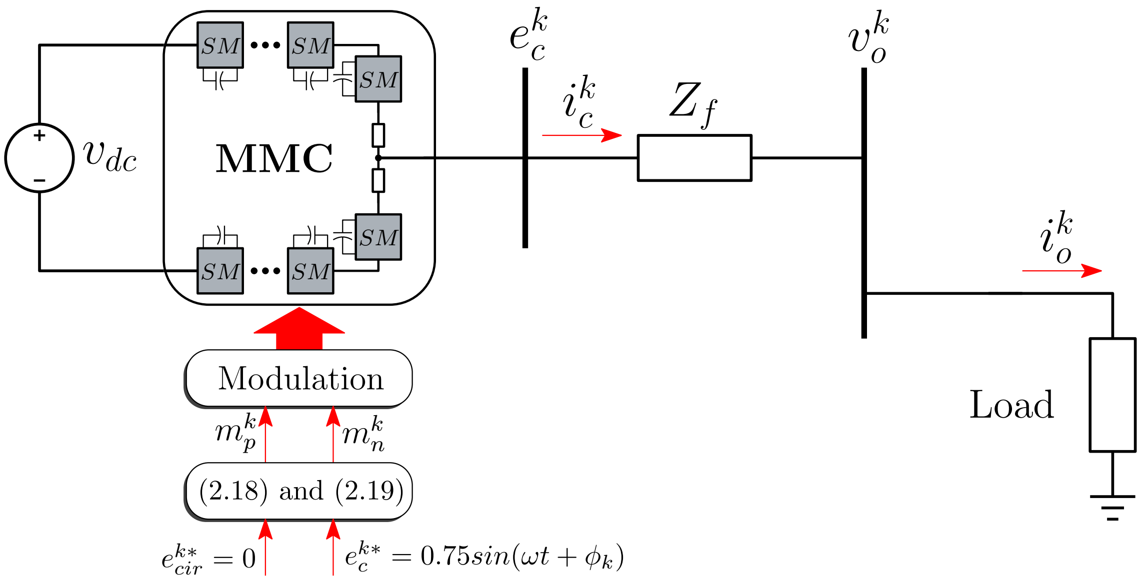

Figure 3.5: Schematic of the system used in the open-loop simulation.

could not be made null. In the PSCAD/EMTDC model, the total resistance of the SMs of an arm is 0.2Ω and to match the effects, the resistance R was changed from 1Ω to 1.2Ω in the averaged model. Finally, the averaged model was simulated in PSIM for any other reason than the simplicity in implementation in this software. In summary, the MMC was driven in open loop, as shown in Figure 3.5 presents the system considered. In this case, the reference signals e_c^{k*} were set with 0.75-peak 60Hz sinusoidal signals, so that the produced voltages e_c^k reached the rated value given in Table 2.2. As for e_{cir}^{k*}, they were kept null to allow verifying whether the non-linear model matches the detailed PSCAD model when it comes to the circulating current i_{cir}^k. Last, yet not least, the dc voltage v_{dc} was set to its rated value $150kV$ and the load was considered to be purely resistive, also assuming its rated values of 47.6Ω.

Figures 3.6 and 3.7 present the results corresponding to the phase **a** for the produced voltage e_c^a, output current i_c^a, circulating current i_{cir}^a and the equivalent dc voltages v_{dc}^{pa} and v_{dc}^{na} for the transient and steady-state condition. In all cases, it was used solid blue lines for the results of the switching-level PSCAD/EMTDC model and dash-dotted red lines for the results of the proposed average-value PSIM model. It is possible to observe that the model presented in the last section accurately predicts the behavior of the MMC both in steady-state and transient regime. The small differences between the results for i_{cir}^a in Figure 3.6c, though, are caused by some switching effects that are not included in the average-value model.

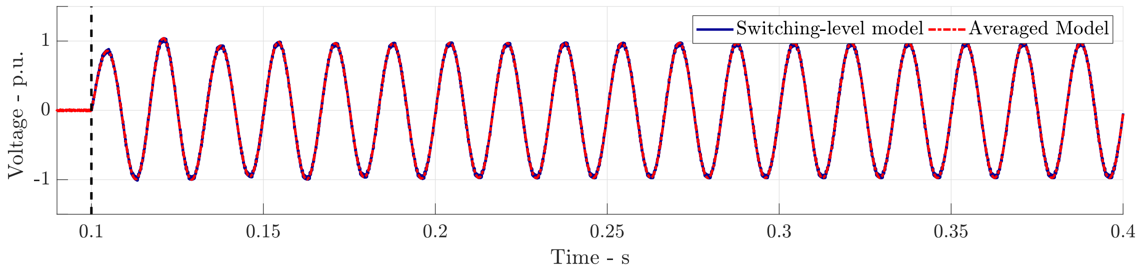

(a) Produced voltage e_c^a

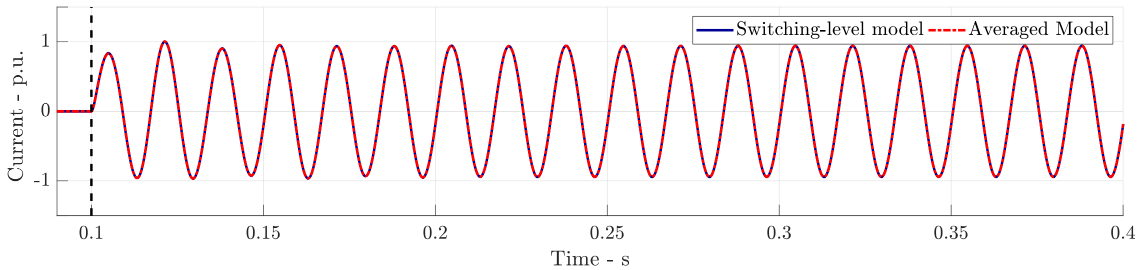

(b) Output current i_c^a

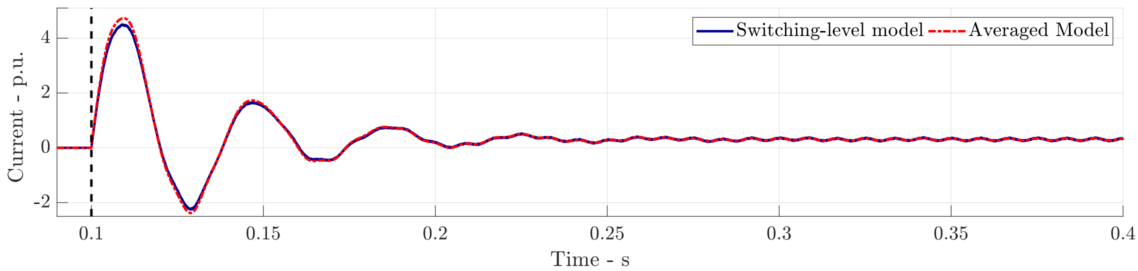

(c) Circulating current i_{cir}^a

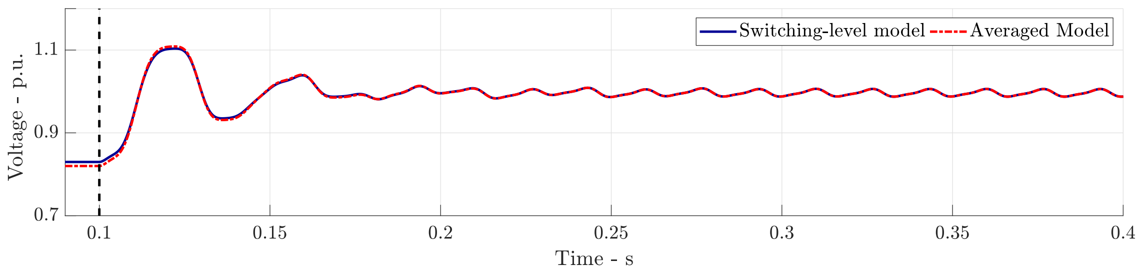

(d) Upper-arm equivalent dc voltage v_{dc}^{pa}

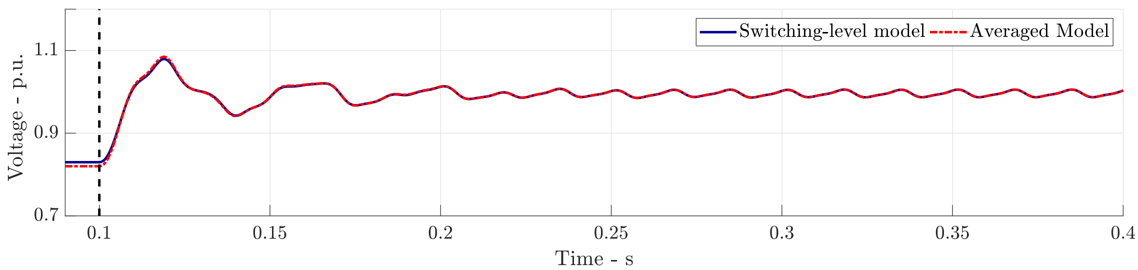

(e) Lower-arm equivalent dc voltage v_{dc}^{na}

Figure 3.6: Comparison between the results obtained with the switching-level model and the averaged model. The switching model was implemented in PS-CAD/EMTDC, whereas the averaged model (non-linear, time-domain model) was implemented in PSIM. Only the results for the phase **a** are presented for the sake of space.

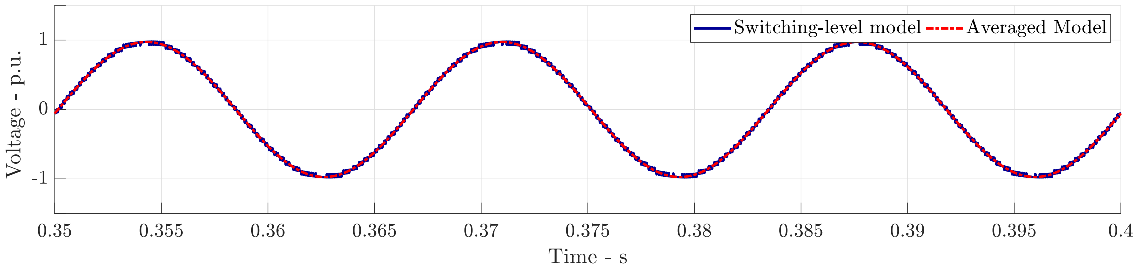

(a) Produced voltage e_c^a

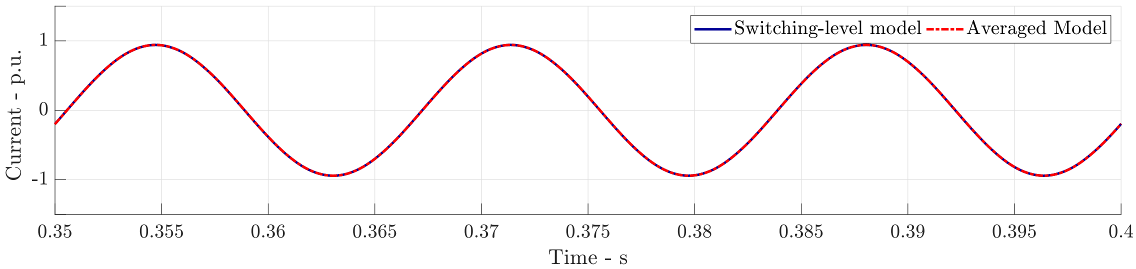

(b) Output current i_c^a

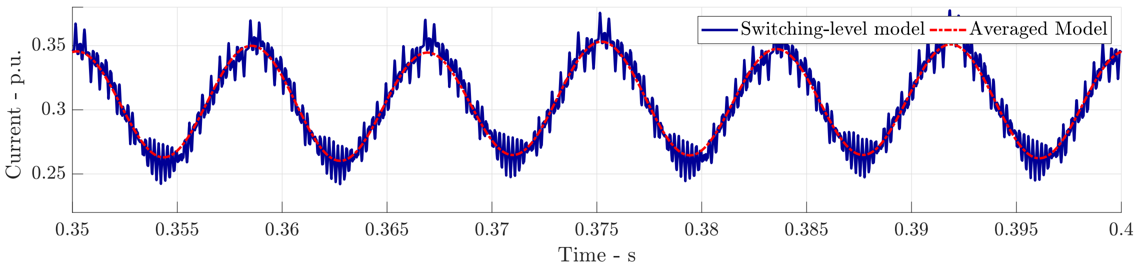

(c) Circulating current i_{cir}^a

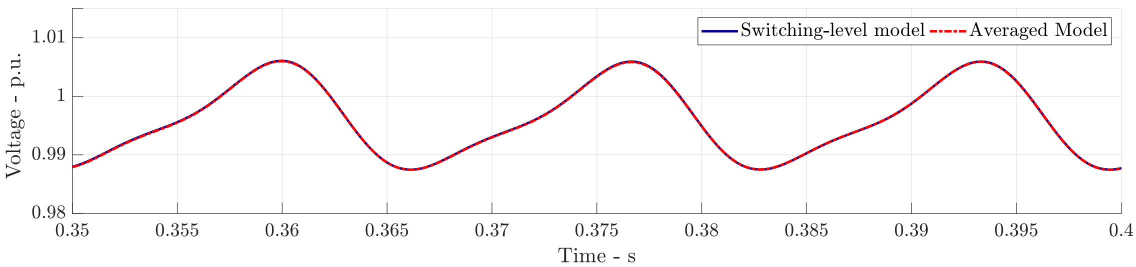

(d) Upper-arm equivalent dc voltage v_{dc}^{pa}

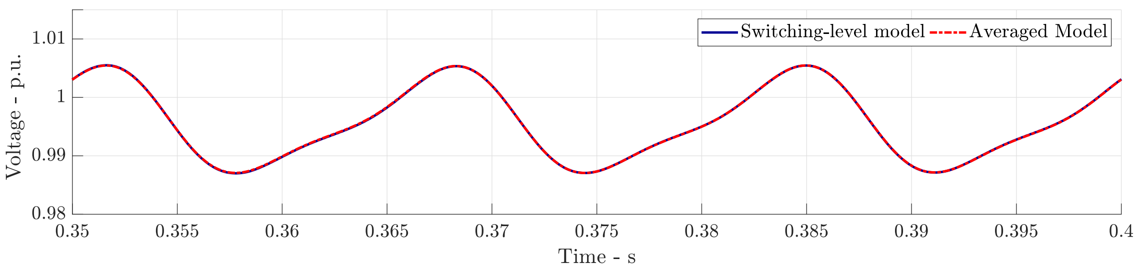

(e) Lower-arm equivalent dc voltage v_{dc}^{na}

Figure 3.7: Comparison between the results obtained with the switching-level model and the averaged model: Steady-state results. The switching model was implemented in PSCAD/EMTDC, whereas the averaged model (non-linear, time-domain model) was implemented in PSIM. Only the results for the phase **a** are presented for the sake of space.

3.3 Natural-reference frame state equations of the MMC

Before starting developing the state equations of the MMC, it is useful to explain which variables are chosen to be state variables of the model and which are the as inputs and disturbances of the system. In this point, it is already known that the equivalents dc voltages are state variables, but is necessary to obtain one extra variable for each energy-storage element in the circuit. Looking back to Figure 3.4, the three inductors per phase indicate the necessity of three state variables, i_c^k, i_{cp}^k and i_{cn}^k. However, it is commonly found in the literature [36, 37, 54, 102] the replacement of i_{cp}^k and i_{cn}^k by the circulating current i_{cir}^k. In this case, the use of one state variable to represent the dynamic of two energy-storage elements is possible due to the fact that this inductors both interfere directly in the dynamics of i_{cir}^k and that the upper and lower arms operate symmetrically. As for the input variables, logically, the insertion indices m_p^k and m_n^k are assigned. Here it is important to include two disturbance variables that are present in the Figure 3.4, the main-bus ac voltage v_o^k and the dc-bus voltage v_{dc}. Thus, four state equation per phase are needed to represent the MMC.

Since the group of SMs of an arm is replaced, considering the dc side, by a current source feeding an equivalent capacitor C_{eq}, it is possible to write the following equations:

$$C_{eq}\frac{dv_{dc}^{pk}}{dt}(t) = m_p^k(t)i_{cp}^k(t), \tag{3.11}$$

$$C_{eq}\frac{dv_{dc}^{nk}}{dt}(t) = m_n^k(t)i_{cn}^k(t). \tag{3.12}$$

By substituting the results presented in (2.8) in (3.11) and (3.12) it is finally possible to reach the state equations which represent the dynamics of the equivalent dc voltages v_{dc}^{pk} and v_{dc}^{nk}:

$$C_{eq}\frac{dv_{dc}^{pk}}{dt}(t) = m_p^k(t)\left[i_{cir}^k(t) + \frac{1}{2}i_c^k(t)\right], \tag{3.13}$$

$$C_{eq}\frac{dv_{dc}^{nk}}{dt}(t) = m_n^k(t)\left[i_{cir}^k(t) - \frac{1}{2}i_c^k(t)\right]. \tag{3.14}$$

Before continuing, it is necessary to emphasize that the voltage between the dc-bus middle point 0 and the ac-side ground is considered null in this work. Because of this, it is possible to write the following net equations:

$$e_c^k(t) + Ri_{cp}^k(t) + L\frac{di_{cp}^k}{dt}(t) + v_{ac}^{pk}(t) - \frac{1}{2}v_{dc}(t) = 0, \tag{3.15}$$

$$e_c^k(t) - Ri_{cn}^k(t) - L\frac{di_{cp}^k}{dt}(t) - v_{ac}^{nk}(t) + \frac{1}{2}v_{dc}(t) = 0. \tag{3.16}$$

Here the voltage v_{dc} is presented as a time variable instead of a constant to follow the definitions in the first paragraph of this section. In fact, depending on the application, this might be either a constant or a variable. Once more using the results presented in (2.8), the last equations can be rewritten as follows:

$$e_c^k(t) + R\left[i_{cir}^k(t) + \frac{1}{2}i_c^k(t)\right] + L\left[\frac{di_{cir}^k}{dt}(t) + \frac{1}{2}\frac{di_c^k}{dt}(t)\right] + v_{ac}^{pk}(t) - \frac{1}{2}v_{dc}(t) = 0, \tag{3.17}$$

$$e_c^k(t) - R\left[i_{cir}^k(t) - \frac{1}{2}i_c^k(t)\right] - L\left[\frac{di_{cir}^k}{dt}(t) - \frac{1}{2}\frac{di_c^k}{dt}(t)\right] - v_{ac}^{nk}(t) + \frac{1}{2}v_{dc}(t) = 0. \tag{3.18}$$

At this point, to obtain the state equation associated to i_{cir}^k it is simply necessary to subtract (3.17) from (3.18) and substitute v_{ac}^{pk} and v_{ac}^{nk} by the results presented in (3.5) and (3.6), respectively. Thus:

$$2L\frac{di_{cir}^k}{dt}(t) = -2Ri_{cir}^k(t) - m_p^k(t)v_{dc}^{pk}(t) - m_n^k(t)v_{dc}^{nk}(t) + v_{dc}(t). \tag{3.19}$$

The state equations associated to i_c^k is obtained in three steps. Firstly, (3.17) and (3.18) are added together and v_{ac}^{pk} and v_{ac}^{nk}, once more, substituted by (3.5) and (3.6), leading to the following result:

$$2e_c^k(t) + Ri_c^k(t) + L\frac{di_c^k}{dt}(t) + m_p^k(t)v_{dc}^{pk}(t) - m_n^k(t)v_{dc}^{nk}(t) = 0. \tag{3.20}$$

Secondly, the output net equation is obtained as follows:

$$e_c^k(t) - R_f i_c^k(t) - L_f\frac{di_c^k}{dt}(t) = v_o^k(t). \tag{3.21}$$

Finally, substituting (3.21) in (3.20) it is possible to reach the last state equation of the system:

$$\left(L + 2L_f\right)\frac{di_c^k}{dt}(t) = m_n^k(t)v_{dc}^{nk}(t) - m_p^k(t)v_{dc}^{pk}(t) - 2v_o^k(t) - \left(R + 2R_f\right)i_c^k(t). \tag{3.22}$$

It is important to notice that in all four state equations,(3.13), (3.14), (3.19), (3.22), there are input variables, m_p^k and m_n^k, multiplying state variables, i_c^k, i_{cir}^k, v_{dc}^{pk} and v_{dc}^{nk}. Consequently, this set of equations forms a non-linear state-space model, which can be rewritten in matrix form as follows:

$$\frac{d}{dt}\begin{bmatrix} i_{cir}^k \\ i_c^k \\ v_{dc}^{pk} \\ v_{dc}^{nk} \end{bmatrix} = \begin{bmatrix} -\frac{R}{L} & 0 & -\frac{m_p^k}{2L} & -\frac{m_n^k}{2L} \\ 0 & -\frac{R+2R_f}{L+2L_f} & -\frac{m_p^k}{L+2L_f} & \frac{m_n^k}{L+2L_f} \\ \frac{m_p^k}{C_{eq}} & \frac{m_p^k}{2C_{eq}} & 0 & 0 \\ \frac{m_n^k}{C_{eq}} & -\frac{m_n^k}{2C_{eq}} & 0 & 0 \end{bmatrix}\begin{bmatrix} i_{cir}^k \\ i_c^k \\ v_{dc}^{pk} \\ v_{dc}^{nk} \end{bmatrix} + \begin{bmatrix} 0 & \frac{1}{2L} \\ -\frac{2}{L+2L_f} & 0 \\ 0 & 0 \\ 0 & 0 \end{bmatrix}\begin{bmatrix} v_o^k \\ v_{dc} \end{bmatrix}. \tag{3.23}$$

3.4 Changes of variables in the model

As mentioned in Chapter 2, the insertion indices are composed of two normalized signals, e_c^* and e_{cir}^*, which intend to control the produced ac voltage and mitigate the second-harmonic component of i_{cir}^k, respectively. As these signals are to be produced by the control system, it is useful to present the state-space model of the MMC as function of them instead of the insertion indices. Stating that, the substitution of (2.18) and (2.19) in (3.13), (3.14), (3.19) and (3.22) leads to the following set of state equations:

$$2C_{eq}\frac{dv_{dc}^{pk}}{dt}(t) = \left[1 - e_c^{k*}(t) - e_{cir}^{k*}(t)\right]\left[i_{cir}^k(t) + \frac{1}{2}i_c^k(t)\right] \tag{3.24}$$

$$2C_{eq}\frac{dv_{dc}^{nk}}{dt}(t) = \left[1 + e_c^{k*}(t) - e_{cir}^{k*}(t)\right]\left[i_{cir}^k(t) - \frac{1}{2}i_c^k(t)\right] \tag{3.25}$$

$$\begin{aligned} 4L\frac{di_{cir}^k}{dt}(t) = -4Ri_{cir}^k(t) - \left[1 - e_{cir}^{k*}(t)\right]\left[v_{dc}^{kp}(t) + v_{dc}^{kn}(t)\right] \\ + e_c^{k*}(t)\left[v_{dc}^{pk}(t) - v_{dc}^{nk}(t)\right] + 2v_{dc}(t) \end{aligned} \tag{3.26}$$

$$\begin{aligned} 2\left(L + 2L_f\right)\frac{di_c^k}{dt}(t) = -\left[1 - e_{cir}^{k*}(t)\right]\left[v_{dc}^{kp}(t) - v_{dc}^{kn}(t)\right] \\ + e_c^{k*}\left[v_{dc}^{kp}(t) + v_{dc}^{kn}(t)\right] - 4v_o^k(t) - 2\left(R + 2R_f\right)i_c^k(t) \end{aligned} \tag{3.27}$$

In addition to the previous change, in order to simplify forthcoming mathematical processing, two new state variables, $v_{dc}^{\Delta k}$ and $v_{dc}^{\Sigma k}$, are introduced:

$$v_{dc}^{\Delta k}(t) = v_{dc}^{pk}(t) - v_{dc}^{nk}(t), \tag{3.28}$$

$$v_{dc}^{\Sigma k}(t) = v_{dc}^{pk}(t) + v_{dc}^{nk}(t). \tag{3.29}$$

It is important to mention that such variable change is commonly employed for obtaining analytical models for the MMC and can be found in [36, 53, 54, 103]. Considering the state equations related to the currents, the variable change is performed by simply substitution of (3.28) and (3.29) in (3.32) and (3.27). However, an extra step is necessary when it comes to the state equations related to the voltages. Thus, before the substitution it is necessary to compute the results for the addition and subtraction of (3.24) and (3.25). The final results are given by:

$$2C_{eq}\frac{dv_{dc}^{\Sigma k}}{dt}(t) = 2\left[1 - e_{cir}^{k*}(t)\right] i_{cir}^{k}(t) - e_{c}^{k*}(t) i_{c}^{k}(t), \tag{3.30}$$

$$2C_{eq}\frac{dv_{dc}^{\Delta k}}{dt}(t) = -2e_{c}^{k*}(t) i_{cir}^{k}(t) + \left[1 - e_{cir}^{k*}(t)\right] i_{c}^{k}(t), \tag{3.31}$$

$$4L\frac{di_{cir}^{k}}{dt}(t) = -4Ri_{cir}^{k}(t) - \left[1 - e_{cir}^{k*}(t)\right] v_{dc}^{\Sigma k}(t) + e_{c}^{k*}(t) v_{dc}^{\Delta k}(t) + 2v_{dc}(t), \tag{3.32}$$

$$2\left(L + 2L_f\right)\frac{di_{c}^{k}}{dt}(t) = e_{c}^{k*}(t) v_{dc}^{\Sigma k}(t) - \left[1 - e_{cir}^{k*}(t)\right] v_{dc}^{\Delta k}(t) - 4v_{o}^{k}(t) - 2\left(R + 2R_f\right) i_{c}^{k}(t). \tag{3.33}$$

These equations can be organized in a matrix form as follows:

$$\frac{d}{dt}\begin{bmatrix} i_{cir}^{k} \\ i_{c}^{k} \\ v_{dc}^{k\Sigma} \\ v_{dc}^{k\Delta} \end{bmatrix} = \begin{bmatrix} -\frac{R}{L} & 0 & -\left(\frac{1-e_{cir}^{k*}}{4L}\right) & \frac{e_{c}^{k*}}{4L} \\ 0 & -\left(\frac{R+2R_f}{L+2L_f}\right) & \frac{e_{c}^{k*}}{L+2L_f} & -\left(\frac{1-e_{cir}^{k*}}{L+2L_f}\right) \\ \frac{1-e_{cir}^{k*}}{C_{eq}} & -\frac{e_{c}^{k*}}{2C_{eq}} & 0 & 0 \\ -\frac{e_{c}^{k*}}{C_{eq}} & \frac{1-e_{cir}^{k*}}{2C_{eq}} & 0 & 0 \end{bmatrix} \begin{bmatrix} i_{cir}^{k} \\ i_{c}^{k} \\ v_{dc}^{k\Sigma} \\ v_{dc}^{k\Delta} \end{bmatrix} + \begin{bmatrix} 0 & \frac{1}{2L} \\ -\frac{2}{L+2L_f} & 0 \\ 0 & 0 \\ 0 & 0 \end{bmatrix} \begin{bmatrix} v_{o}^{k} \\ v_{dc} \end{bmatrix}. \tag{3.34}$$

3.5 Analytical model for the MMC in steady-state condition

This section aims at presenting a steady-state analytical solution for the MMC and comparing the influence of parameters such as ac and dc voltages, active and reactive power on state variables as circulating currents and the equivalent dc voltages of the arms of the MMC. Figure 3.8 represents the system considered in this section. Notice that, the results to be presented are independently from the control mode adopted, i.e., they are suitable to describe the MMC either as an open-loop voltage controlled converter, or as a current controlled grid-connected converter, or as a voltage controlled grid-forming converter. The only control-loop neglected is the one responsible by the mitigation of the second-harmonic component of i^k_{cir}.

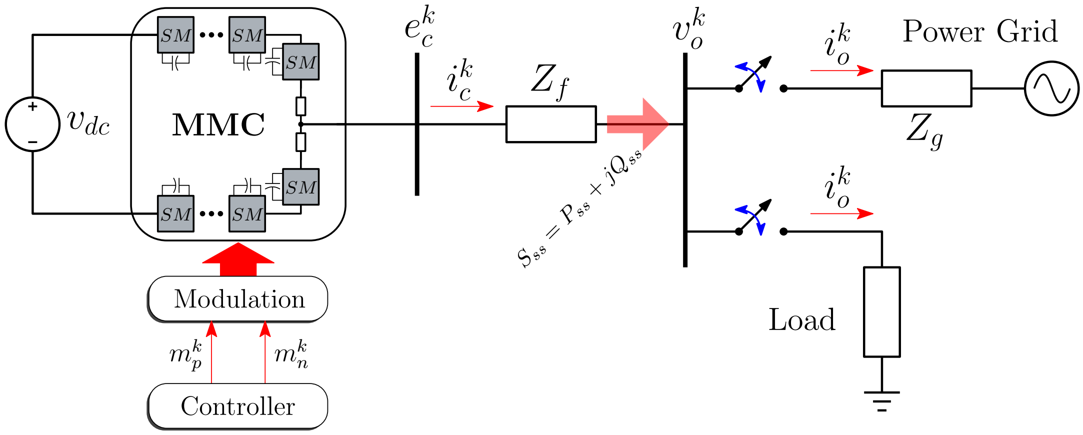

Figure 3.8: Considered circuit for the steady-state analysis.

3.5.1 Steady-state values of i^k_c and v^k_o

Independently of the way the converter is controlled, the steady-state value of the main-bus voltage, $v^k_{o,ss}$, can be described by:

$$v^k_{o,ss}(t) = \sqrt{2}V_{ss}\sin(\omega t + \phi_k), \tag{3.35}$$

where V_{ss} is the RMS value of the voltage and $\phi_k = 0,\ -2\pi/3,\ 2\pi/3$ rad is the phase displacement between the phases of the system.

Analogously, the steady-state current, $i^k_{c,ss}$, produced by the MMC can be written as follows:

$$i^k_{c,ss}(t) = \sqrt{2}I_{ss}\sin(\omega t + \phi_i + \phi_k), \tag{3.36}$$

where I_{ss} is the RMS value of the current and ϕ_i is the displacement angle between the voltage $v^k_{o,ss}$ and the current $i^k_{c,ss}$.

If the complex power produced by the MMC is given by $S_{ss} = P_{ss} + jQ_{ss}$, where P_{ss} and Q_{ss} are the active and reactive powers, it is possible to write the following results:

$$\phi_i = -\tan^{-1}\left(\frac{Q_{ss}}{P_{ss}}\right), \tag{3.37}$$

$$I_{ss} = \frac{\sqrt{P^2_{ss} + Q^2_{ss}}}{3V_{ss}}. \tag{3.38}$$

The substitution of (3.37) and (3.38) in (3.36) leads to:

$$i^k_{c,ss}(t) = \frac{\sqrt{2}}{3}\frac{\sqrt{P^2_{ss} + Q^2_{ss}}}{V_{ss}}\sin\left[\omega t + \phi_k - \tan^{-1}\left(\frac{Q_{ss}}{P_{ss}}\right)\right]. \tag{3.39}$$

3.5.2 Steady-state values of m_p^k and m_n^k

The first step to obtain m_p^k and m_n^k is determining $e_{c,ss}^k$. Thus, according to Figure 3.8, the net-equation which links the internal voltage $e_{c,ss}^k$ to the output voltage $v_{o,ss}^k$ is given by:

$$e_{c,ss}^k(t) = v_{o,ss}^k(t) + L_f \frac{di_{c,ss}^k}{dt}(t) + R_f i_{c,ss}^k(t), \tag{3.40}$$

which, indeed, is an adaptation of (3.21).

Still from chapter 3, (3.20) can be adapted and combined with (3.40) to form the following result:

$$m_{n,ss}^k(t)\, \overline{v_{dc}^{kn}} - m_{p,ss}^k(t)\, \overline{v_{dc}^{kp}} = 2v_{o,ss}^k(t) + (2L_f + L)\, \frac{di_{c,ss}^k}{dt}(t) + (2R_f + R)\, i_{c,ss}^k(t), \tag{3.41}$$

where the bars over v_{dc}^{kn} and v_{dc}^{kp} represent average values over a fundamental-frequency spam. Consequently, it is possible to state that $\overline{v_{SM_{cc}}^{kp}} = \overline{v_{SM_{cc}}^{kn}} \approx V_{dc,ss}$.

Continuing, the substitution of the insertion indices defined in (2.18) and (2.19), neglecting the signal used in the mitigation of the second-harmonic component of i_{cir}^k, leads to:

$$e_{c,ss}^{k*} = \frac{2}{V_{dc,ss}} v_{o,ss}^k + \frac{1}{V_{dc,ss}} (2L_f + L)\, \frac{di_{c,ss}^k}{dt} + \frac{1}{V_{dc,ss}} (2R_f + R)\, i_{c,ss}^k. \tag{3.42}$$

The results presented in (3.35) and (3.36) can be substituted in (3.42) to form, after some arrangements, the steady-state analytical model for the control signal e_c^k:

$$e_{c,ss}^{k*} = E_{ss}^* \sin\left(\omega t + \gamma_e + \phi_k\right), \tag{3.43}$$

where:

$$E_{ss}^{s*} = \frac{\sqrt{2}}{V_{cc}} \left[2V_{ss} - I_{ss}\omega\, (2L_f + L) \sin(\phi_i) + I_{ss}\, (2R_f + R) \cos(\phi_i)\right], \tag{3.44}$$

$$E_{ss}^{c*} = \frac{\sqrt{2}}{V_{cc}} \left[I_{ss}\omega\, (2L_f + L) \cos(\phi_i) + I_{ss}\, (2R_f + R) \sin(\phi_i)\right]. \tag{3.45}$$

$$E_{ss}^* = \sqrt{(E_{ss}^{s*})^2 + (E_{ss}^{c*})^2}, \tag{3.46}$$

$$\gamma_e = \tan^{-1}\left(\frac{E_{ss}^{c*}}{E_{ss}^{s*}}\right), \tag{3.47}$$

Finally, the steady-state conditions of the insertion indices, neglecting the component due to the mitigation of the circulating currents, are given by:

$$m_{p,ss}^{k} = \frac{1}{2} - \frac{1}{2} E_{ss}^{*} \sin\left(\omega t + \gamma_e + \phi_k\right), \tag{3.48}$$

$$m_{n,ss}^{k} = \frac{1}{2} + \frac{1}{2} E_{ss}^{*} \sin\left(\omega t + \gamma_e + \phi_k\right). \tag{3.49}$$

3.5.3 Steady-state value of the dc components of i_{cir}^{k}, v_{dc}^{kp} and v_{dc}^{kn}

As already mentioned in previous chapter, the circulating current is composed by both dc, $\bar{i}_{cir}^{k}$, and ac, $\tilde{i}_{cir}^{k}$, components, such as follows:

$$i_{cir,ss}^{k}(t) = \bar{i}_{cirss}^{k} + \tilde{i}_{cir,ss}^{k}(t). \tag{3.50}$$

The dc portion of $i_{cir,ss}^{k}$ is related to the distribution of energy from the DC bus to the SMs of each phase. To maintain the energy balance the converter output power must be equal to the dc bus power. This is equivalent to write:

$$3V_{dc,ss}\, \bar{i}_{cir,ss}^{k} - 3R\, \left(\bar{i}_{cir,ss}^{k}\right)^2 \triangleq \frac{1}{2\pi} \int_0^{2\pi} 3\, e_{c,ss}^{k}\, i_{c,ss}^{k}\, d\omega t = P_{ss} + 3R_f I_{ss}^2. \tag{3.51}$$

The solution of (3.51) is:

$$\bar{i}_{cir,ss}^{k} = \frac{3V_{dc,ss} - \sqrt{9V_{dc,ss}^2 - 12R\left(P_{ss} + 3R_f I_{ss}^2\right)}}{6R}. \tag{3.52}$$

As for the equivalent dc voltages, their dc components can be approximately represented by:

$$\bar{v}_{dc}^{pk} = \bar{v}_{dc}^{nk} \approx V_{dc,ss}. \tag{3.53}$$

3.5.4 Steady-state value of the harmonic components of i_{cir}^{k}, v_{dc}^{kp} and v_{dc}^{kn}

This section presents the steady-state value of three state variables altogether because they besides depending from the previous results, they also interfere in each other. Here, the approach followed was to compute the forced solution for the differential equations expressed in (3.13), (3.14), (3.19).

After analyzing some simulation results and consulted some references [104, 105], it was concluded that the equivalent voltages v_{dc}^{pk} and v_{dc}^{nk} comprise five major components, the dc, the fundamental, the second-, third-, and fourth-harmonic components. Because of that, it was adopted a forced solution for the phase **a** of the MMC as given by:

$$v_{dc,ss}^{na}(t) = V_{dc,ss} + \sum_{i=1,2,3,4} V_{dc_{ic}}^{na} \cos(i\omega t) + \sum_{i=1,2,3,4} V_{dc_{is}}^{na} \sin(i\omega t), \tag{3.54}$$

$$v_{dcss}^{pa}(t) = V_{dcss} + \sum_{i=1,2,3,4} V_{dc_{ic}}^{pa} \cos(i\omega t) + \sum_{i=1,2,3,4} V_{dc_{is}}^{pa} \sin(i\omega t), \tag{3.55}$$

where i represents a harmonic component order ($i = 1,\ 2,\ 3,\ 4$) and $V_{dc_{ic}}^{na}$, $V_{dc_{is}}^{na}$, $V_{dc_{ic}}^{pa}$, $V_{dc_{is}}^{pa}$ are the amplitudes of the harmonic components.

Using the same approach, the simulation results indicated that the circulating current i_{cir}^{k} always present three major components, the dc, the second-harmonic and the fourth-harmonic components. Consequently, it was decided to consider the following forced solution:

$$i_{cirss}^{a}(t) = I_{cir_{ss}} + \sum_{i=1,2,4} I_{cir_{ic}} \cos(i\omega t) + \sum_{i=1,2,4} I_{cir_{is}} \sin(i\omega t) \tag{3.56}$$

where $I_{cir_{ic}}$ and $I_{cir_{is}}$ are the amplitude of the harmonic components of the circulating current.

Substituting (3.48), (3.49), (3.54), (3.55) and (3.56) into the differential equations given by (3.13), (3.14), (3.19) it is possible to obtain a linear system with 22 variables and 22 equations. Notice that, each one of these variables is in fact one of the amplitudes of the harmonic components presented in this section. Because of its size, it is presented here only a generic matrix representation of this system:

$$\mathbf{A}_{ss}\mathbf{X}_{ss} = \mathbf{B}_{ss}, \tag{3.57}$$

where $\mathbf{A}_{ss}$ is a 22×22 matrix; $\mathbf{X}_{ss}$ is the column vector with the variables of the system, the amplitude of the harmonic components of the circulating current and of the equivalent dc voltages, presented in (3.58)-(3.61); $\mathbf{B}_{ss}$ is a constant column vector. The values of $\mathbf{B}_{ss}$ and $\mathbf{A}_{ss}$ are presented, respectively, in (B.5) and (B.9) on the Appendix B.

$$\mathbf{X}_{ss} = \begin{bmatrix} X_{icir} & X_{vdcp} & X_{vdcn} \end{bmatrix}^{T}, \tag{3.58}$$

$$X_{icir} = \begin{bmatrix} I_{cir_{1s}} & I_{cir_{1c}} & I_{cir_{2s}} & I_{cir_{2c}} & I_{cir_{4s}} & I_{cir_{4c}} \end{bmatrix}, \tag{3.59}$$

$$X_{vdcn} = \begin{bmatrix} V_{dc_{1s}}^{n} & V_{dc_{1c}}^{n} & V_{dc_{2s}}^{n} & V_{dc_{2c}}^{n} & V_{dc_{3s}}^{n} & V_{dc_{3c}}^{n} & V_{dc_{4s}}^{n} & V_{dc_{4c}}^{n} \end{bmatrix}, \tag{3.60}$$

$$X_{vdcp} = \begin{bmatrix} V_{dc_{1s}}^{p} & V_{dc_{1c}}^{p} & V_{dc_{2s}}^{p} & V_{dc_{2c}}^{p} & V_{dc_{3s}}^{p} & V_{dc_{3c}}^{p} & V_{dc_{4s}}^{p} & V_{dc_{4c}}^{p} \end{bmatrix}. \tag{3.61}$$

Thus, the solution containing the analytical expressions for each of the harmonic components in steady-state is obtained by making:

$$\mathbf{X}_{ss} = \mathbf{A}_{ss}^{-1}\mathbf{B}_{ss}. \tag{3.62}$$

Once more, due to the size of the equations, it was decided to present them on the Appendix B.

3.5.5 Validation of the steady-sate model

The approach used to validate the obtained results was to compare them with the results obtained from the switching-level simulation of the Chapter 2. Some adjustments were necessary to be made to match the two results. Firstly, as in the simulations of the Chapter 2 the zero-displacement signal was e_c^{a*}, the steady-state model was modified to contain a displacement δ in v_o^a as in:

$$v_o^a(t) = \sqrt{2}V_{ss}\sin\left(\omega t - \delta\right). \tag{3.63}$$

As consequence, all the other components of the steady-state model present this displacement. Secondly, the active power was set to $0.89p.u.$ which was the value found in the simulations of the switching-level model of the Chapter 2.

With these considerations, the results obtained by the analytical steady-state model are presented in Figure 3.9. It is observed in Figure 3.9a that the analytical solution was able to track the average-value characteristic of the circulating current.

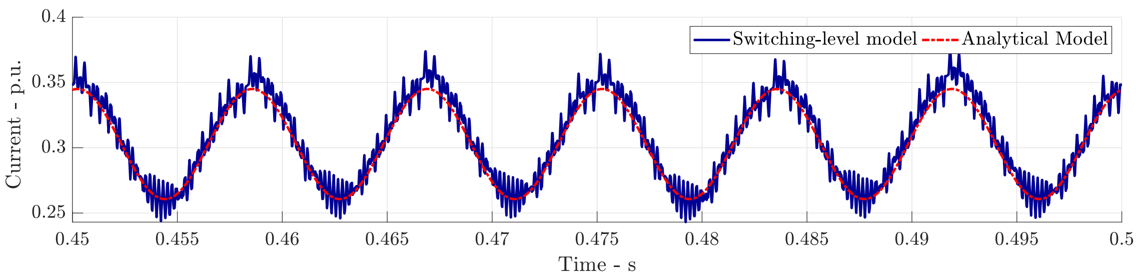

(a) Circulating current.

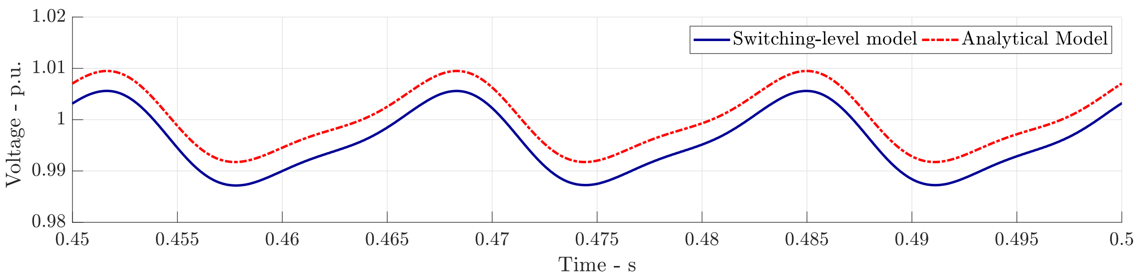

(b) Lower-arm equivalent dc voltage.

Figure 3.9: Comparison between the results obtained from the analytical steady-state model and the switching level model.

When it comes to the equivalent dc voltage depicted in Figure 3.9b, however, there is a small offset of $0.0042p.u.$ between the results. This offset is due to the fact that the dc component of the voltage was considered equal to V_{ss} when, in fact, it is not (the small dc voltage drops that were not considered are the responsible for this difference). Analyzing the ac component of the voltage, it is possible to notice that the analytical model matches accurately the behavior presented by the switching-level model.

It is important to reassure that, despite the fact that the steady-state was validated considering an open-loop voltage controlled MMC, it is able to accurately represent the MMC under either closed-loop voltage and current control as well. It was decided not to present results for these other control modes to cut off some repetitiveness.

3.5.6 Influence of the active and reactive powers on the MMC in steady-state condition

Using the analytical results obtained in this section it was analyzed the influence of the active and reactive power in the components of the circulating current and in the components of the lower-arm equivalent dc voltage of the phase **a** of the MMC[2]. For this matter, P and Q were varied from 0 to $1p.u.$ and the equivalent components of i_{cir}^{a} and v_{dc}^{na} were computed for these values. It is important to notice that, as each harmonic component has two parts, one aligned to the sine and another to the cosine, the equivalent of each harmonic component is computed by a vector sum of its parts. The results are presented in contour maps in Figures 3.10 and 3.11.

The results for the circulating current are presented in Figure 3.10. Analyzing firstly the chart in Figure 3.10a, it is possible to notice that reactive power has no significant effect in the dc component of the circulating current. As this chart represents one of the phases of the converter, the maximum value for this component is $0.33p.u.$ when the active power reaches $1p.u.$ The second-harmonic component presented in the Figure 3.10b, differently, suffers influence from both active and reactive power, with a leading advance for this last. As observed in the figure, the maximum value this component presents is about $0.08p.u.$ and because of that it is generally mitigated through control action. The fourth-harmonic component, on the other hand, has an insignificant amplitude. According to the Figure 3.10c, its maximum value is around $0.0003p.u.$ and because of that it is generally not made any effort to mitigate it.

The components of the equivalent dc voltages are presented in Figure 3.11. It

[2]As the upper and lower equivalent dc voltages are equal in amplitude when the dc voltages are balanced, differing only in displacement, it was decided to present only the lower-arm dc voltages.

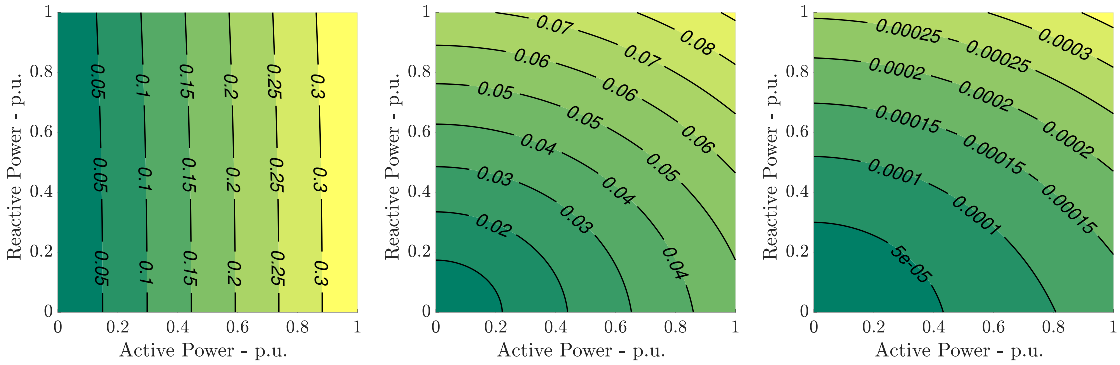

(a) dc component (b) Second-harmonic (c) Fourth-harmonic

Figure 3.10: Influence of active and reactive power in the components of i^k_{cir0}; the contour lines indicated the p.u. value of the components of the circulating current.

can be observed that the fundamental component is the greatest among the ac components reaching up to $0.015p.u.$ depending on the produced power by the MMC. It is also observed that both active and reactive power influence equally the amplitude of the components.

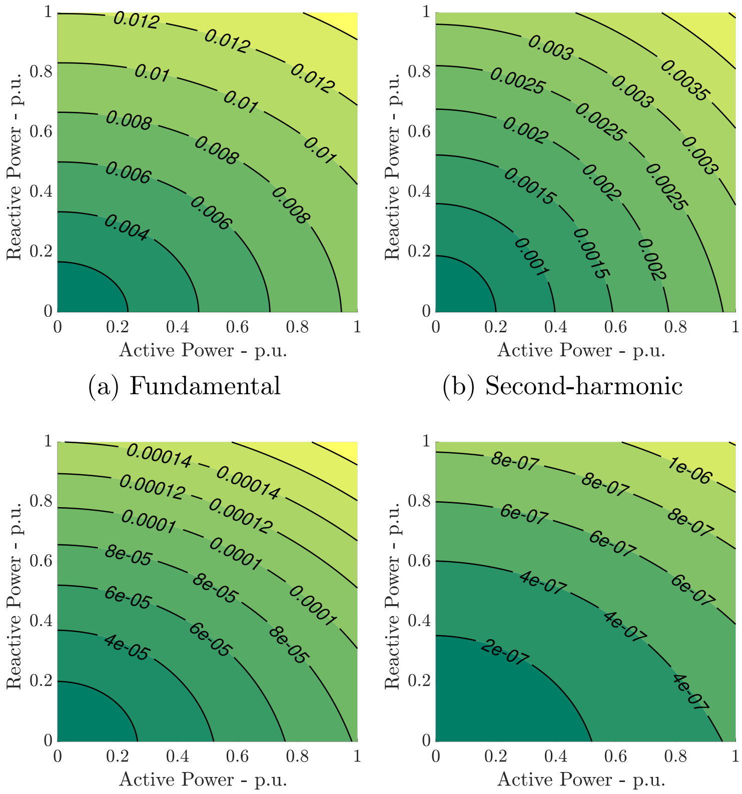

(a) Fundamental (b) Second-harmonic

(c) Third-harmonic (d) Fourth-harmonic

Figure 3.11: Influence of active and reactive power in the components of v^k_{dc0}; the contour lines indicated the p.u. value of the components of the equivalent dc voltages. The magnitude of the components are equal for both the upper and lower arms.

3.6 Small-signal model of the MMC

The models developed so far present non-linear features that make them not suitable for most of the classical control-theory analysis, despite the fact they represent the MMC more accurately. In views of that, the model in Section 3.4 needs to be linearized, and this new version might serve as starting point for the models will be developed in the Sections 4.1 and 4.2. This linearized model is generally called small-signal model.

The linearization process consists of expanding the non-linear target function into a Taylor series and, thereafter, cutting off the non-linear terms of the result. To better understand the process, consider a generic system of n state variables, m input variables, and p disturbances, such as:

$$\begin{cases} \dot{x}_1 = f_1(x_1,\ \dots\ , x_n,\ u_1,\ \dots\ , u_m,\ q_1,\ \dots\ , q_p) \\ \vdots \\ \dot{x}_n = f_n(x_1,\ \dots\ , x_n,\ u_1,\ \dots\ , u_m,\ q_1,\ \dots\ , q_p) \end{cases} , \tag{3.64}$$

where f_1, f_2, ..., f_n are non-linear functions of the system; x_1, x_2, ..., x_n are the state variables; u_1, u_2, ..., u_m are the input variables; q_1, q_2, ..., q_p are the disturbances.

The small-signal model can be obtained by making:

$$\begin{bmatrix} \dot{\tilde{x}}_1 \\ \vdots \\ \dot{\tilde{x}}_n \end{bmatrix} = \begin{bmatrix} \frac{\partial f_1}{\partial x_1} & \dots & \frac{\partial f_1}{\partial x_n} \\ \vdots & \ddots & \vdots \\ \frac{\partial f_n}{\partial x_1} & \dots & \frac{\partial f_n}{\partial x_n} \end{bmatrix} \begin{bmatrix} \tilde{x}_1 \\ \vdots \\ \tilde{x}_n \end{bmatrix} + \begin{bmatrix} \frac{\partial f_1}{\partial u_1} & \dots & \frac{\partial f_1}{\partial u_m} \\ \vdots & \ddots & \vdots \\ \frac{\partial f_n}{\partial u_1} & \dots & \frac{\partial f_n}{\partial u_m} \end{bmatrix} \begin{bmatrix} \tilde{u}_1 \\ \vdots \\ \tilde{u}_m \end{bmatrix} + \begin{bmatrix} \frac{\partial f_1}{\partial q_1} & \dots & \frac{\partial f_1}{\partial q_p} \\ \vdots & \ddots & \vdots \\ \frac{\partial f_n}{\partial q_1} & \dots & \frac{\partial f_n}{\partial q_p} \end{bmatrix} \begin{bmatrix} \tilde{q}_1 \\ \vdots \\ \tilde{q}_p \end{bmatrix} \tag{3.65}$$

where the tilde over the letters, as in $\tilde{x}_n$, $\tilde{u}_m$ and $\tilde{q}_p$, indicate small-signal variables (small variation of the corresponding variable around the equilibrium point) and the subscript 0, as in x_{n0}, u_{m0} and q_{p0}, indicate these are the equilibrium point around which the linearization has been performed. Their relationships are presented in (3.66). Besides that, the differential terms correspond to the linear part of the Taylor series of the system. This model is valid in the range where even for a small-signal deviation it still matches the non-linear model. This valid range should be confirmed by simulation and comparison of the two models.

$$
\begin{aligned}
\tilde{x}_n &= x - x_{n0} \\
\tilde{u}_m &= u - u_{m0} \;\; . \\
\tilde{q}_n &= q - q_{p0}
\end{aligned}
\tag{3.66}
$$

Differently from the non-linear model in (3.64), the small-signal model in (3.65) allows the separation between the dynamic, input, and disturbance matrices and the system can always be described as:

$$
\dot{\tilde{\mathbf{X}}}(t) = \mathbf{A}\tilde{\mathbf{X}}(t) + \mathbf{B}\tilde{\mathbf{U}}(t) + \mathbf{E}\tilde{\mathbf{Q}}(t), \tag{3.67}
$$

being $\mathbf{A}$, $\mathbf{B}$ and $\mathbf{E}$ the dynamic, input and disturbance matrices and $\tilde{\mathbf{X}}$, $\tilde{\mathbf{U}}$ and $\tilde{\mathbf{Q}}$ the vectors with the state, input and disturbance small-signal variables.

Applying this methodology for (3.30)-(3.33) leads to the following results:

$$
2C_{eq}\frac{d\tilde{v}_{dc}^{\Sigma k}}{dt}(t) = 2\left(1 - e_{cir0}^{k*}\right)\tilde{i}_{cir}^{k}(t) - 2i_{cir0}^{k}\tilde{e}_{cir}^{k*}(t) - e_{c0}^{k*}\tilde{i}_{c}^{k}(t) - i_{c0}^{k}\tilde{e}_{c}^{k*}(t), \tag{3.68}
$$

$$
2C_{eq}\frac{d\tilde{v}_{dc}^{\Delta k}}{dt}(t) = -2e_{c0}^{k*}\tilde{i}_{cir}^{k}(t) - 2i_{cir0}^{k}\tilde{e}_{c}^{k*}(t) + \left(1 - e_{cir0}^{k*}\right)\tilde{i}_{c}^{k}(t) - i_{c0}^{k}\tilde{e}_{cir}^{k*}(t), \tag{3.69}
$$

$$
\begin{aligned}
4L\frac{d\tilde{i}_{cir}^{k}}{dt}(t) = -4R\tilde{i}_{cir}^{k}(t) - \left(1 - e_{cir0}^{k*}\right)\tilde{v}_{dc}^{\Sigma k}(t) + {} \\
v_{dc0}^{\Sigma k}\tilde{e}_{cir}^{k*}(t) + e_{c0}^{k*}\tilde{v}_{dc}^{\Delta k}(t) + v_{dc0}^{\Delta k}\tilde{e}_{c}^{k*}(t) + 2\tilde{v}_{dc}(t),
\end{aligned}
\tag{3.70}
$$

$$
\begin{aligned}
2\left(L + 2L_f\right)\frac{d\tilde{i}_{c}^{k}}{dt}(t) = e_{c0}^{k*}\tilde{v}_{dc}^{\Sigma k} + v_{dc0}^{\Sigma k}\tilde{e}_{c}^{k*}(t) - \left(1 - e_{cir0}^{k*}\right)\tilde{v}_{dc}^{\Delta k}(t) + {} \\
v_{dc0}^{\Delta k}\tilde{e}_{cir}^{k*}(t) - 4\tilde{v}_{o}^{k}(t) - 2\left(R + 2R_f\right)\tilde{i}_{c}^{k}(t).
\end{aligned}
\tag{3.71}
$$

It is possible to show that, in the equilibrium point, the average value of the equivalent dc voltages approaches to V_{dc0} (average dc voltage), while their oscillating components are negligible in comparison to these average values, provided that the circuit components were designed for this situation. As a result, it comes without great consequence that $v_{dc0}^{\Delta k} \approx 0$ and $v_{dc0}^{\Sigma k} \approx 2V_{dc0}$. Likewise the DC voltages, the circulating current comprises both dc and ac components. Nonetheless, in the equilibrium point, the major ac component (second harmonic) is already minimized provided a specific controller was properly designed, and, for this reason, the dc component overshadows the other components. Thus, i_{cir0}^{k} can be assigned to its average value $S_0/(3V_{dc0})$. When it comes to the signals without dc component - i_c^k, e_c^{k*} and e_{cir}^{k*} - the decision on how to choose their equilibrium values is undoubtedly more complicated. If their real equilibrium values, which, in fact, are sinusoidal, are chosen, the model will end up being non-linear. In this case, other techniques, such as harmonic linearizarion [47, 106, 107], are needed to be employed. In this work, nonetheless, it was decided to keep the plain approach of considering i_{c0}^k, e_{c0}^{k*} and e_{cir0}^{k*} equal to zero. As the model intends to represent the MMC in frequency domain for small-signal analysis, this approach will bring no great issues. With these considerations, (3.68) - (3.71) can be rewritten as follows:

$$2C_{eq}\frac{d\tilde{v}_{dc}^{\Sigma k}}{dt}(t) = 2\tilde{i}_{cir}^k(t) - \frac{2S_0}{3V_{dc0}}\tilde{e}_{cir}^{k*}(t), \tag{3.72}$$

$$2C_{eq}\frac{d\tilde{v}_{dc}^{\Delta k}}{dt}(t) = -\frac{2S_0}{3V_{dc0}}\tilde{e}_c^{k*}(t) + \tilde{i}_c^k(t), \tag{3.73}$$

$$4L\frac{d\tilde{i}_{cir}^k}{dt}(t) = -4R\tilde{i}_{cir}^k(t) - \tilde{v}_{dc}^{\Sigma k}(t) + 2V_{dc0}\tilde{e}_{cir}^{k*}(t) + 2\tilde{v}_{dc}(t), \tag{3.74}$$

$$2\left(L + 2L_f\right)\frac{d\tilde{i}_c^k}{dt}(t) = +2V_{dc0}\tilde{e}_c^{k*}(t) - \tilde{v}_{dc}^{\Delta k}(t) - 4\tilde{v}_o^k(t) - 2\left(R + 2R_f\right)\tilde{i}_c^k(t). \tag{3.75}$$

Finally, considering the pattern presented in (3.67), the linearized state equations can be rewritten as follows:

$$\frac{d}{dt}\begin{bmatrix} \tilde{i}_{cir}^k \\ \tilde{i}_c^k \\ \tilde{v}_{dc}^{\Sigma k} \\ \tilde{v}_{dc}^{\Delta k} \end{bmatrix} = \begin{bmatrix} -\frac{1}{L} & 0 & -\frac{1}{4L} & 0 \\ 0 & -\frac{R+2R_f}{L+2L_f} & 0 & -\frac{1}{2}\frac{1}{L+2L_f} \\ \frac{1}{C_{eq}} & 0 & 0 & 0 \\ 0 & \frac{1}{2C_{eq}} & 0 & 0 \end{bmatrix}\begin{bmatrix} \tilde{i}_{cir}^k \\ \tilde{i}_c^k \\ \tilde{v}_{dc}^{\Sigma k} \\ \tilde{v}_{dc}^{\Delta k} \end{bmatrix} +$$

$$\begin{bmatrix} 0 & \frac{V_{dc0}}{2L} \\ \frac{V_{dc0}}{L+2L_f} & 0 \\ 0 & -\frac{S_0}{3V_{dc0}}\frac{1}{C_{eq}} \\ -\frac{S_0}{3V_{dc0}}\frac{1}{C_{eq}} & 0 \end{bmatrix}\begin{bmatrix} \tilde{e}_c^{k*} \\ \tilde{e}_{cir}^{k*} \end{bmatrix} + \begin{bmatrix} 0 & \frac{1}{2L} \\ -\frac{2}{L+2L_f} & 0 \\ 0 & 0 \\ 0 & 0 \end{bmatrix}\begin{bmatrix} \tilde{v}_o^k \\ \tilde{v}_{dc} \end{bmatrix} \tag{3.76}$$

3.7 Partial conclusions

This chapter started showing that the inherent characteristics of the MMC can be mimicked by an average-value model in which the group of SMs of an arm is substituted by a pair of controlled sources (a voltage source in the ac side and a current source in the dc side) and an equivalent capacitor C_{eq}. As explained in the chapter, this pair of sources has the objective of representing the effect of capacitor insertion in the ac side without the need of using capacitance-variable elements. The simulation results obtained with this model matched the results pointed out by the switching-level model of the previous chapter, validating the average-value modeling approach. Amongst the variables, the circulating current presented some noticeable, though, negligible, differences when comparing both models. Indeed, these differences are caused by non-linear effects introduced by the switching of the SMs. With the average-value model at hand, the non-linear state-space model of the MMC was derived. In this regard, it was considered four state variables, the circulating and output currents to represent the dynamic imposed by the inductors of the circuit, and the equivalent dc voltages to represent the dynamic imposed by the equivalent capacitors. Some changes of variable were performed and, then, this model was finally linearized. This linearized version presented in (3.72) - (3.75) are to be used in the models developed in the Sections 4.1 and 4.2. It was also derived in the chapter a steady-state solution for the differential equations of the MMC. This results showed the influence of the active and reactive powers on the components of circulating current and equivalent dc voltage. As already expected, the reactive power has insignificant influence in the dc component of i_{cir}^k. For all the harmonic components of i_{cir}^k and v_{dc}^{nk}, however, active and reactive power play mostly equal role. Still in this analysis, it was shown that the difference between the second- and fourth-order harmonic components of the circulating current is roughly in the order of 250 times, which justify the inclusion of a mitigation loop for the second, but not for the fourth harmonic component.

Chapter 4

Linearized Closed-loop models for the MMC

This chapter is divided into two parts, the first one dealing with the NRF-controlled MMC and the second with the SRF-controlled, each of them focused on deriving frequency-domain models for the MMC in different control modes. For the NRF-controlled MMC, the linear time-domain model presented in Chapter 3 is transformed into Laplace domain and combined with the control loops so as to form the closed-loop equivalent models of the MMC. Initially, it is presented the conversion of the MMC model into the Laplace domain and the closed-loop equivalent model for the mitigation loop of the second-harmonic component of the circulating current. After that, it is presented the ac-side equivalent MMC models for three different control approaches, current control, single-loop voltage control, and double-loop voltage control. In the first case, the MMC is considered either a grid-tied or off-grid converter, whereas in the other two approaches it plays the role of a grid-forming converter. The resonant controllers were used in all the control loops in order to guarantee null steady-state error [108] of the controlled variables. It is important to mention that the major contributions in this segment of the chapter were published in [62]. As for the SRF-controlled MMC, the linearized equations presented in Chapter 3 are converted into SRF and then into the Laplace domain. Afterward, the model for representing the mitigation loop of the circulating current is derived, followed by the model for the MMC under current control and under single- and double-loop voltage control. The models were validated through simulations using the non-linear, time-domain model (average-value model) of the Chapter 3.

4.1 MMC controlled in Natural Reference Frame

This section presents the models for representing the MMC in NRF. It is important to notice that, not only the models are derived in NRF, but also the control loops. Differently from SRF control systems, where the ac signals are turned into dc quantities, the proportional-integral controllers do not present a good performance in face of sinusoidal signals as in the NRF systems. Because of that, it was used proportional-resonant controllers which guarantee zero steady-state error [109]. The following subsection presents the Laplace-domain representation of the MMC, wheres the subsequent sections are focused on deriving the models for the different control modes analyzed.

4.1.1 Laplace-domain representation of the MMC

The linearized model of the MMC, considering the simplification discussed in the Chapter 3, is given by (3.72)-(3.75). These equations represent the MMC in time domain and can be transformed into Laplace domain as follows:

$$2sC_{eq}\tilde{V}_{dc}^{k\Sigma}(s) = 2\tilde{I}_{cir}^{k}(s) - \frac{2S_0}{3V_{dc0}}\tilde{E}_{cir}^{k*}(s), \tag{4.1}$$

$$2sC_{eq}\tilde{v}_{dc}^{k\Delta}(s) = -\frac{2S_0}{3V_{dc0}}\tilde{E}_{c}^{k*}(s) + \tilde{I}_{c}^{k}(s), \tag{4.2}$$

$$4Z\tilde{I}_{cir}^{k}(s) = -\tilde{V}_{dc}^{k\Sigma}(s) + 2V_{dc0}\tilde{E}_{cir}^{k*}(s) + 2\tilde{V}_{dc}(s), \tag{4.3}$$

$$2\left(Z + 2Z_f\right)\tilde{I}_{c}^{k}(s) = 2V_{dc0}\tilde{E}_{c}^{k*}(s) - \tilde{V}_{dc}^{k\Delta}(s) - 4\tilde{V}_{o}^{k}(s). \tag{4.4}$$

Notice that the capital letters stand for the Laplace-domain equivalent of each time-domain variable and that $Z = sL+R$ and $Z_f = sL_f+R_f$ were used for aesthetic reasons. Figure 4.1 present the block diagrams which represent these equations.

4.1.2 Circulating current control loop

As previously mentioned, the second-order harmonic component of the circulating current is generally mitigated through a control action. Basically, some controller is used to compute the signal e_{cir}^{k*} which blocks the generation of this component. When the controller is implemented in natural reference frame, this approach combines a resonant controller with a feedback loop which can be described by the following

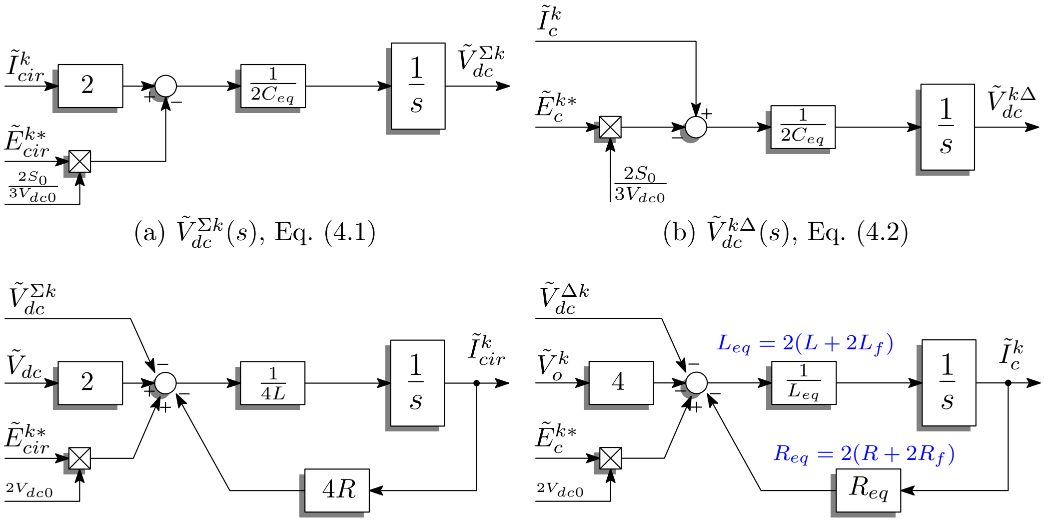

(a) $\tilde{V}^{\Sigma k}_{dc}(s)$, Eq. (4.1)

(b) $\tilde{V}^{k\Delta}_{dc}(s)$, Eq. (4.2)

(c) $\tilde{I}^{k}_{cir}(s)$, Eq. (4.3)

(d) $\tilde{I}^{k}_{c}(s)$, Eq. (4.4)

Figure 4.1: Block diagrams of the linearized model of the MMC.

control law:

$$\tilde{E}^{k*}_{cir}(s) = C_{cir}(s)\tilde{I}^{k}_{cir}(s), \tag{4.5}$$

$$C_{cir}(s) = -\frac{k_r^{cir}s}{s^2 + 4\omega_0^2}, \tag{4.6}$$

where $C_{cir}(s)$ is the controller responsible for keeping the arms free from the second order harmonic component. In this case, k_r^{cir} is the resonant gain, whereas ω_0 is the fundamental angular frequency. The term $(2\omega_0)^2 = 4\omega_0^2$ indicates that this controller resonate at the frequency of the second-order harmonic component. Even though this is a linear controller, the tilde notation, which indicates a small-signal variable, is kept for aesthetic reasons. It is important to notice that the forthcoming sections might present this control loop into their control diagrams, thus, for more insights on how the mitigation loop is introduced into the MMC control system, please refer to Figures 4.4, 4.7 and 4.10.

It is important to mention that, as the circulating current presents dc component and its state equation, (4.3), contains $\tilde{V}_{dc}$, the model which represents the circulating current, in fact, is the model for the dc side of the MMC. The first step to reach this model is to combine (4.1) and (4.3), which leads to:

$$(4sC_{eq}Z + 1)\,\tilde{I}^{k}_{cir}(s) = \left(\frac{S_0}{3V_{dc0}} + 2sC_{eq}V_{dc0}\right)\tilde{E}^{k*}_{cir}(s) + 2sC_{eq}\tilde{V}_{dc}(s). \tag{4.7}$$

After that, substituting (4.5) in (4.7) and making some mathematical manipulations, it is possible to find:

$$\tilde{I}_{cir}^{k}(s) = Y_{dc}(s)\tilde{V}_{dc}(s), \tag{4.8}$$

where:

$$Y_{dc}(s) = \frac{2sC_{eq}}{4sC_{eq}Z + 1 - \left(\frac{S_0}{3V_{dc0}} + 2sC_{eq}V_{dc0}\right)C_{cir}(s)}. \tag{4.9}$$

where Y_{dc} is the equivalent admittance of the dc side of the MMC. It is important to notice that this admittance is affected by the circulating-current controller $C_{cir}(s)$ and by the values of some passive elements. However, the currents and voltages of the ac side take no part in this behavior. In fact, once this is a linearized model, this result is held only for small variations of the variables around their operating point. Equation (4.8) can be represented by the circuit in Figure 4.2.

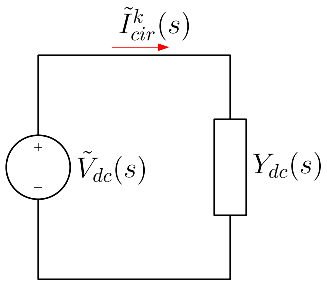

Figure 4.2: Equivalent circuit of the circulating current.

In order to validate the developed analytical model represented by (4.9), its frequency response was compared with the frequency response obtained from the non-linear, time-domain model presented in the Chapter 3. It is worthwhile mentioning that this non-linear model was used, instead of the switching-level model, to reduce the computational burden and speed up the process of validation. It is also important to mention that this approach is widely used in the literature [47, 53, 54, 110] and is to be used to validate all the transfer functions obtained in this work. For the sake of practicability, the non-linear model was implemented in PSIM, and its frequency response was obtained by applying a disturbance in the circuit and observing its effect on the analyzed variable. In the case of the dc-side dynamic admittance, for instance, a sinusoidal disturbance was applied on the dc voltage and the effect was observed in the circulating current. For more information about how the frequency response are extracted from the non-linear, time-domain, model, please refer to the Appendix C. One last point before presenting the results, for this analysis and the forthcoming, the control gain k_r^{cir} was set to $0.1A^{-1}rad/s$.

Figure 4.3 presents the bode diagram containing the frequency response for the analytical model in a blue straight line (Obtained with the use of Matlab [111]), and for the non-linear model in red circles. It is observed that both responses are

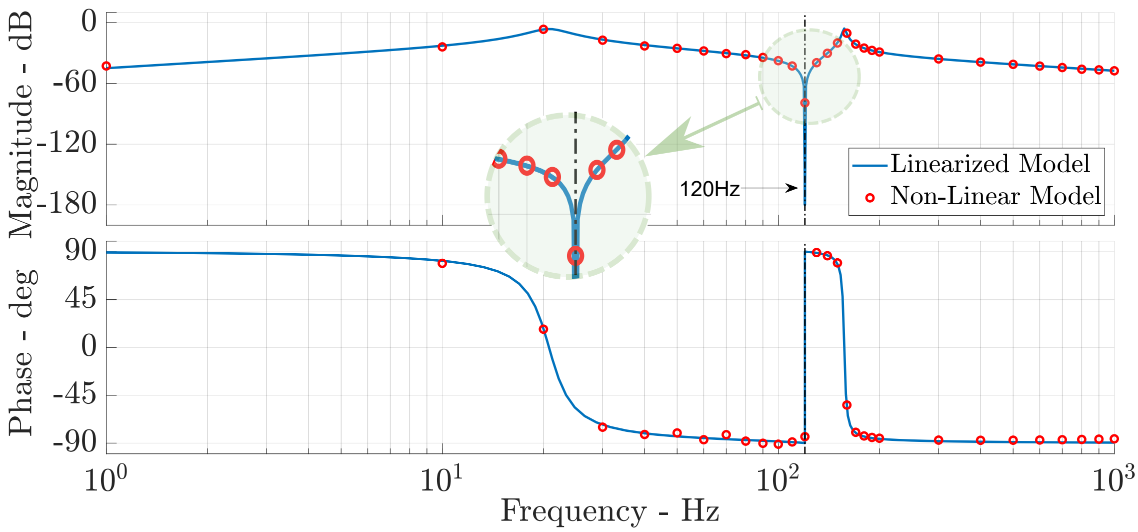

Figure 4.3: Frequency Response of the dc-side admittance, Y_{dc}: comparison between the linearized model and the non-linear, time-domain model.

similar, although some small errors can be spotted, specially in the second harmonic frequency. In fact, the resonant controller compels the dc admittance to present a very small (tending to $-\infty dB$) value at the frequency $2\omega_0$, which corresponds to the mitigation of the respective component of the circulating current. Nonetheless, some factors such as the digital implementation of the resonant controller and the numerical errors in the simulation influenced the results obtained from the non-linear, time-domain model. As a matter of fact, the digital implementation of a resonant controller presents some differences in relation to the continuous-time transfer function used in the linearized model. As for the numerical errors, they are directly influenced by the integration time step used in the simulation. In this case, a trade off between accuracy and computational burden is raised. These factors altogether collaborated for the theoretical magnitude $-180dB$ of the second-order harmonic component, indicated by the proposed model, has not been achieved in the simulation of the non-linear system.

4.1.3 Current controlled MMC

In this section the MMC is considered under current control such as represented in Figure 4.4. The model to be presented can either represent the MMC as grid-tied or as off-grid converter and because of that the figure presents both possibilities. The PLL (phase-locked loop) presented in the figure, of course, is only necessary in the grid-tied mode. As observed in the figure, the control law is given by:

$$\tilde{E}_c^{k*}(s) = C_i(s)\left[\tilde{I}_c^{k*}(s) - \tilde{I}_c^{k}(s)\right], \tag{4.10}$$

$$C_i(s) = k_p^i + \frac{k_r^i s}{s^2 + \omega_0^2}, \tag{4.11}$$

where $C_i(s)$ is the transfer function of the current control loop and k_p^i and k_r^i are, respectively, its proportional and resonant gains. Observe that term ω_0^2 indicates that the resonant frequency of the controller corresponds to the fundamental component.

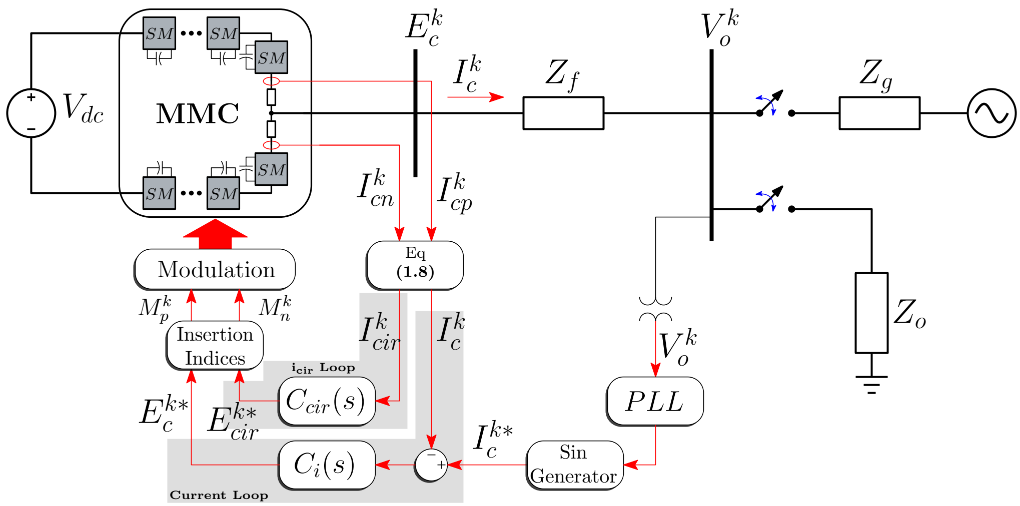

Figure 4.4: Block diagram of the MMC under current control in natural reference frame. It is also included the mitigation loop of the second-order harmonic component of i_{cir}.

The first step to reach the model for the current controller MMC is to combine (4.2) and (4.4). This procedure leads to the following result:

$$\left[4sC_{eq}\left(Z + 2Z_f\right) + 1\right] \tilde{I}_c^k(s) = \left(4sC_{eq}V_{dc0} + \frac{2S_0}{3V_{dc0}}\right) \tilde{E}_c^{k*}(s) - 8sC_{eq}\tilde{V}_o^k(s). \tag{4.12}$$

Substituting $\tilde{E}_c^{k*}(s)$ from (4.10) in (4.12) one can reach the following result:

$$\tilde{I}_c^k(s) = G_i^{cl}(s) I_c^{k*}(s) - Y_{ac}(s)\tilde{V}_o^k(s), \tag{4.13}$$

where:

$$G_i^{cl}(s) = \frac{\left(4sC_{eq}V_{dc0} + \frac{2S_0}{3V_{dc0}}\right) C_i(s)}{4sC_{eq}\left(Z + 2Z_f\right) + \left(4sC_{eq}V_{dc0} + \frac{2S_0}{3V_{dc0}}\right) C_i(s) + 1} \tag{4.14}$$

$$Y_{ac}(s) = \frac{8sC_{eq}}{4sC_{eq}\left(Z + 2Z_f\right) + \left(4sC_{eq}V_{dc0} + \frac{2S_0}{3V_{dc0}}\right) C_i(s) + 1} \tag{4.15}$$

It is important to notice that, the result presented in (4.13) is actually the Norton-equivalent representation of the MMC under current control loop. In this case, the equivalent circuit, depicted in Figure 4.5, have a current source $C_i^{cl}(s)I_c^{k*}(s)$ and an admittance $Y_{ac}(s)$. It is possible to see that both elements are influenced by the current controller, yet the circulating current takes no part in ac-side behavior. As the circulating current mitigation loops is present, it was decided also to present it in Figure 4.5 , despite the fact it is not coupled to the ac side of the converter.

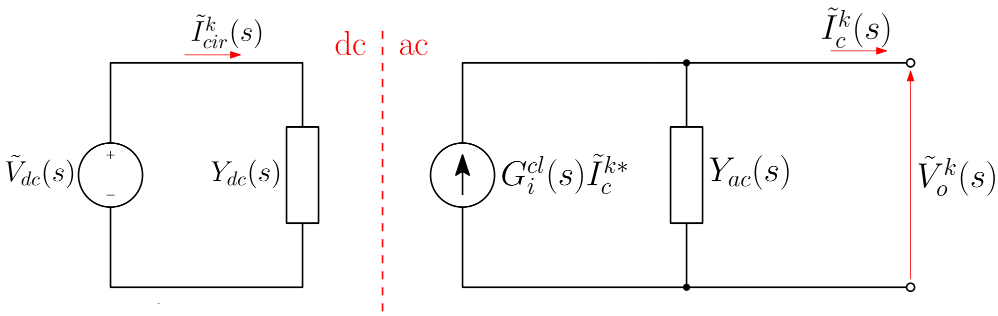

Figure 4.5: Norton-equivalent circuit of the MMC under current control. As the MMC always has a circulating current mitigation control, it was included in the figure the circuit developed in Section 4.1.2.

For the validation, it was considered $k_p^i = 0.0001A^{-1}$ and $k_r^i = 0.01A^{-1}rad/s$ and repeated the procedure previously mentioned, and explained in Appendix C. Figure 4.6 presents this comparison and from it one can notice that the results match almost perfectly, except at the resonant frequency in magnitude chart of the equivalent admittance (Figure 4.6a). The same reason presented in the last section, i.e., errors introduced by the discretization of the resonant parcel and by the simulation, can be credited as the source of this difference. It is important to notice that Y_{ac} indicates how the bus voltage disturbs the current control and, as far as it is possible to notice, this influence in the fundamental component tends to zero or to a negligibly value. It is also spotted other small differences in the phase chart of Y_{ac} in the frequency range that goes from $600Hz$ to $1kHz$. As for the closed-loop gain G_i^{cl}, it is not noticed any significant difference. Notice that at $60Hz$

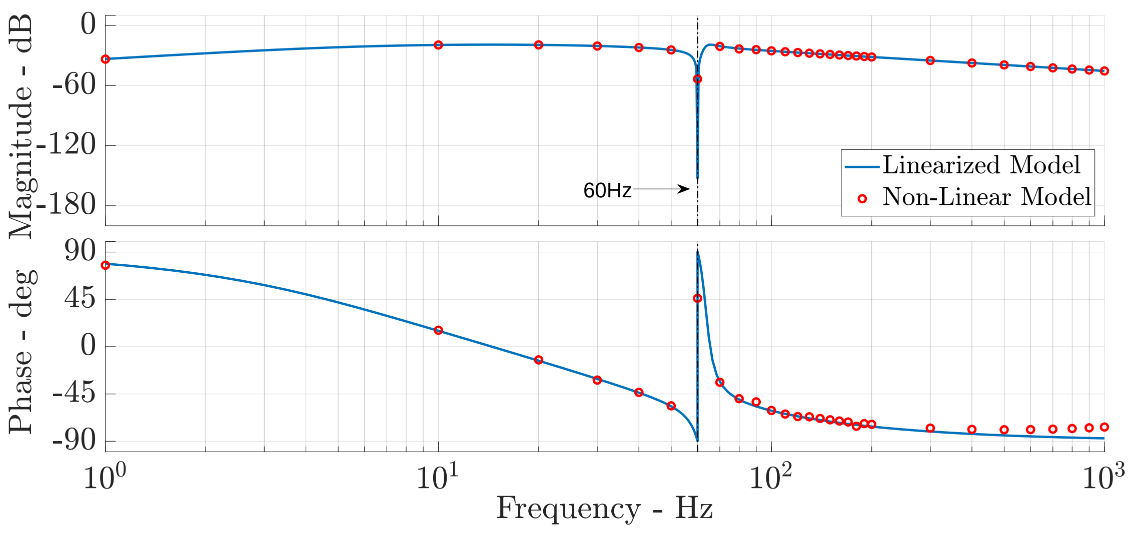

(a) Norton admittance, Y_{ac}

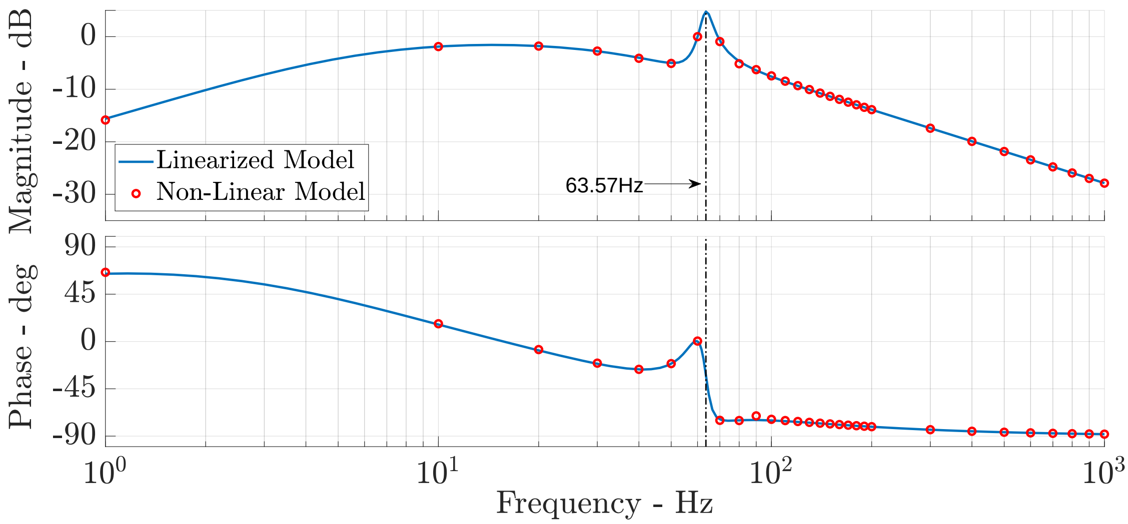

(b) Norton gain, G_i^{cl}

Figure 4.6: Frequency Response of Y_{ac} and G_i^{cl}: comparison between the linearized model and the non-linear, time-domain model

both results indicate $0dB$, which means that the current source in the Figure 4.5 produces exactly the current indicated by I_c^{k*}.

4.1.4 Single-loop voltage controlled MMC

This section considers the MMC as a grid-forming converter supplying a generic load represented by the current source i_o^k in Figure 4.7. In this case, along with the $R_f - L_f$ circuit, the output net comprises a capacitor bank C_f. As for the control system, the error between the reference signal v_o^{k*} and the measured voltage in the main-bus v_o^k is amplified by a proportional resonant controller to produce e_c^{k*}. Thus, the control law can be represented by:

$$\tilde{E}_c^{k*}(s) = C_v^{sl}(s)\left[\tilde{V}_o^{k*}(s) - \tilde{V}_o^k(s)\right], \tag{4.16}$$

$$C_v^{sl}(s) = k_p^{v,sl} + \frac{k_r^{v,sl}s}{s^2+\omega_0^2}, \tag{4.17}$$

where $C_v^{sl}(s)$ is the transfer function of the voltage controller, $k_p^{v,sl}$ and $k_r^{v,sl}$ are, respectively, its proportional and resonant gains, and the superscript sl denotes single-loop. Notice that, as already happened to the current-controlled MMC, the circulating-current mitigation loop is also included in Figure 4.7 for the sake of information, yet it does not affect the voltage control.

Considering the result presented in (4.12) and displayed here for practical pur-

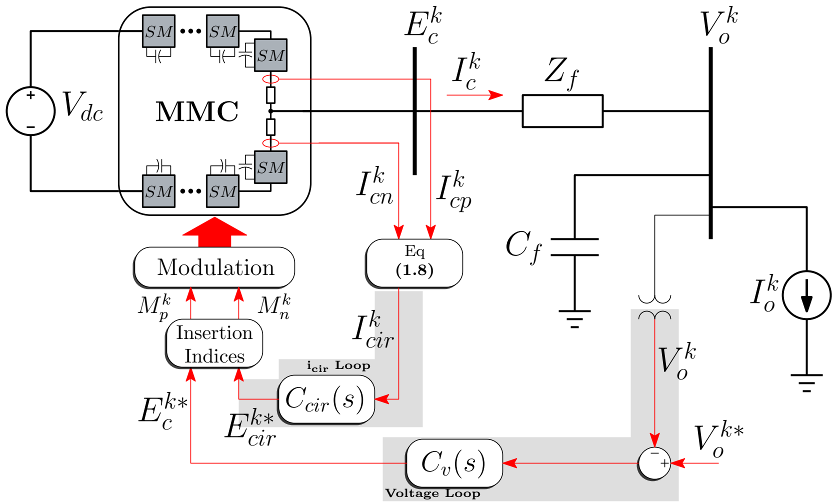

Figure 4.7: Block diagram of the MMC under single-loop voltage control in natural reference frame. It is also included the mitigation loop of the second-order harmonic component of i_{cir}.

poses,

$$\left[4sC_{eq}\left(Z+2Z_f\right)+1\right]\tilde{I}_c^k(s)=\left(4sC_{eq}V_{dc0}+\frac{2S_0}{3V_{dc0}}\right)\tilde{E}_c^{k*}(s)-8sC_{eq}\tilde{V}_o^k(s), \quad (4.18)$$

it is possible to obtain the following result when substituting $\tilde{E}_c^{k*}(s)$ by its definition in (4.16):

$$\tilde{V}_o^k(s)=G_{v,cl}^{sl}(s)\tilde{V}_o^{k*}(s)-Z_{ac}^{sl}(s)\tilde{I}_c^k(s) \quad (4.19)$$

where:

$$G_{v,cl}^{sl}(s)=\frac{\left(4sC_{eq}V_{dc0}+\frac{2S_0}{3V_{dc0}}\right)C_v^{sl}(s)}{8sC_{eq}+\left(4sC_{eq}V_{dc0}+\frac{2S_0}{3V_{dc0}}\right)C_v^{sl}(s)} \quad (4.20)$$

$$Z_{ac}^{sl}(s)=\frac{4sC_{eq}\left(Z+2Z_f\right)+1}{8sC_{eq}+\left(4sC_{eq}V_{dc0}+\frac{2S_0}{3V_{dc0}}\right)C_v^{sl}(s)} \quad (4.21)$$

Notice that (4.19) represents a voltage net equation and because of that, it is possible to draw the equivalent circuit depicted in Figure 4.8a. For the sake of referencing, it was decided to call this circuit the inner equivalent circuit of the MMC under voltage control. In this case, Z_{ac}^{sl} is the inner equivalent impedance of the MMC, whereas $G_{v,cl}^{sl}$ is the closed-loop transfer function relating the measured and reference voltages. As the MMC together with the capacitor bank plays the role of a voltage source, the use of a Thévenin-equivalent circuit is more suitable for analysis purposes. For this reason, the circuit in in Figure 4.8a was rearranged into the circuit presented in Figure 4.8b, where Z_{th}^{sl} is Thévenin impedance obtained by combining Z_{ac}^{sl} and the impedance of the capacitor bank, Z_{Cf}, and $G_{th}^{sl}\tilde{V}_o^{k*}$ is the

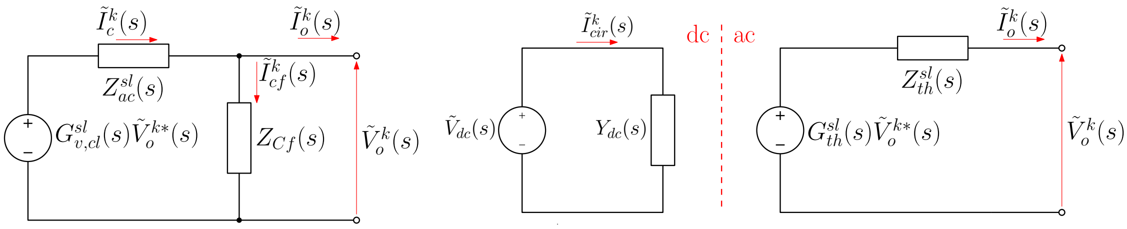

(a) Inner equivalent circuit (b) Thévenin-equivalent circuit

Figure 4.8: Equivalent circuits of the MMC under single-loop voltage control. As the MMC always has a circulating current mitigation control, it was included in the figure the circuit developed in Section 4.1.2.

open circuit voltage. In this case, it is possible to write:

$$\tilde{V}^k_o(s) = G^{sl}_{th}(s)\tilde{V}^{k*}_0(s) - Z^{sl}_{th}(s)\tilde{I}^k_o(s), \tag{4.22}$$

where:

$$G^{sl}_{th}(s) = \frac{G^{sl}_{v,cl}(s)}{sC_f Z^{sl}_{ac}(s) + 1}, \tag{4.23}$$

$$Z^{sl}_{th}(s) = \frac{Z^{sl}_{ac}(s)}{sC_f Z^{sl}_{ac}(s) + 1}. \tag{4.24}$$

It is important to notice that with this approach, the equivalent circuit presents fewer variables in comparison to the circuit in Figure 4.8a and assumes the form of a standard voltage behind impedance model.

The validation process was carried out considering $k^{v,sl}_p = 0.0001V^{-1}$ and $k^{v,sl}_p = 0.001V^{-1}rad/s$, and the results are presented in Figure 4.9. It is possible to observe that, once more, the responses predicted by the linearized model match the responses of the non-linear system with few exceptions. To be more specific, the differences

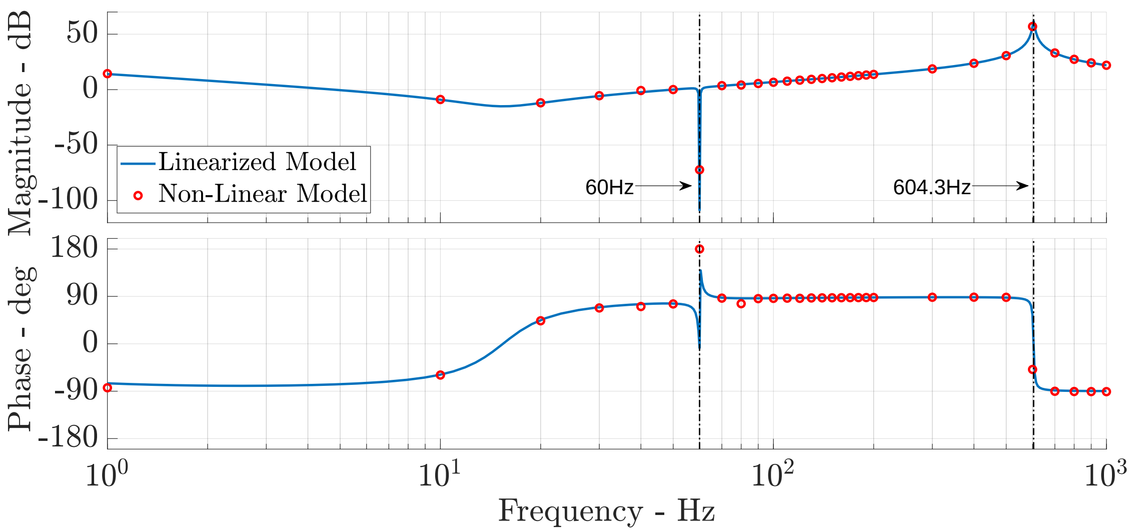

(a) Thévenin impedance, Z^{sl}_{th}

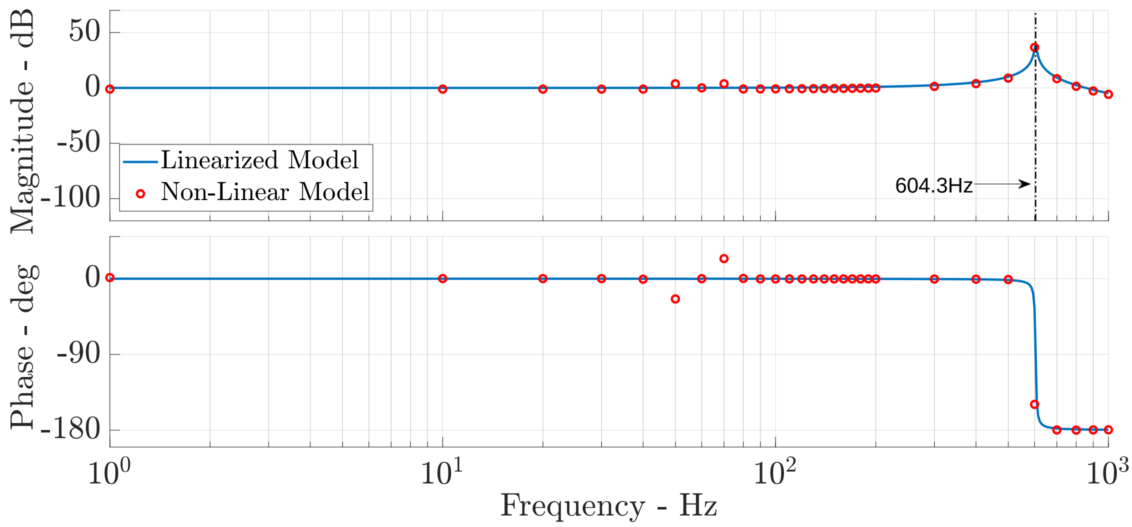

(b) Thévenin gain, G_{th}^{sl}

Figure 4.9: Frequency Response of Z_{th}^{sl} and G_{th}^{sl}: comparison between the linearized model and the non-linear, time-domain model

are observed on the magnitude and phase charts of Z_{th}^{sl} at $60Hz$ and in the phase chart of G_{th}^{sl} at 50 and $70Hz$.

4.1.5 Doubly-loop Voltage controlled MMC

Still considering the MMC as a grid-forming converter, other control approach is to include an inner current loop in addition to the outer voltage control, as depicted in Figure 4.10. In this case, the output of the voltage controller computes the reference signal i_c^{k*} which is used by the current controller to compute the signal e_c^{k*}. This approach provides the MMC with the capacity of limiting the produced current in case of ac faults in the system.

In this case, the reference current for the inner loop is computed as follows:

$$\tilde{I}_c^{k*}(s) = C_v^{dl}(s)\left[\tilde{V}_o^{k*}(s) - \tilde{V}_o^{k}(s)\right], \tag{4.25}$$

$$C_v^{dl}(s) = k_p^{v,dl} + \frac{k_r^{v,dl} s}{s^2 + \omega_0^2}, \tag{4.26}$$

where C_v^{dl} is the voltage controller, and $k_p^{v,dl}$ and $k_r^{v,dl}$ are its proportional and resonant gains, respectively. It goes without saying that the resonant part of the controllers is tuned into the fundamental frequency.

For obtaining an analytical model for the double-loop-controlled grid-forming MMC, it is possible to make use of the Norton-equivalent result presented in Section 4.1.3 for representing the inner current loop. Thus, the outer voltage control

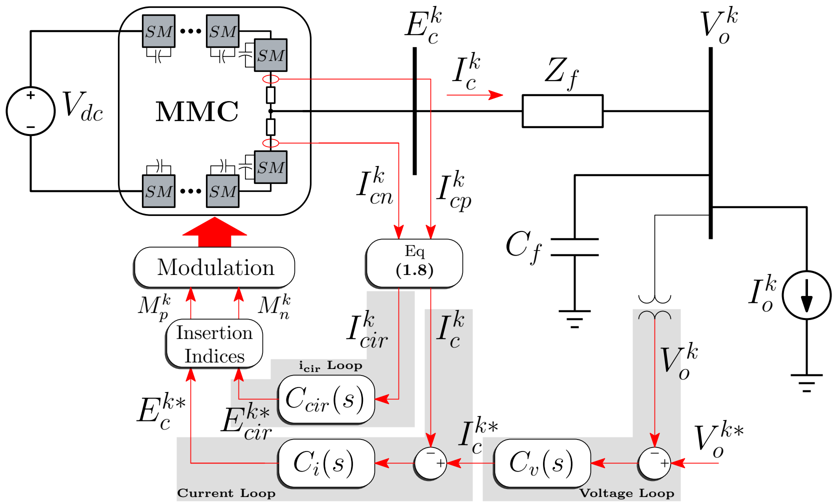

Figure 4.10: Block diagram of the MMC under double-loop voltage control in natural reference frame. With the mitigation loop of the second-order harmonic component of i_{cir}. included

loop can be included in the model by substituting (4.25) in (4.13), which leads to:

$$\tilde{V}_o^k(s) = G_{c,cl}^{dl}(s)\tilde{V}_o^{k*}(s) - Z_{ac}^{dl}(s)\tilde{I}_c^k(s), \tag{4.27}$$

where:

$$G_{v,cl}^{dl}(s) = \frac{G_i^{cl}(s)C_v^{dl}(s)}{Y_{ac}(s) + G_i^{cl}(s)C_v^{dl}(s)}, \tag{4.28}$$

$$Z_{ac}^{dl}(s) = \frac{1}{Y_{ac}(s) + G_i^{cl}(s)C_v^{dl}(s)}. \tag{4.29}$$

Once more, $G_{v,cl}^{dl}$ and Z_{ac}^{dl} are the closed-loop voltage gain and the inner equivalent impedance of the system, respectively. As in the previous section, the model described by (4.27) represents the characteristic of the MMC without considering the capacitor bank in the main bus. In this case, the circuit realization of (4.27) is equal to that presented in the previous sections, though it is once more presented in Figure 4.11 for the sake of practicality. Following the same methodology used in last section, it is possible to reach the Thévenin-equivalent analytical model given by:

$$\tilde{V}_o^k = G_{th}^{dl}(s)\tilde{V}_o^{k*}(s) - Z_{th}^{dl}(s)\tilde{I}_o^k(s), \tag{4.30}$$

where:

$$G_{th}^{dl}(s) = \frac{G_{v,dl}^{dl}(s)}{sC_f Z_{ac}^{dl}(s) + 1}, \tag{4.31}$$

$$Z_{th}^{v} = \frac{Z_{ac}^{dl}(s)}{sC_f Z_{ac}^{dl}(s) + 1}. \tag{4.32}$$

Finally, the circuit realization of (4.30) is presented in Figure 4.11b.

The results used for validating the proposed model are presented in Figure 4.12.

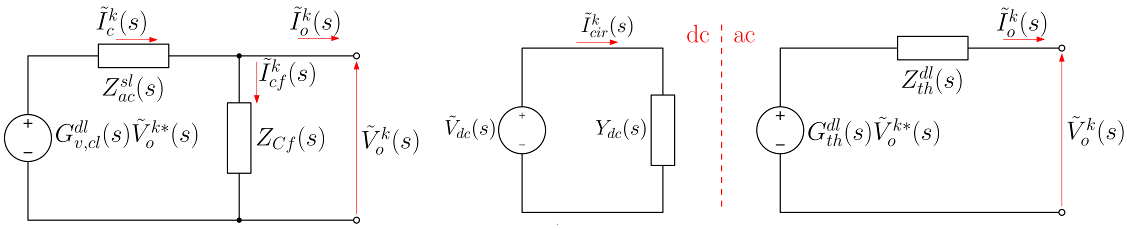

(a) Inner equivalent circuit (b) Thévenin-equivalent circuit

Figure 4.11: Equivalent circuits of the MMC under double-loop voltage control.

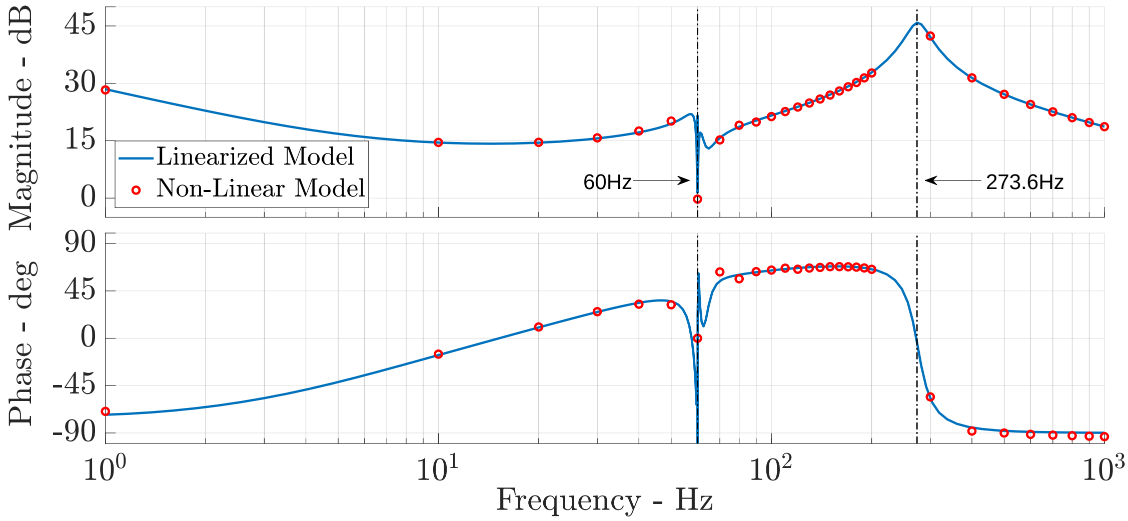

(a) Thévenin impedance, Z_{th}^{dl}

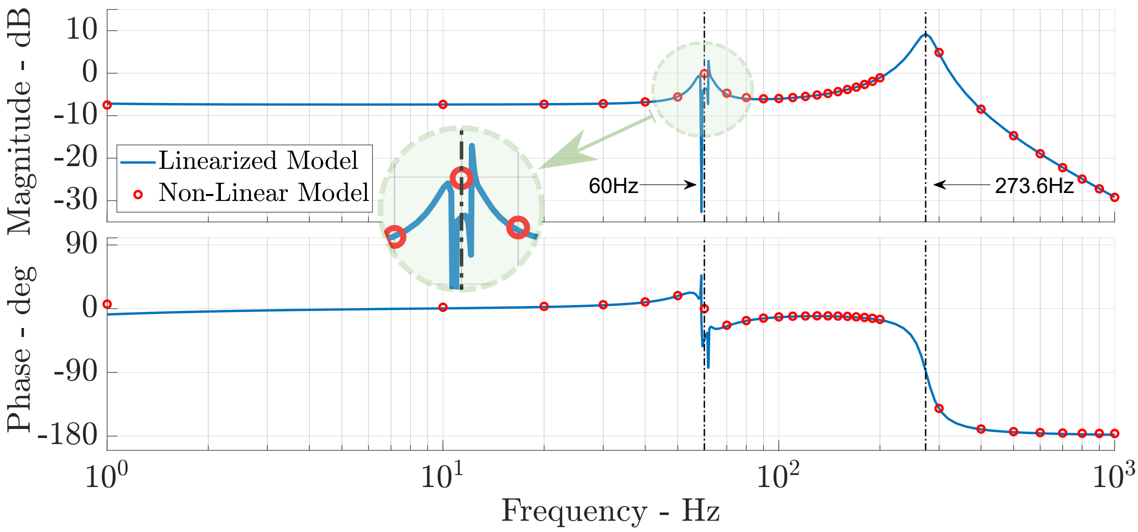

(b) Thévenin gain, G_{th}^{dl}

Figure 4.12: Frequency Response of Z_{th}^{dl} and G_{th}^{dl}: comparison between the linearized model and the non-linear, time-domain model

Considering the frequency response for Z_{th}^{dl}, it is noticeable that the proposed model results matches perfectly the results obtained by the non-linear time-domain model, except for a small difference at $70Hz$ on the phase chart. A similar characteristic is observed for G_{th}^{dl}, yet, in this case, the major difference occurs in the magnitude chart at $60Hz$ where the non-linear model indicates $0dB$, whereas the proposed model points to $-3.5dB$. To finish this section, it is important to highlight that the Thévenin model presented in (4.30) is the major contribution of this thesis and published in the reference [62].

4.2 MMC controlled in Synchronous Reference Frame

This section presents the models for representing the MMC in SRF. It is important to notice that, not only the models are derived in SRF, but also the control loops are implemented in SRF. Because of that, it was used proportional-integral controllers to guarantee zero steady-state error. The following subsection presents the Laplace-domain representation of the MMC in SRF, wheres the subsequent sections are focused on deriving the models for the different control modes analyzed.

4.2.1 Laplace-domain representation of the MMC in SRF

Before obtaining the MMC equations in SRF, it is necessary to introduce the approach followed in the forthcoming sections. As in the previous chapter, the MMC is due to produce either current or voltage at the fundamental frequency. For this reason, the Park transformation to be presented uses a reference synchronously aligned with the fundamental component. However, the component of the circuiting current to be mitigated corresponds to the second-order harmonic and because of that it is necessary to use a referential synchronously aligned to this component in this control loop. For this reason, the MMC state equations used in the voltage/-current control loop are to be transformed into SRF, whereas the equations used in the circulating current loop are to be transformed into doubly-SRF (D-SRF). More details on the mathematical implications of the reference-frame transformation used in this section are presented in Appendix A. To facilitate the understanding of this section, the state equations in (3.72)-(3.75) are rewritten here:

$$2C_{eq}\frac{d\tilde{\mathbf{v}}_{dc}^{abc\Sigma}}{dt} = 2\tilde{\mathbf{i}}_{cir}^{abc} - \frac{2S_0}{3V_{dc0}}\tilde{\mathbf{e}}_{cir}^{abc*}, \tag{4.33}$$

$$2C_{eq}\frac{d\tilde{\mathbf{v}}_{dc}^{abc\Delta}}{dt} = -\frac{2S_0}{3V_{dc0}}\tilde{\mathbf{e}}_{c}^{abc*} + \tilde{\mathbf{i}}_{c}^{abc}, \tag{4.34}$$

$$4L\frac{d\tilde{\mathbf{i}}_{cir}^{abc}}{dt} = -4R\tilde{\mathbf{i}}_{cir}^{abc} - \tilde{\mathbf{v}}_{dc}^{abc\Sigma} + 2V_{dc0}\tilde{\mathbf{e}}_{cir}^{abc*} + 2\tilde{\mathbf{v}}_{dc}^{abc}, \tag{4.35}$$

$$2\left(L+2L_f\right)\frac{d\tilde{\mathbf{i}}_c^{abc}}{dt}=2V_{dc0}\tilde{\mathbf{e}}_c^{abc*}-\tilde{\mathbf{v}}_{dc}^{abc\Delta}-4\tilde{\mathbf{v}}_o^{abc}-2\left(R+2R_f\right)\tilde{\mathbf{i}}_c^{abc}. \tag{4.36}$$

Notice that it is introduced a new notation in (4.33)-(4.36). In this case, the bold letters represent either vectors or matrices, and vector notations such as

$$\begin{aligned}\mathbf{x}^{abc}&=\left[x^a,\ x^b,\ x^c\right]^T,\\ \mathbf{x}^{dq0}&=\left[x^d,\ x^q,\ x^0\right]^T,\end{aligned} \tag{4.37}$$

respectively representing natural- and synchronous-reference frame quantities, shall be used hereafter in order to reduce the size of equations and allow the use of matrix algebra.

Through this chapter, the frame transformations are represented in the figures by the blocks marked with $\mathbf{T}_{dq0}$ and $\mathbf{T}_{dq0}^{-1}$, representing, respectively, the Park transformation and its inverse. Thus:

$$\mathbf{T}_{dq0}=\frac{2}{3}\begin{bmatrix}\cos\left(\theta\right) & \cos\left(\theta-\frac{2\pi}{3}\right) & \cos\left(\theta+\frac{2\pi}{3}\right)\\ \sin\left(\theta\right) & \sin\left(\theta-\frac{2\pi}{3}\right) & \sin\left(\theta+\frac{2\pi}{3}\right)\\ \frac{1}{2} & \frac{1}{2} & \frac{1}{2}\end{bmatrix}, \tag{4.38}$$

$$\mathbf{T}_{dq0}^{-1}=\begin{bmatrix}\cos\left(\theta\right) & \sin\left(\theta\right) & 1\\ \cos\left(\theta-\frac{2\pi}{3}\right) & \sin\left(\theta-\frac{2\pi}{3}\right) & 1\\ \cos\left(\theta+\frac{2\pi}{3}\right) & \sin\left(\theta+\frac{2\pi}{3}\right) & 1\end{bmatrix}, \tag{4.39}$$

where θ is basically the angle related to the fundamental component of v_o^a. In a grid connected converter, this angle is obtained by the PLL. On the other hand, when it comes to a grid-forming converter this angle can be computed as $\theta=\omega_0 t$. Of course, in the case of D-SRF, $\theta=-2\omega_0 t$, so that the second-order harmonic component in the current produced by the negative-sequence can be transformed into dc quantities.

According to the premises established in the first paragraph, (4.34) and (4.36) should be transformed in SRF, and (4.33) and (4.35) into D-SRF. The results, already transformed into Laplace domain are presented here:

$$2C_{eq}\left(2\mathbf{\Omega}+s\mathbf{I}\right)\tilde{\mathbf{V}}_{dc}^{2dq0\Sigma}=2\tilde{\mathbf{I}}_{cir}^{2dq0}-\frac{2S_0}{3V_{dc0}}\tilde{\mathbf{E}}_{cir}^{2dq0*}, \tag{4.40}$$

$$2C_{eq}\left(\mathbf{\Omega}+s\mathbf{I}\right)\tilde{\mathbf{V}}_{dc}^{dq0\Delta}=-\frac{2S_0}{3V_{dc0}}\tilde{\mathbf{E}}_c^{dq0*}+\tilde{\mathbf{I}}_c^{dq0}, \tag{4.41}$$

$$4L\left(2\mathbf{\Omega}+s\mathbf{I}\right)\tilde{\mathbf{I}}_{cir}^{2dq0}=-4R\tilde{\mathbf{I}}_{cir}^{2dq0}-\tilde{\mathbf{V}}_{dc}^{2dq0\Sigma}+2V_{dc0}\tilde{\mathbf{E}}_{cir}^{2dq0*}+2\tilde{\mathbf{V}}_{dc}^{2dq0}, \tag{4.42}$$

$$2\left(L+2L_f\right)\left(\mathbf{\Omega}+s\mathbf{I}\right)\tilde{\mathbf{I}}_c^{dq0} = 2V_{dc0}\tilde{\mathbf{E}}_c^{dq0*} - \tilde{\mathbf{V}}_{dc}^{dq0\Delta} - 4\tilde{\mathbf{V}}_o^{dq0} - 2\left(R+2R_f\right)\tilde{\mathbf{I}}_c^{dq0}. \quad (4.43)$$

In this case, $\mathbf{I}$ is a 3×3 identity matrix and $\mathbf{\Omega}$ is the matrix that indicates the coupling between the axes. It is given by:

$$\mathbf{\Omega} = \begin{bmatrix} 0 & -\omega_0 & 0 \\ \omega_0 & 0 & 0 \\ 0 & 0 & 0 \end{bmatrix}. \quad (4.44)$$

For the sake of simplifying equations, from this point on, the matrices $\mathbf{\Omega}+s\mathbf{I}$ and $2\mathbf{\Omega}+s\mathbf{I}$ are to be dubbed SRF complex frequency $\mathbf{s}_{dq}$ and D-SRF complex frequency $\mathbf{s}_{2dq}$. Also, for aesthetic reasons the voltage of the dc-bus is represented using matrix notation by $\tilde{V}_{dc}^{abc} = \left[\tilde{V}_{dc},\ \tilde{V}_{dc},\ \tilde{V}_{dc}\right]^T$ in natural reference frame, which leads to $\tilde{V}_{dc}^{dq0} = \tilde{V}_{dc}^{2dq0} = \left[0,\ 0,\ \tilde{V}_{dc}\right]^T$ in SRF and D-SRF. Finally, Figure 4.13 presents the block-diagram realization of SRF/D-SRF model of the MMC. The diagrams for the zero-sequence component were omitted to save space, once they are equal to those

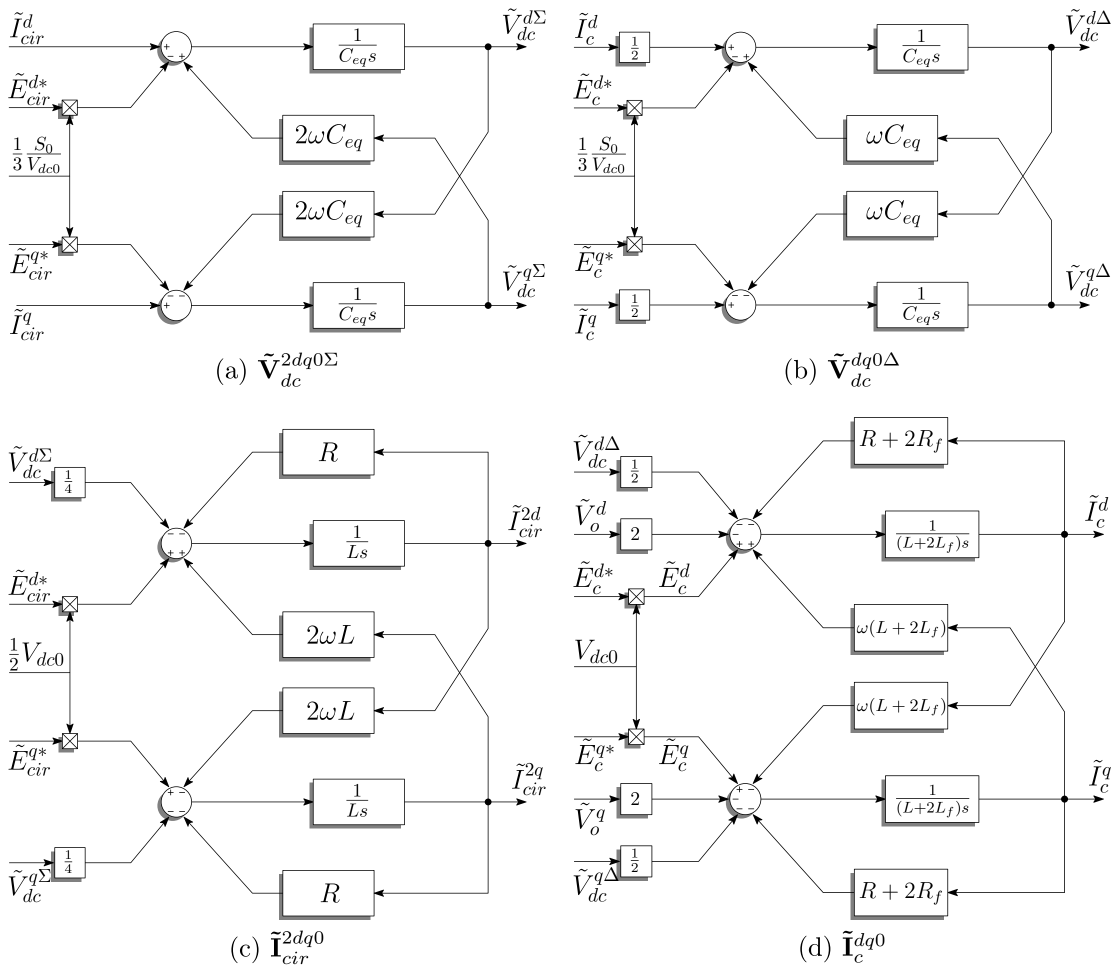

Figure 4.13: Block diagrams in dq coordinates of the linearized model of the MMC in SRF.

presented in Figure 4.1.

Before continuing to the following sections, it is necessary do discuss some important points on the matrices that represent equivalent admittances, impedances and closed-loop gains alike[1]. In general, they might present the following pattern:

$$\mathbf{M} = \begin{bmatrix} M_{dd} & M_{dq} & 0 \\ M_{qd} & M_{qq} & 0 \\ 0 & 0 & M_0 \end{bmatrix}, \tag{4.45}$$

where $\mathbf{M}$ can be either one of the equivalent admittances/impedances/closed-loop gains of the system. Besides that, the terms M_{dd} and M_{qq} are the d- and q-axis self-related terms and M_{dq} and M_{qd} are the cross-coupling terms between the axes. In addition, M_0 is related to the zero sequence of the system.

As the symmetry[2]is held for this system, it is known that $M_{dd} = M_{qq}$ and $M_{dq} = -M_{qd}$ [112]. Consequently, the terms self-related, cross-coupling and zero-sequence might be used to refer to M_{dd} and M_{qq}, M_{dq} and M_{qd}, and M_0, respectively.

4.2.2 Circulating current control loop

As it was previously explained, the circulating-current control loop intends to suppress the second harmonic content of i_{cir} making use of PI controllers. In this case, the circulating currents are firstly transformed into D-SRF so that the $2\omega_0$ components become dc quantities and then used to compute the control signals $\tilde{\mathbf{E}}_{cir}^{2dq0*}$. It is important to highlight that the angle θ of the transformation must be aligned with the angle of the negative-sequence-generated second-order harmonic component, i.e., $\theta = -2\omega_0$, otherwise the 120Hz-component would not be transformed into dc quantities. Consequently, the control law can be given by:

$$\tilde{\mathbf{E}}_{cir}^{2dq0*}(s) = -\mathbf{C}_{cir}^{2dq0}(s)\tilde{\mathbf{I}}_{cir}^{2dq0}(s). \tag{4.46}$$

where $\mathbf{C}_{cir}^{2dq0}$ is the transfer matrix of the controller which is responsible by this task. In order to compute the insertion indices used to modulate the MMC, the vector $\tilde{\mathbf{E}}_{cir}^{2dq0*}$ might be transformed back into NRF. Although it is not presented any diagram at this time, the diagrams of the forthcoming sections (Figures 4.16, 4.20 and 4.24) include the control loop given by (4.46).

[1]As in the Chapter 4.1, the equivalent admitances, impedances and closed-loop gains of the MMC are to be presented. In this case, they correspond to the matrices $\mathbf{Y}_{ac}^{dq0}$, $\mathbf{G}_{icl}^{dq0}$,$\mathbf{G}_{dl,th}^{dq0}$, $\mathbf{Z}_{dl,th}^{dq0}$, and $\mathbf{Y}_{dc}^{2dq0}$.

[2]In this case, symmetry means that for each complex pole in the system there is another conjugated to it so that the transfer functions present no complex coefficients. This characteristic also holds for the zeros of the transfer functions.

When it comes to the transfer matrix $\mathbf{C}_{cir}^{2dq0}$, it is possible to represented it as follows:

$$\mathbf{C}_{cir}^{2dq0}(s) = \begin{bmatrix} C_{cir}(s) & 0 & 0 \\ 0 & C_{cir}(s) & 0 \\ 0 & 0 & 0 \end{bmatrix}, \tag{4.47}$$

$$C_{cir}(s) = k_p^{icir} + \frac{k_i^{icir}}{s}, \tag{4.48}$$

where C_{cir} represents the transfer function of the PI controller used in the loop, and k_p^{icir} and k_i^{icir} its proportional and integral gains.

Combining the results presented in (4.40) and (4.42) and substituting thereafter the control law in (4.46) it is possible to find the analytical model which represents the circulating current dynamics in D-SRF:

$$\tilde{\mathbf{I}}_{cir}^{2dq0}(s) = \mathbf{Y}_{dc}^{2dq0}(s)\tilde{\mathbf{V}}_{dc}^{2dq0}(s). \tag{4.49}$$

As previously mentioned, the circulating current is due to the oscillating components in the dc voltages, i.e. $\tilde{\mathbf{V}}_{dc}^{2dq0}$. Consequently, $\mathbf{Y}_{dc}^{2dq0}$ is the dc-side equivalent admittance of the MMC. This result can be represented by the equivalent circuit in Figure 4.14 and the admittance can be given by:

$$\mathbf{Y}_{dc}^{2dq0}(s) = 2C_{eq}\mathbf{\Gamma}_{cir}^{-1}(s)\mathbf{s}_{2dq}, \tag{4.50}$$

where

$$\mathbf{\Gamma}_{cir}(s) = \mathbf{I} + 4LC_{eq}\mathbf{s}_{2dq}^2 + 4RC_{eq}\mathbf{s}_{2dq} + \left(\frac{S_0}{3V_{dc0}}\mathbf{I} + 2V_{dc0}C_{eq}\mathbf{s}_{2dq}\right)\mathbf{C}_{cir}^{2dq0}(s), \tag{4.51}$$

is a dimensionless factor, and

$$\mathbf{s}_{2dq} = 2\mathbf{\Omega} + s\mathbf{I} \tag{4.52}$$

is a matrix defined as the D-SRF complex frequency.

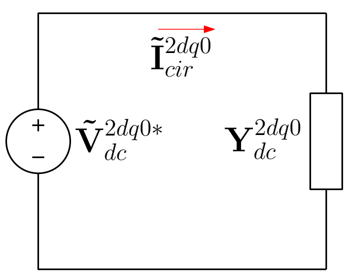

Figure 4.14: Equivalent circuit of the circulating current in D-SRF.

The dc-side admittance, as represented in (4.49), links the small-signal disturbances in the voltage of the dc bus to the circulating currents i_{cir}. It stood out from this definition that the self-related and cross-axis terms of $\mathbf{Y}_{dc}^{2dq0}$ are negligible once the three legs of the converter are connected to the same dc bus. Because of that, the model validation was carried out considering only the zero-sequence term of $\mathbf{Y}_{dc}^{2dq0}$ and the outcomes are presented in Figure 4.15. In this case, proportional and integral gains, k_p^{icir} and k_i^{icir}, were set for $0.01A^{-1}$ and $0.1A^{-1}$, respectively. According to the results, the characteristic predicted by the proposed model matched the characteristic obtained from the non-linear, time-domain model with a single exception in $60Hz$. In this case, the non-linearities of the MMC were responsible for a difference of roughly $20dB$ in the magnitude chart.

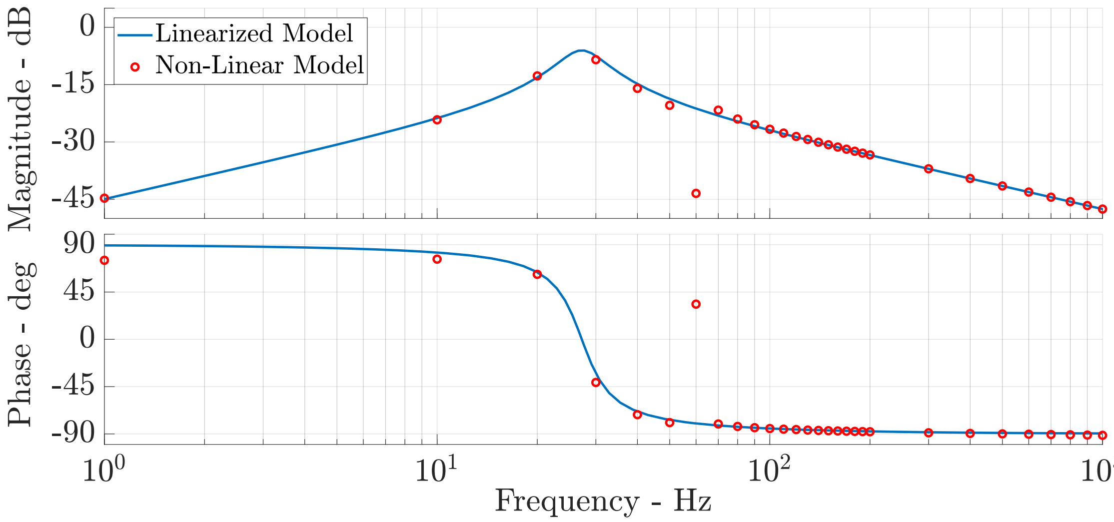

Figure 4.15: Frequency Response of the dc-side admittance, $\mathbf{Y}_{dc}^{2dq0}$: comparison between the linearized model and the non-linear, time-domain model.

It is important to understand that the zero-sequence term of $\mathbf{Y}_{dc}^{2dq0}$ conveys the relationship between the oscillating components of v_{dc} and the zero-sequence component of i_{cir}. In this regard, despite the fact the circulating current controller $G_{cir}(s)$ plays an important role in the dc-side admittance, the zero-sequence term of $\mathbf{Y}_{dc}^{2dq0}$ has nothing to do with the current which is mitigated employing the circulating-current control loop. As a matter of fact, the second-harmonic components mitigated by the circulating-current control loop have a negative sequence.

4.2.3 Current controlled MMC

Figure 4.16 presents the MMC under current control. In this case, the converter can be either attached to the grid, in which case it would be necessary a PLL circuit, or driving a generic load such as in a motor-drive application. The current control, as already explained, is implemented in SRF and because of that it is noticed blocks $\mathbf{T}_{dq0}$ and $\mathbf{T}_{dq0}^{-1}$ in the figure. According to the figure, the error between output current, $\tilde{\mathbf{I}}_c^{dq0}$, and its reference, $\tilde{\mathbf{I}}_c^{dq0*}$, is amplified by the controller $\mathbf{C}_i^{dq0}$ to produce the reference vector $\tilde{\mathbf{E}}_c^{dq0*}$, i.e.:

$$\tilde{\mathbf{E}}_c^{dq0*} = \mathbf{C}_i^{dq0}(s)\left[\tilde{\mathbf{I}}_c^{dq0*}(s) - \tilde{\mathbf{I}}_c^{dq0}(s)\right] + \mathbf{D}_i^{dq}\tilde{\mathbf{I}}_c^{dq0}(s). \tag{4.53}$$

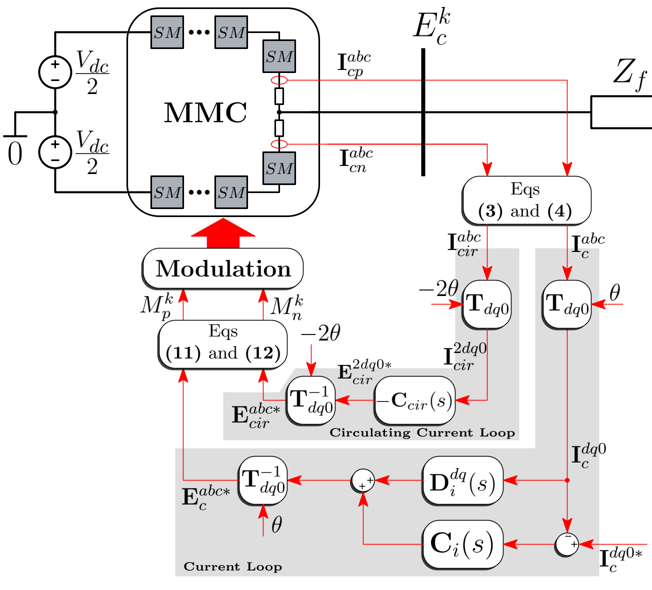

Figure 4.16: Block diagram of the MMC under current control in SRF. It is also included the mitigation loop of the second-order harmonic component of i_{cir}.

Two point must be minded regarding (4.53). Firstly, $\tilde{\mathbf{I}}_c^{dq0}$ is a 3×3 transfer matrix which components $G_i(s)$ represent the transfer function of PI controllers used for direct- and quadrature-axis control. Following the pattern used so far, k_p^i and k_i^i are the proportional and integral gains of $G_i(s)$. Secondly, the term $\mathbf{D}_i^{dq}$ corresponds to the factor used to decouple the direct and quadrature axis. These points can be mathematically expressed by:

$$\mathbf{C}_i^{dq0}(s) = \begin{bmatrix} C_i(s) & 0 & 0 \\ 0 & C_i(s) & 0 \\ 0 & 0 & 0 \end{bmatrix}, \tag{4.54}$$

$$C_i(s) = k_p^i + \frac{k_i^i}{s}, \tag{4.55}$$

$$\mathbf{D}_i^{dq} = \frac{L + 2L_f}{V_{dc0}}\boldsymbol{\Omega}. \tag{4.56}$$

Combining (4.41) and (4.43), and then substituting (4.53) into the result, it is possible to reach the model for the current loop of the MMC:

$$\tilde{\mathbf{I}}_c^{dq0}(s) = \mathbf{G}_{icl}^{dq0}(s)\tilde{\mathbf{I}}_c^{dq0*}(s) - \mathbf{Y}_{ac}^{dq0}(s)\tilde{\mathbf{V}}_o^{dq0}(s). \tag{4.57}$$

As the result presented in Chapter 4.1, (4.57) corresponds to the node equation of the Norton-equivalent circuit drawn in Figure 4.17. As the MMC always has a circulating current mitigation control, it was included in the figure the circuit developed in Section 4.2.2. Regarding $\mathbf{G}_{icl}^{dq0}$ and $\mathbf{Y}_{ac}^{dq0}$, they are matrices representing the closed-loop current gain and output admittance of the converter and are given by:

$$\mathbf{Y}_{ac}^{dq0}(s) = 8C_{eq}\mathbf{\Gamma}_i^{-1}(s)\mathbf{s}_{dq}, \tag{4.58}$$

$$\mathbf{G}_{icl}^{dq0}(s) = \mathbf{\Gamma}_i^{-1}(s)\left(4C_{eq}V_{dc0}\mathbf{s}_{dq} + \frac{2S_0}{3V_{dc0}}\mathbf{I}\right)\mathbf{C}_i^{dq0}(s), \tag{4.59}$$

where $\mathbf{\Gamma}_i$, expressed in (4.61), is a dimensionless term used to make the result more readable, and $\mathbf{s}_{dq}$ is a matrix defined as the SRF complex frequency and given by:

$$\mathbf{s}_{dq} = \mathbf{\Omega} + s\mathbf{I} \tag{4.60}$$

$$\mathbf{\Gamma}_i(s) = \mathbf{I} + \left(4C_{eq}V_{dc0}\mathbf{s}_{dq} + \frac{2S_0}{3V_{dc0}}\mathbf{I}\right)\mathbf{C}_i^{dq0}(s) + 4C_{eq}\left(Z + 2Z_f\right)\mathbf{s}_{dq} - \frac{2S_0}{3V_{dc0}}\mathbf{D}_i^{dq}. \tag{4.61}$$

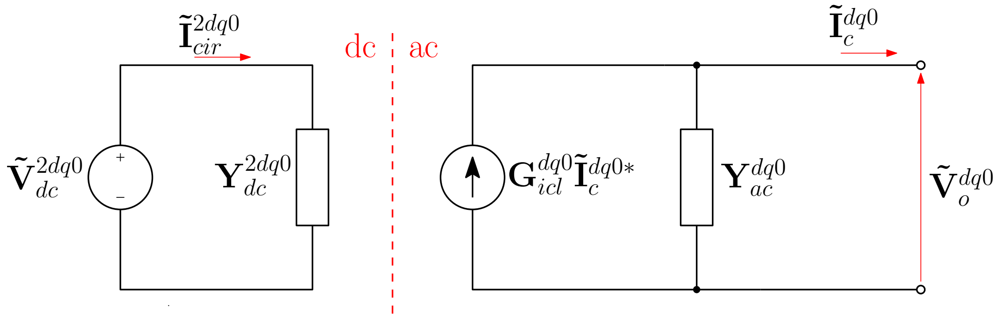

Figure 4.17: Norton-equivalent circuit of the MMC under current control in SRF.

Figures 4.18 and 4.19 present the results obtained following the validation strategy already explained. It is worthwhile noticing that, once the decoupling loop is employed, the cross-axis terms of $\mathbf{Y}_{ac}^{dq0}$ and $\mathbf{G}_{icl}^{dq0}$ are overwhelmingly smaller than their counterparts and because of that are not shown here. Moreover, the zero-sequence term of $\mathbf{G}_{icl}^{dq0}$ is not shown either once the zero in the position (3,3) of (4.54) makes it null. Still considering the zero-sequence terms, it was decided to present the validation results for $\mathbf{Y}_{ac}^{dq0}$, yet it is necessary to bear in mind that this term only exists if the middle point of the dc bus is in the same potential of the ac-side ground. Finally, for the tests presented here, it was considered $k_p^i = 0.001A^{-1}$ and $k_i^i = 0.1A^{-1}rad/s$.

Concerning the ac admittance $\mathbf{Y}_{ac}^{dq0}$, both the self-related and zero-sequence terms, presented in Figures 4.18a and 4.18b respectively, matched the correct behavior pointed by the non-linear time-domain model of the system with a single small exception at $60Hz$. Bear in mind that in SRF, $60Hz$ corresponds to either dc or

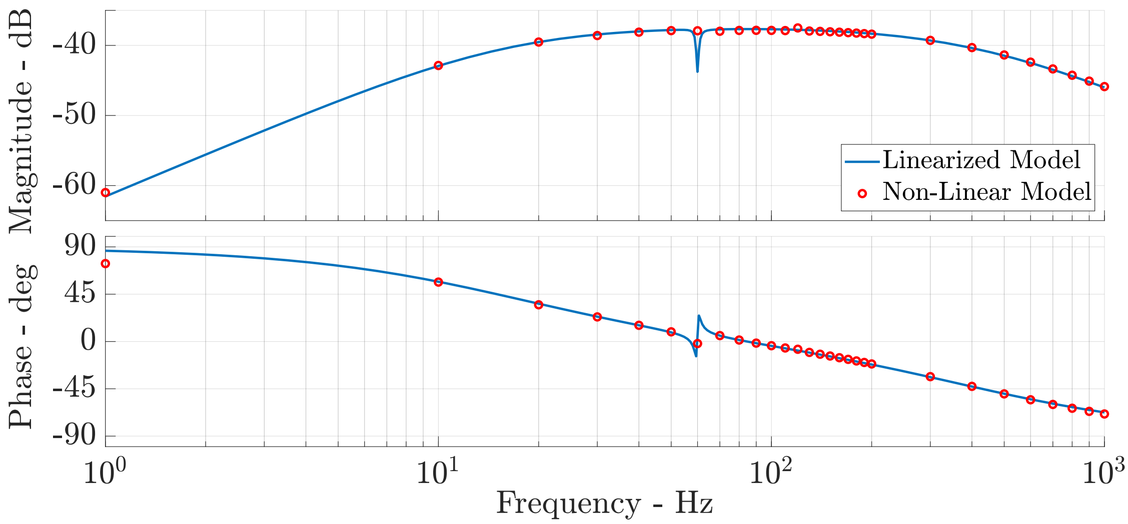

(a) Self-related term

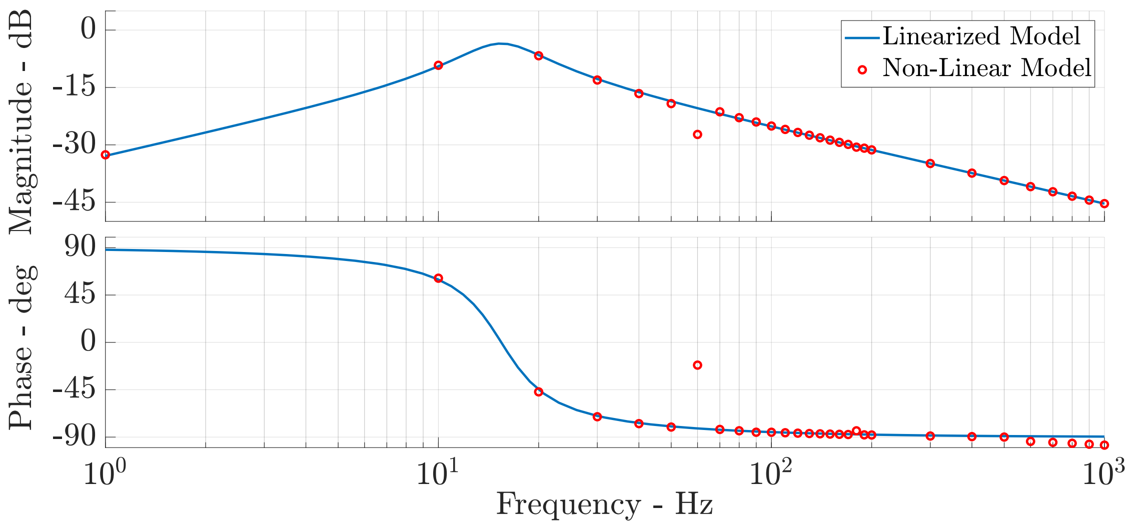

(b) Zero-sequence term

Figure 4.18: Frequency Response of $\mathbf{Y}_{ac}^{dq0}$: comparison between the linearized model and the non-linear, time-domain model.

$120Hz$ in NRF, consequently, this difference might not raise concerns once there are no typical components at this frequency on the ac main bus. Apart from that, it is important to notice that as the frequency tends to zero, the magnitudes of the admittances tend to $-\infty dB$. This effect is created by the current controller which, in turn, compels the converter to act as a current source at fundamental frequency[3]. As for the self-related term of the closed-loop gain $\mathbf{G}_{icl}^{dq0}$, the proposed model showed high accuracy except at the frequencies of 60 and $120Hz$. It is also worthwhile noticing that the magnitude presents $0dB$ when the frequency tends to zero, which is also under the natural characteristic of the current control: the current source of the Figure 4.17 might produce exactly the current indicated by the reference.

[3]In SRF, the dc component corresponds to the positive-sequence component of the fundamental

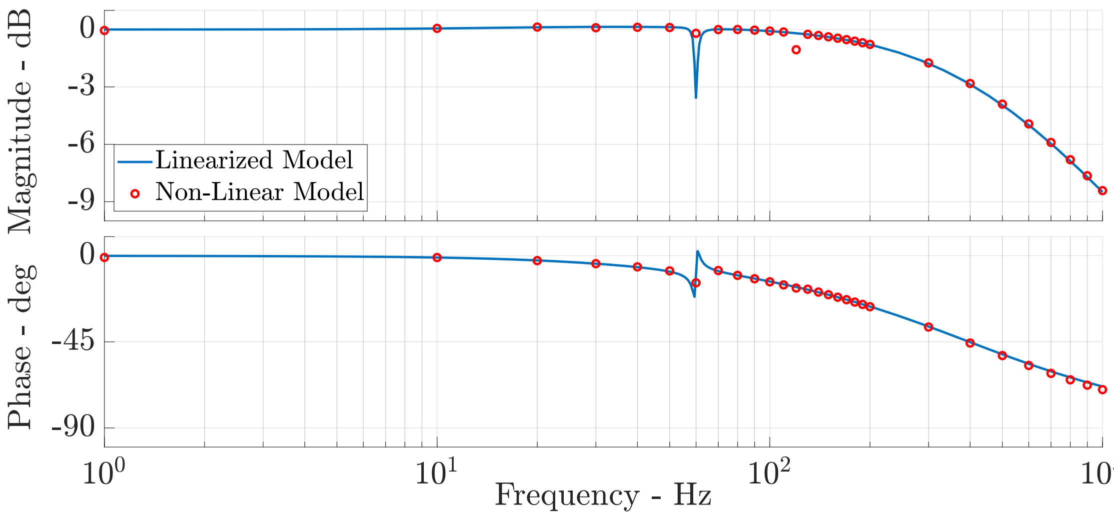

Figure 4.19: Frequency Response of the self-related term of $\mathbf{G}_{icl}^{dq0}$: comparison between the linearized model and the non-linear, time-domain model. The cross-axis and zero-sequence term are negligible and because of that not presented.

4.2.4 Single-loop voltage controlled MMC

Figure 4.20 presents the schematic of the grid-forming MMC under single-loop voltage control from which it is possible to write the following control law in SRF:

$$\tilde{\mathbf{E}}_c^{dq0*}(s) = \mathbf{C}_{v,sl}^{dq0}(s)\left[\tilde{\mathbf{V}}_o^{dq0*}(s) - \tilde{\mathbf{V}}_o^{dq0}(s)\right]. \tag{4.62}$$

In this case, $\mathbf{C}_{v,sl}^{dq0}$ is the matrix containing the control transfer functions and $\tilde{\mathbf{V}}_o^{dq0*}$ is the reference vector for the produced voltage. As in the previous section, the voltage control is based in PI controllers with proportional and integral gains represented by $k_p^{v,sl}$ and $k_i^{v,sl}$, respectively. Following this convention, it is possible to write:

$$\mathbf{C}_{v,sl}^{dq0}(s) = \begin{bmatrix} C_{v,sl}(s) & 0 & 0 \\ 0 & C_{v,sl}(s) & 0 \\ 0 & 0 & 0 \end{bmatrix}, \tag{4.63}$$

$$C_{v,sl}(s) = k_p^{v,sl} + \frac{k_i^{v,sl}}{s}. \tag{4.64}$$

To reduce the produced equations, a series of definitions are to be made in this section. The first consists on defining the SFR impedances $\mathbf{Z}_{dq}$ and $\mathbf{Z}_{fdq}$ given by:

$$\mathbf{Z}_{dq}(s) = L\mathbf{s}_{dq} + R\mathbf{I}, \tag{4.65}$$

$$\mathbf{Z}_{fdq}(s) = L_f\mathbf{s}_{dq} + R_f\mathbf{I}. \tag{4.66}$$

frequency in NRF.

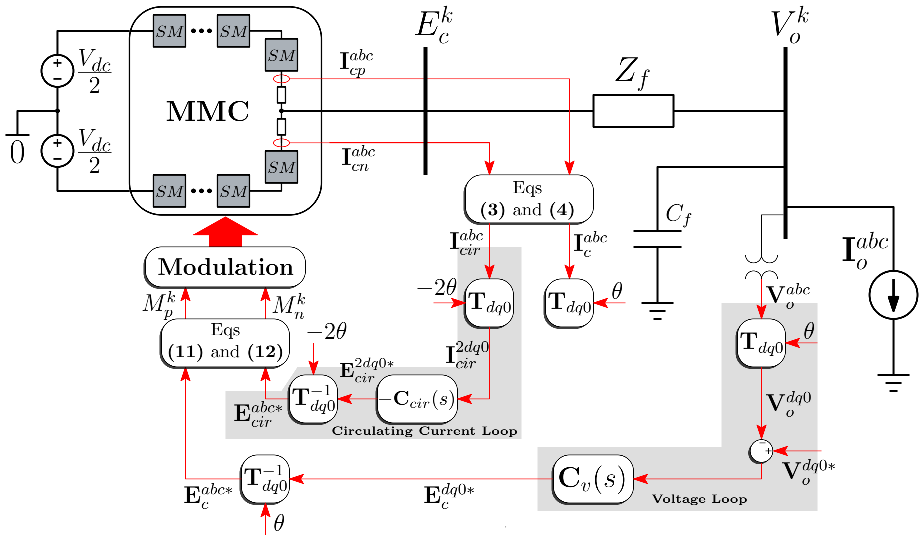

Figure 4.20: Block diagram of the MMC under single-loop voltage control in SRF. It is also included the mitigation loop of the second-order harmonic component of i_{cir}.

Using the presented definition, it is possible to find the following result after multiplying (4.43) by $2C_{eq}\mathbf{s}_{dq}$:

$$4C_{eq}\mathbf{s}_{dq}\left(\mathbf{Z}_{dq}+2\mathbf{Z}_{fdq}\right)\tilde{\mathbf{I}}_c^{dq0} = 4V_{dc0}C_{eq}\mathbf{s}_{dq}\tilde{\mathbf{E}}_c^{dq0*} - 2C_{eq}\mathbf{s}_{dq}\tilde{\mathbf{V}}_{dc}^{dq0\Delta} - 8C_{eq}\mathbf{s}_{dq}\tilde{\mathbf{V}}_o^{dq0}, \quad (4.67)$$

which is the base equation for the equivalent model developed in this section.

For the next step it is necessary to notice that the term $2C_{eq}\mathbf{s}_{dq}\tilde{\mathbf{V}}_{dc}^{dq0\Delta}$ in (4.67) corresponds to the left side of (4.41). Consequently, combining these equations produces:

$$\mathbf{\Gamma}_{v,in}^{sl}(s)\tilde{\mathbf{I}}_c^{dq0}(s) = \left(4V_{dc0}C_{eq}\mathbf{s}_{dq} + \frac{2S_0}{3V_{dc0}}\right)\tilde{\mathbf{E}}_c^{dq0*}(s) - 8C_{eq}\mathbf{s}_{dq}\tilde{\mathbf{V}}_o^{dq0}(s), \quad (4.68)$$

$$\mathbf{\Gamma}_{v,in}^{sl}(s) = \left[4C_{eq}\mathbf{s}_{dq}\left(\mathbf{Z}_{dq}+2\mathbf{Z}_{fdq}\right)+\mathbf{I}\right], \quad (4.69)$$

where $\mathbf{\Gamma}_{v,in}^{sl}$ is a dimensionless factor defined, once more, to reduce the size of the equations.

In this point, substituting the control law given by (4.62) into (4.68) leads to the equivalent model which does not take into account the capacitor bank C_f, i.e., the equation which relates the vectors $\tilde{\mathbf{V}}_o^{dq0}$, $\tilde{\mathbf{V}}_o^{dq0*}$ and $\tilde{\mathbf{I}}_c^{dq0}$. This result, after some algebraic manipulations, is expressed as follows:

$$\tilde{\mathbf{V}}_o^{dq0}(s) = \mathbf{G}_{v,sl,cl}^{dq0}(s)\tilde{\mathbf{V}}_o^{dq0*}(s) - \mathbf{Z}_{in}^{sl}(s)\mathbf{\Gamma}_{v,in}^{sl}(s)\tilde{\mathbf{I}}_c^{dq0}(s), \quad (4.70)$$

$$\mathbf{Z}_{in}^{sl}(s) = \left[\left(4V_{dc0}C_{eq}\mathbf{s}_{dq} + \frac{2S_0}{3V_{dc0}}\right)\mathbf{C}_{v,sl}^{dq0}(s) + 8C_{eq}\mathbf{s}_{dq}\right]^{-1}, \quad (4.71)$$

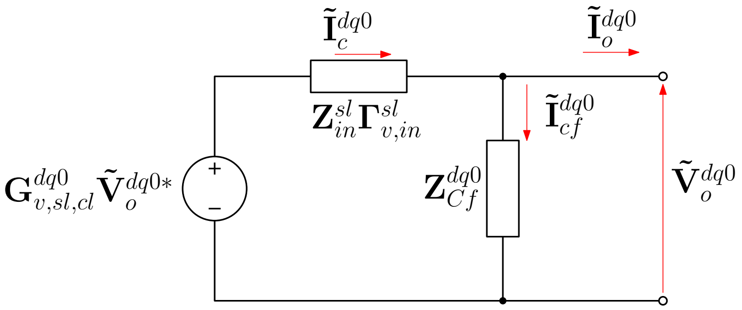

(a) Inner equivalent circuit

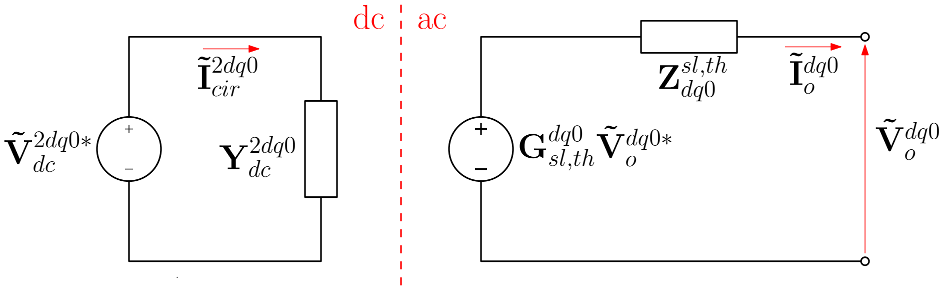

(b) Thévenin-equivalent circuit

Figure 4.21: Equivalent circuits of the MMC under single-loop voltage control in SRF.

$$\mathbf{G}_{v,sl,cl}^{dq0}(s) = \mathbf{Z}_{in}^{sl}(s)\left(4V_{dc0}C_{eq}\mathbf{s}_{dq} + \frac{2S_0}{3V_{dc0}}\right)\mathbf{C}_{v,sl}^{dq0}(s), \tag{4.72}$$

where $\mathbf{Z}_{in}^{sl}\mathbf{\Gamma}_{v,in}^{sl}$ represents the inner impedance of the system and $\mathbf{G}_{v,sl,cl}^{dq0}$ is the closed-loop voltage gain as depicted in Figure 4.21a.

For obtaining the Thévenin-equivalent model depicted in Figure 4.21b, it is necessary to get rid of the produced current $\tilde{\mathbf{I}}_c^{dq0}$ and manipulate the equation so as the main-bus voltage is a function of the current $\tilde{\mathbf{I}}_o^{dq0}$ drawn by the load. This can be accomplished by substituting the following node equation into (4.70):

$$\tilde{\mathbf{I}}_c^{dq0}(s) = \tilde{\mathbf{I}}_o^{dq0}(s) + \tilde{\mathbf{I}}_{cf}^{dq0}(s) = \tilde{\mathbf{I}}_o^{dq0}(s) + C_f\mathbf{s}_{dq}\tilde{\mathbf{V}}_o^{dq0}(s). \tag{4.73}$$

Finally, the Thévenin-equivalent model is given by:

$$\tilde{\mathbf{V}}_o^{dq0}(s) = \mathbf{G}_{sl,th}^{dq0}(s)\tilde{\mathbf{V}}_o^{dq0*}(s) - \mathbf{Z}_{sl,th}^{dq0}(s)\tilde{\mathbf{I}}_o^{dq0}(s) \tag{4.74}$$

$$\mathbf{G}_{sl,th}^{dq0}(s) = \left[C_f\mathbf{Z}_{in}^{sl}(s)\mathbf{\Gamma}_{v,in}^{sl}(s)\mathbf{s}_{dq} + \mathbf{I}\right]^{-1}\mathbf{G}_{v,sl,cl}^{dq0}(s) \tag{4.75}$$

$$\mathbf{Z}_{sl,th}^{dq0}(s) = \left[C_f\mathbf{Z}_{in}^{sl}(s)\mathbf{\Gamma}_{v,in}^{sl}(s)\mathbf{s}_{dq} + \mathbf{I}\right]^{-1}\mathbf{Z}_{in}^{sl}(s)\mathbf{\Gamma}_{v,in}^{sl}(s) \tag{4.76}$$

where $\mathbf{G}_{sl,th}^{dq0}$ in the Thévenin-equivalent closed-loop matrix gain and $\mathbf{Z}_{sl,th}^{dq0}$ is the Thévenin-equivalent impedance matrix.

The results obtained from the validation process are presented in Figures 4.22 and 4.23. In this context, it was considered $k_p^{v,sl} = 0.000001V^{-1}$ and $k_i^{v,sl} =$

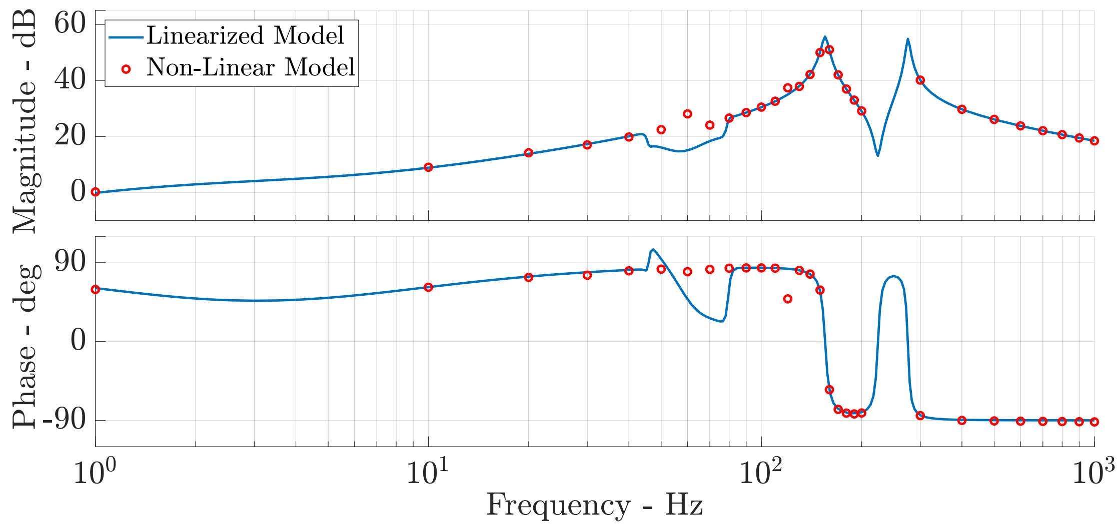

(a) Self-related term

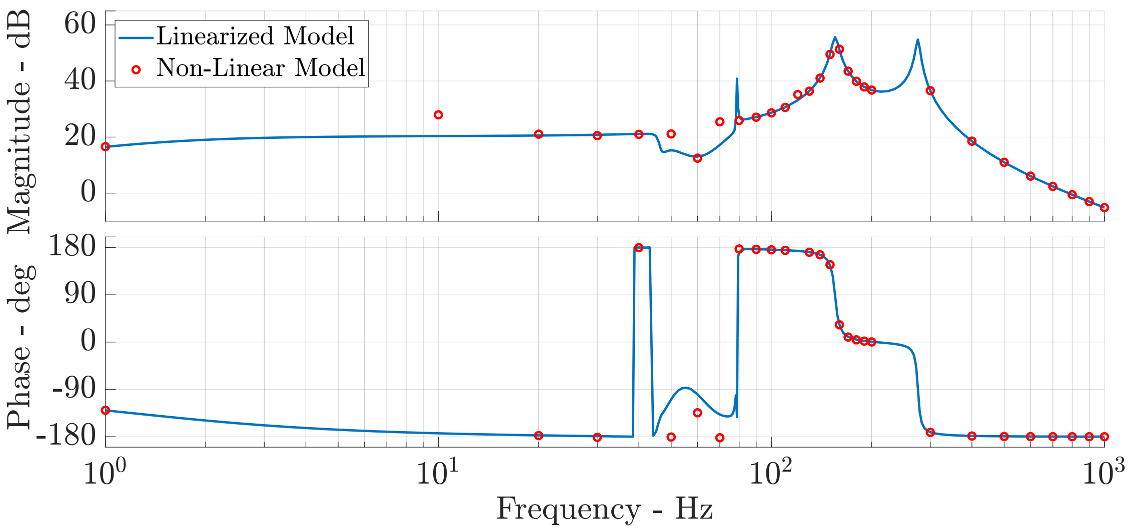

(b) Cross-axis term

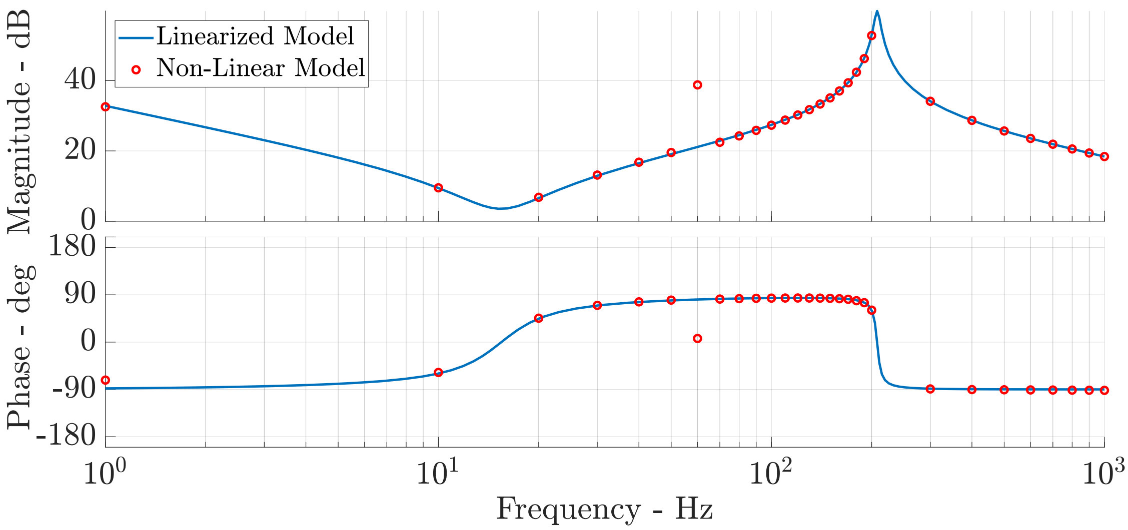

(c) Zero-sequence term

Figure 4.22: Frequency Response of $\mathbf{Z}_{sl,th}^{dq0}$: comparison between the linearized model and the non-linear, time-domain model.

$0.0001V^{-1}rad/s$. Differently from the previous section, it is presented the frequency response for the self-related and cross-axis terms of both $\mathbf{Z}^{dq0}_{sl,th}$ and $\mathbf{G}^{dq0}_{sl,th}$. In this case, it was not possible to neglect the cross-axis terms once the capacitor bank C_f and the impedances $\mathbf{Z}_{dq}$ and $\mathbf{Z}_{fdq}$ couple the direct and quadrature axis of the system. Besides that, it is also provided the results for the zero-sequence term of $\mathbf{Z}^{dq0}_{sl,th}$. Bear in mind, though, that the presence of zero sequence components in the system is conditioned to a connection between the middle point of the dc bus and the ac-side ground.

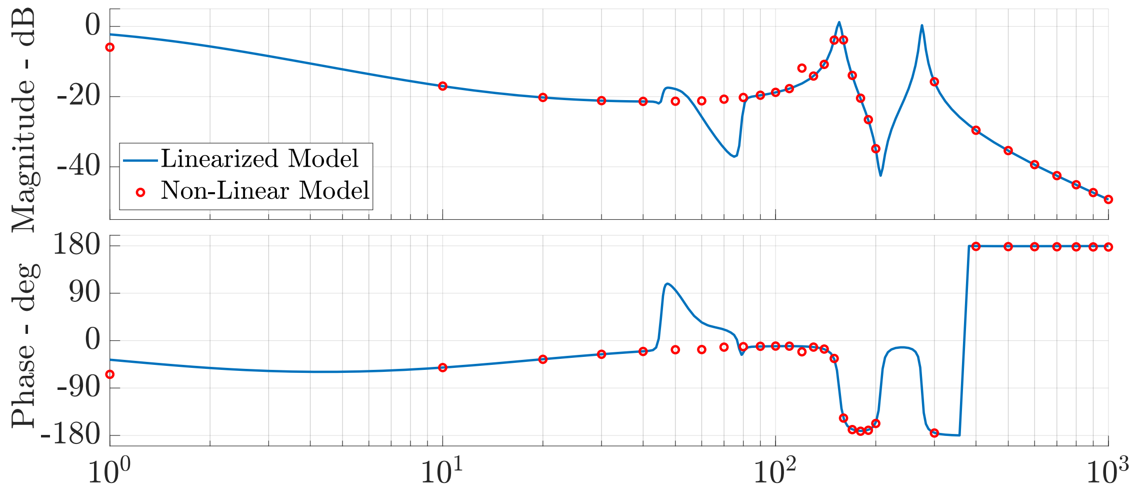

(a) Self-related term

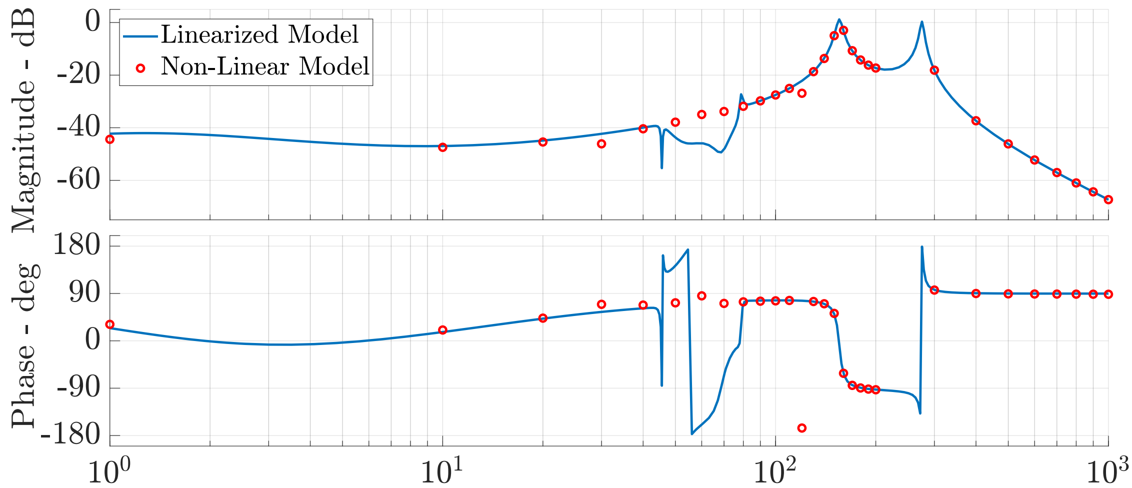

(b) Cross-axis term

Figure 4.23: Frequency Response of $\mathbf{G}^{dq0}_{sl,th}$: comparison between the linearized model and the non-linear, time-domain model. The zero-sequence term is negligible, then it is not presented.

It stood out in Figures 4.22a, 4.22b, 4.23a and 4.23b a significant disparity between the results in the frequency range that goes from 50 to $70Hz$. The data obtained from the non-linear time-domain model, in this case, indicate smoother responses than the responses obtained with the proposed analytical model. As far as it is possible to understand this issue, it is possible to conclude it is due to approximations and numerical errors in the process of computing the matrices $\mathbf{Z}_{sl,th}^{dq0}$ and $\mathbf{G}_{sl,th}^{dq0}$. Despite the fact the model presented in (4.74)-(4.76) is simple and compact, the matrix inversions and multiplications presented in it lead to hundred-degree polynomes. Of course, the inversion of such matrices presents some small numerical errors which in case of the presence of these huge polynomes affect severely the characteristic described by the model. As this is recurrent issue on the forthcoming models, it is deeply addressed in Section 4.2.6.

Aside from the previously mentioned discrepancies, it is also observed differences between the model at $120Hz$. In this case, though, it probably comes from non-linear characteristics that are not covered by the analytical model.

4.2.5 Double-loop Voltage controlled MMC

The idea of double-loop voltage control presented here is similar as that presented in Chapter 4.1, i.e, an outer voltage control loop computing the reference for an inner current control loop, as depicted in Figure 4.24. Consequently, the approach of using the current-controlled-MMC model as a starting point is also suitable here. In this regard, the control law for the outer loop is given by:

$$\tilde{\mathbf{I}}_c^{dq0*}(s) = \mathbf{C}_v^{dq0}(s)\left[\tilde{\mathbf{V}}_o^{dq0*}(s) - \tilde{\mathbf{V}}_o^{dq0}(s)\right], \tag{4.77}$$

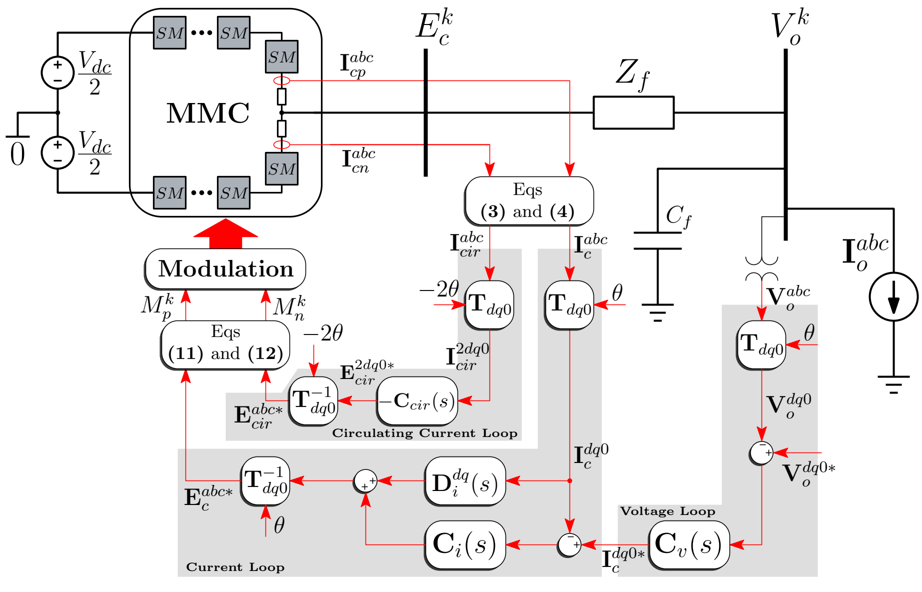

Figure 4.24: Block diagram of the MMC under double-loop voltage control in SRF. It is also included the mitigation loop of the second-order harmonic component of i_{cir}.

$$\mathbf{C}_v^{dq0}(s) = \begin{bmatrix} C_v(s) & 0 & 0 \\ 0 & C_v(s) & 0 \\ 0 & 0 & 0 \end{bmatrix}, \tag{4.78}$$

$$C_{v,sl}(s) = k_p^{v,dl} + \frac{k_i^{v,dl}}{s}. \tag{4.79}$$

Substituting (4.77) in (4.57) and making some arrangements it is possible to find the following result:

$$\tilde{\mathbf{V}}_o^{dq0}(s) = \mathbf{Z}_{in}^{dl}(s)\mathbf{G}_{icl}^{dq0}(s)\mathbf{C}_v^{dq0}(s)\tilde{\mathbf{V}}_o^{dq0*}(s) - \mathbf{Z}_{in}^{dl}(s)\tilde{\mathbf{I}}_c^{dq0}(s),$$

where $\tilde{\mathbf{V}}_o^{dq0}$ is the inner impedance (without count the capacitor bank) and it is given by:

$$\mathbf{Z}_{in}^{dl}(s) = \left[\mathbf{G}_{icl}^{dq0}(s)\mathbf{C}_v^{dq0}(s) + \mathbf{Y}_{ac}^{dq0}(s)\right]^{-1}. \tag{4.80}$$

In this point, it is possible to use the node equation described by (4.73) to find the Thévenin-equivalent model as follows:

$$\tilde{\mathbf{V}}_o^{dq0} = \mathbf{G}_{dl,th}^{dq0}\tilde{\mathbf{V}}_o^{dq0*} - \mathbf{Z}_{dl,th}^{dq0}\tilde{\mathbf{I}}_o^{dq0} \tag{4.81}$$

where the Thévenin-equivalent closed-loop gain $\mathbf{G}_{dl,th}^{dq0}$ and the Thévenin-equivalent impedance $\mathbf{Z}_{dl,th}^{dq0}$ are given by:

$$\mathbf{G}_{dl,th}^{dq0}(s) = \left[\mathbf{I} + C_f\mathbf{Z}_{in}^{dl}(s)\mathbf{s}_{dq}\right]^{-1}\mathbf{Z}_{in}^{dl}(s)\mathbf{G}_{icl}^{dq0}(s)\mathbf{C}_v^{dq0}(s), \tag{4.82}$$

$$\mathbf{Z}_{dl,th}^{dq0} = \left[\mathbf{I} + C_f\mathbf{Z}_{in}^{dl}(s)\mathbf{s}_{dq}\right]^{-1}\mathbf{Z}_{in}^{dl}(s). \tag{4.83}$$

Once more, the equivalent circuit is presented in Figure 4.25.

The validation process was carried out considering $k_p^i = 0.001A^{-1}$, $k_i^i = 0.1A^{-1}$, $k_p^{v,dl} = 0.01A^{-1}$, $k_i^{v,dl} = 1A^{-1}$ and the results are summarized in Figures 4.26 and 4.27. When it comes to the terms of the Thévevin impedance matrix $\mathbf{Z}_{dl,th}^{dq0}$, the only significant difference between the responses for the proposed model and the

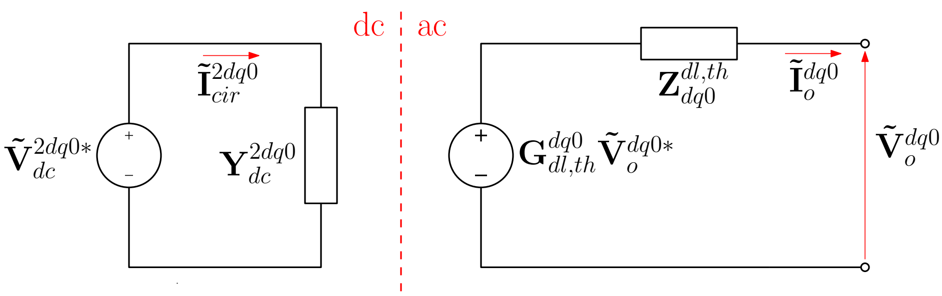

Figure 4.25: Equivalent circuits of the MMC under double-loop voltage control in SRF.

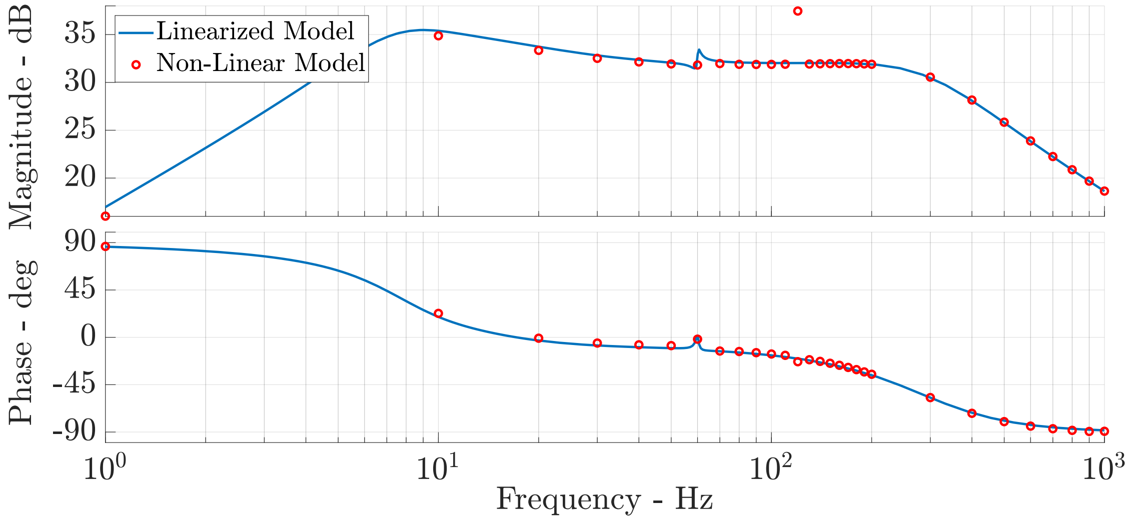

(a) Self-related term

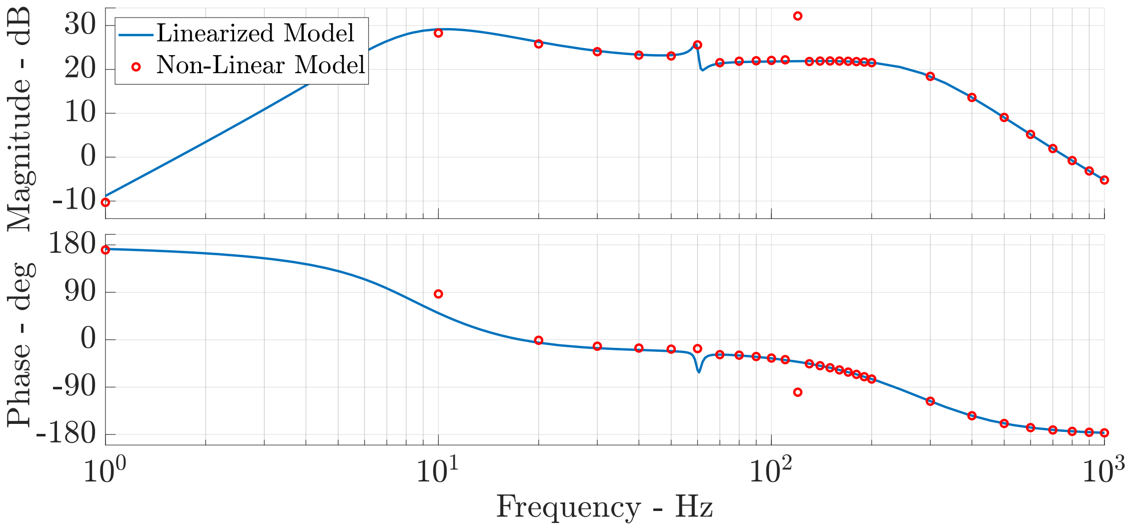

(b) Cross-axis term

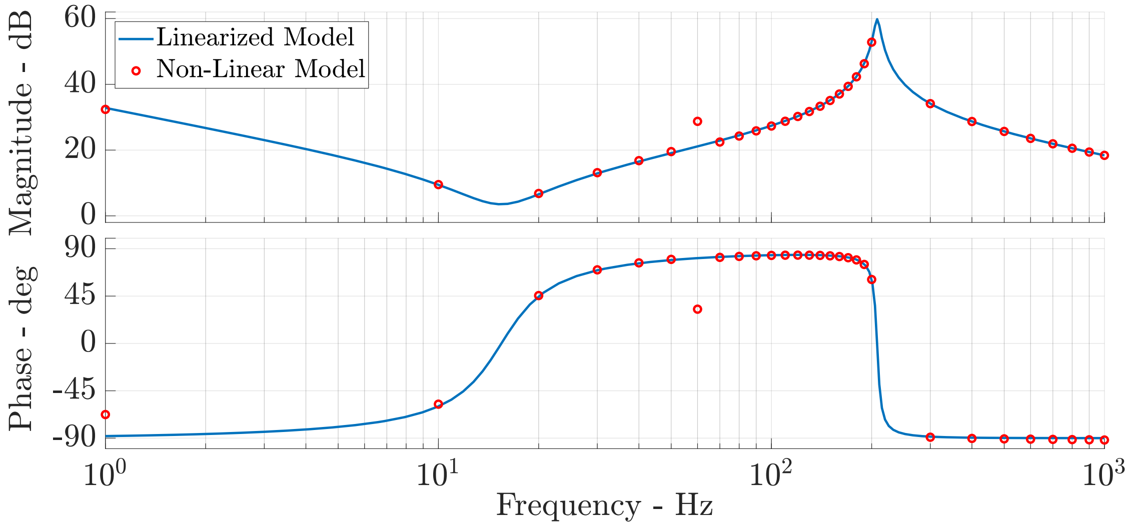

(c) Zero-sequence term

Figure 4.26: Frequency Response of $\mathbf{Z}_{dl,th}^{dq0}$: comparison between the linearized model and the non-linear, time-domain model.

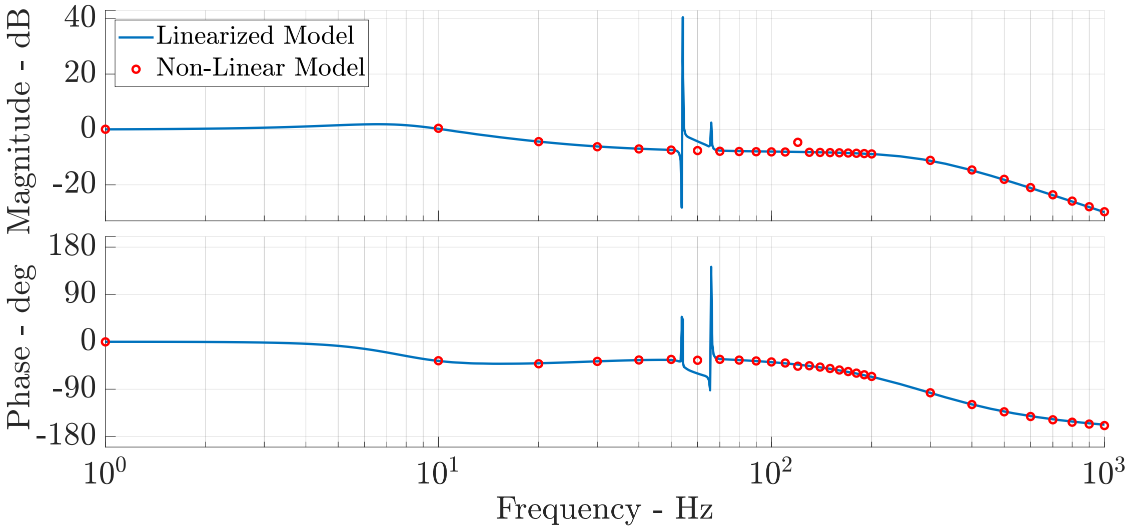

(a) Self-related term

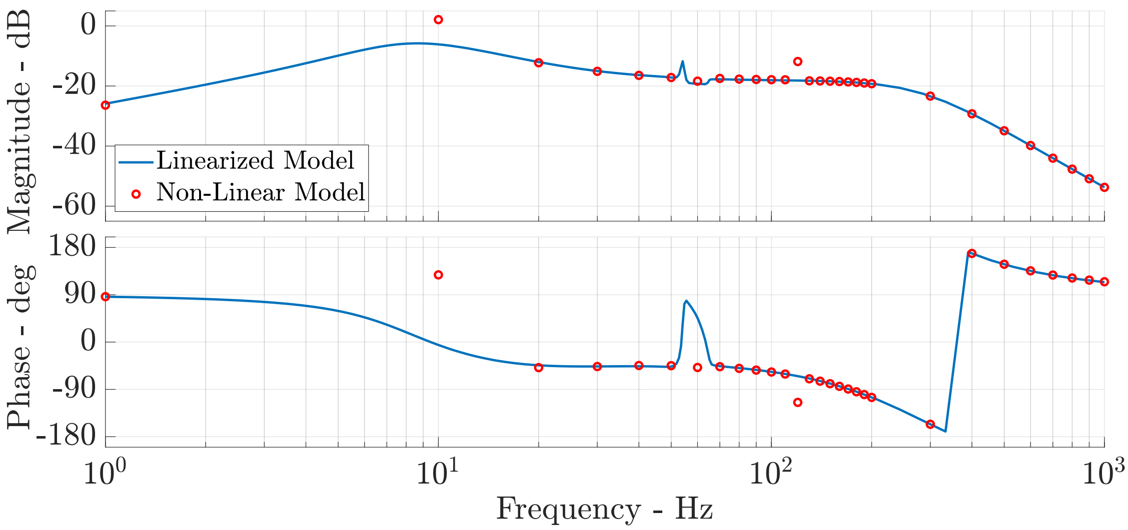

(b) Cross-axis term

Figure 4.27: Frequency Response of $\mathbf{G}_{dl,th}^{dq0}$: comparison between the linearized model and the non-linear, time-domain model. The zero-sequence term is negligible, then it is not presented.

non-linear time-domain is observed at the frequency of $120Hz$, on the self-related and cross-axis terms, and at $60Hz$ on the zero-sequence term. Once more, this difference must be the effect of the linearization cutting off some non-linear characteristics of the system. As for the terms of $\mathbf{G}_{dl,th}^{dq0}$, it is noticeable a significant disparity at the frequency of $10Hz$ in the cross-axis term, besides the presence of sharp patterns around the frequency of $60Hz$ not indicated by the results of the non-linear time-domain model. These patterns were probably generated by the numeric issues on inverting matrices with hundred-order polynomes, as previously reported in Section 4.2.4.

4.2.6 Issues sparkled by the use of matrix notation in the SRF models

This Section shows a glimpse of the computational issues created by the matrix approach used in the modeling of SRF-controlled MMCs. Besides that, it is also intended here to present some strategies to allow the computation of the proposed models with minimal or even zero computational errors. For this analysis, it is considered the s-domain control functions of Matlab, yet the idea can be extrapolated to Octave [113] (and, with some adjustments, extrapolated to python [114]). The codes analyzed in this section, together with the not so much organized codes used in the rest of the thesis, can be found in the *GitHub* repository indicated in [115].

To start, consider the model for the current-controlled MMC rewritten here for facilitating the reading:

$$\mathbf{Y}_{ac}^{dq0}(s) = 8C_{eq}\mathbf{\Gamma}_i^{-1}(s)\mathbf{s}_{dq}, \tag{4.84}$$

$$\mathbf{G}_{icl}^{dq0}(s) = \mathbf{\Gamma}_i^{-1}(s)\left(4C_{eq}V_{dc0}\mathbf{s}_{dq} + \frac{2S_0}{3V_{dc0}}\mathbf{I}\right)\mathbf{C}_i^{dq0}(s), \tag{4.85}$$

$$\mathbf{\Gamma}_i(s) = \mathbf{I} + \left(4C_{eq}V_{dc0}\mathbf{s}_{dq} + \frac{2S_0}{3V_{dc0}}\mathbf{I}\right)\mathbf{C}_i^{dq0}(s) + 4C_{eq}\left(Z + 2Z_f\right)\mathbf{s}_{dq} - \frac{2S_0}{3V_{dc0}}\mathbf{D}_i^{dq}. \tag{4.86}$$

Considering the settings used throughout this chapter (including numeric values of passive elements and control gains), the transfer matrix $\mathbf{\Gamma}_i$ can be written as:

$$\mathbf{\Gamma}_i(s) = \begin{bmatrix} \Gamma_{dd} & \Gamma_{dq} & 0 \\ \Gamma_{qd} & \Gamma_{qq} & 0 \\ 0 & 0 & \Gamma_0 \end{bmatrix} \tag{4.87}$$

where,

$$\Gamma_{dd}(s) = \Gamma_{qq}(s) = \frac{0.1062\,s^3 + 275.4\,s^2 + 28444.0\,s + 44444.0}{1000s}, \tag{4.88}$$

$$\Gamma_{dq}(s) = -\Gamma_{qd}(s) = -\frac{40.04\,s^2 + 1.038\times10^5\,s + 1.018\times10^7}{1000s}, \tag{4.89}$$

$$\Gamma_0(s) = \frac{1}{1000}\left(0.1062\,s^2 + 5.4\,s + 1000.0\right). \tag{4.90}$$

In this case, it is possible to state that the self-related terms of $\mathbf{\Gamma}_i$ have order three, wheres the mutual and zero-sequence terms have order equal to two. It is necessary to compute $\mathbf{\Gamma}_i^{-1}$, so as to determine the admittance and gain presented in (4.84) and (4.85). In this case, $\mathbf{\Gamma}_i^{-1}$ also presents a matrix form as follows:

$$\mathbf{\Gamma}_i{}^{-1}(s) = \begin{bmatrix} \Gamma_{inv,dd} & \Gamma_{inv,dq} & 0 \\ \Gamma_{inv,qd} & \Gamma_{inv,qq} & 0 \\ 0 & 0 & \Gamma_{inv,0} \end{bmatrix}, \tag{4.91}$$

where

$$\Gamma_{inv,dd}(s) = \Gamma_{inv,qq}(s) = \frac{\begin{array}{r} 9416.0\, s^4 + 2.442 \times 10^7\, s^3 + 2.522 \times 10^9\, s^2 \\ + 3.941 \times 10^9\, s - 0.6177 \end{array}}{\begin{array}{r} s^6 + 5186.0\, s^5 + 7.403 \times 10^6\, s^4 + 2.127 \times 10^9\, s^3 \\ + 1.101 \times 10^{12}\, s^2 + 1.875 \times 10^{14}\, s + 9.186 \times 10^{15} \end{array}}, \tag{4.92}$$

$$\Gamma_{inv,dq}(s) = -\Gamma_{inv,qd}(s) = \frac{\begin{array}{r} 3.55 \times 10^6\, s^3 + 9.2 \times 10^9\, s^2 \\ + +9.025 \times 10^{11}\, s - 0.1199 \end{array}}{\begin{array}{r} s^6 + 5186.0\, s^5 + 7.403 \times 10^6\, s^4 + 2.127 \times 10^9\, s^3 \\ + 1.101 \times 10^{12}\, s^2 + 1.875 \times 10^{14}\, s + 9.186 \times 10^{15} \end{array}}, \tag{4.93}$$

$$\Gamma_{inv,0}(s) = \frac{9416.0}{s^2 + 50.85s + 9416.0} \tag{4.94}$$

Notice that the operation of inversion by itself produced sixth-order polynomials as transfer functions. As the matrix operations are computed, the order of the polynomials grows up and the implementation does play an important hole in this process. Just to have a glimpse into the subject, observe in the following code in which the Norton-equivalent admittance was computed using two different approaches:

```
1 % First approach
2 Y_norton = 8*Ceq.*inv(Gamma_i)*sdq;
3
4 % Second approach
5 Y_norton_2 = 8*Ceq.*(Gamma_i\sdq);
```

In this case, `sdq` corresponds to the transfer matrix $\mathbf{s}_{dq}$ and `Gamma_i` to (4.86). Observe that in line 2, `Gamma_i` is inverted using the Matlab function `inv`, whereas in line 5, the backslash is used. In general, `inv(Gamma_i)*sdq = Gamma_i\sdq`, yet the second approach presents better numerical accuracy for solving linear systems [116].

The Norton-equivalent admittance is given by:

$$\mathbf{Y}_{ac}^{dq0}(s)(s) = \begin{bmatrix} Y_{dd} & Y_{dq} & 0 \\ Y_{qd} & Y_{qq} & 0 \\ 0 & 0 & Y_0 \end{bmatrix}, \tag{4.95}$$

$$Y_{dd}(s) = Y_{qq}(s) = \frac{Y_{dd,num}}{Y_{den}}, \tag{4.96}$$

$$Y_{qd}(s) = -Y_{dq}(s) = \frac{Y_{qd,num}}{Y_{den}}, \tag{4.97}$$

Using the first approach (line 2 of the piece of code presented), it is found polynomials with orders up to twelfth, given by:

$$\begin{aligned} Y_{dd,num,1} = {} & 33.9\, s^{11} + 2.637 \times 10^{5}\, s^{10} + 7.208 \times 10^{8}\, s^{9} \\ & + 8.074 \times 10^{11}\, s^{8} + 3.932 \times 10^{14}\, s^{7} + 2.315 \times 10^{17}\, s^{6} \\ & + 6.774 \times 10^{19}\, s^{5} + 1.978 \times 10^{22}\, s^{4} + 3.82 \times 10^{24}\, s^{3} \\ & + 3.445 \times 10^{26}\, s^{2} + 1.125 \times 10^{28}\, s - 1.495 \times 10^{15}, \end{aligned} \tag{4.98}$$

$$\begin{aligned} Y_{qd,num,1} = {} & -2.728 \times 10^{-11}\, s^{10} + 21044.0\, s^{9} \\ & + 2.829 \times 10^{8}\, s^{8} + 1.063 \times 10^{12}\, s^{7} + 1.359 \times 10^{15}\, s^{6} \\ & + 4.324 \times 10^{17}\, s^{5} + 2.066 \times 10^{20}\, s^{4} + 3.867 \times 10^{22}\, s^{3} \\ & + 2.6 \times 10^{24}\, s^{2} + 4.913 \times 10^{25}\, s - 1.656 \times 10^{14}, \end{aligned} \tag{4.99}$$

$$\begin{aligned} Y_{den,1} = {} & s^{12} + 10388.0\, s^{11} + 4.17 \times 10^{7}\, s^{10} + 8.104 \times 10^{10}\, s^{9} \\ & + 7.906 \times 10^{13}\, s^{8} + 4.328 \times 10^{16}\, s^{7} + 2.278 \times 10^{19}\, s^{6} \\ & + 7.553 \times 10^{21}\, s^{5} + 2.145 \times 10^{24}\, s^{4} + 4.518 \times 10^{26}\, s^{3} \\ & + 5.538 \times 10^{28}\, s^{2} + 3.445 \times 10^{30}\, s + 8.439 \times 10^{31}. \end{aligned} \tag{4.100}$$

On the other hand, considering the second approach (line 5 of the piece of code presented), the results presented orders no greater than six, as follows:

$$\begin{aligned} Y_{dd,num,2} = {} & 33.9 s^{5} + 8.791 \times 10^{4} s^{4} + 1.39 \times 10^{7} s^{3} \\ & + 1.25 \times 10^{10} s^{2} + 1.225 \times 10^{12} s + 0.001193, \end{aligned} \tag{4.101}$$

$$Y_{qd,num,2} = 2.104 \times 10^{4} s^{3} + 1.738 \times 10^{8} s^{2} + 5.348 \times 10^{9} s + 4.507, \tag{4.102}$$

$$Y_{den,2} = s^6 + 5186s^5 + 7.403 \times 10^6 s^4 + 2.127 \times 10^9 s^3 + 1.101 \times 10^{12} s^2 + 1.875 \times 10^{14} s + 9.186 \times 10^{15} \quad (4.103)$$

Despite the fact the results appear to be quite different, their frequency responses present no difference whatsoever in the frequency range considered in this work (from 1Hz to 1kHz), and even in broader frequency ranges. It was chosen not to plot these results here to save space. Still in this Section, some comparisons between frequency responses obtained from different code implementation are to be shown. Tables 4.1 and 4.2 present, respectively, the poles of the admittance and the zeros of its self-related term for each one of the code implementation approaches. Notice that, the model computed with the first approach presents two pairs of poles in the neighborhoods of $-0.10238 \pm j0.00099$ $k\ rad/s$, while the other one presents a single pair of poles. Besides that, the first-approach model presents a pair of zeros exactly in this neighborhood, yet the other model does not. This pair of zeros must have been crossed off with one of the mentioned pairs of poles, nonetheless, due to numerical errors, this did not happen. To be more precise, the mentioned numerical errors caused differences between these poles and zeros in the fifth/sixth decimal digits (which corresponds to errors lower than ± 0.01 rad/s), paving the way for polynomials with order greater than the necessary to represent the system.

Table 4.1: Poles from the Norton-equivalent admittance with different code implementations

First Approach ($k\ rad/s$)	**Second Approach** ($k\ rad/s$)
$-2.485617549224798 + 0.000767191197238j$	$-2.485617601764149 + 0.000582319303508j$
$-2.485617549224798 - 0.000767191197238j$	$-2.485617601764149 - 0.000582319303508j$
$-2.485617654303014 + 0.000299347975960j$	$-0.005220670583661 + 0.376577177024133j$
$-2.485617654303014 - 0.000299347975960j$	$-0.005220670583661 - 0.376577177024133j$
$-0.005220667604554 + 0.376577186176171j$	$-0.102382066635165 + 0.000996260709563j$
$-0.005220667604554 - 0.376577186176171j$	$-0.102382066635165 - 0.000996260709563j$
$-0.005220673560191 + 0.376577167872322j$	-
$-0.005220673560191 - 0.376577167872322j$	-
$-0.102382286917142 + 0.000996263460398j$	-
$-0.102382286917142 - 0.000996263460398j$	-
$-0.102381846356404 + 0.000996258006741j$	-
$-0.102381846356404 - 0.000996258006741j$	-

The issue related to the process of matrix inversion is not the only challenge when computing the models for the SRF-controlled MMC. Consider now the model for the single-loop, voltage-controlled MMC, rewritten here with some extra indication (some intermediary variables that are used in the code) to facilitate understanding the next piece of code:

$$\boldsymbol{\Gamma}^{sl}_{v,in}(s) = \left[4C_{eq}\mathbf{s}_{dq}\left(\mathbf{Z}_{dq} + 2\mathbf{Z}_{fdq}\right) + \mathbf{I}\right], \tag{4.104}$$

$$\mathbf{Z}^{sl}_{in}(s) = \left[\overbrace{\underbrace{\left(4V_{dc0}C_{eq}\mathbf{s}_{dq} + \frac{2S_0}{3V_{dc0}}\right)\mathbf{C}^{dq0}_{v,sl}(s)}_{\Gamma_{mid}} + 8C_{eq}\mathbf{s}_{dq}}^{Y_{in}}\right]^{-1}, \tag{4.105}$$

$$\mathbf{G}^{dq0}_{v,sl,cl}(s) = \mathbf{Z}^{sl}_{in}(s)\underbrace{\left(4V_{dc0}C_{eq}\mathbf{s}_{dq} + \frac{2S_0}{3V_{dc0}}\right)\mathbf{C}^{dq0}_{v,sl}(s)}_{\Gamma_{mid}}, \tag{4.106}$$

$$\mathbf{G}^{dq0}_{sl,th}(s) = \left[\underbrace{C_f\mathbf{Z}^{sl}_{in}(s)\boldsymbol{\Gamma}^{sl}_{v,in}(s)\mathbf{s}_{dq} + \mathbf{I}}_{\Gamma_{out}}\right]^{-1}\mathbf{G}^{dq0}_{v,sl,cl}(s) \tag{4.107}$$

$$\mathbf{Z}^{dq0}_{sl,th}(s) = \left[\underbrace{C_f\mathbf{Z}^{sl}_{in}(s)\boldsymbol{\Gamma}^{sl}_{v,in}(s)\mathbf{s}_{dq} + \mathbf{I}}_{\Gamma_{out}}\right]^{-1}\mathbf{Z}^{sl}_{in}(s)\boldsymbol{\Gamma}^{sl}_{v,in}(s) \tag{4.108}$$

It follows the entire Matlab function coded to compute the parameters of the single-loop, voltage-controlled MMC. The name of each variable in the algorithm matches the symbols previously established in this thesis, consequently, they might not be explained one by one here. The important points to notice are that the function receives as input a structure with the MMC data and produces as output another structure with all the computed matrix (in these cases, transfer matrices). Besides that, to evaluate the impact of the coding implementation, some of the matrices were computed several times following different approaches. For instance,

Table 4.2: Zeros from the self-related term of the Norton-equivalent admittance with different code implementations

First Approach ($k\ rad/s$)	**Second Approach** ($k\ rad/s$)
$-2.485617574288163 + 0.000582319282110j$	$-2.485617271621857 + 0.000000000000000j$
$-2.485617574288163 - 0.000582319282110j$	$-0.002604064103253 + 0.376776662588592j$
$-2.485617326573334 + 0.000000000000000j$	$-0.002604064103253 - 0.376776662588592j$
$-0.002604064103246 + 0.376776662588599j$	$-0.102394939154689 + 0.000000000000000j$
$-0.002604064103246 - 0.376776662588599j$	$-0.000000000000000 + 0.000000000000000j$
$-0.005220670582379 + 0.376577177024240j$	-
$-0.005220670582379 - 0.376577177024240j$	-
$-0.102394939154283 + 0.000000000000000j$	-
$-0.102382066636976 + 0.000996260709208j$	-
$-0.102382066636976 - 0.000996260709208j$	-
$+0.000000000000000 + 0.000000000000000j$	-

in lines 33-35 of the following code, Γ_{out} was computed in three different ways. In this case, the greater the index, the more accurate is the result, i.e., `Gamma_out_3` has more accuracy than `Gamma_out_2` and so on.

```
1  function Model = MODEL_SRF_VC_SL(MMC,Cv_sl)
2      % Model for the Single-loop, Voltage-Controlled MMC
3      % MMC -> Structure with the MMC's parameters
4      % Cv_sl -> s-domain transfer function (voltage controller)
5  
6      % Definitions
7      I = eye(3);                        % Identity matrix
8      s = tf('s');                       % Complex frequency
9      Ceq = MMC.C/MMC.N;                 % Equivalent capacitance
10 
11     W = [0 -MMC.w0 0;MMC.w0 0 0;0 0 0]; % Coupling Matrix
12     sdq = W + s.*I;                    % Matrix frequency
13     Zdq = MMC.R*I + MMC.L*sdq;         % Inner Impedance
14     Zfdq = MMC.Rf*I + MMC.Lf*sdq;      % Outer Impedance
15 
16     Cv_dq = [Cv_sl 0 0;0 Cv_sl 0;0 0 0];% Controller
17 
18     % Some ajustments to fit in the screem
19     Vdc0 = MMC.Vdc0;                   % Rated dc voltage
20     SN = MMC.SN;                       % Rated dc power
21     Cf = MMC.Cf;                       % Capacitor banck
22 
23     % Model:
24     % It is computed in different ways to show the numeric
25     % effects of different implementations
26     Gamma_in = 4*Ceq*sdq*(Zdq+2*Zfdq) + I;
27 
28     Gamma_mid = (4*Vdc0*Ceq*sdq + I*2*SN/(3*Vdc0))*Cv_dq;
29 
30     Y_in = Gamma_mid + 8*Ceq*sdq;
31     Z_in = inv(Y_in); % Equation (4.69) of the thesis
32 
33     Gamma_out = Cf*Z_in*Gamma_in*sdq + I;
34     Gamma_out_2 = Cf*Z_in*(Gamma_in*sdq) + I;
35     Gamma_out_3 = Cf*(Y_in\(Gamma_in*sdq)) + I;
36 
37     Gamma_out_inv = inv(Gamma_out);
38     Gamma_out_inv_2 = inv(Gamma_out_2);
```

```
39
40      Z_th = Gamma_out_inv*Z_in*Gamma_in;
41      Z_th_2 = Gamma_out_inv_2*Z_in*Gamma_in;
42      Z_th_3 = Gamma_out_inv_2*(Z_in*Gamma_in);
43      Z_th_4 = Gamma_out_2\(Z_in*Gamma_in);
44      Z_th_5 = Gamma_out_3\(Y_in\Gamma_in);
45
46      G_th = Gamma_out_inv_2*(Z_in*Gamma_mid);
47      G_th_2 = Gamma_out_3\(Y_in\Gamma_mid);
48
49      % Output structure
50      Model = struct('Gamma_in',Gamma_in,...
51                     'Gamma_mid',Gamma_mid,...
52                     'Y_in',Y_in,...
53                     'Z_in',Z_in,...
54                     'Gamma_out',Gamma_out,...
55                     'Gamma_out_2',Gamma_out_2,...
56                     'Gamma_out_3',Gamma_out_3,...
57                     'Gamma_out_inv',Gamma_out_inv,...
58                     'Gamma_out_inv_2',Gamma_out_inv_2,...
59                     'Z_th',Z_th,...
60                     'Z_th_2',Z_th_2,...
61                     'Z_th_3',Z_th_3,...
62                     'Z_th_4',Z_th_4,...
63                     'Z_th_5',Z_th_5,...
64                     'G_th',G_th,...
65                     'G_th_2',G_th_2);
66  end
```

Continuing on the segment between the lines 33 and 35, at first glance `Gamma_out_2 = Gamma_out`, but that is not a precise assumption. The Parentheses, which is the difference between the two lines, change the order of computation and that affects the results. On line 33, first the matrices `Z_in` and `Gamma_in` are multiplied and then the result is multiplied by `sdq`. On line 34, on the other hand, first the matrices `Gamma_in` and `sdq` are multiplied and then their result is multiplied by `Z_in`. Analytically this makes no difference, but computationally it does. The order of the polynomials in `Z_in` and `Gamma_in` are greater than the order in `sdq`, and computational errors associated with polynomial multiplications grow with the order of them. In this case, the computational error ($\varepsilon_{cp}\{\bullet\}$) can be relatively estimated as either one of the possibilities[4]:

$$\varepsilon_{cp}\{(\mathbf{Z}_{in}\mathbf{\Gamma}_{in})\,\mathbf{s}_{dq}\} > \varepsilon_{cp}\{\mathbf{Z}_{in}\mathbf{\Gamma}_{in}\} > \varepsilon_{cp}\{\mathbf{Z}_{in}\,(\mathbf{\Gamma}_{in}\mathbf{s}_{dq})\} > \varepsilon_{cp}\{\mathbf{\Gamma}_{in}\mathbf{s}_{dq}\}, \tag{4.109}$$

$$\varepsilon_{cp}\{(\mathbf{Z}_{in}\mathbf{\Gamma}_{in})\,\mathbf{s}_{dq}\} > \varepsilon_{cp}\{\mathbf{Z}_{in}\,(\mathbf{\Gamma}_{in}\mathbf{s}_{dq})\} > \varepsilon_{cp}\{\mathbf{Z}_{in}\mathbf{\Gamma}_{in}\} > \varepsilon_{cp}\{\mathbf{\Gamma}_{in}\mathbf{s}_{dq}\}. \tag{4.110}$$

Analyzing the results, `Gamma_out`, `Gamma_out_2` and `Gamma_out_3` produced transfer matrices with polynomials of order up to 18, 9, and 6, respectively. As with the current-controlled admittance, the numerical errors prevented the pole-zero cancellation in the approaches with lower accuracy[5]. For this result, it is also possible to conclude that a simple change of multiplication order (the difference between `Gamma_out` and `Gamma_out_2`) significantly increases the accuracy and prevent huge-order polynomials when dealing with transfer matrices.

Going straight for the Thévenin impedance (lines 40 - 44 of the code), the different implementations also lead to different-order polynomials, say it, 160 for `Z_th`, 96 for `Z_th_2`, 56 for `Z_th_3`, 28 for `Z_th_4` and `Z_th_5`. Figure 4.28a presents the frequency response for each one of these implementations of the Thévenin impedance. It is possible to notice that all the curves are coincident, except in the frequency range in the red-shadowed region, due to the numeric errors already explained. To be more precise, the error range of `Z_th` spams from 35 to 100Hz, yet the others are kept within 45 to 80Hz. The zoomed frequency responses shown in Figure 4.28b allow better visualization of the mentioned issue and, as far as it is possible to guarantee, the response for `Z_th_5` the most precise (because it was computed considering the greatest possible number of numerical-error-preventing strategies, as can be seen in the code)[6]. It suffices to say that, as the model is in SRF, the frequency range that goes from 40-100Hz does not encompass any important harmonic component of the power grid and for this reason does not raise any warning. It is important to mention that these issues are also valid for the model of the doubly-loop, voltage-controlled MMC.

4.2.7 Analyzing the non-linearities of the MMC

As mentioned in some parts of this Chapter, the developed models presented errors in specific points of the frequency spectrum due to the inherent non-linearities of the MMC. In this regard, it is presented here a more detailed analysis of one of the cases,

[4]The Matlab documentation [117] already suggests the use of parenthesis to force the multiplication of smaller matrices first, to reduce memory usage. Nonetheless, not much is explained about computational errors.

[5]To save space, neither transfer functions nor the zeros and poles are shown here.

[6]The results presented in the previous sections are a little bit different in this region due to the use of different combinations of computational implementations. Out there, the Matlab function `inv` was more prevalent.

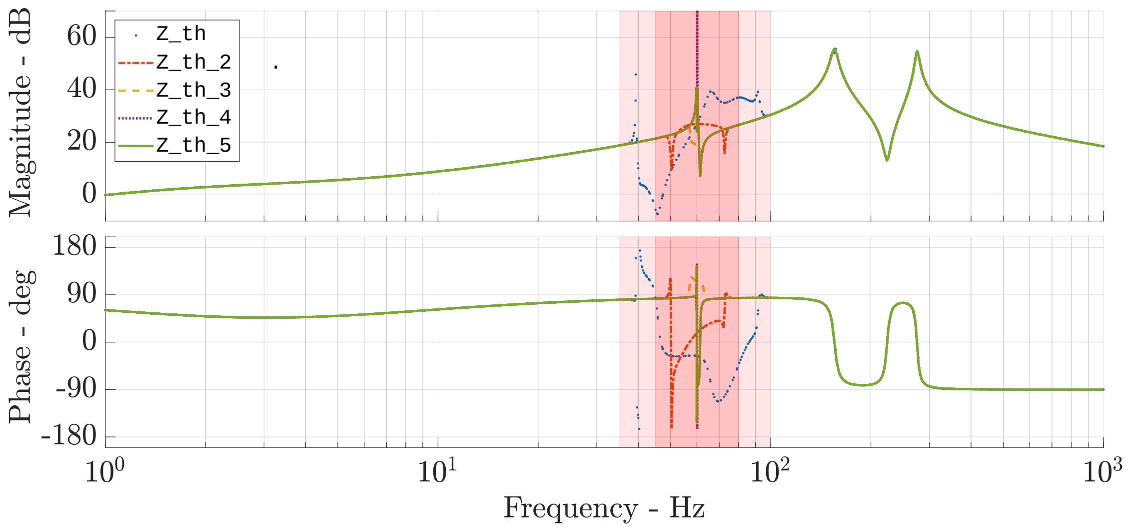

(a) Frequency response

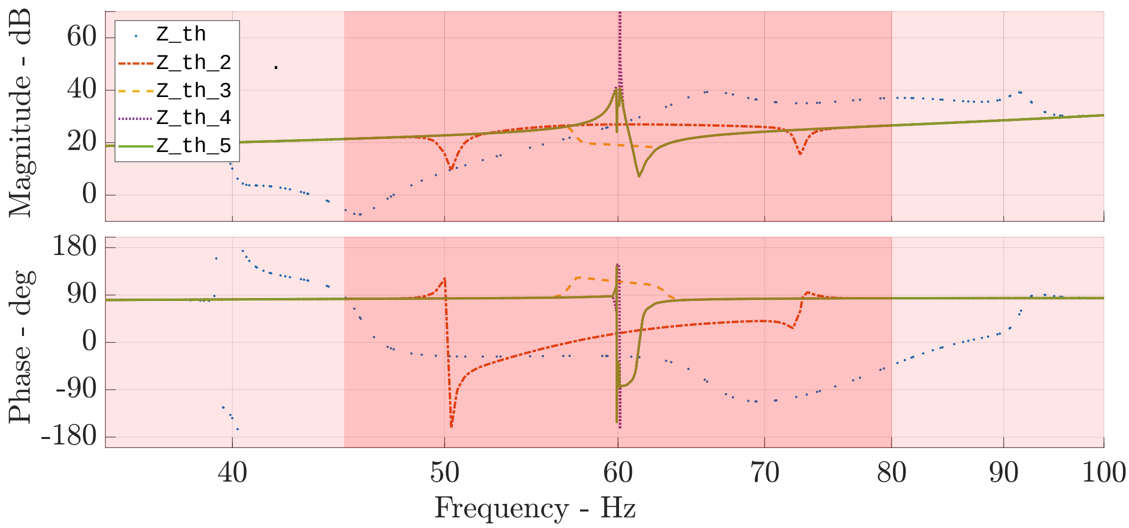

(b) Zoomed frequency response

Figure 4.28: Frequency Response of the self-related term of the Thévenin impedance for different computational implementation

more specifically the discrepancy at $60Hz$ in the zero-sequence component of the dc admittance $\mathbf{Y}_{dc}^{2dq0}$, so that this issue could be better understood. For this matter, the frequency response of Figure 4.15 is represented one more time in Figure 4.29 to increase the readability of the text. Notice that not only the $60Hz$ frequency was highlighted, but also the results for frequencies of $50Hz$ and $70Hz$. These two points, where the linearized model precisely predicted the behavior of the system were chosen only to provide us with means of comparison.

The frequency response of the linearized model indicates that a 60Hz-disturbance in the dc-bus voltage produces a 60Hz zero-sequence component in the circulating current with amplitude close to the amplitudes of the components caused by the 50 and 70Hz disturbances. Nonetheless, this was not observed in the non-linear

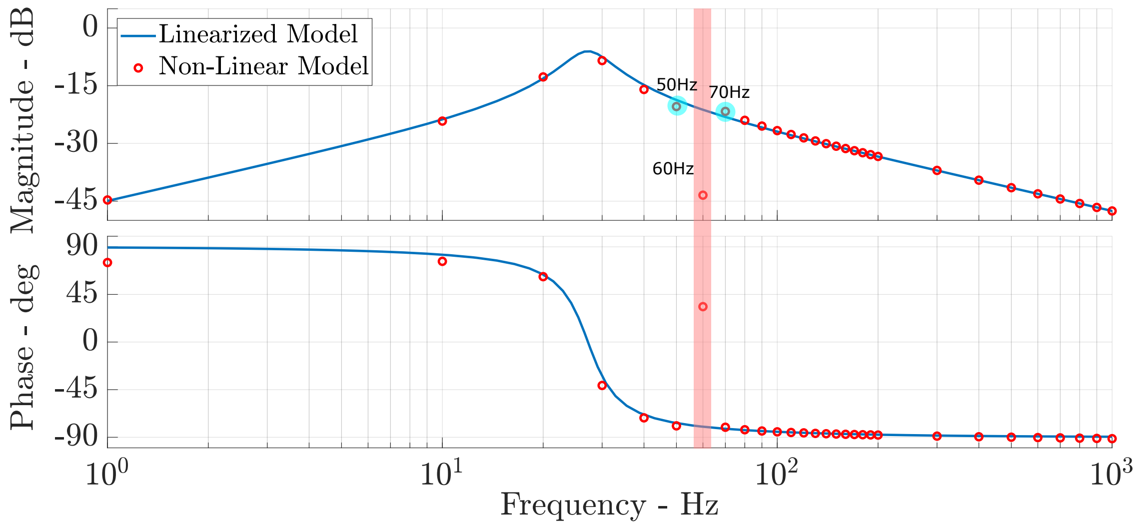

Figure 4.29: Frequency Response of the dc-side admittance, $\mathbf{Y}_{dc}^{2dq0}$.

time-domain model, and a -45dB result was obtained when it should have returned some value around -20dB. In absolute numbers, this represents a difference of over seventeen times between the results obtained from the linear and non-linear models. To better understand this result, Figure 4.30 presents the dc-bus voltage

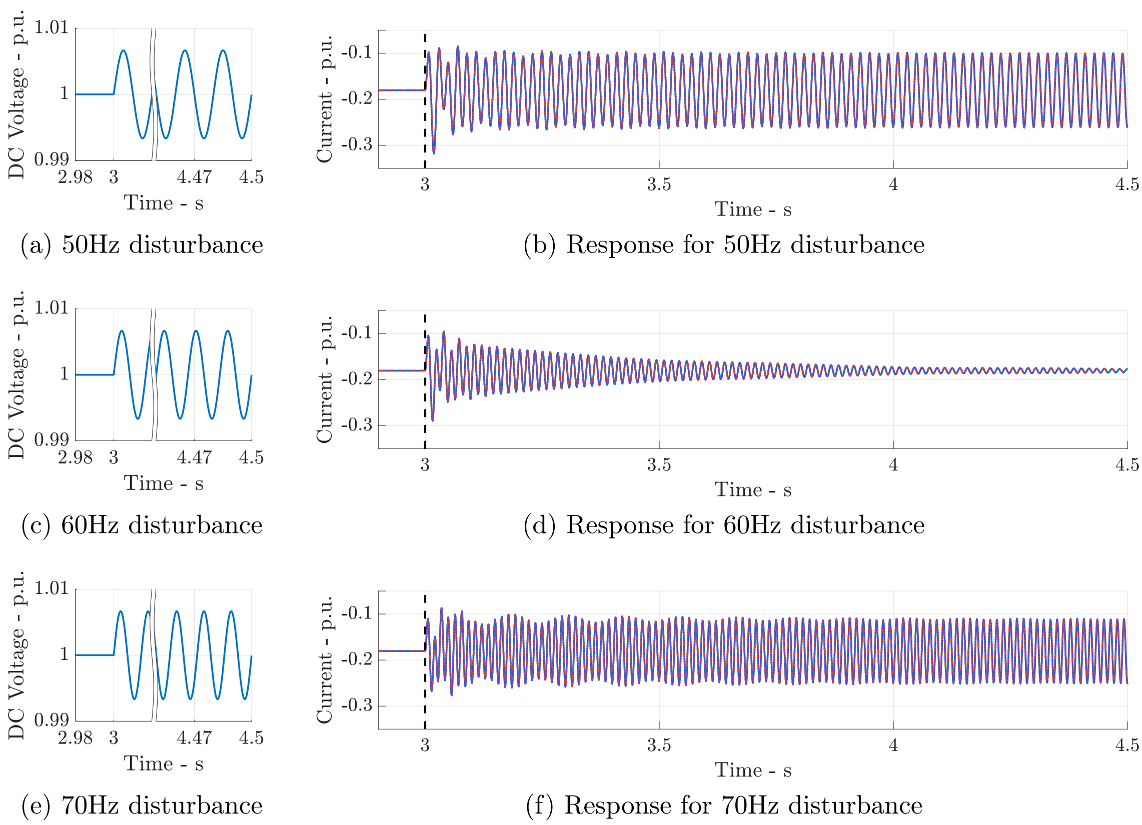

Figure 4.30: Time Response of the circulating current when different disturbances occur in the dc-bus voltage.

and circulating current for each one of the three cases analyzed (50, 60, and 70Hz disturbances), considering that the disturbances started at $t = 3s$. The graphs for the dc-bus voltages, Figures 4.30a, 4.30c and 4.30e, were horizontally cropped for aesthetics reasons, say it, allow a good visualization of the results. Notice that different from the other two cases, the circulating current due to the 60Hz disturbance dies out, as displayed in Figures 4.30d. It is possible to state that this is caused by inherent nonlinearities of the system, which the proposed model does not account for because of the linearization.

The disturbances in the dc-bus voltage also affect the equivalent dc voltages of the SM, as can be seem in Figures 4.31 and 4.32. These figures represent the upper- and lower-arm equivalent dc voltages of each phase of the MMC with a full transient display on the left graphs and zoomed versions next to them showing the steady-state conditions before and after the disturbance. For the 50 and 70Hz cases, these voltages ended up presenting a 10Hz component, while for the 60Hz case there were changes in the average values of the dc voltages. Notice in phase a, for instance, that the upper-arm dc voltage decreased while in the lower increased, indicating that this component inferred an energy exchange within the legs of the converter (the same can be noticed with the other phases as well). In all the three cases, these effects are

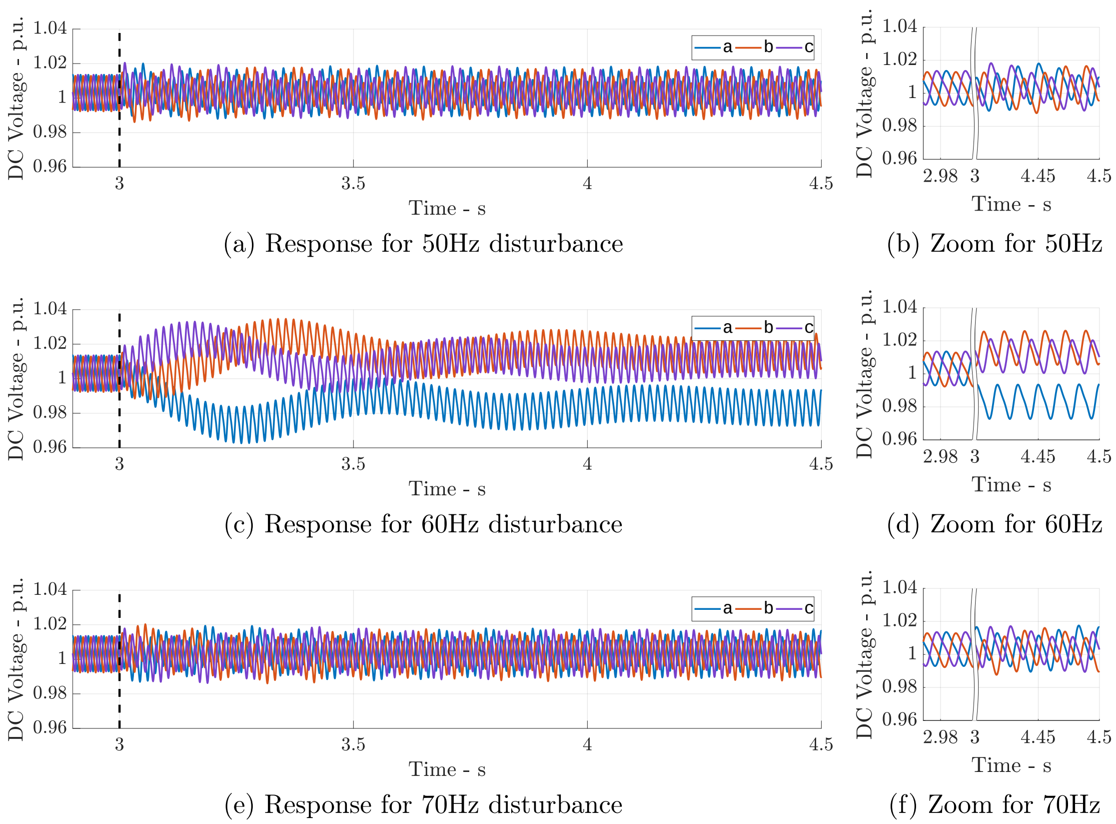

(a) Response for 50Hz disturbance (b) Zoom for 50Hz

(c) Response for 60Hz disturbance (d) Zoom for 60Hz

(e) Response for 70Hz disturbance (f) Zoom for 70Hz

Figure 4.31: Time Response of the upper-arm equivalent dc voltages when different disturbances occur in the dc-bus voltage.

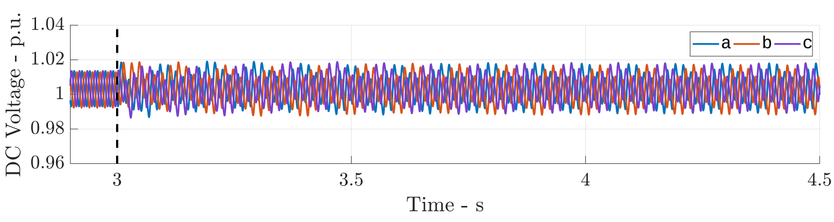

(a) Response for 50Hz disturbance

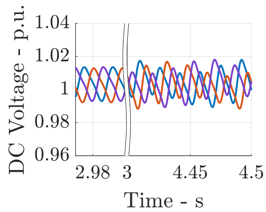

(b) Zoom for 50Hz

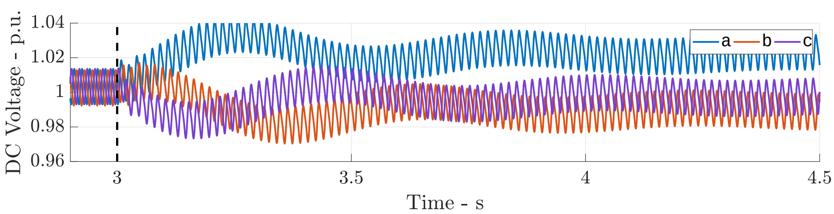

(c) Response for 60Hz disturbance

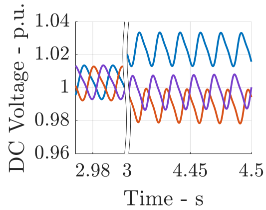

(d) Zoom for 60Hz

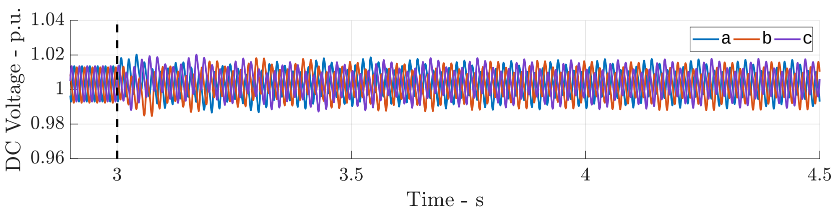

(e) Response for 70Hz disturbance

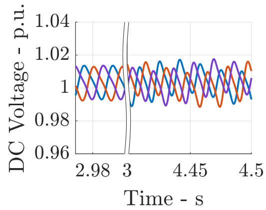

(f) Zoom for 70Hz

Figure 4.32: Time Response of the lower-arm equivalent dc voltages when different disturbances occur in the dc-bus voltage.

caused by the interaction between the current component due to the disturbance, let it be called $i^k_{cir,0}$ for it has zero sequence, with the equivalent ac voltage of the SMs. Figure 4.33 depicts the MMC during the period where the disturbance $v(t)$ is applied to the dc-bus voltage and, for what was defined in previous chapters, the

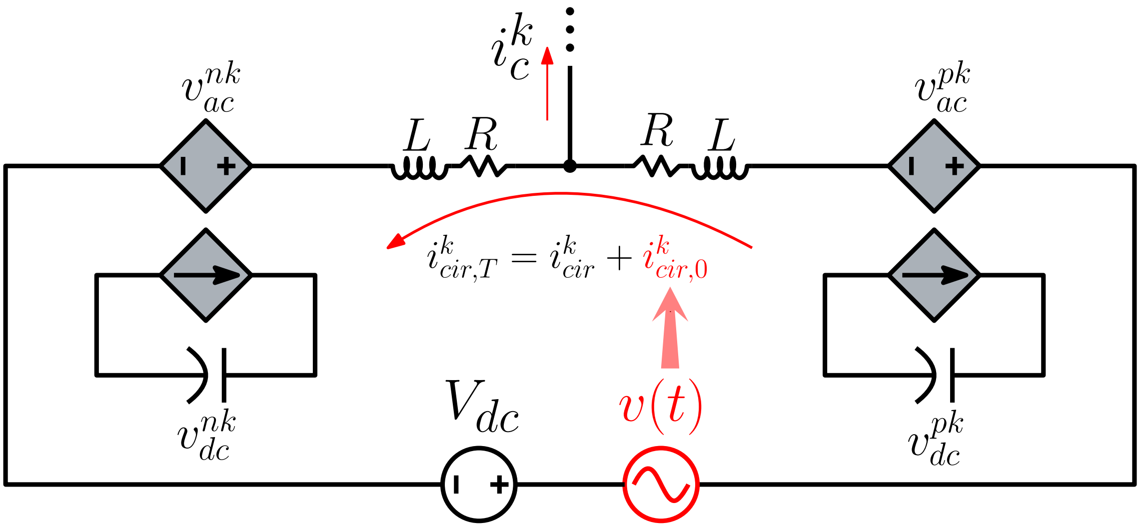

Figure 4.33: Equivalent circuit of the MMC under dc-bus voltage disturbance.

following relationships govern the MMC:

$$v_{ac}^{pk}(t) = m_p^k(t) v_{dc}^{pk}(t), \tag{4.111}$$

$$v_{ac}^{nk}(t) = m_n^k(t) v_{dc}^{nk}(t). \tag{4.112}$$

When $i_{cir,0}^k$ presents 50/70Hz components, its interaction with the fundamental component of v_{ac}^{pk} and v_{ac}^{nk} produces the 10Hz oscillations mentioned. On the other hand, when $i_{cir,0}^k$ presents 60Hz component, its interaction with v_{ac}^{pk} and v_{ac}^{nk} produces active power, changing the average values of $v_{dc}^{pk}(t)$ and $v_{dc}^{nk}(t)$. In this case, the equivalent dc voltages become unbalanced, as can be confirmed analyzing Figures 4.31 and 4.32. As the fundamental components of v_{ac}^{pk} and v_{ac}^{nk} depend on the average values of $v_{dc}^{pk}(t)$ and $v_{dc}^{nk}(t)$, they become unbalanced as well. This imbalance between the upper and lower equivalent ac voltages get rid of the zero-sequence current $i_{cir,0}^k$. Here it is important to realize that, if the 60Hz-related $i_{cir,0}^k$ had not faded away, the transference of energy between the upper- and lower-arm capacitors would have continued until one of them reached the zero-voltage level and the other the level of $2V_{dc0}$. Bearing in mind that this mechanism presents a non-linear characteristic, once it is due to the multiplication of two variables, and because of that can not be predicted by the developed linear models. The same idea explained here can be extrapolated for the other cases where occurred disparities between the proposed models and the non-linear time-domain model.

4.3 Some comparisons between the MMC and two-level inverters from a model point of view

This Section is focused on presenting a brief comparison between the MMC and a regular two-level converter for a better understanding of its inherent characteristics. It is important to mention that a similar analysis was conducted by BEERTEN *et al.* [118], but with an eigenvalue-oriented approach. Here, on the other hand, the focus is the differences in the analytic transfer functions of the converters, without considering any specific test case. Not to be too long, it is considered only the current- and single-loop voltage-controlled modes in NRF, yet the analysis can easily be extended for SRF models. Besides that, the doubly-loop voltage control is not present either, since the difference between the two converters is due to the inner current loop, already analyzed in the current-controlled mode.

A two-level converter and its average-value model are displayed in Figure 4.34. Similar notation is used here, thus, e_c^* is the modulating signal and v_{dc} is the dc voltage feeding the inverter. Thus, considering the $v_{dc} = V_{dc0} = const$, it is possible to write the following average-valued voltage if the typical delay caused by the PWM modulation is not considered:

$$e_c(t) \approx \frac{V_{dc0}}{2} e_c^*. \tag{4.113}$$

The Laplace-domain net equation of the circuit is given by:

$$\frac{V_{dc0}}{2} E_c^*(s) - (sL + R)\, I_c(s) = V_o(s), \tag{4.114}$$

where $sL + R$ is the output impedance that might be called Z from now on to simplify the equations, and $I_c(s)$ is the output current.

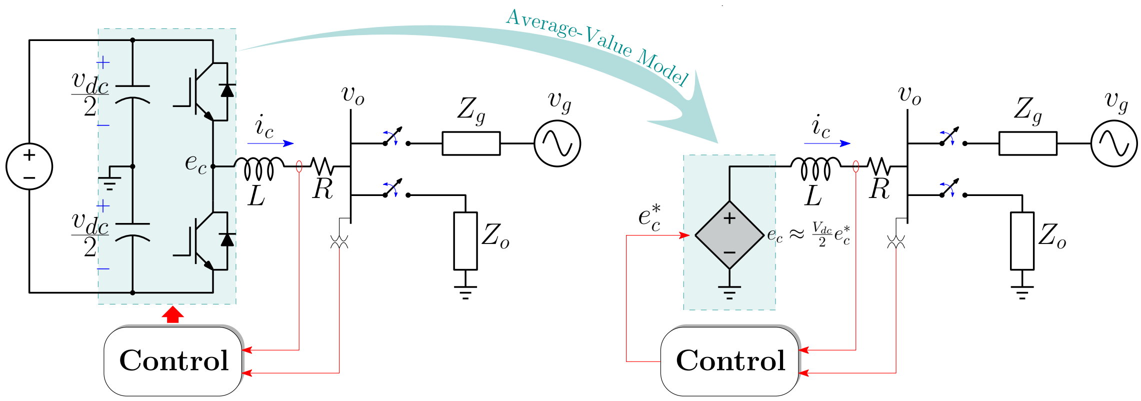

Figure 4.34: Two-level converter and its average-value model.

The following two control laws can be used, respectively, for controlling the output current or the ac-bus voltage, also following the notation used in previous sections:

$$E_c^*(s) = C_i(s) \left[I_c^*(s) - I_c(s) \right], \tag{4.115}$$

$$E_c^*(s) = C_v(s) \left[V_o^*(s) - V_o(s) \right]. \tag{4.116}$$

Substituting (4.115) and (4.116) in (4.114), separately, and rearanging the expressions, it is possible to reach the Norton-equivalent model for the current-controlled inverter and the inner Thévenin-equivalent (without considering the capacitor bank) model for the voltage-controlled one:

$$I_c(s) = G_i^{cl}(s) I_c^*(s) - Y_{ac}(s) V_o(s) \tag{4.117}$$

$$V_o(s) = G_{v,cl}(s) I_c^*(s) - Z_{ac}(s) V_o(s) \tag{4.118}$$

$$G_i^{cl}(s) = \frac{V_{dc0} C_i(s)}{V_{dc0} C_i(s) + 2Z} \tag{4.119}$$

$$Y_{ac}(s) = \frac{2}{V_{dc0} C_i(s) + 2Z} \tag{4.120}$$

Table 4.3: Comparison between the models for MMC and two-level inverters

		MMC	Two-level
Current-Controlled	$Y_{ac}(s)$	$\frac{8sC_{eq}}{4sC_{eq}\left(Z+2Z_f\right)+\left(4sC_{eq}V_{dc0}+\frac{2S_0}{3V_{dc0}}\right)C_i(s)+1}$	$\frac{2}{V_{dc0}C_i(s)+2Z}$
	$G_i^{cl}(s)$	$\frac{\left(4sC_{eq}V_{dc0}+\frac{2S_0}{3V_{dc0}}\right)C_i(s)}{4sC_{eq}\left(Z+2Z_f\right)+\left(4sC_{eq}V_{dc0}+\frac{2S_0}{3V_{dc0}}\right)C_i(s)+1}$	$\frac{V_{dc0}C_i(s)}{V_{dc0}C_i(s)+2Z}$
Voltage-Controlled	$Z_{ac}(s)$	$\frac{4sC_{eq}\left(Z+2Z_f\right)+1}{8sC_{eq}+\left(4sC_{eq}V_{dc0}+\frac{2S_0}{3V_{dc0}}\right)C_v^{sl}(s)}$	$\frac{2Z}{2+V_{dc0}C_v(s)}$
	$G_{v,cl}(s)$	$\frac{\left(4sC_{eq}V_{dc0}+\frac{2S_0}{3V_{dc0}}\right)C_v^{sl}(s)}{8sC_{eq}+\left(4sC_{eq}V_{dc0}+\frac{2S_0}{3V_{dc0}}\right)C_v^{sl}(s)}$	$\frac{V_{dc0}C_v(s)}{2+V_{dc0}C_v(s)}$

$$G_{v,cl}(s) = \frac{V_{dc0}C_v(s)}{2 + V_{dc0}C_v(s)} \tag{4.121}$$

$$Z_{ac}(s) = \frac{2Z}{2 + V_{dc0}C_v(s)} \tag{4.122}$$

Table 4.3 presents the parameters of the equivalent models of the two-level converter side-by-side with the results related to the MMC. The first difference to be noticed is the effect of the equivalent dc capacitance C_{eq} in the ac-side of the MMC, something that is not observed in the two-level converter. Thus, terms such as $4sC_{eq}(Z + 2Z_f)$ and $4sC_{eq}C_i(s)$ provides the MMC with frequency-domain characteristics that the other converter does not present. Of course, it is possible to state that two-level converters need ac capacitors to filter out their switching-frequency harmonic components, and that would make the frequency-domain behavior of both converters equivalents. However, ac capacitors (used as filters in two-level inverters) are considerably smaller than dc capacitors (used in the SMs of the MMC) in this difference may make the MMC prone to low-frequency resonances, whereas the two-level to high-frequency. Another notable difference presented in Table 4.3 is that the produced power S_0 influences the dynamics of the MMC, yet not the two-level converter.

4.4 Partial Conclusions

This chapter presented frequency-domain model to represent the MMC under different control modes, implemented in natural and synchronous reference frame. Considering first the NRF models, it was shown that the circulating current dynamics together with its mitigation loop can be represented by an admittance which is influenced by the values of passive elements and the values of control parameters. As for the ac control loops, the chapter showed that under current control the MMC can be represented by a Norton-equivalent electric circuit, while under voltage control it is possible to reach a Thévenin-equivalent representation of the system. In these cases, impedances and admittances are also influenced by passive elements and control parameters. In all the cases, analytical gains, admittances and impedances were validated comparing them to the results obtained from the non-linear time-domain model. These comparisons showed that the proposed models matched the reference model with few discrepancies. Some of these differences appeared at the frequencies of resonance of the controllers, and it was concluded that numerical errors and digital implementation of the non-linear model played an important role on them.

For the SRF-controlled MMC, the model describing the effect of the dc-bus voltage on i_{cir} was developed in D-SRF. Still in this regard, it was shown that only a zero-sequence term is necessary to represent this part of the model once all the phases of the MMC are connected to the same dc bus. It was also concluded that this zero-sequence component has nothing to do with the component which is mitigated by the control action. This is a component that can appear in case the voltage of the dc bus presents oscillating components. As already explained in the previous chapter, when the MMC is under current control its ac-side model can be depicted as a Norton-equivalent circuit, whereas the Thévenin-equivalent is used whenever the MMC is under voltage control. The validation results, presented in the form of Bode diagrams, showed that the developed model matched accurately the characteristic of the MMC with a few exceptions. Some of them, especially the ones at the frequencies of 60 and $120Hz$ are due to the linearization which the model underwent in Chapter 3. The disparities observed in the models considering the MMC under voltage control, though, were triggered by numeric issues in the realizations of the proposed model in Matlab. In this regard, it was discussed that the matrices inversions in these models together with the matrices multiplications spawned hundred-order polynomes which appear to be in the kernel of the problem. Nevertheless, these disparities affected the model only in a narrow band between 50 and $70Hz$ (which corresponds -10 to $10Hz$ for positive sequence, and 110 to $130Hz$ for negative sequence in natural reference frame) which are not key frequencies of the system.

Chapter 5

Further analysis of the developed models

It is known that the characteristic of equivalent admittances/impedances presented in Chapter 4 play an important role in the performance of the MMC. Indeed, depending on these characteristics the MMC may or may not be affected by harmonic components drawn by non-linear loads or present in the voltage patterns of a power grid [119]. For instance, the presence of harmonic distortion in the main bus voltage (background harmonics) may cause harmonic distortion in the produced current of the current-controlled MMC depending on the shape and values of the equivalent admittance. In the same direction, non-linear loads may distort the produced voltage depending on the Thévenin impedance of the grid-forming MMC. In this context, this chapter aims firstly to demonstrate how the control settings interfere in the frequency response of the equivalent admittances/impedances of the MMC and secondly to present/propose ways to shape the equivalent admittance/impedance of the MMC in a way that it becomes immune to background harmonics and similar issues. Towards the end of the chapter, some test cases are presented to demonstrate how the developed models can be used to speed-up time-domain simulations and into stability analysis of power-electronic-based systems. These last two points are also included in the reference [62], which are results of this thesis. One last point, in this chapter the frequency responses were obtained from the linearized models, but the time-domain simulations were obtained either by the non-linear or switching-level models.

5.1 Control settings influence on the equivalent admittances/impedance of the MMC

This section analyzes the influence of control settings on the shape of equivalent admittances/impedances of the MMC under different operational modes. To be more specific, it is analyzed the dc-side equivalent admittance of the circulating-current loop, the ac-side equivalent admittance of the current-controlled MMC and the ac-side equivalent impedance of the voltage-controlled MMC. The analyses here are conducted in the frequency domain considering the MMC both controlled in NRF or SRF. It is important to have in mind that, so far, all the control settings used in the analyzes were randomly chosen without considering constraints other than the stability of the system. In this regard, it is always considered three different values for each of the control gains.

5.1.1 NRF-controlled MMC

This section presents the analysis for the NRF-controlled MMC under its different control modes. As previously mentioned, three different values are assigned to each of the control gains, all of them presented in Table 5.1, to observe the role which that parameter plays in the equivalent admittances/impedances. Considering the Table 5.1, under the "base value"column are presented the control settings used in the validation process presented in Chapter 4.1. The other two conditions were chosen so as to provide the analysis with both greater and smaller values for the gains. It is important to mention that in any case, the terms "min"and "max"in the table indicate that these are the minimum/maximum possible values for the gains, they are just generic values chosen (but all of them guarantee the stability of the system). For analysis purposes, it was decided to vary only one gain at a time, holding the other(s) constant during the process, otherwise, a huge number of cases would be necessary to be presented. For instance, whenever the focus is to analyze the influence of the proportional gain, the resonant gain is kept constant with the base value assigned to it, and vice versa. The following topics present the analysis for each of the control loops.

dc admittance

The results which show the influence of the resonant gain in the equivalent admittance used to model the dynamics of the circulating-current loop are presented in Figure 5.1. It can be observed that for each of the three cases, the magnitude in the resonant frequency $2\omega_0$ is relatively small, yet the response shows the existence of other resonant peaks each side of $2\omega_0$. It is concluded that the value assigned to

Table 5.1: Considered values for the analysis of the control settings influence on the equivalent admittance/impedance: NRF-controlled MMC.

Control Mode	Parameter	Symbol	Max. Value	Base Value	Min. Value
Circulating Current	Resonant Gain	k_r^{cir}	1.00000	0.10000	0.01000
Current-Controlled	Proportional Gain	k_p^i	0.00100	0.00010	0.00001
	Resonant Gain	k_r^i	0.10000	0.01000	0.00100
Single-Loop Voltage-Controlled	Proportional Gain	$k_p^{v,sl}$	0.00100	0.00010	0.00001
	Resonant Gain	$k_r^{v,sl}$	0.01000	0.00100	0.00010
Double-Loop Voltage-Controlled	Proportional Gain: Inner Loop	$k_p^{i,dl}$	0.00100	0.00010	0.00001
	Resonant Gain: Inner Loop	$k_r^{i,dl}$	0.05000	0.01000	0.00100
	Proportional Gain: Outer Loop	$k_p^{v,dl}$	0.50000	0.10000	0.01000
	Resonant Gain: Outer Loop	$k_r^{v,dl}$	9.00000	1.00000	0.09000

k_r^{cir} affects the frequency position of these extra resonant peaks. On the left side of $120Hz$, for instance, these resonant peaks are located at 9.8, 20.5 and $26.8Hz$, depending on the value of k_r^{cir}, not implying any significant issue. On the right side of $120Hz$, on the other hand, the resonant peaks located at 124.3, 157.1 and $339.1Hz$, for each value of k_r^{cir}, do raise some concerns in views that they neighbor frequencies of typical oscillatory components of the dc voltage, e.g., $4\omega_0$. In a nutshell, the resonant gain must be chosen carefully so as not to amplify some oscillatory components in the circulating current.

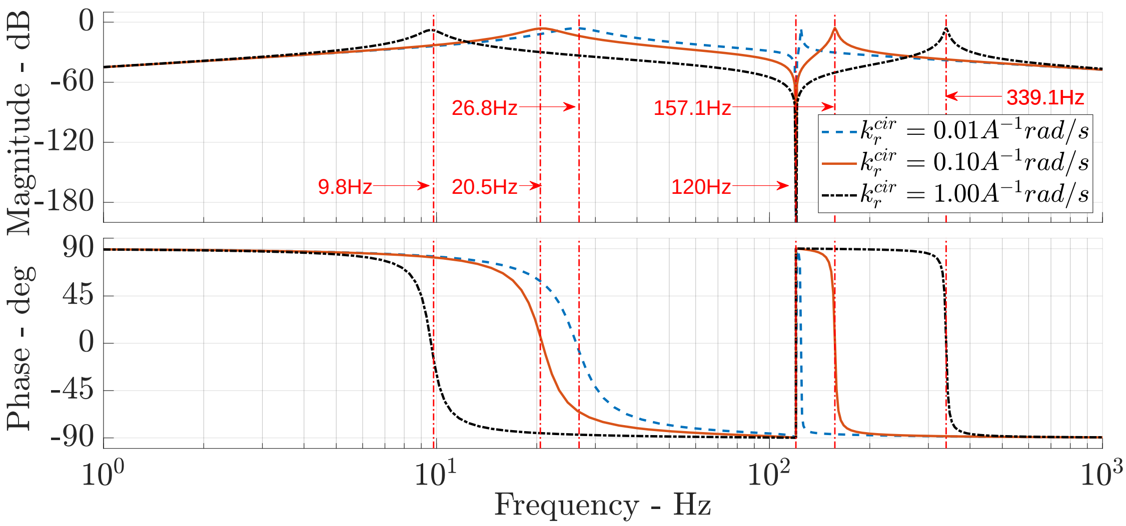

Figure 5.1: Influence of the control settings on the dc-side equivalent admittance in the NRF-controlled MMC.

MMC under current control

The influence of the proportional and resonant gains on the equivalent ac-side admittance of the MMC under current control is presented in Figure 5.2. Notice that, in general, the influence of the control settings here is less apparent than in the case of the dc admittance. The major effect is caused by the proportional gain, i.e., the greater the gain, the lower the admittance. In the ideal condition, it is desired the converter acting as a current source with equivalent admittance tending to 0 ($-\infty dB$). Thus, it stood out that higher values for the proportional gain are better for the current loop, yet it is necessary to bear in mind that stability constraints have to be satisfied. On the other hand, the decreasing of the proportional gain may inflict a resonant peak at $14Hz$, besides elevating the magnitude of the equivalent admittance as a whole. The resonant gain, considering the range used in the analysis, does not present any significant effect in the shape of the admittance.

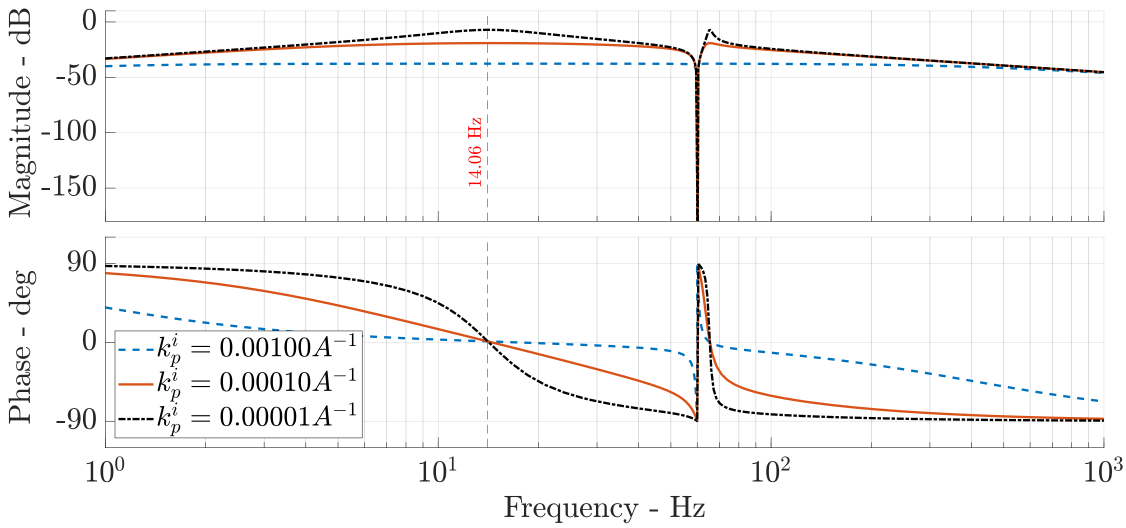

(a) Influence of k_p^i

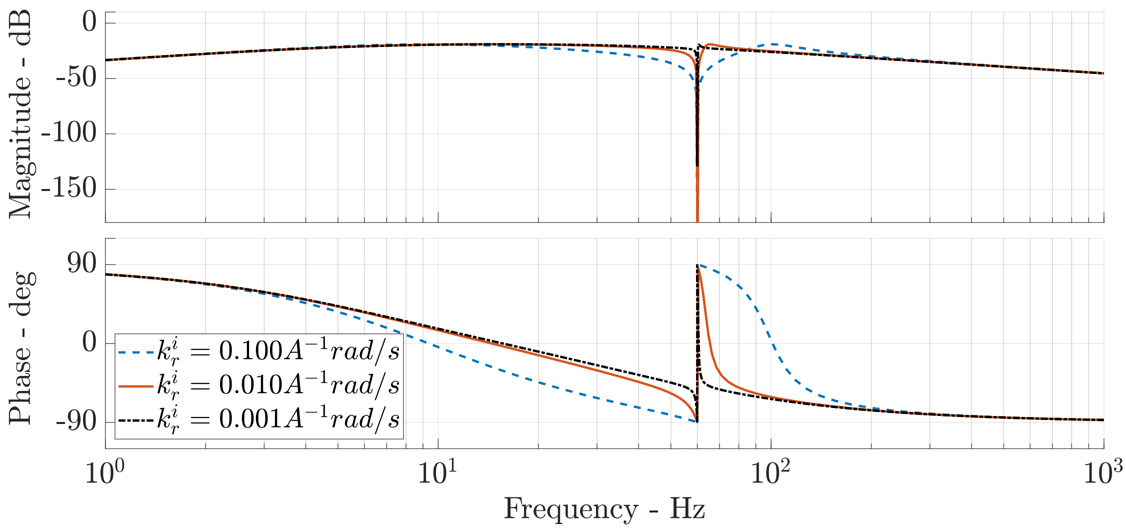

(b) Influence of k_r^i

Figure 5.2: Influence of the control settings on the Norton-equivalent admittance in the NRF current-controlled MMC. Only one of the gains (proportional and resonant) was varied at a time accordingly Table 5.1. In this case, the base value was assigned to the other.

MMC under single-loop voltage control

Figure 5.3 sheds light on the effects of the proportional and resonant gain on the shape of the Thévenin-equivalent impedance of the MMC under single-loop voltage control. Once more, the proportional gain influence on the impedance stood out. Indeed, the assigned proportional gains played an important role in the average level of the magnitude curve and the position of a resonant peak. Observe that higher values of $k_p^{v,sl}$ reduce the average level of the impedance and, consequently, make the converter to operate near the ideal condition (ideal voltage source). Nonetheless, increasing the proportional gain shifts the resonant peak towards the right, moving it from $274.4Hz$ to $604.3Hz$, for instance. Notice that these frequencies are in

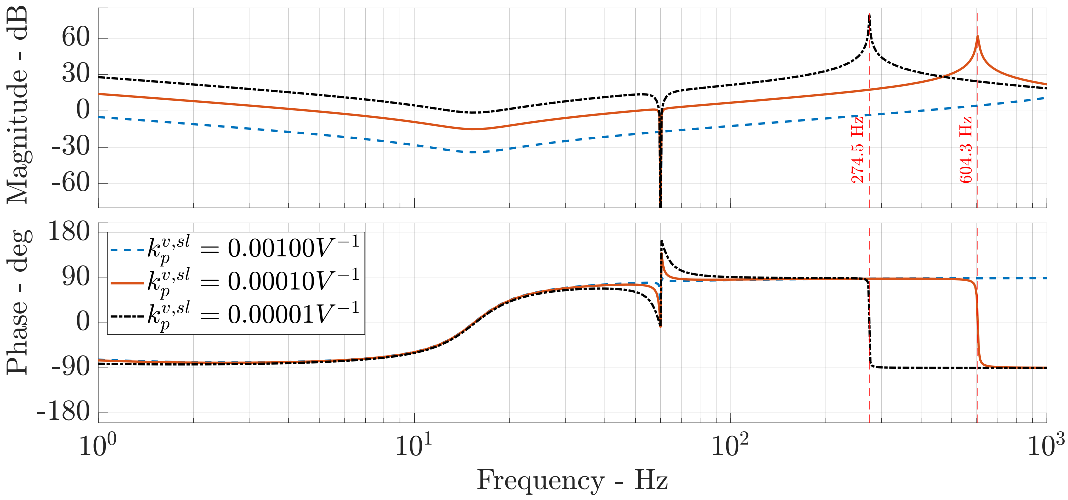

(a) Influence of $k_p^{v,sl}$

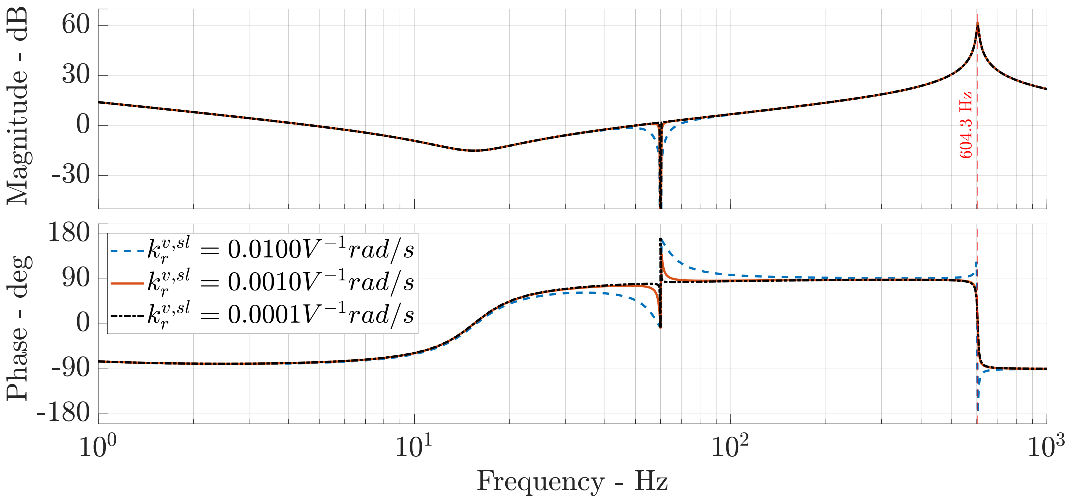

(b) influence of $k_r^{v,sl}$

Figure 5.3: Influence of the control settings on the Thévenin-equivalent impedance in the single-loop NRF voltage-controlled MMC. Only one of the gains (proportional and resonant) was varied at a time accordingly Table 5.1. In this case, the base value was assigned to the other.

the neighborhood of the fifth- and eleventh-order harmonic components, which in a nutshell indicates that higher values of $k_p^{v,sl}$ are more suitable for six-pulse-based non-linear loads, while small values are better for twelve-pulse-based loads[1].

MMC under double-loop voltage control

The double loop approach implies that four parameters, rather than two, can be tuned, i.e., the proportional and resonant gain of the current controller and those of the voltage controller. For this reason, Figure 5.4 presents four diagrams, each one focusing on the influence of one of the control gains. As with the previous control modes, the resonant parts show a weak influence on the shape of the equivalent impedance. Nonetheless, it stands out in Figure 5.4b that higher values of the resonant gain of the current control loop may increase the amplitude of the resonant peak located at $276.9Hz$. Meanwhile, the proportional gains do exert great influence on the shape of the equivalent impedance shifting the position of the resonant peaks, as highlighted in Figures 5.4b and 5.4d. As these peaks cover the frequency range of the main harmonic components in an ac system, the values for the proportional gains might be carefully chosen. It is also noticed that, while $k_p^{v,dl}$ only shifts the resonant peak, $k_p^{i,dl}$ tend also to damp it with its increasing.

[1]The fifth-order is the major harmonic component in six-pulse rectifies, while the eleventh-order is the major harmonic component in twelve-pulse rectifies. Consequently, six-pulse rectifiers could cause greater harmonic distortion in the voltage if the resonant peak of the Thévenin impedance lies nears the fifth-order-harmonic frequency. The same is analogously true for the twelve-pulse rectifier and its corresponding major-harmonic-component frequency.

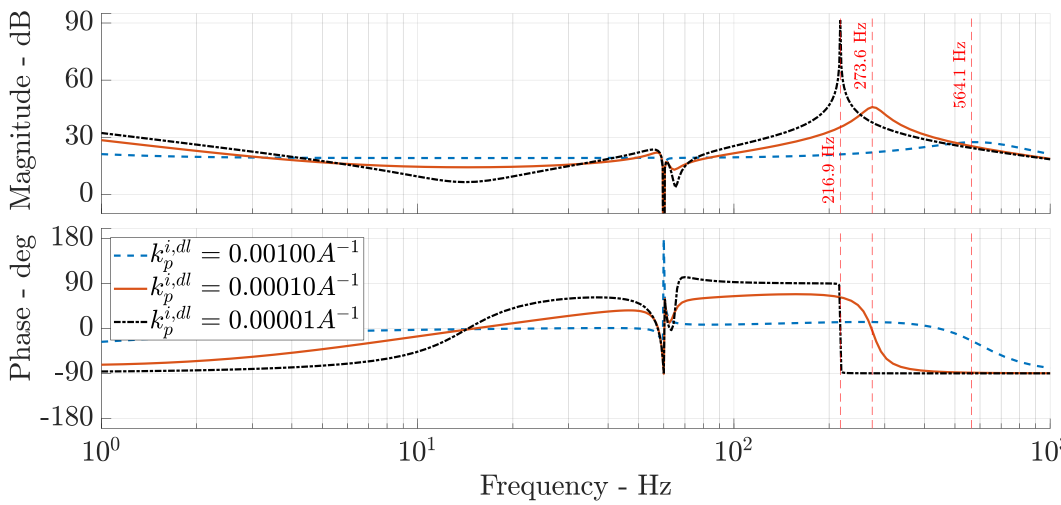

(a) Influence of $k_p^{i,dl}$

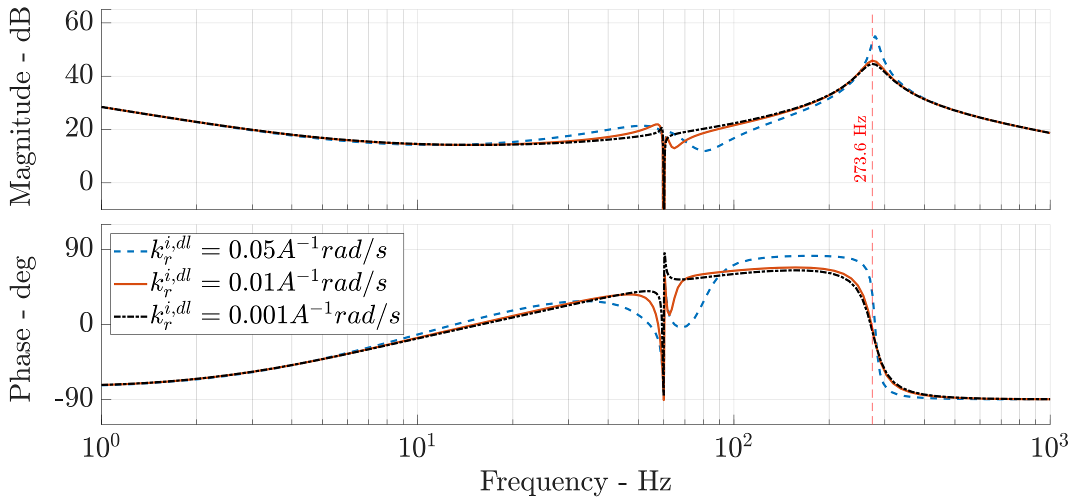

(b) Influence of $k_r^{i,dl}$

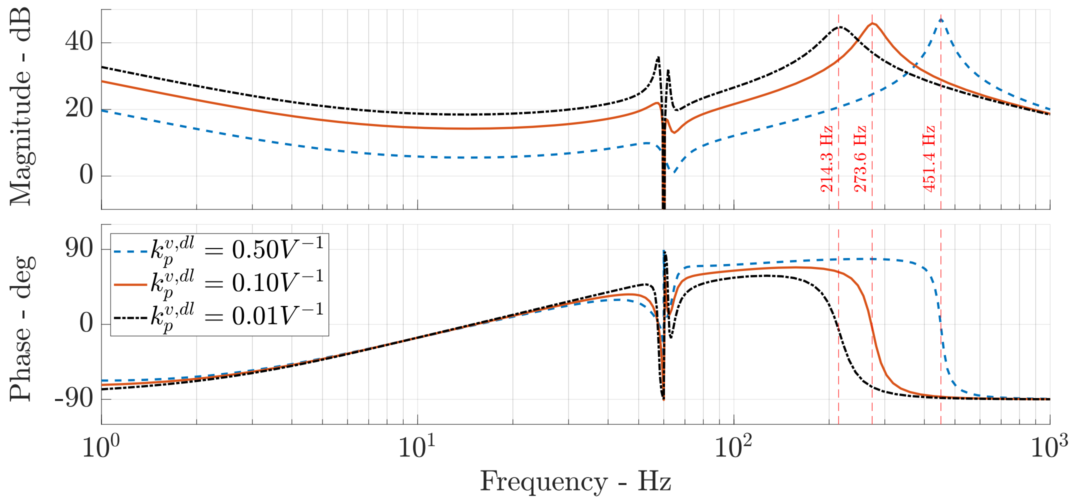

(c) Influence of $k_p^{v,dl}$

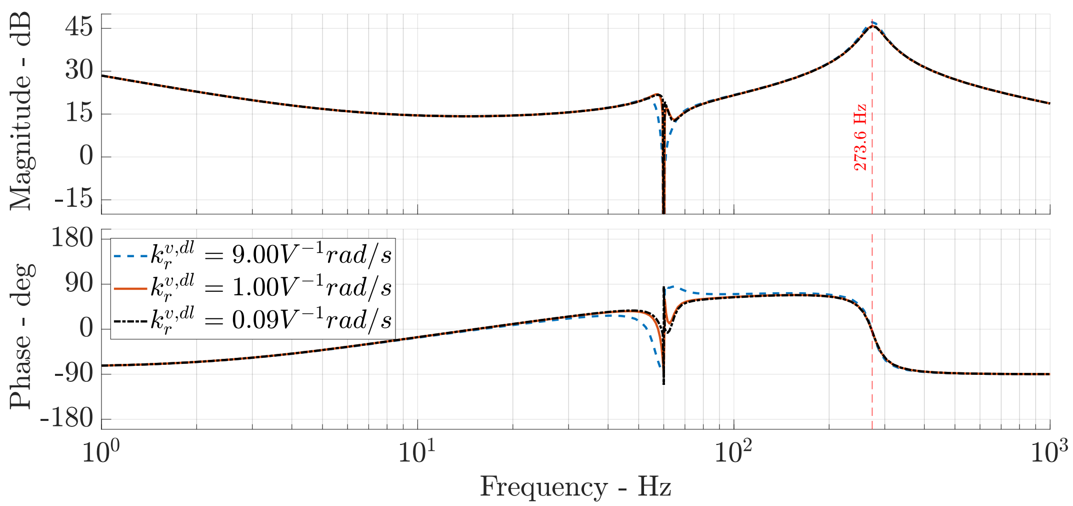

(d) Influence of $k_r^{v,dl}$

Figure 5.4: Influence of the control settings on the Thévenin-equivalent impedance in the double-loop NRF voltage-controlled MMC. Only one of the gains (proportional and resonant) was varied at a time accordingly Table 5.1. In this case, the base value was assigned to the other.

Table 5.2: Considered values for the analysis of the control settings influence on the equivalent admittance/impedance: SRF-controlled MMC.

Control Mode	Parameter	Symbol	Max. Value	Base Value	Min. Value
Current-Controlled	Proportional Gain	k_p^i	0.0050000	0.0010000	0.0001000
	Integral Gain	k_i^i	1.0000000	0.1000000	0.0100000
Single-Loop Voltage-Controlled	Proportional Gain	$k_p^{v,sl}$	0.0000100	0.0000010	0.0000001
	Integral Gain	$k_i^{v,sl}$	0.0010000	0.0001000	0.0000100
Double-Loop Voltage-Controlled	Proportional Gain: Inner Loop	$k_p^{i,dl}$	0.0100000	0.0010000	0.0001000
	Integral Gain: Inner Loop	$k_i^{i,dl}$	1.0000000	0.1000000	0.0100000
	Proportional Gain: Outer Loop	$k_p^{v,dl}$	0.1000000	0.0100000	0.0010000
	Integral Gain: Outer Loop	$k_i^{v,dl}$	10.0000000	1.0000000	0.1000000

5.1.2 SRF-controlled MMC

As in the previous section, here it is presented the influence of the control settings on the equivalent admittance/impedance of the SRF-controlled MMC under different control modes. It is followed the same approach of considering three different values for each gain and splitting the analysis in subsections focusing each control mode. Table 5.2 presents the considered control settings and its "base value"column indicated the condition utilized in Section 4.2 of the Chapter 4. One different aspect in comparison to the previous section is that here the analysis of the dc-side equivalent admittance was omitted. As explained in Section 4.2, the zero-sequence term of this admittance was the only one considered for analysis and as this component is not controlled by the circulating current loop, the control setting does not affect it.

Before proceeding with the analysis, it is necessary to bear in mind that in SRF the fundamental components are placed in $0Hz$ (dc) and that other important harmonic components are shifted as well. For instance, negative-sequence fifth-order and positive-sequence seventh-order harmonic components are moved into $360Hz$, while negative-sequence eleventh-order and positive-sequence thirteenth-order components are merged at $720Hz$. As these are the major components found in the power system, it is desired that equivalent admittances/impedances present as lower value as possible in 0, 360 and $720Hz$ to provide the MMC with immunity to disturbances.

MMC under current control

Figure 5.5 embodies the results for the influence of the proportional and integral gains in the shape of the self-related term of the Norton-equivalent admittance of the MMC. Considering first the effect produced by the proportional gain, it is noticeable that the curves converge to the same trajectory both when the frequency tends to zero and ∞. Nonetheless, the level of the magnitude curves swells with the decrease of the gain in the frequency range that goes from 10 to $600Hz$. As the key frequency of $360Hz$ is within this interval, lower values of k_p^i must be avoided or else the produced current would be affected in face of harmonic distortion in the grid voltage. As for the integral gain, it seems that greater values shape the curve so that the magnitude converges to $-\infty$ faster when the frequency tends to zero. However, the increase of the integral gain is responsible for a boost in the magnitude in the region bounded by 200 and $600Hz$ (region where key harmonic components are located).

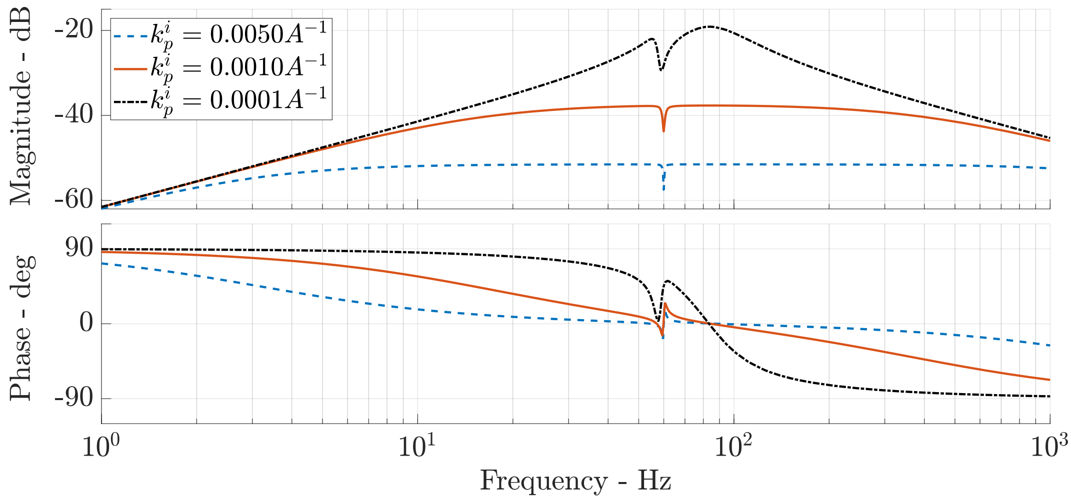

(a) Influence of k_p^i

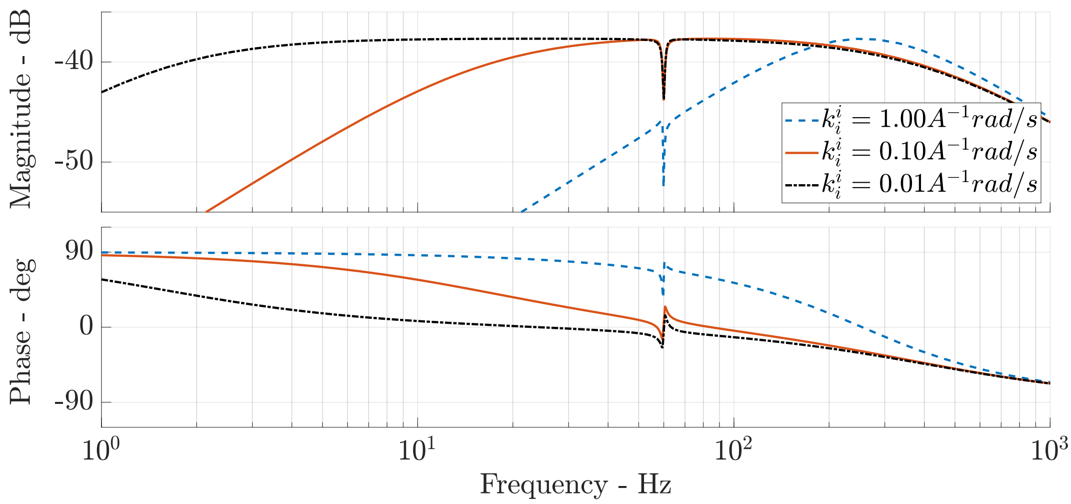

(b) Influence of k_i^i

Figure 5.5: Influence of the control settings on the self-related term of the Norton-equivalent admittance in the SRF current-controlled MMC. Only one of the gains (proportional and integral) was varied at a time accordingly Table 5.2. In this case, the base value was assigned to the other.

MMC under single-loop voltage control

Figure 5.6 presents the results for the MMC under SRF single-loop voltage control. The influence of the proportional gain in similar for the self-related and cross-axis terms as it can be seem in Figures 5.6a and 5.6c. In general, the resonant peaks on the right side of $60Hz$ are shifted to higher frequencies with the increase of the proportional gain. In the worst scenario, which correspond to the highest value of $k_p^{v,sl}$ considered, one of the resonant peaks lay at $334.5Hz$ which is close to one of the key frequencies mentioned in the beginning of this section. The entanglements observed around $60Hz$ are due to the numerical issues discussed in Section 4.2. As for the integral gain, the major issue related to it is a swelling on resonant peak at $275.3Hz$ caused by its increasing. Here it is important to notice that the amplitude of this resonance is increased with the increase of the integral gain.

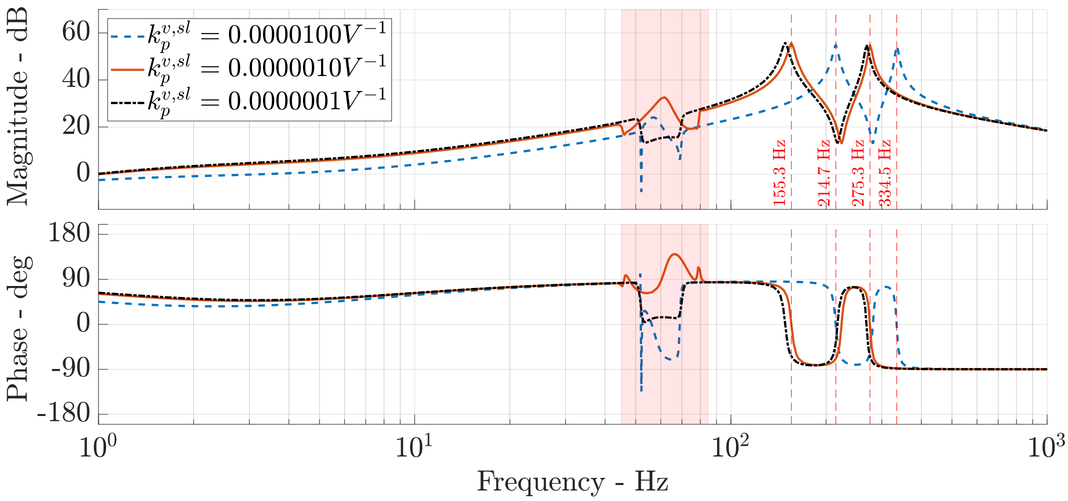

(a) Self-related term: influence of $k_p^{v,sl}$

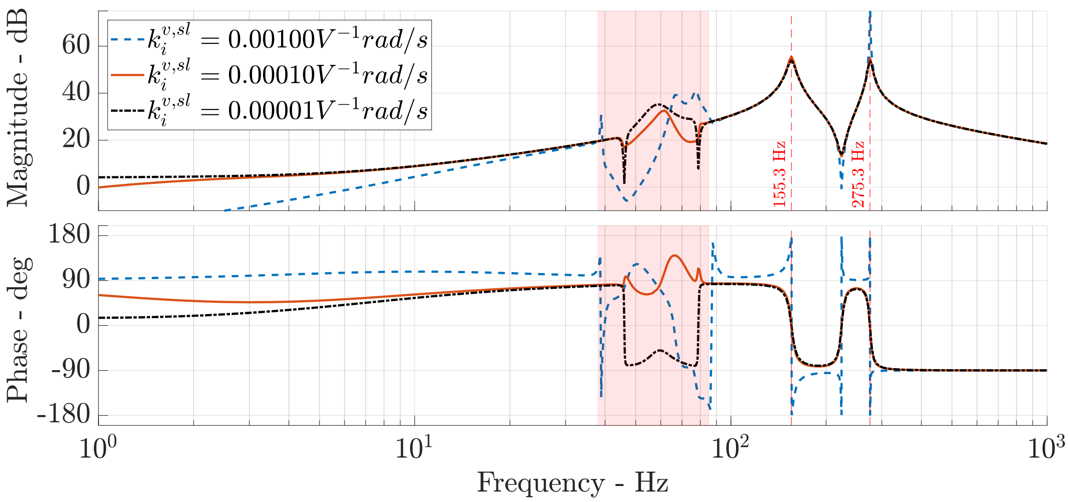

(b) Self-related term: influence of $k_i^{v,sl}$

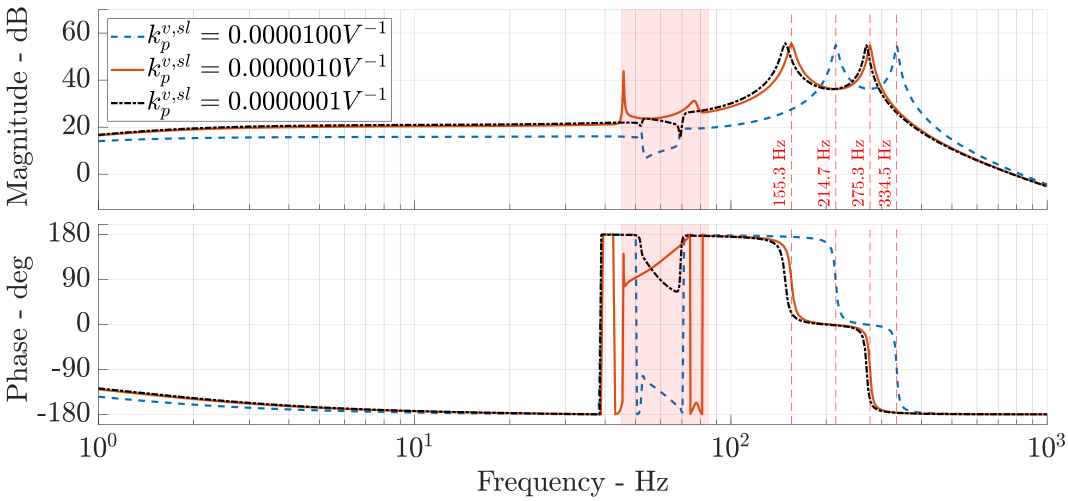

(c) Cross-axis term: influence of $k_p^{v,sl}$

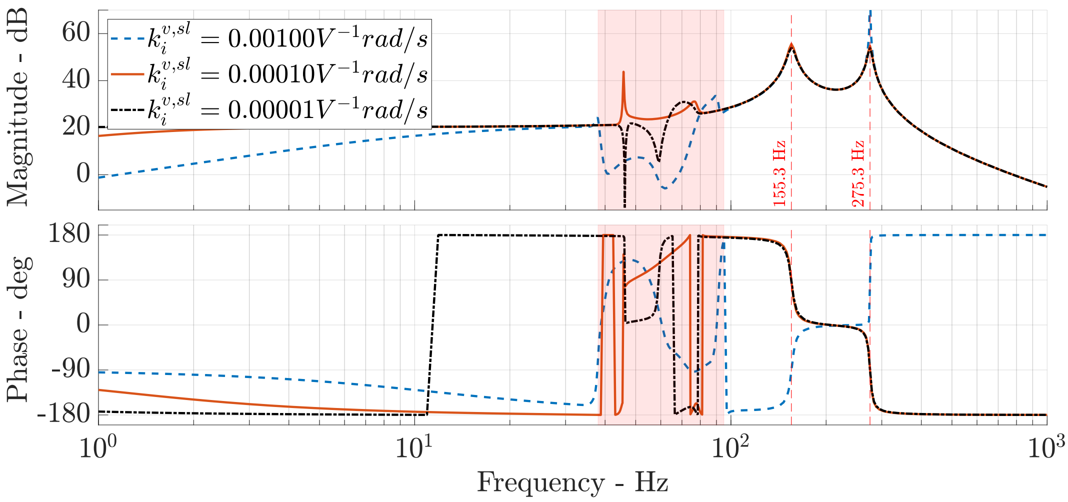

(d) Cross-axis term: influence of $k_i^{v,sl}$

Figure 5.6: Influence of the control settings on the Thévenin-equivalent impedance in the SRF single-loop voltage-controlled MMC. Only one of the gains (proportional and integral) was varied at a time accordingly Table 5.2. In this case, the base value was assigned to the other.

MMC under double-loop voltage control

The analysis results considering the MMC under double-loop voltage control are presented in Figure 5.7. It stood out in the charts the strong influence of the parameters of the outer voltage control loop into the shape of the Thévenin-equivalent impedance, especially the proportional gain. As observed in the figures, the greater this gain, the lower the level of the admittance, following the rule already observed in the previous cases. As for the inner current loop, its major effects were caused by the proportional gain in the frequency range of 10 - 300Hz. Notice that the smallest proportional gain is responsible for a pair of resonant peaks at 201 and 260Hz, on the self-related term of the impedance, and at 256Hz in the cross-axes term.

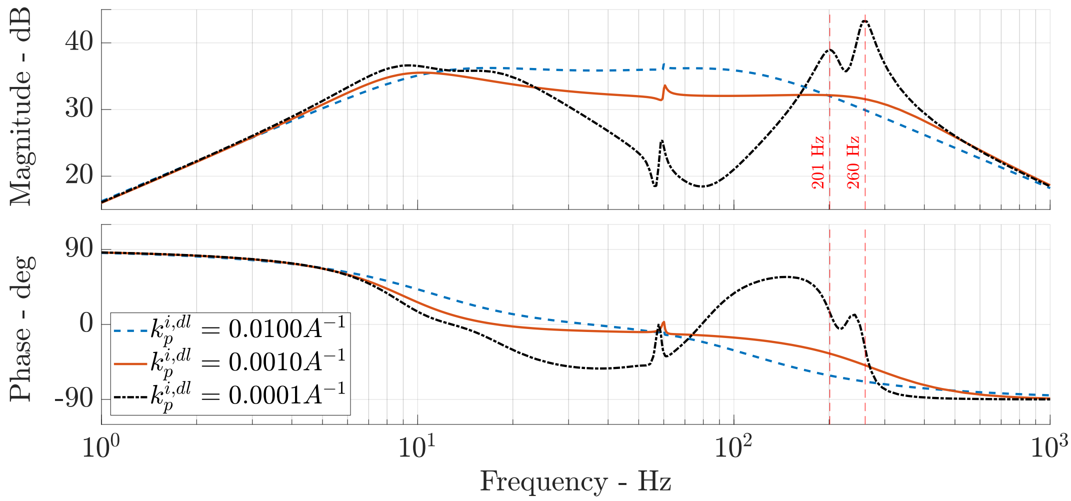

(a) Self-related term: influence of $k_p^{i,dl}$

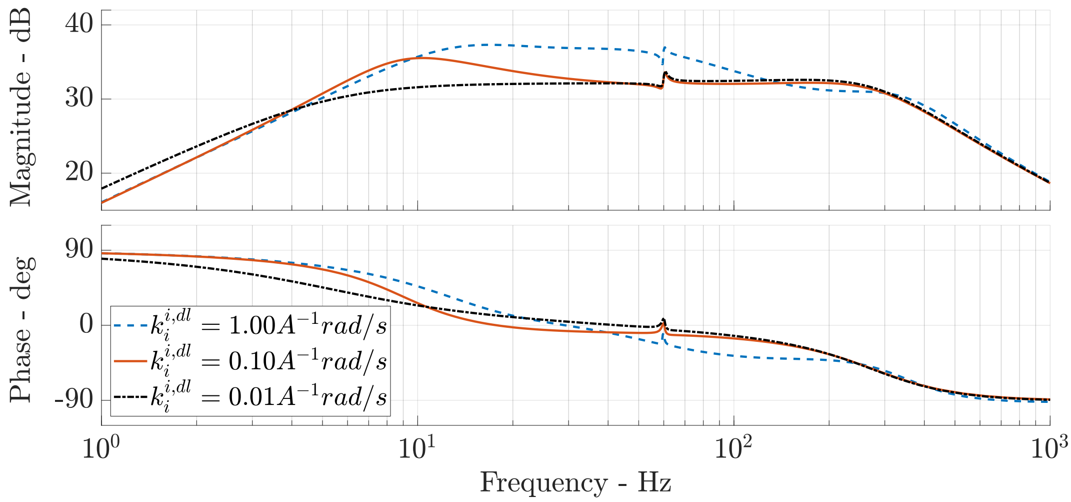

(b) Self-related term: influence of $k_i^{i,dl}$

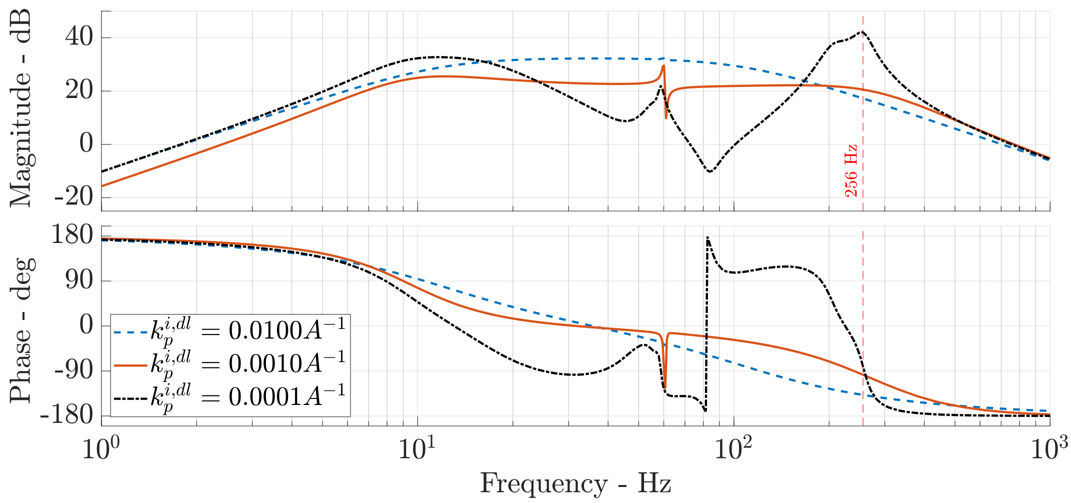

(c) Cross-axis term: influence of $k_p^{i,dl}$

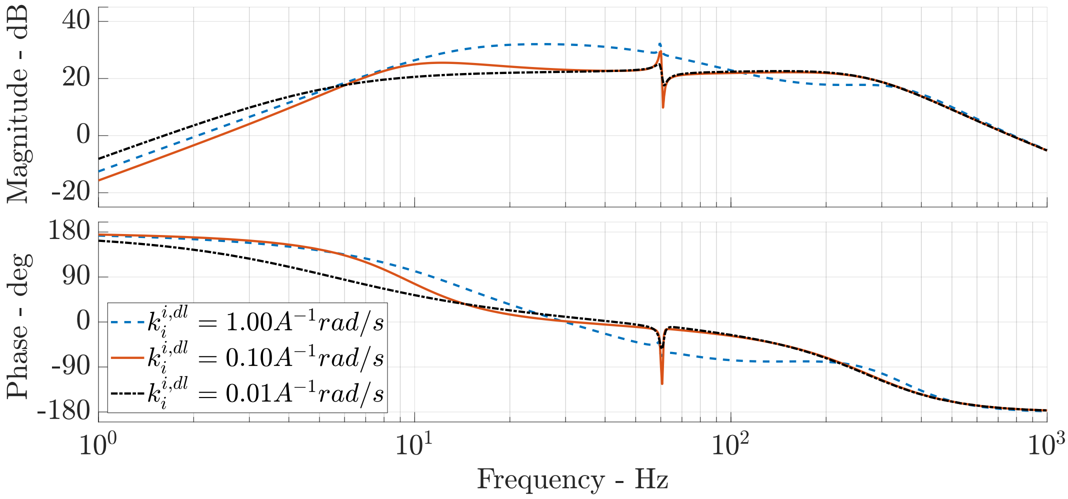

(d) Cross-axis term: influence of $k_i^{i,dl}$

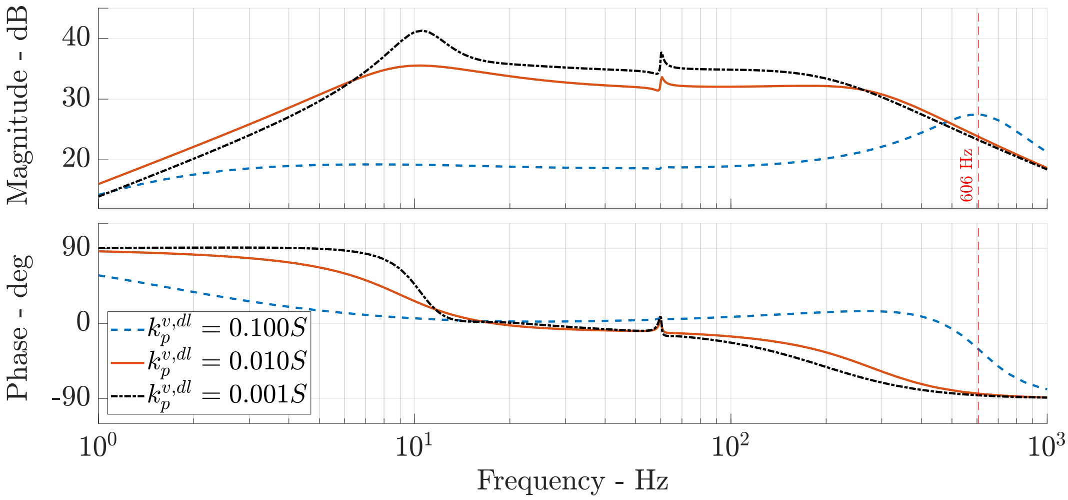

(e) Self-related term: influence of $k_p^{v,dl}$

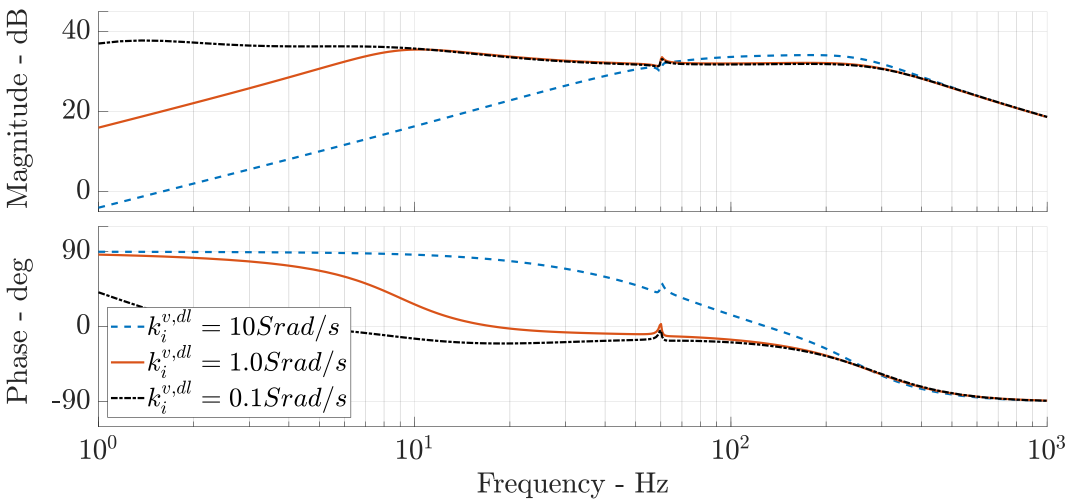

(f) Self-related term: influence of $k_i^{v,dl}$

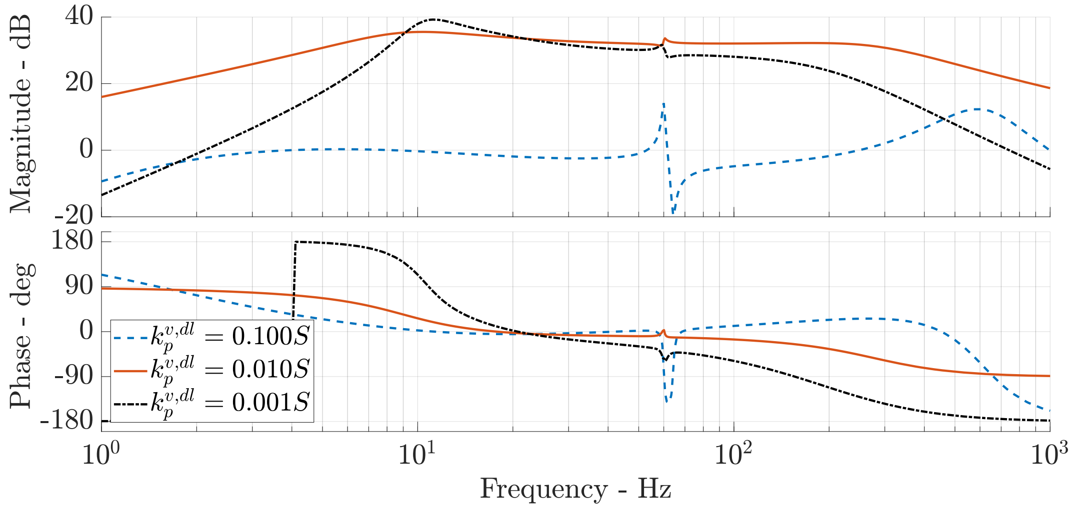

(g) Cross-axis term: influence of $k_p^{v,dl}$

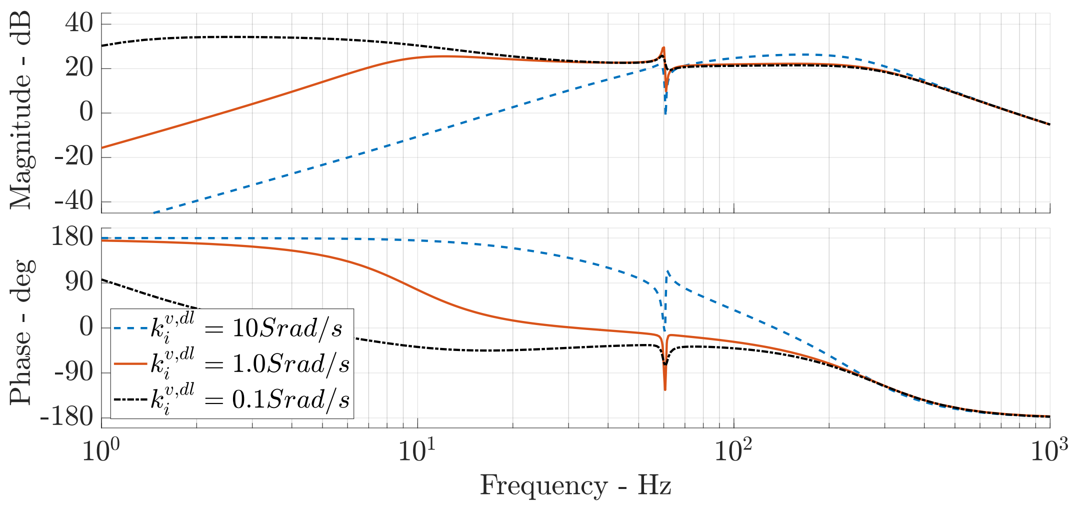

(h) Cross-axis term: influence of $k_i^{v,dl}$

Figure 5.7: Influence of the control settings on the Thévenin-equivalent impedance in the SRF double-loop voltage-controlled MMC. Only one of the gains (proportional and integral) was varied at a time accordingly Table 5.2. In this case, the base value was assigned to the other.

5.2 Control actions for enhancing the performance of the MMC

The present section sheds light on control approaches for shaping the ac-side admittances/impedances of the MMC in a way that it becomes immune to distorted-currents loads and distorted voltages. Firstly it is presented techniques based on multiple resonant loops applied to either NRF- or SRF-controlled MMC and then the use of virtual elements (admittance or impedance). In this last case, it was derived both the feed-forward action to produce the virtual element and the equivalent virtual admittance/impedance produced. Here, it is important to explain that time-domain simulations were carried out considering the non-linear time-domain model, presented in Chapter 3, to show the effectiveness of the proposed controls. In this regard, the simulations included harmonic distortion in either the grid voltages or in the load currents, starting at the time $t = 1.5s$, to visualize how the MMC behaves under harmonic distortion conditions and how the presented control approaches enhance its performance in these conditions.

5.2.1 Multi-resonant loops in the NRF-controlled MMC

The effect of the resonant loops used in Section 4.1 is to produce a notch in the magnitude curve of the admittance/impedance at the frequency it is tuned. Consequently, the admittance/impedance drops to an insignificantly small value at this point, and the system becomes close to an ideal current/voltage source and, consequently, immune to any ac-side disturbance related to this frequency. This approach can be improved by using multiple resonant loops such as in Figure 5.8 [120, 121]. This figure presents generic signals F^k, F^{k*} and U^{k*} because it can be applied for any of the control modes. That is, under current control, $F^k = I_c^k$ and $U^{k*} = E_c^{k*}$, and a similar logic can be extended for the other control modes. Notice that in comparison to the controllers used back in Section 4.1, this generic controller $C_c(s)$ comprises resonant loops for fifth- and seventh-order harmonic components in addition to the fundamental component. Thus, the generic controller to be used in the following subsections can be described by:

$$C_c(s) = k_p + \frac{k_{r1}s}{s^2 + \omega_0^2} + \frac{k_{r5}s}{s^2 + (5\omega_0)^2} + \frac{k_{r7}s}{s^2 + (7\omega_0)^2}, \tag{5.1}$$

where k_p, k_{r1}, k_{r5} and k_{r7} are the proportional and resonant gains of the controller. Table 5.3 present the values used for the analyses in the forthcoming subsections.

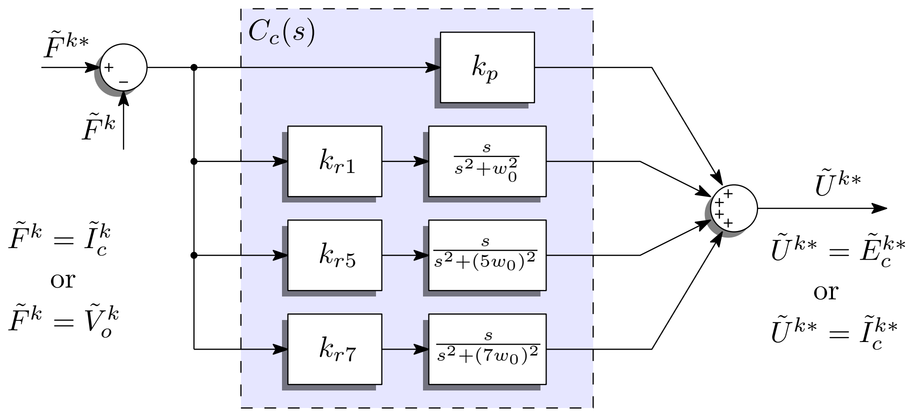

Figure 5.8: Structure of a proportional resonant control system based in multi resonant loops. The resonant loops, in this case, are tuned into the fundamental, fifth- and seventh-order harmonic components frequencies.

Table 5.3: Control settings used in the analysis of the influence of multiple resonant loops on the equivalent admittance/impedance of the MMC: NRF-controlled MMC.

Control Mode	**Loop**	**Proportional gain**	**Fundamental Resonant gain**	**Fifth-order Resonant gain**	**Seventh-order Resonant gain**
Current-Controlled	-	0.0001	0.0100	0.6000	2.0000
Single-Loop Voltage-Controlled	-	0.0001	0.0010	0.0100	0.0400
Double-Loop Current-Voltage-Controlled	Inner current loop	0.0010	0.0100	0.0100	0.0030
	Outter voltage loop	0.1000	1.0000	10.0000	15.0000

MMC under current control

Considering the parameters in Table 5.3, the Norton-equivalent admittance of the current-controlled MMC is reshaped as depicted in Figure 5.9a. Differently from

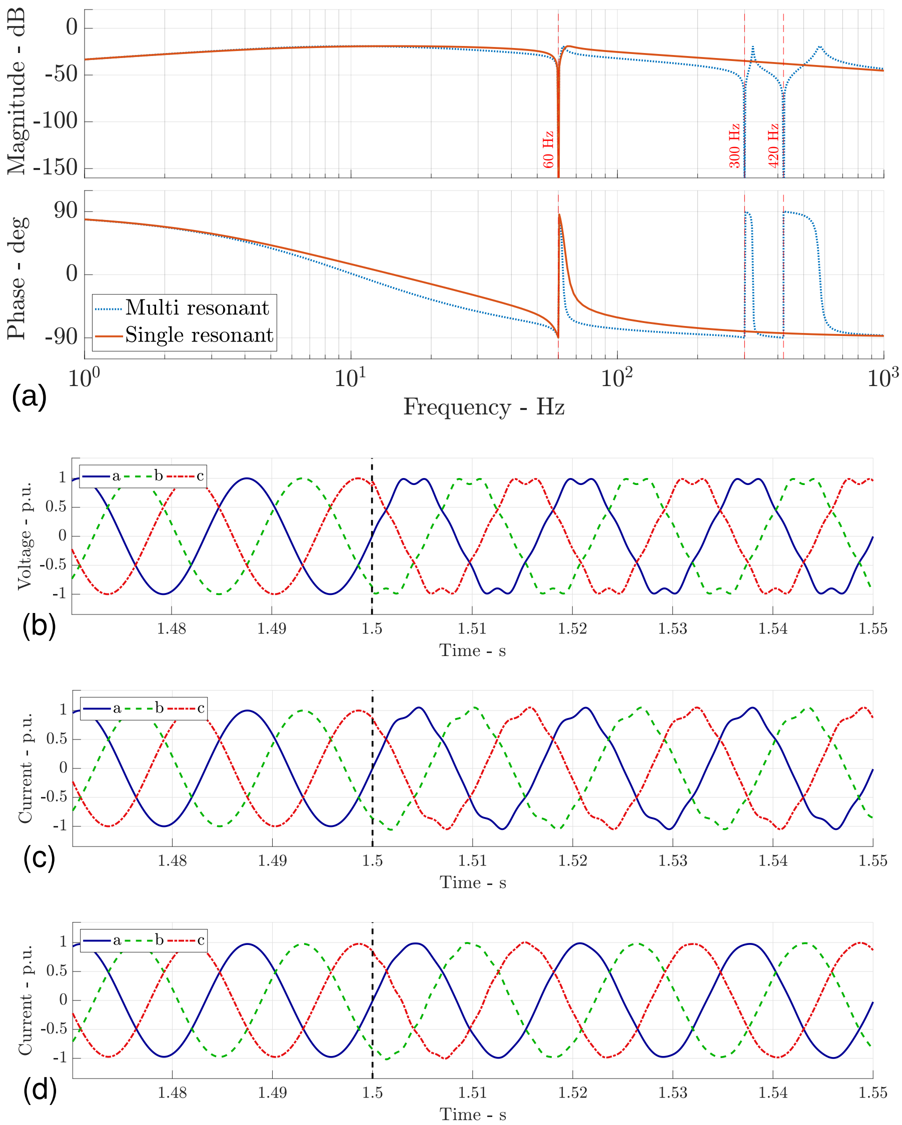

Figure 5.9: Results showing the influence of multiple resonant loops: NRF current-controlled MMC. (a) Frequency response; (b) Grid voltages; (c) Converter currents with single resonant loop; (d) Converter currents with multiple resonant loop.

the case with a single resonant loop, also shown in the figure for comparison purposes, the admittance presents two new notches at 300 and 420Hz. Considering the performance of the MMC, the harmonic distortion at the grid voltages, shown in Figure 5.9b, distorted the produced current when only the fundamental-frequency resonant loop was used. On the other hand, as depicted in Figure 5.9d, the extra resonant loops prevented this to happen.

MMC under single-loop voltage control

Figure 5.10 presents the analysis results for the single-loop voltage-controlled MMC. As in the previous section, it is possible to notice additional notches in the magnitude curve of the Thévenin-equivalent impedance presented in Figure 5.10a. The

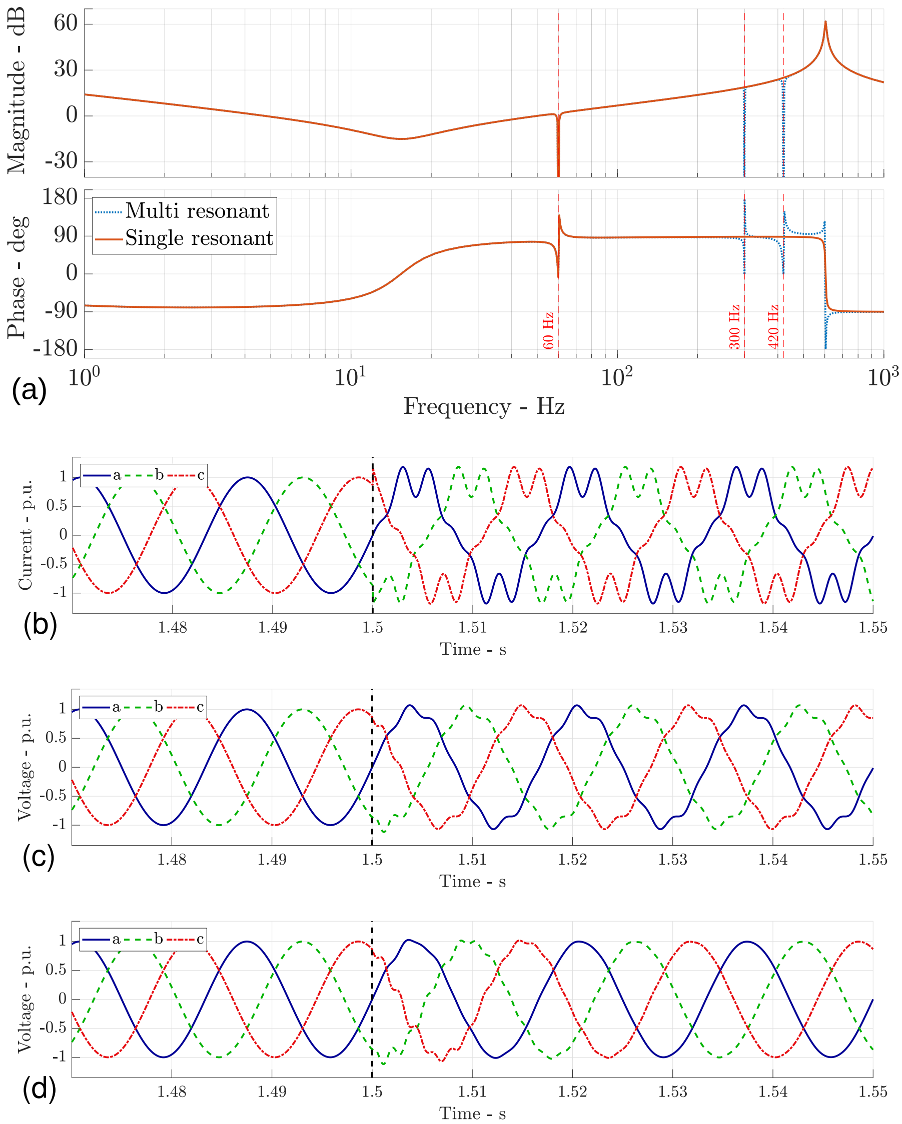

Figure 5.10: Results showing the influence of multi resonant loops: NRF single-loop voltage-controlled MMC. (a) Frequency response; (b) Load currents; (c) Grid voltages with single resonant loop; (d) Grid voltages with multi resonant loop.

time-domain simulation shows that with single-resonant-loop approach, the output voltages in Figure 5.10c become distorted once the load current, Figure 5.10b, does. In the multiple-resonant-loop approach, on the other hand, this issue is not observed as can be seen in voltage waveforms in Figure 5.10d.

MMC under double-loop voltage control

As previously highlighted in Table 5.3, the double-loop voltage control uses the multiple-resonant-loop approach twice: in the inner current and the outer voltage control loops. That being said, Figure 5.11 presents the results of the analysis. Once more, the additional resonant loops created additional notches in the frequencies they were tuned, which is shown in Figure 5.11a. The time-domain simulation

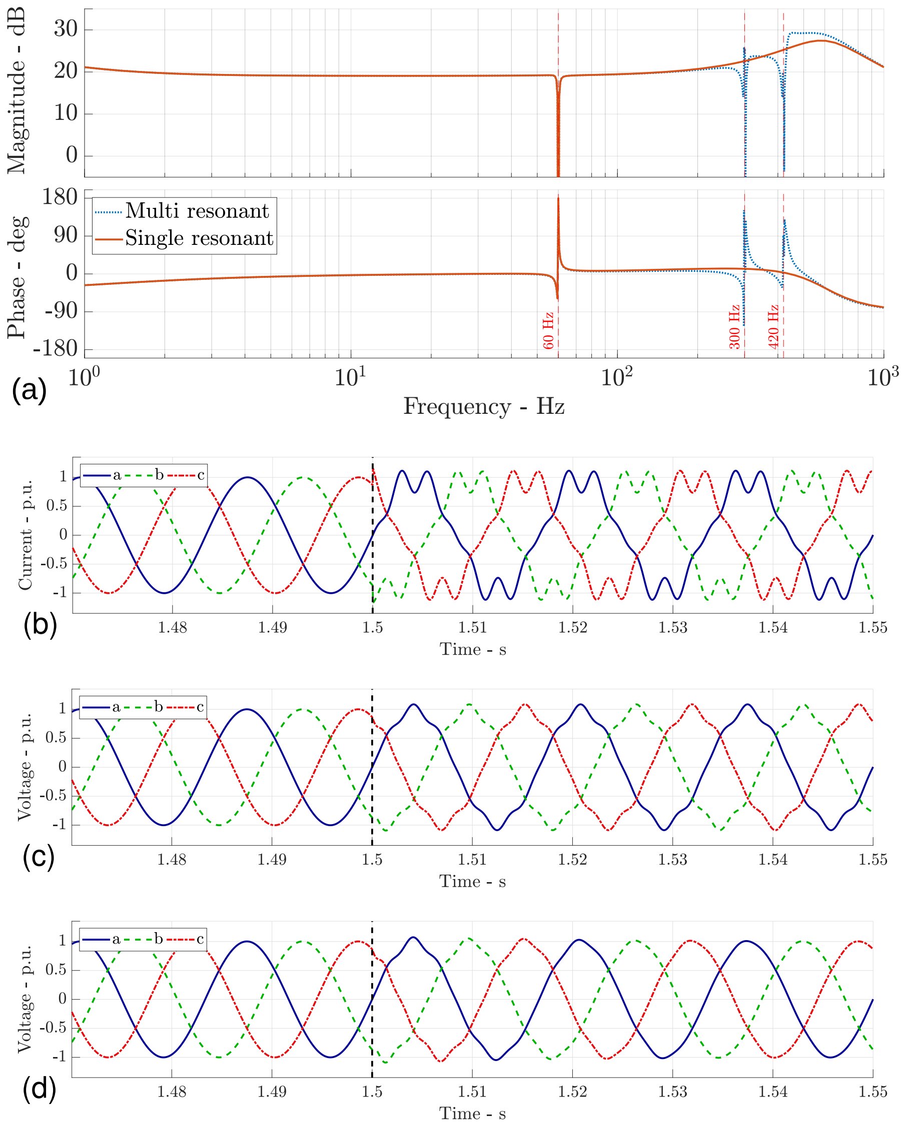

Figure 5.11: Results showing the influence of multi resonant loops: NRF double-loop voltage-controlled MMC. (a) Frequency response; (b) Load currents; (c) Grid voltages with single resonant loop; (d) Converter currents with multi resonant loop.

results in Figures 5.11b - 5.11d proved the effectiveness of the control. Finishing off this section, a summary of the results containing the THD of voltages and currents in all conditions is presented Table 5.4. In this case, it was considered a 20kHz bandwidth for computing the total harmonic distortion.

Table 5.4: Summary of the results for the analysis of the use of multiple resonant loops in NRF-controlled MMC.

Control Mode	THD_v (%)		THD_i (%)	
	Single Resonant	**Multi Resonant**	**Single Resonant**	**Multi Resonant**
Current-Controlled	7.1	7.1	5.3	1.1
Single-Loop Voltage-Controlled	6.3	0.4	25.0	25.0
Double-Loop Current-Voltage-Controlled	8.1	0.4	25.0	25.0

5.2.2 Combining resonant loops with PI controllers in the SRF-controlled MMC

In Section 5.2.1 it was shown that using controllers with multiple resonant loops it is possible to reshape either the equivalent ac-side admittance (MMC under current control) or impedance (MMC under voltage control) so that it presents insignificant values at key frequencies, providing the grid-forming MMC with immunity to distorted currents and the grid-connected with immunity to distortions in the bus

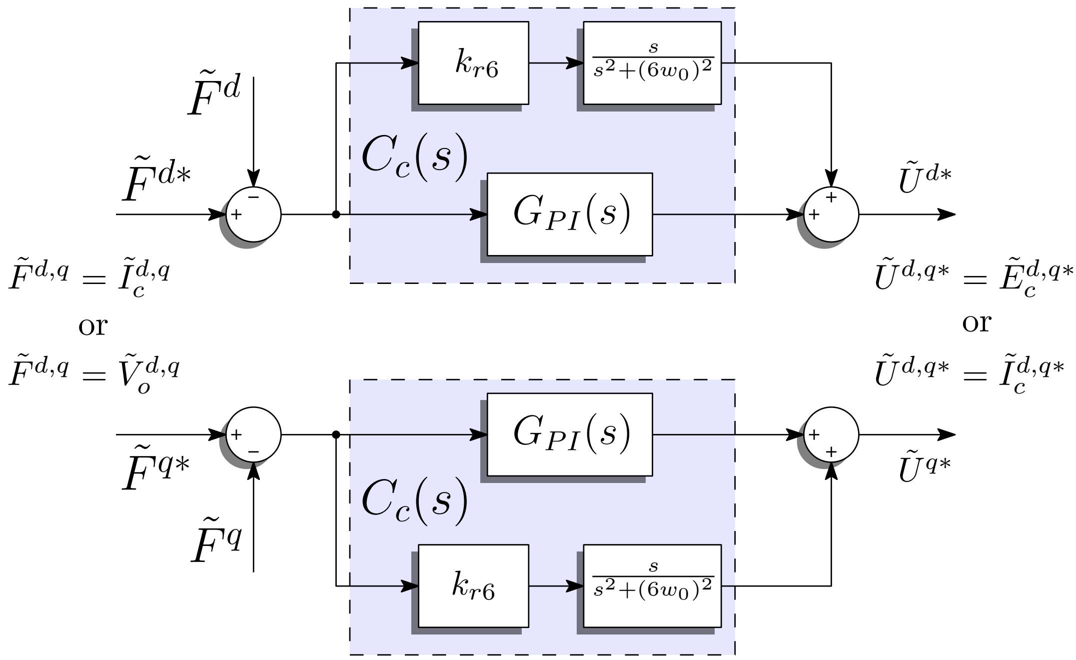

Figure 5.12: Structure of a proportional integral resonant control system for SRF-controlled converter. The resonant loop is tuned in $6\omega_0$ which corresponds to the frequency of both fifth- and seventh-order harmonic components in SRF.

voltage. The same approach can be applied to the SRF-controlled MMC with a few arrangements [122]. It is quite common that the major harmonic components are the negative-sequence fifth-order and positive-sequence seventh-order. In SRF these components are merged at $360Hz$[2]. Consequently, using a resonant loop tuned in $6\omega_0$ in parallel with the PI controller it is possible to enhance the performance of the MMC in the mentioned situations[3]. This approach is generically depicted in Figure 5.12, where F and U can be exchanged by different reference signals depending on the control mode. The analysis carried out considered the control setting in Table 5.5 and are discussed in the following subsections.

Table 5.5: Control settings used in the analysis of the influence of PIR controllers in the equivalent admittance/impedance of the MMC: SRF-controlled MMC.

Control Mode	**Loop**	**Proportional gain**	**Integral gain**	**Resonant gain**
Current-Controlled	-	0.0010	0.1000	0.5000
Single-Loop Voltage-Controlled	-	0.0002	0.0200	0.0100
Double-Loop Voltage-Controlled	Inner current loop	0.0010	0.1000	2.0000
	Outter voltage loop	0.0100	1.0000	15.0000

MMC under current control

The frequency response of the self-related term of the equivalent admittance of the MMC under current control is presented in Figure 5.13a. It is possible to observe that the resonant loop created a notch at the frequency of $360Hz$, as predicted. Following the procedure used in the previous section, a set of time-domain simulation results are presented to show the effectiveness of the resonant loop into cleaning out the harmonic distortion. Once more, the bus voltages were changed at $t = 1.5s$ to present harmonic distortion, as shown in Figure 5.13b. Notice in Figure 5.13c that the voltage distortion distorts the produced currents when only the PI controller is used. On the other hand, the PIR approach guarantee that the converter delivers currents free of harmonic content, as observed in Figure 5.13d.

[2] In unbalanced conditions, it is possible that the system presents positive-sequence fifth-order and negative-sequence seventh-order harmonic components. In SRF this components appear respectively in $240Hz$ and $480Hz$.

[3] The association of proportional integral controllers with resonant controller is called PIR controller.

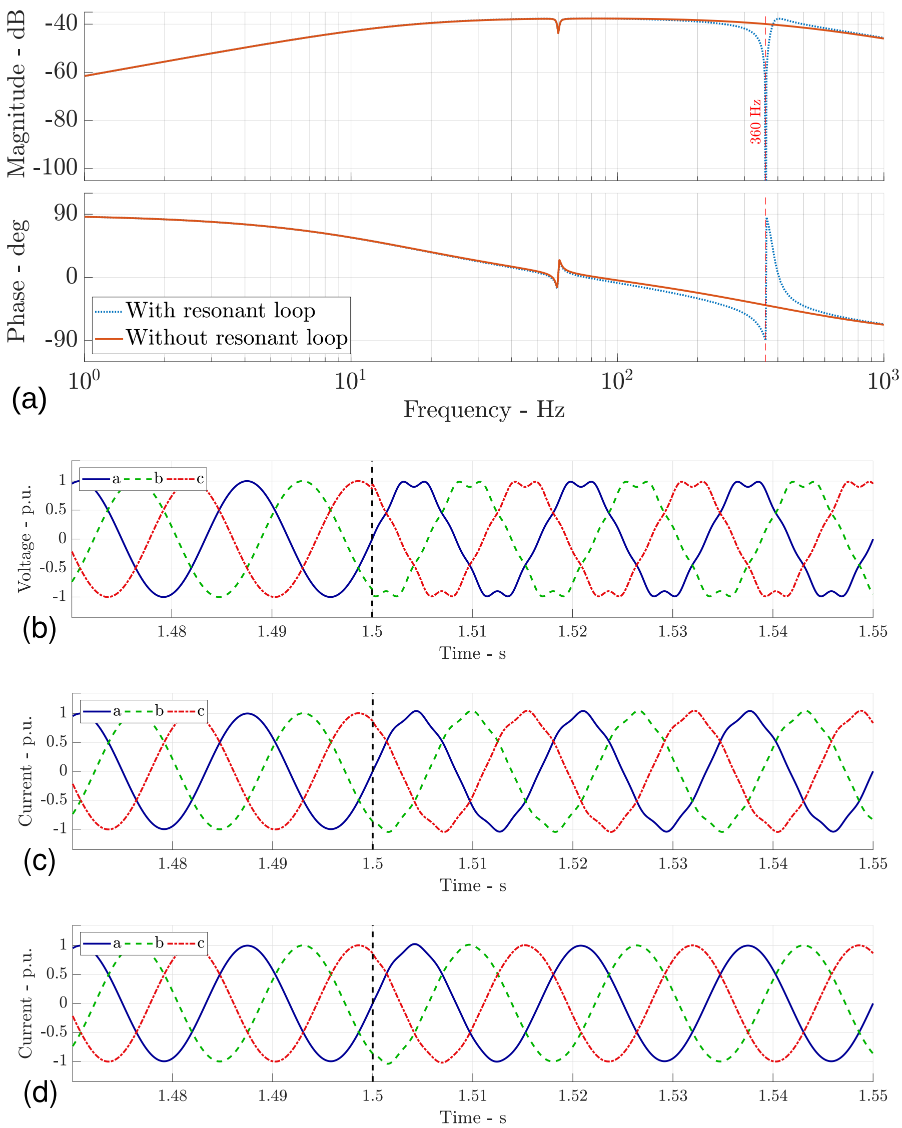

Figure 5.13: Results showing the influence of PIR controller: SRF current-controlled MMC. (a) Frequency response; (b) Grid voltages; (c) Converter currents with PI controller; (d) Converter currents with PIR controller.

MMC under single-loop voltage control

The results comparing the PIR to the PI approaches for the single-loop voltage-controlled MMC are presented in Figure 5.14. Before proceeding with the discussion it is important to point out that the large-order transfer functions obtained required some model reductions for computations reasons. These reductions were carried out using the Octave/Matlab function *minreal* and caused some errors in the highlighted regions of Figures 5.14a and 5.14b[4].

Considering now the effect of the PIR controller, it is noticed both in the self-

[4] To reduce the order of the models, the *minreal* [123, 124] was used to cancel zero-pole pairs within a certain tolerance. It was noticed that depending on the chosen tolerance the curves assumed different shapes withing the highlighted region.

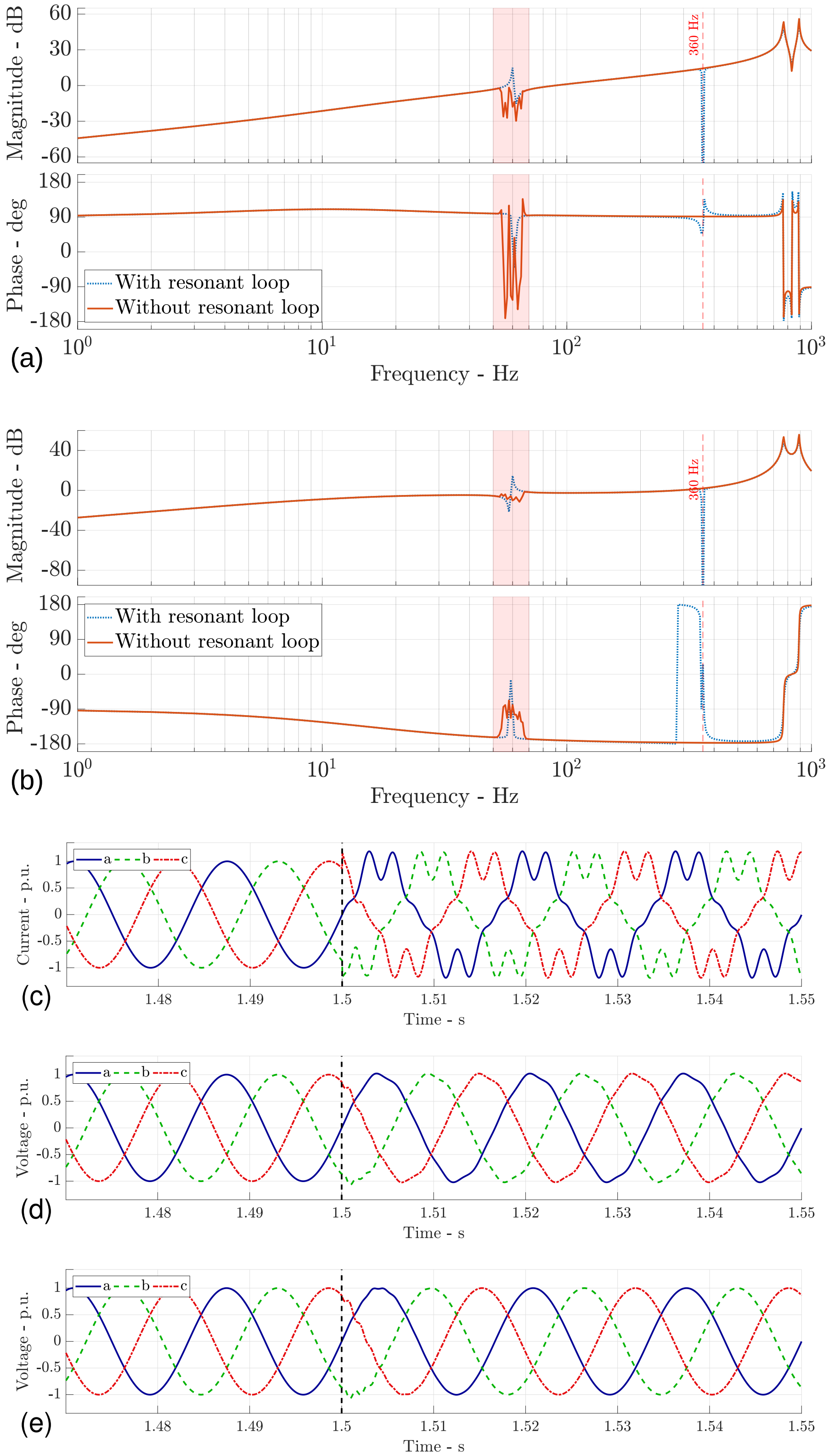

Figure 5.14: Results showing the influence of PIR controller: SRF single-loop voltage-controlled MMC. (a) Frequency response of the self-related term; (b) Frequency response of the cross-axis term; (c) Load currents; (d) Output terminal voltages with PI controller; (d) Output terminal voltages with PIR controller.

related and cross-axis terms the distinguishable mark of the notch in $360Hz$. The time-domain results presented in Figures 5.14c - 5.14e confirm that the output voltages are free from harmonic distortion when the PIR approach is used, even when the converter supplies a non-linear load.

MMC under double-loop voltage control

The results showing the influence of the PIR approach for the double-loop voltage-controlled MMC are presented in Figure 5.15. As in the previous cases, the PIR solution created notches at the self-related and cross-axis terms of the equivalent impedance as shown in Figures 5.15a and 5.15b. The time-domain performance is also aligned to the results obtained for the other control modes. As shown in Figure 5.15e, the voltage distortion caused by the non-linear currents rapidly dye out due to the use of the PIR controller. To finish off the section, Table 5.6 provides the THD values (computed with a 20kHz bandwidth) of voltages and currents analyzed in the subsections.

Table 5.6: Summary of the results for the analysis of the use of resonant loops in SRF-controlled MMC.

Control Mode	THD_v (%)		THD_i (%)	
	Without Resonant	**With Resonant**	**Without Resonant**	**With Resonant**
Current-Controlled	7.1	7.1	3.4	0.5
Single-Loop Voltage-Controlled	2.7	0.4	25.0	25.0
Double-Loop Voltage-Controlled	16.2	0.5	25.0	25.0

5.2.3 Use of virtual elements for enhancing the performance: NRF-controlled MMC

This section presents the virtual-elements (admittance and impedance) approach to enhance the power quality obtained when the MMC is under NRF control. The general idea is to include feed-forward control loops which undermine the effect of harmonic components in the MMC. The following subsections present how these feed-forward control loops relate to virtual admittances and impedances. The control settings considered in this section are in accordance with the values used in the Section 5.2.1 and presented in Table 5.3.

MMC under current control

To explain how the feed-forward control loop is applied to the current-controlled MMC, the block diagram in Figure 4.1d is redrawn to encompass the control loops and presented in Figure 5.16. By this time it is already a common sense that harmonic content in the bus voltage v_o can distort the output current i_c. For this reason, it is desired to eliminate the effect of v_o on the control system, which could hypothetically be achieved by adding the signal $V^k_{o,ap}$ in the position highlighted in Figure 5.16. Notice that, if $V^k_{o,ap} = 4V^k_o$, the influence of the grid voltage is cut off from the control system. Nonetheless, the point in which $V^k_{o,ap}$ is inserted in the diagram corresponds to the model of the MMC and there is no direct access to it. In other words, the sum block in which $V^k_{o,ap}$ does not corresponds to an input of the system. The only input of the MMC model (not considering the control loop) is the signal E^*_c. Thus, the solution to this problem is inserting a feed-forward signal in E^*_c that forces the converter to produce the effect of $V^k_{o,ap}$. In this case, the control law can be rewritten as follows:

$$\tilde{E}^{k*}_c(s) = C_i(s)\left[\tilde{I}^{k*}_c(s) - \tilde{I}^k_c(s)\right] + \Lambda^{abc}_i \tilde{V}^k_o(s), \tag{5.2}$$

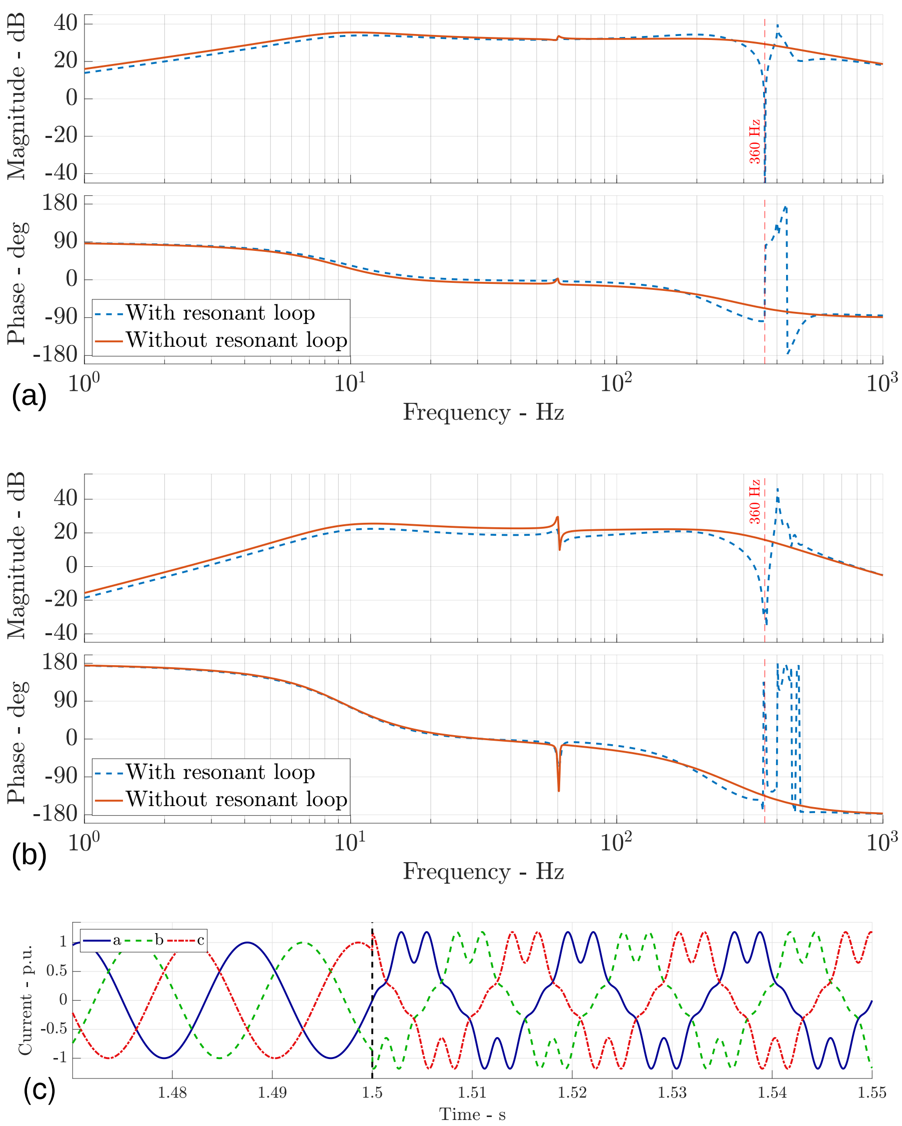

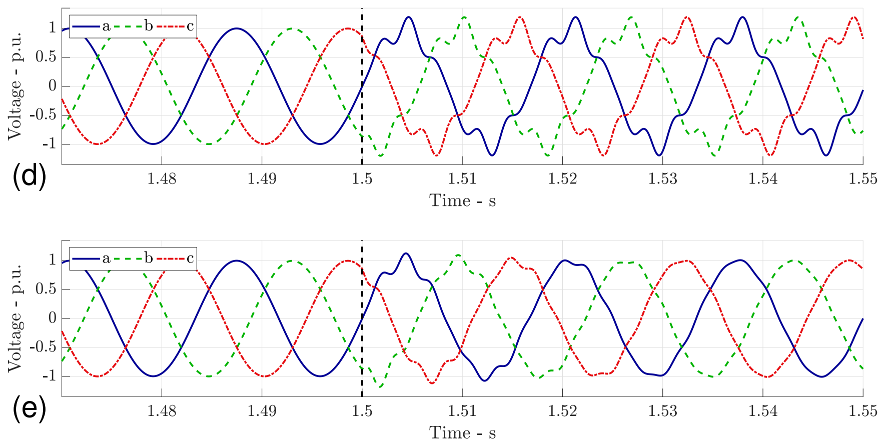

Figure 5.15: Results showing the influence of PIR controller: SRF double-loop voltage-controlled MMC. (a) Frequency response of the self-related term; (b) Frequency response of the cross-axis term; (c) Load currents; (d) Output terminal voltages with PI controller; (e) Output terminal voltages with PIR controller.

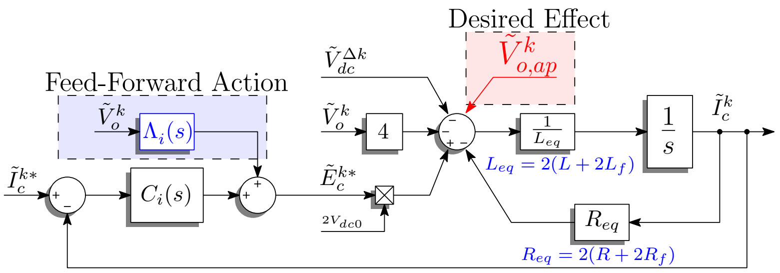

Figure 5.16: Block of the NRF current-controlled MMC with virtual admittance loop. The “desired effect"highlighted in red is not included in the system. It is only represented here for didactic purposes.

$$\Lambda_i^{abc} = \frac{2}{V_{dc0}}. \tag{5.3}$$

Notice that, once the grid voltages are already measured for synchronization purposes, this approach does not require new variables to be measured. Besides that, it is necessary to know the dc voltage V_{dc0}, which is precisely not an issue for most of the applications. Following the same steps presented in Section 4.1.3, it is possible to reach the equivalent model which now encompasses a virtual admittance Y_{vir} in addition to the Norton-equivalent admittance Y_{ac} previously determined:

$$\tilde{I}_c^k(s) = G_i^{cl}(s)I_c^{k*}(s) - Y_{ac}(s)\tilde{V}_o^k(s) - Y_{vir}(s)\tilde{V}_o^k(s), \tag{5.4}$$

$$Y_{vir}(s) = -\frac{G_i^{cl}(s)}{C_i(s)}\Lambda_i^{abc}. \tag{5.5}$$

These results can be traduced in the equivalent circuit in Figure 5.17. Notice that the role of the virtual admittance is to counteract with the Norton-equivalent admittance to reduce the magnitude of the equivalent admittance of the MMC, and this can be observed in the graph of Figure 5.18a. Consequently, the influence of the harmonic

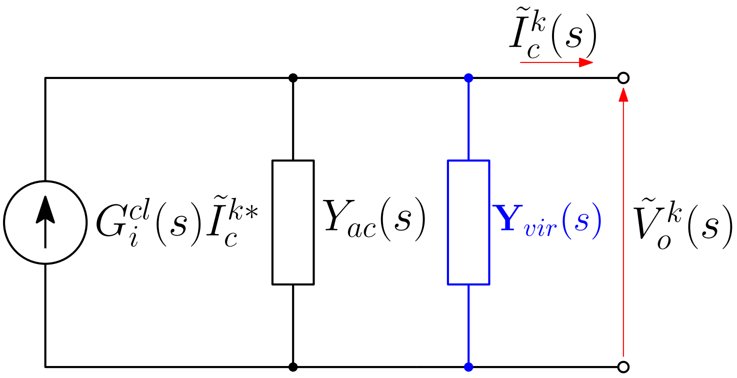

Figure 5.17: Equivalent circuit of the NFR current-controlled with virtual admittance.

content in the grid voltages on the output currents is weakened, as observed in the time-domain graphs of Figure 5.18.

MMC under single-loop voltage control

When under voltage control, the block diagram of Figure 4.1d must be complemented to include the capacitor bank C_f, resulting in the schematic in Figure 5.19. To make the MMC immune to harmonic components, it is necessary to include a feed-forward action in the control law as follows:

$$\tilde{E}_c^{k*}(s) = C_v^{sl}(s)\left[\tilde{V}_o^{k*}(s) - \tilde{V}_o^k(s)\right] + \Lambda_{v,sl}^{abc}(s)\tilde{I}_o^k(s). \tag{5.6}$$

In this case, $\Lambda_{v,sl}^{abc}$ should be chosen so as the feed-forward action produces the effect of a current $i_{o,ap}$ counteracting the load current i_o. It is important to notice that, differently from the previous case, here it is necessary to measure new variables, the load currents i_o^k.

The value of $\Lambda_{v,sl}^{abc}$ can be obtained by moving the signal $i_{o,ap}^k$ towards E_c^{k*} in the block diagram of Figure 5.19, yet it is not presented in this section. For more information, a detailed step-by-step walk-through of this procedure is presented in the Appendix D. The result is given by:

$$\Lambda_{v,sl}^{abc}(s) = \frac{1}{2V_{dc0}}\left[(R + 2R_f) + (L + 2L_f)\frac{\omega_c s}{s + \omega_c}\right]. \tag{5.7}$$

Observe that a low pass filter with cut-off frequency ω_c is associated with the derivative term $(L + 2L_f)s$ to prevent prohibitive control-signal values when the load undergoes fast changes. This filter can undermine the effectiveness of the feed-forward action and, because of that, its cut-off frequency must be carefully chosen. It is also worthwhile noticing that a good response of this feed-forward action relies on the accuracy in which resistances and inductances of the MMC are known.

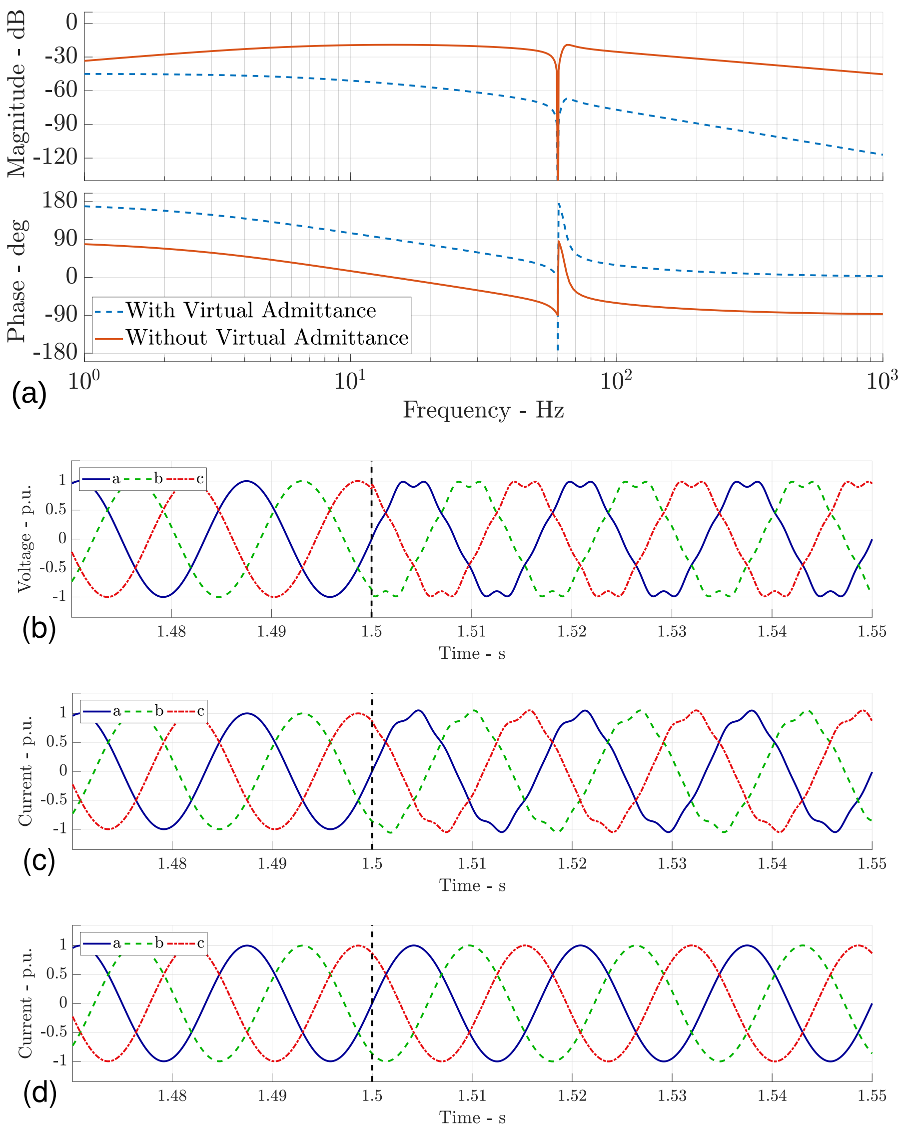

Figure 5.18: Results showing the influence of virtual admittance: NRF current-controlled MMC. (a) Frequency response of the equivalent admittance with and without the virtual term; (b) Grid voltages; (c) output currents without virtual admittance, and (d) output currents with virtual admittance.

The novel equivalent model of the system can be achieved by following the same steps presented in Section 4.1.4. In contrast to the model developed in Chapter 4.1,

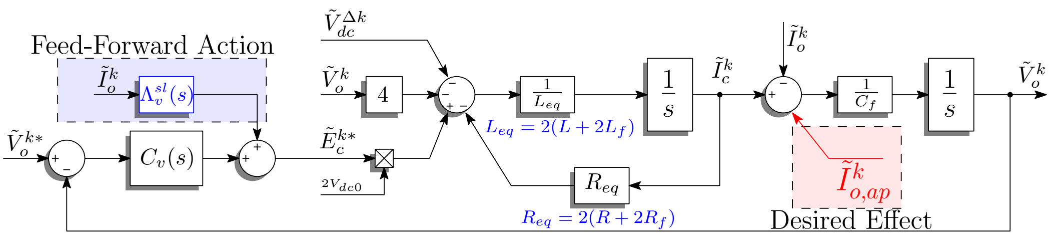

Figure 5.19: Block of the NRF single-loop voltage-controlled MMC with virtual impedance loop. The "desired effect"highlighted in red is not included in the system. It is only represented here for didactic purposes.

now the MMC displays a virtual impedance Z_{vir}^{sl} crafted by the feed-forward action, as shown in Figure 5.20, and its analytical representation is given by:

$$\tilde{V}_o^k(s) = G_{th}^{sl}(s)\tilde{V}_0^{k*}(s) - Z_{th}^{sl}(s)\tilde{I}_o^k(s) - Z_{vir}^{sl}(s)\tilde{I}_o^k(s), \tag{5.8}$$

$$Z_{vir}^{sl}(s) = -\frac{G_{th}^{sl}(s)}{C_v^{sl}(s)}\Lambda_{v,sl}^{abc}(s). \tag{5.9}$$

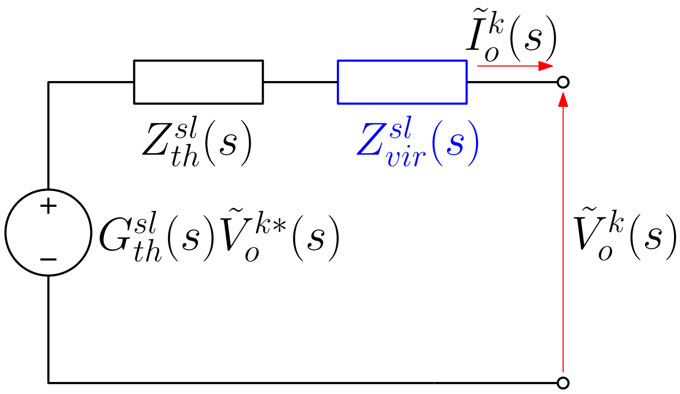

Figure 5.20: Equivalent circuit of the NFR single-loop voltage-controlled MMC with virtual admittance.

The frequency response of the equivalent impedance is illustrated in Figure 5.21 considering a case without virtual impedance and three cases with virtual impedances implemented with different cut-off frequencies. In general, the effect of the feed-forward was degraded by the low pass filter. The best result was achieved with cut-off frequency at $1kHz$, where the equivalent impedance was reduced from $18.5dB$ $(0.18p.u.)$ to $12.8dB$ $(0.09p.u.)$ at $300Hz$. Nonetheless, it stands out that the virtual impedance was not able to cope with the resonant peak at $604.3Hz$. The time-domain simulation in Figures 5.21b-5.21f shows a small difference in the THD of the output voltages from 6.3% to 4.1% in the best scenario.

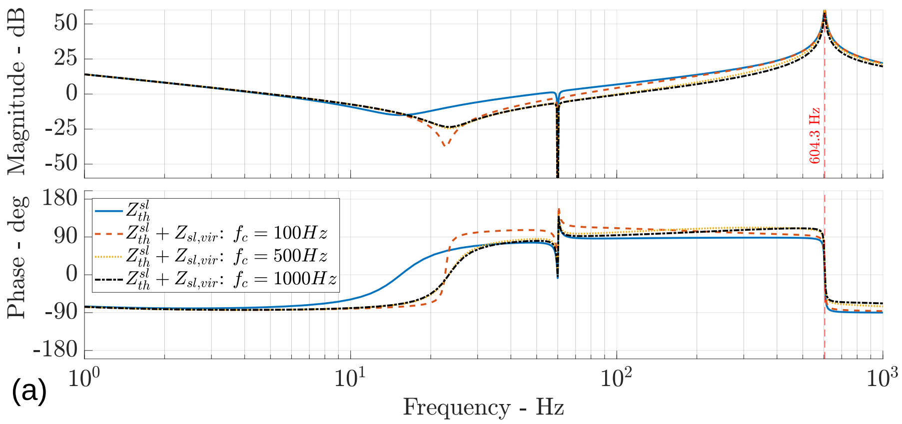

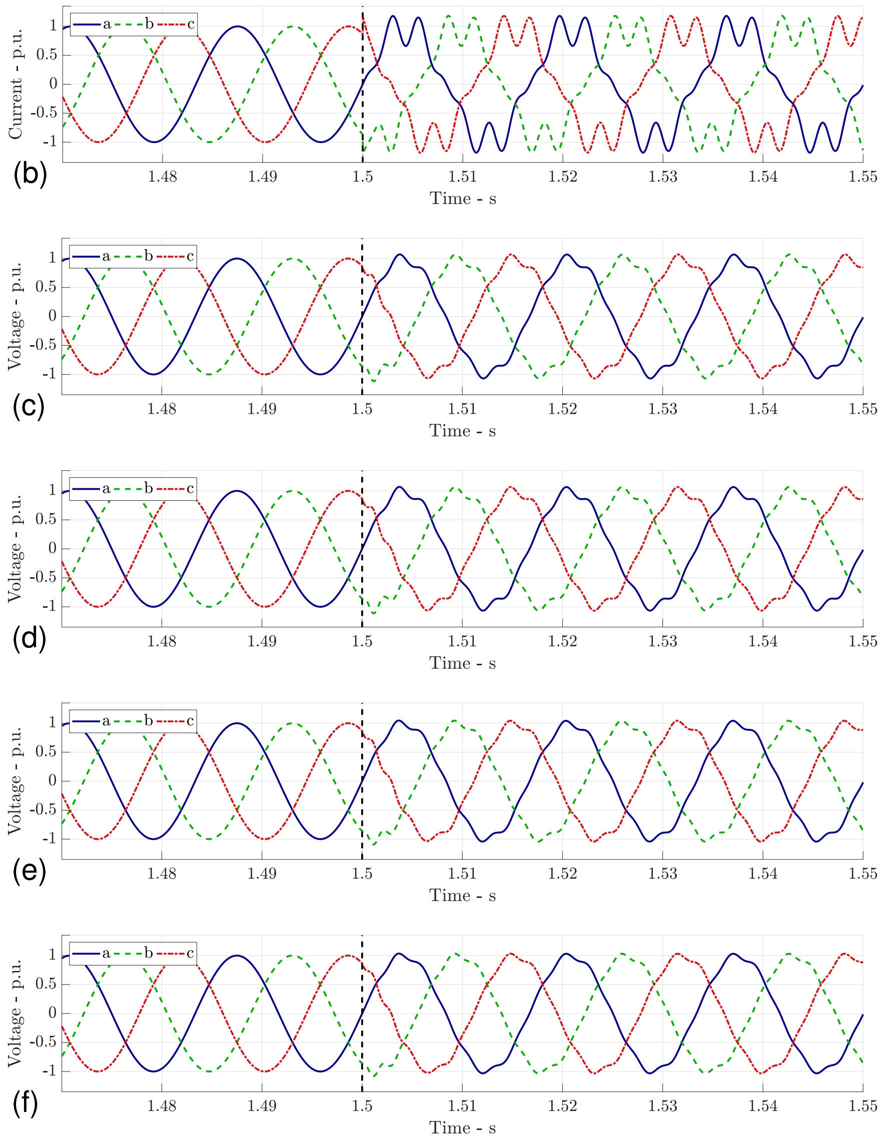

Figure 5.21: Results showing the influence of virtual admittance: NRF single-loop voltage-controlled MMC. (a) Frequency response of the equivalent impedance with and without the virtual term; (b) Load currents; (c) output voltages without virtual admittance, and output voltages with (d) $100Hz$-bandwidth, (e) $500Hz$-bandwidth and (f) $1000Hz$-bandwidth virtual impedance.

MMC under double-loop voltage control

The Figure 5.22 presents the block diagram of the MMC under double-loop current-voltage control. As in the previous case, the highlighted “desired effect" in the diagram blocks out the influence of the load currents in the produced voltage. With this in mind, it is possible to rewrite the control law of the inner current loop as follows:

$$\tilde{E}_c^{k*}(s) = C_i(s)\left[\tilde{I}_c^{k*}(s) - \tilde{I}_c^{k}(s)\right] + \Lambda_{v,dl}^{abc}(s)\tilde{I}_o^{k}(s). \tag{5.10}$$

The coefficient $\Lambda_{v,dl}^{abc}$ in (5.10) can be obtained manipulating the block diagram of the system and, once again, the step-by-step walk-through is presented in the

Appendix D. The result is given by:

$$\Lambda_{v,dl}^{abc}(s) = \frac{1}{2V_{dc0}}\left[(R+2R_f)+(L+2L_f)\frac{\omega_c s}{s+\omega_c}\right]+C_i(s) \approx \frac{1}{2V_{dc0}}\left[(R+2R_f)+(L+2L_f)\frac{\omega_c s}{s+\omega_c}\right]+k_p^{i,dl}. \quad (5.11)$$

Notice that instead of using the current controller with its two parcels, it was decided to consider only the proportional part of it. The resonant part, though, was kept out because it is a second-order integrator tuned at the frequency of fundamental component, which means that it continuously amplifies the $60Hz$ signals the pass through it, causing stability issues. This decision brings no harm to the effectiveness of the feed-forward action once the values of the resonant part of C_i are overwhelmingly small in frequencies other than the fundamental. Besides that, and probably more important, the difference between the proportional and resonant gains at key frequencies is considerably huge (e.g. $-60dB$ to $-105dB$ for $300Hz$).

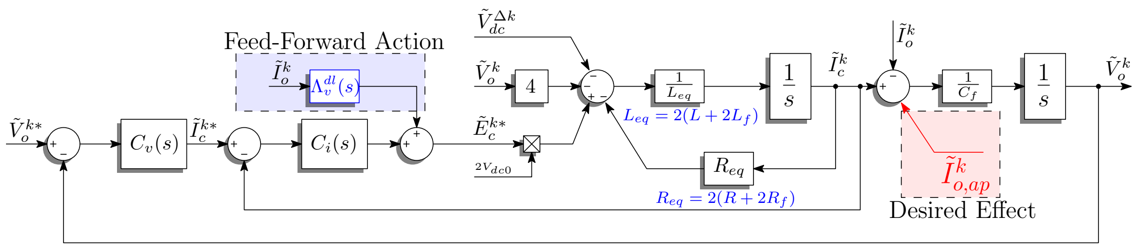

Figure 5.22: Block of the NRF double-loop voltage-controlled MMC with virtual impedance loop. The "desired effect"highlighted in red is not included in the system. It is only represented here for didactic purposes.

Following the procedure presented in Section 4.1.5 it is possible to find the following Thévenin-equivalent model for the MMC:

$$\tilde{V}_o^k = G_{th}^{dl}(s)\tilde{V}_o^{k*}(s) - Z_{th}^{dl}(s)\tilde{I}_o^k(s) - Z_{vir}^{dl}(s)\tilde{I}_o^k(s), \quad (5.12)$$

$$Z_{vir}^{dl}(s) = -Z_{th}^{dl}(s)\Lambda_{v,dl}^{abc}(s)\frac{G_i^{cl}(s)}{C_i(s)}, \quad (5.13)$$

where $\Lambda_{v,dl}^{abc}$ in the virtual impedance produced by the feed-forward action.

Figure 5.23 presents the analysis results for the MMC under double-loop voltage control with virtual admittance. In comparison to the previous section, it is noticeably a significant difference among the magnitude curves with and without virtual impedance as shown in Figure 5.23a. The best case was achieved with the cut-off frequency of $1kHz$, where the difference at $300Hz$ reached $22.5dB$ $(0.28p.u.)$ to $12.7dB$ $(0.09p.u.)$. This result is confirmed by comparing the produced voltages displayed in Figures 5.23c and 5.23f. Without the virtual impedance, the output

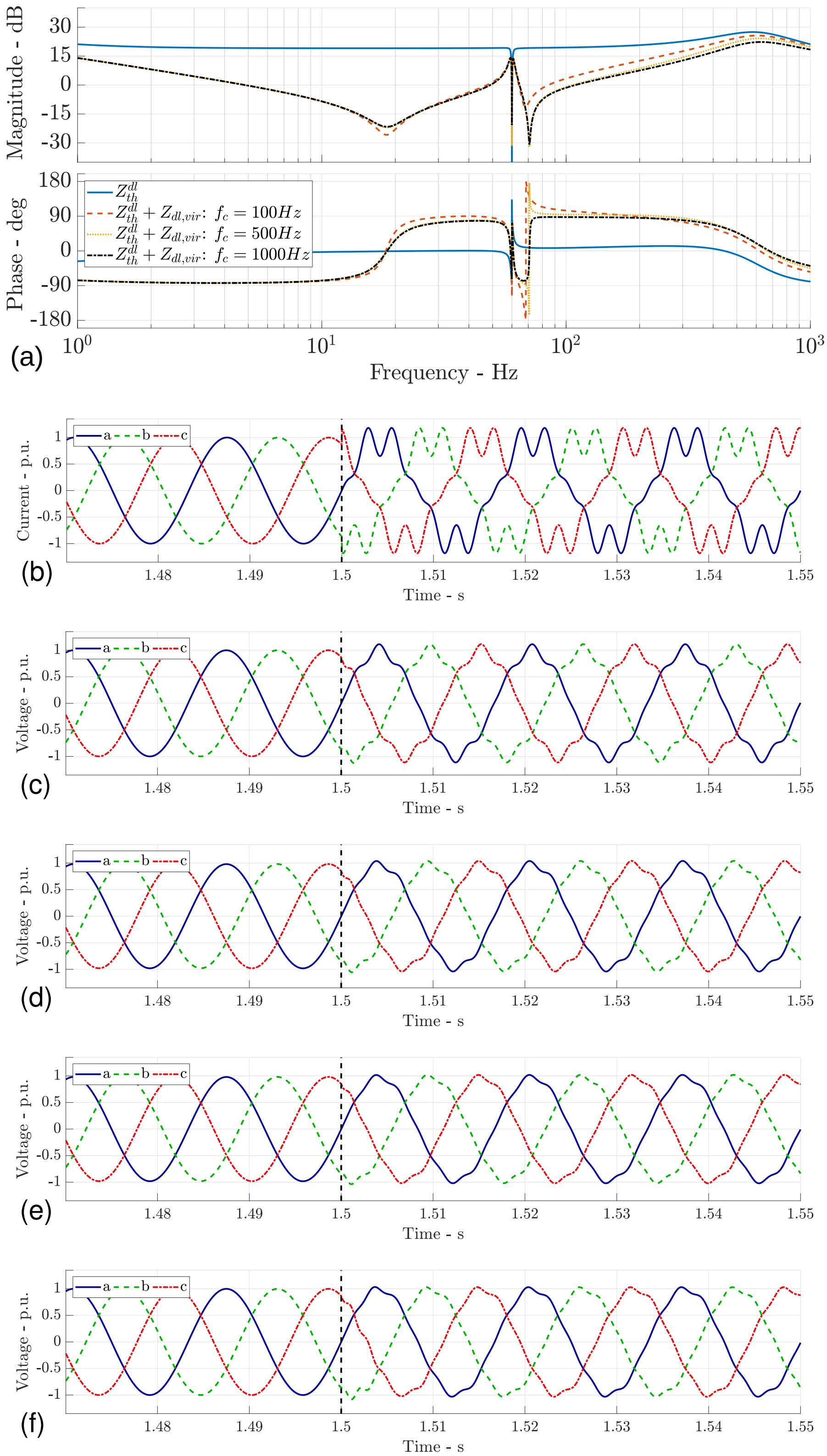

Figure 5.23: Results showing the influence of virtual admittance: NRF double-loop voltage-controlled MMC. (a)Frequency response of the equivalent impedance with and without the virtual term; (b) Load currents; (c) output voltage without virtual admittance, and output voltage with (d) $100Hz$-bandwidth, (e) $500Hz$-bandwidth and (f) $1000Hz$-bandwidth virtual impedance.

voltages presented a THD of 8.1%, whereas using the virtual impedance, this THD marked 3.2% in the best case and 3.9% and 5.2% in the other two cases. A summary present the THD (computed with a 20kHz bandwidth) of voltages and currents in each subsection is presented in Table 5.7.

Table 5.7: Summary of the results for the analysis of the use of virtual elements in NRF-controlled MMC. VirA stands for virtual admittance and VirI for virtual impedance.

Control Mode	**-**	THD_v **(%)**	THD_i **(%)**
Current-Controlled	Without VirA	7.2	5.3
	With VirA	7.2	0.9
Single-Loop Voltage-Controlled	Without VirI	6.4	24.1
	With VirI ($fc = 100Hz$)	6.4	24.9
	With VirI ($fc = 500Hz$)	5.1	26.0
	With VirI ($fc = 1000Hz$)	4.2	25.7
Double-Loop Current-Voltage-Controlled	Without VirI	8.1	25.0
	With VirI ($fc = 100Hz$)	5.2	25.0
	With VirI ($fc = 500Hz$)	3.9	25.0
	With VirI ($fc = 1000Hz$)	3.2	25.0

5.2.4 Use of virtual elements for enhancing the performance: SRF-controlled MMC

As in the previous, this section presents control strategies for blocking out the effects of the disturbances (either main-bus voltage or load current) in the performance of the system. Nonetheless, this time the control systems are implemented in SRF considering the modeling approach of Chapter 4.2. The following subsection deals with each of the control modes already presented.

MMC under current control

The block diagram presented in Figure 5.24 represents the MMC under current control with a feed-forward action to block out the influence of harmonic distortion in the grid voltages on the output currents. As in the previous section, the "desired effect" inputs in the diagram are only displayed to show what is the outcome of the feed-forward action. The current-control law in (4.53) can be expanded as follows to encompass this new parcel:

$$\tilde{\mathbf{E}}_c^{dq0*} = \mathbf{C}_i^{dq0}(s)\left[\tilde{\mathbf{I}}_c^{dq0*}(s) - \tilde{\mathbf{I}}_c^{dq0}(s)\right] + \mathbf{D}_i^{dq}\tilde{\mathbf{I}}_c^{dq0}(s) + \mathbf{\Lambda}_i^{dqo}(s)\tilde{\mathbf{V}}_o^{dq0}(s), \tag{5.14}$$

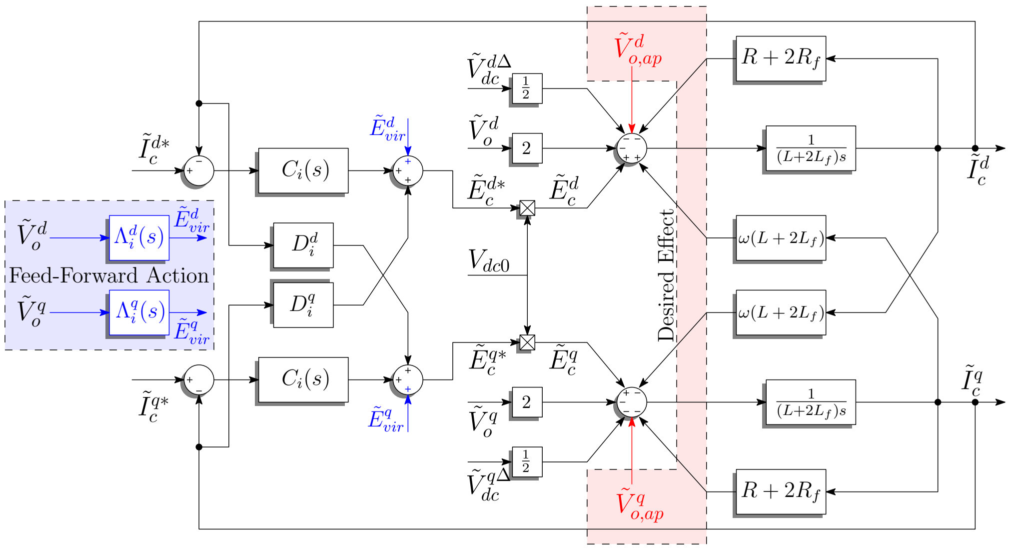

Figure 5.24: Block diagram of the SRF-current-controlled MMC with anti-disturbance feed-forward action. The blue loop comprehending $\boldsymbol{\Lambda}_i^{dqo}$ components middle left part of the diagram is the feed-forward action. The red signals $\tilde{V}_{o,ap}^{d,q}$ correspond to the effect caused by the feed-forward action.

$$\boldsymbol{\Lambda}_i^{dqo}(s) = \frac{2}{V_{dc0}} \begin{bmatrix} 1 & 0 & 0 \\ 0 & 1 & 0 \\ 0 & 0 & 0 \end{bmatrix}.$$

Following the same steps presented in Section 4.2.3, it is possible to reach the following analytical model of the MMC:

$$\tilde{\mathbf{I}}_c^{dq0}(s) = \mathbf{G}_{icl}^{dq0}(s)\tilde{\mathbf{I}}_c^{dq0*}(s) - \mathbf{Y}_{ac}^{dq0}(s)\tilde{\mathbf{V}}_o^{dq0}(s) - \mathbf{Y}_{vir}(s)\tilde{\mathbf{V}}_o^{dq0}(s), \tag{5.15}$$

$$\mathbf{Y}_{vir}(s) = -\boldsymbol{\Gamma}_i^{-1}(s)\left[4V_{dc0}C_{eq}\mathbf{s}_{dq} + \frac{3S_0}{2V_{dc0}}\mathbf{I}\right]\boldsymbol{\Lambda}_i^{dqo}(s), \tag{5.16}$$

where $\mathbf{Y}_{vir}$ is the virtual matrix admittance produced by the feed-forward action. This model can be represented by the equivalent circuit displayed in Figure 5.25.

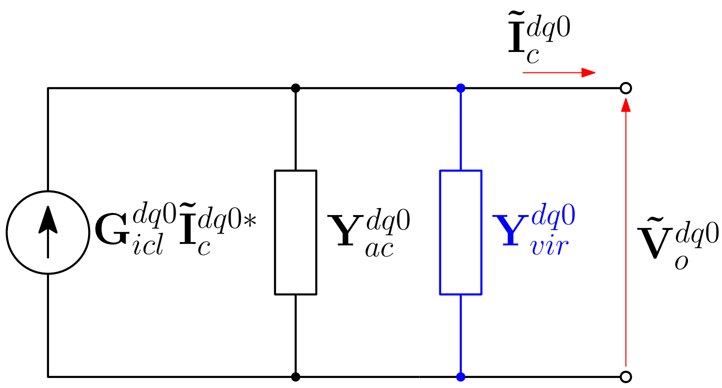

Figure 5.25: Equivalent circuit of the SFR current-controlled with virtual admittance.

The effectiveness of the feed-forward action is proved by the results presented in Figure 5.26. For instance, Figure 5.26a shows that the virtual admittance significantly pulled down the magnitude curve of the equivalent admittance. It can also be observed in the time-domain results in which the current THD was improved from 3.5% to 0.5%.

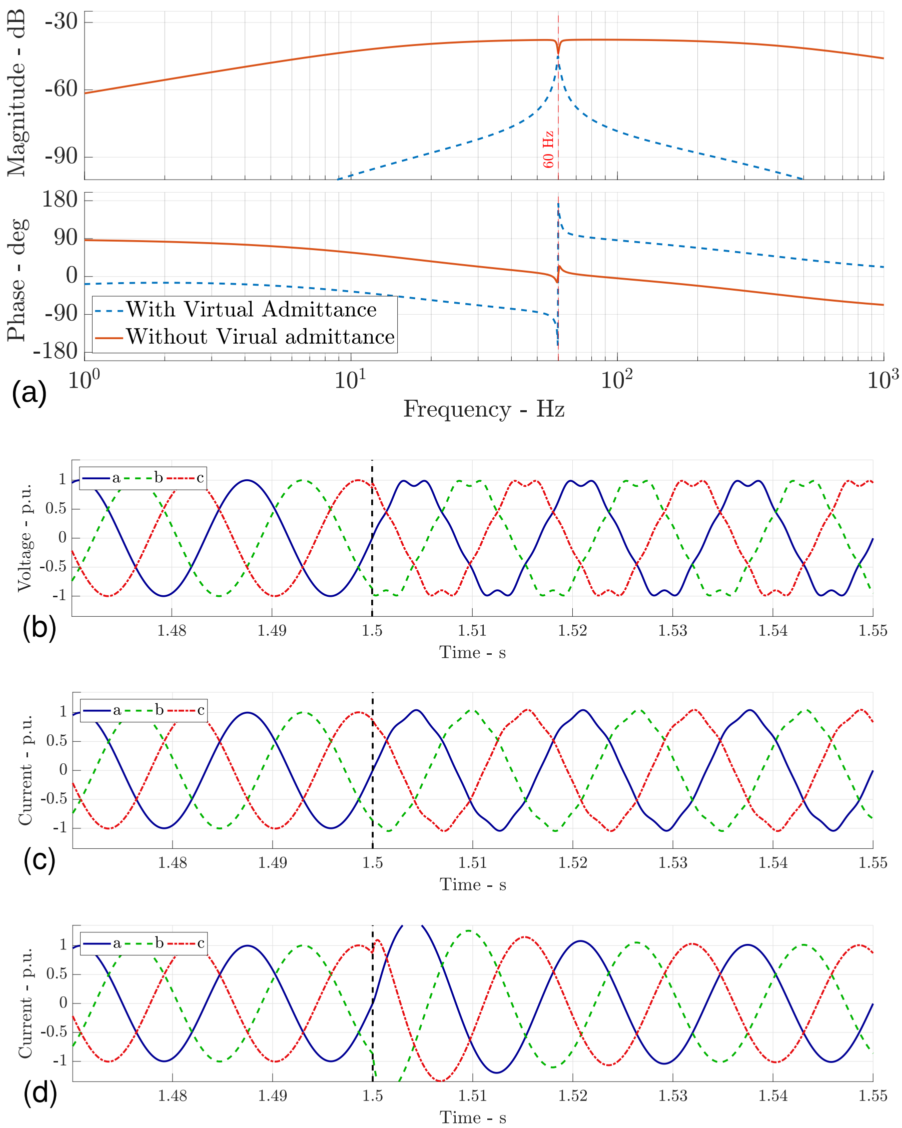

Figure 5.26: Results showing the influence of virtual admittance: SRF current-controlled MMC. (a) Frequency response of the self-related term; (b) Grid voltages; MMC currents (d) without virtual admittance, and (e) with virtual admittance.

MMC under single-loop voltage control

Figure 5.27 presents the block diagram of the single-loop voltage-controlled MMC with feed-forward action. As with the case of NRF-controlled MMC, here it necessary to include new measurements in the control system, i.e., the load currents and change the control law to:

$$\tilde{\mathbf{E}}_c^{dq0*} = \mathbf{C}_{v,sl}^{dq0}(s)\left[\tilde{\mathbf{V}}_o^{dq0*}(s) - \tilde{\mathbf{V}}_o^{dq0}(s)\right] + \mathbf{\Lambda}_{v,sl}^{dqo}(s)\tilde{\mathbf{I}}_o^{dq0}(s). \tag{5.17}$$

The term $\mathbf{\Lambda}_{v,sl}^{dqo}(s)$ in (5.21) represents the transfer matrix of the feed-forward action, which is obtained after systematic manipulation of the block diagram in Figure 5.27. These details are better illustrated in the Figure D.4 of the Appendix D and its result is given by:

$$\mathbf{\Lambda}_{v,sl}^{dqo}(s) = \frac{1}{V_{dc0}}\left[(R+2R_f)\,\mathbf{I} + (L+2L_f)\left(\frac{s\omega_c}{s+\omega_c}\mathbf{I} + \mathbf{\Omega}\right)\right]. \tag{5.18}$$

Once more, a low-pass filter with cut-off frequency ω_c is used to prevent that either suddenly changes in the load or measurement noises sparkle unstable behavior on the system.

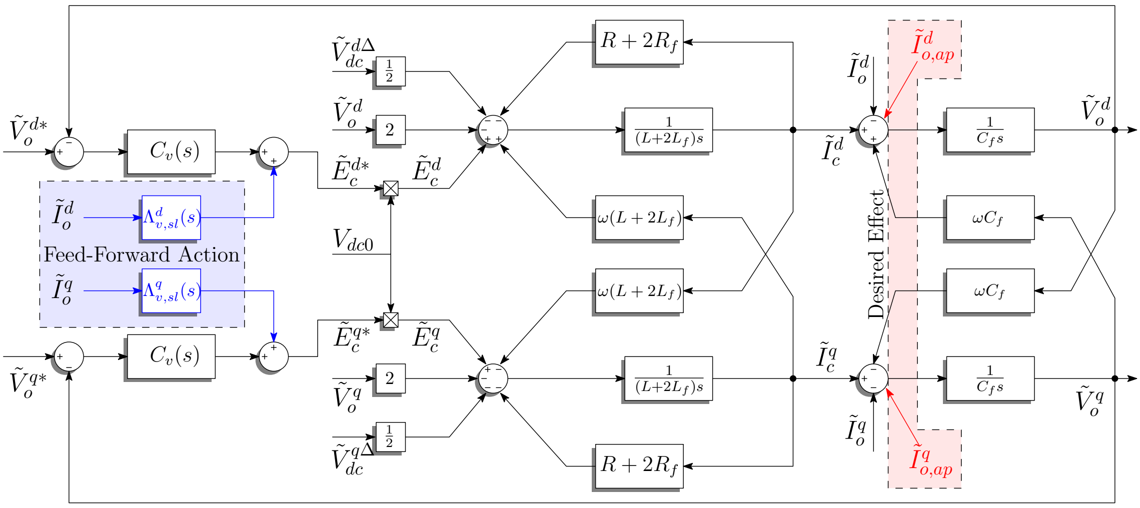

Figure 5.27: Block diagram of the SRF single-loop voltage-controlled MMC with anti-disturbance feed-forward action. The blue loop comprehending $\mathbf{\Lambda}_{v,sl}^{dqo}$ components middle left part of the diagram is the feed-forward action. The red signals $\tilde{I}_{o,ap}^{d,q}$ correspond to the effect caused by the feed-forward action.

Following the methodology described in Section 4.2.4, it is possible to reach the analytical model for the MMC, this time accounting the virtual impedance $\mathbf{Z}_{vir}^{sl,dqo}$:

$$\tilde{\mathbf{V}}_o^{dq0}(s) = \mathbf{G}_{sl,th}^{dq0}(s)\tilde{\mathbf{V}}_o^{dq0*}(s) - \mathbf{Z}_{sl,th}^{dq0}(s)\tilde{\mathbf{I}}_o^{dq0}(s) - \mathbf{Z}_{vir}^{sl,dqo}(s)\tilde{\mathbf{I}}_o^{dq0}(s), \tag{5.19}$$

$$\mathbf{Z}_{vir}^{sl,dqo} = -{\mathbf{\Gamma}_{v,out}^{sl}}^{-1}\mathbf{Z}_{in}^{sl}\left(4V_{dc0}C_{eq}\mathbf{s}_{dq} + \frac{2S_0}{3V_{dc0}}\mathbf{I}\right)\mathbf{\Lambda}_{v,sl}^{dqo}(s). \tag{5.20}$$

The model given in (5.19) can be traduced into the circuit in Figure 5.28.

As in any of the cases involving virtual elements, $\mathbf{Z}_{vir}^{sl,dqo}$, when associated with the $\mathbf{G}_{sl,th}^{dq0}$, reduces the magnitude of the equivalent impedance, as can be seen in

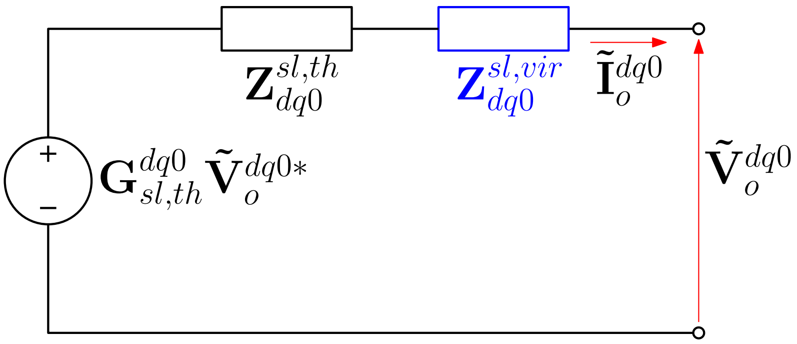

Figure 5.28: Equivalent circuit of the SFR single-loop voltage-controlled MMC with virtual impedance.

Figures 5.29a and 5.29b. It is also noticeable that the higher is the bandwidth of the filter, the smaller in the magnitude of the equivalent impedance, yet the resonant peaks around $850Hz$ are not affected by the feed-forward action. It is important to mention that some numerical errors were observed in the frequency range highlighted in red in Figures 5.29a and 5.29b, the same issues pointed out in Section 5.2.2. As for the time-domain results, the produced voltages presented THD of 11.5% without virtual impedance, case of the graph in Figure 5.29d, and 3.5% in the best virtual-impedance scenario, Figure 5.29g.

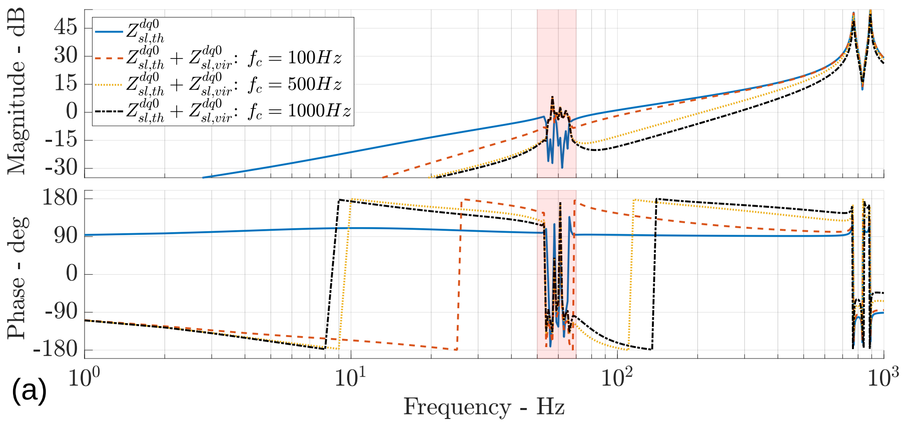

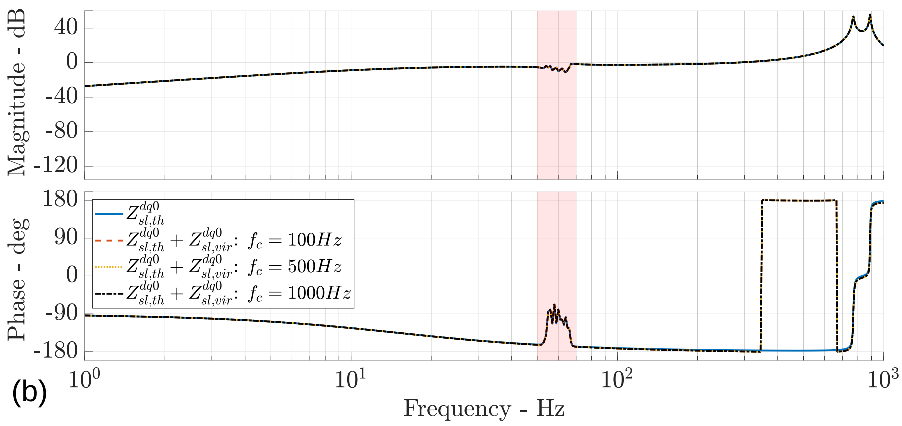

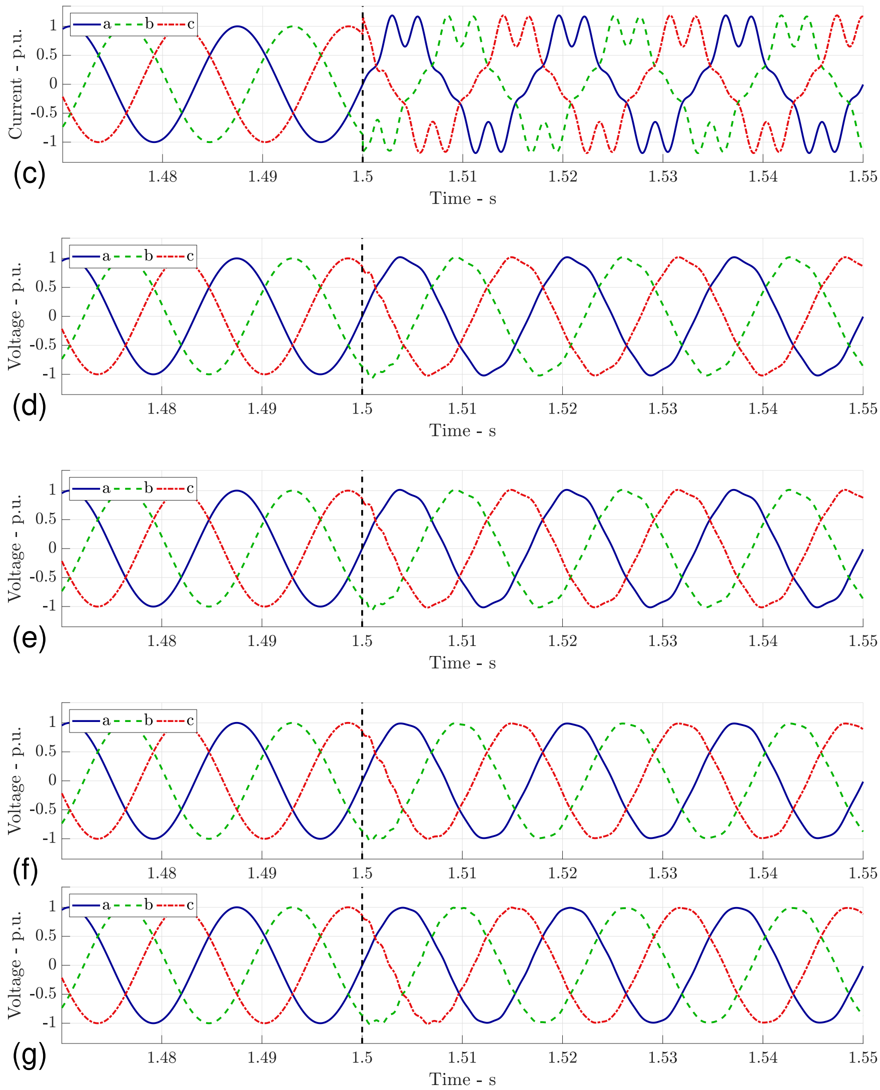

Figure 5.29: Results showing the influence of virtual admittance: SRF single-loop voltage-controlled MMC. Frequency response of the (a) self-related and (b) cross-axis terms; (c) Load currents; (d) produced voltage without virtual admittance, and produced voltage with (e) 100Hz-bandwidth, (f) 500Hz-bandwidth and (g) 1000Hz-bandwidth virtual impedance.

MMC under double-loop voltage control

The approach to derive the feed-forward term for the double-loop voltage-controlled MMC is along the lines of the strategy used for the other control modes. Thus, firstly it is necessary do represent the block diagram of the closed-loop system, which is done in Figure 5.30, then it is necessary to realize which additional term in the control law is necessary to produce the desired effect of blocking out the influence of the load current in the delivered voltage. In views of that, the inner-loop control law and feed-forward transfer matrix can be written as follows:

$$\tilde{\mathbf{E}}_c^{dq0*} = \mathbf{C}_i^{dq0}(s)\left[\tilde{\mathbf{I}}_c^{dq0*}(s) - \tilde{\mathbf{I}}_c^{dq0}(s)\right] + \mathbf{D}_i^{dq}\tilde{\mathbf{I}}_c^{dq0}(s) + \mathbf{\Lambda}_{v,dl}^{dqo}(s)\tilde{\mathbf{I}}_o^{dq0}(s), \tag{5.21}$$

$$\mathbf{\Lambda}_{v,dl}^{dqo} = \frac{1}{V_{dc0}} \left[\frac{\omega_c s}{s+\omega_c} (L+2L_f) + (R+2R_f) \right] \mathbf{I} + \mathbf{C}_i^{dq0}(s) - \mathbf{D}_i^{dq} \approx$$
$$\frac{1}{V_{dc0}} \left[\frac{\omega_c s}{s+\omega_c} (L+2L_f) + (R+2R_f) \right] \mathbf{I} + k_p^{i,dl}\mathbf{I} - \mathbf{D}_i^{dq}. \quad (5.22)$$

Once more, the step-by-step path which lead to the result in (5.22) is presented in the Appendix D. Notice that rather than using $\mathbf{C}_i^{dq0}$, it was chosen to consider only its proportional part. The integral term of the controller would produce an everlasting-growing signal which could bring instability to the system, similarly to the case reported in Section 5.2.3 for the resonant parcel. This approach raises no concerns regarding the effectiveness of the feed-forward action because the proportional term of the current controller exceeds the magnitude of integral at the key frequency of $360Hz$ by a margin of over twenty times.

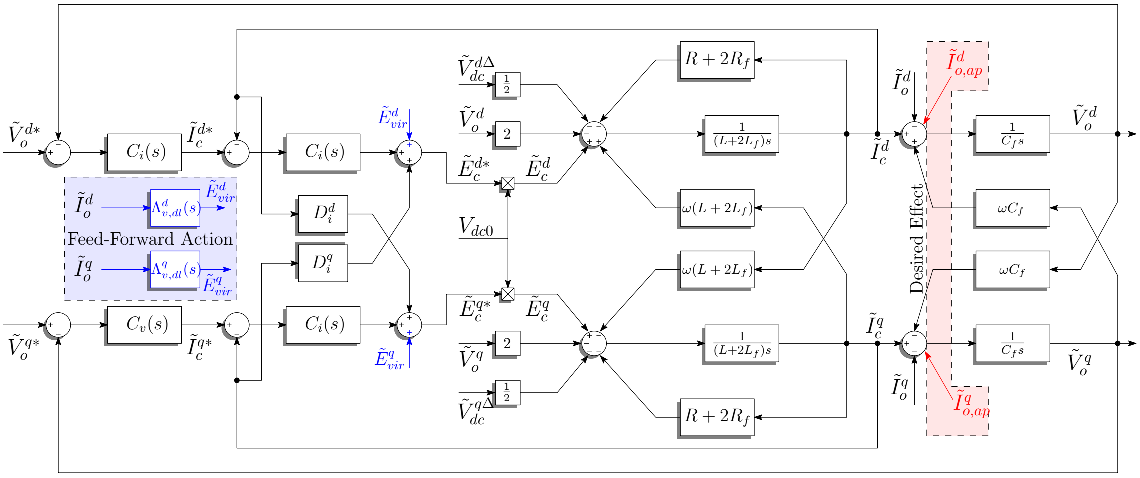

Figure 5.30: Block diagram of the SRF double-loop voltage-controlled MMC with anti-disturbance feed-forward action. The blue loop comprehending $\mathbf{\Lambda}_{v,dl}^{dqo}$ components middle left part of the diagram is the feed-forward action. The red signals $\tilde{I}_{o,ap}^{d,q}$ correspond to the effect caused by the feed-forward action.

The same step-by-step used in Section 4.2.5 can be used to find the following equivalent model:

$$\tilde{\mathbf{V}}_o^{dq0}(s) = \mathbf{G}_{dl,th}^{dq0}(s)\tilde{\mathbf{V}}_o^{dq0*}(s) - \mathbf{Z}_{dl,th}^{dq0}(s)\tilde{\mathbf{I}}_o^{dq0}(s) - \mathbf{Z}_{vir}^{dl,dqo}(s)\tilde{\mathbf{I}}_o^{dq0}(s), \quad (5.23)$$

$$\mathbf{Z}_{vir}^{dl,dqo}(s) = \mathbf{Z}_{dl,th}^{dq0}(s)\mathbf{\Gamma}_{vir}^{dl,dqo}(s), \quad (5.24)$$

$$\mathbf{\Gamma}_{vir}^{dl,dqo}(s) = -\mathbf{\Gamma}_i^{-1}(s) \left[4V_{dc0}C_{eq}\mathbf{s}_{dq} + \frac{3S_0}{2V_{dc0}}\mathbf{I} \right] \mathbf{\Lambda}_{v,dl}^{dqo}(s), \quad (5.25)$$

where $\mathbf{Z}_{vir}^{dl,dqo}$ is the virtual impedance produced by the feed-forward action. Figure 5.31 presents the equivalent circuit based on (5.23).

The frequency responses of the equivalent impedance of the MMC with and without feed-forward term are presented in Figures 5.32a and 5.32b. As with the

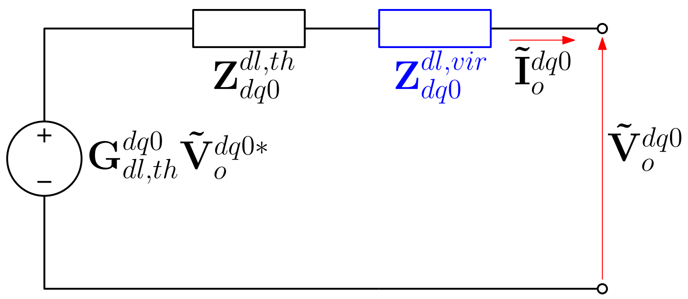

Figure 5.31: Equivalent circuit of the SFR double-loop voltage-controlled MMC with virtual impedance.

results of the other control modes, here the virtual impedance reduced the magnitude of the equivalent impedance of the MMC with better results when the cut-off frequency is higher. It is also important to notice the highlighted region in Figures 5.32a and 5.32b as they indicate the possible existence of numerical errors already explained in other sections of this chapter. The time domain-results in Figures 5.32c-5.32g show the effects of reducing the magnitude of the equivalent impedance, i.e., the harmonic distortion in the output voltages was reduced from 11.5% to 3.5% for the case where the feed-forward action considered cut-off frequency of $1000Hz$. To finish off the section, Table 5.8 summarizes the results for the THD (computed with a 20kHz bandwidth) of voltages and currents in each of the control modes.

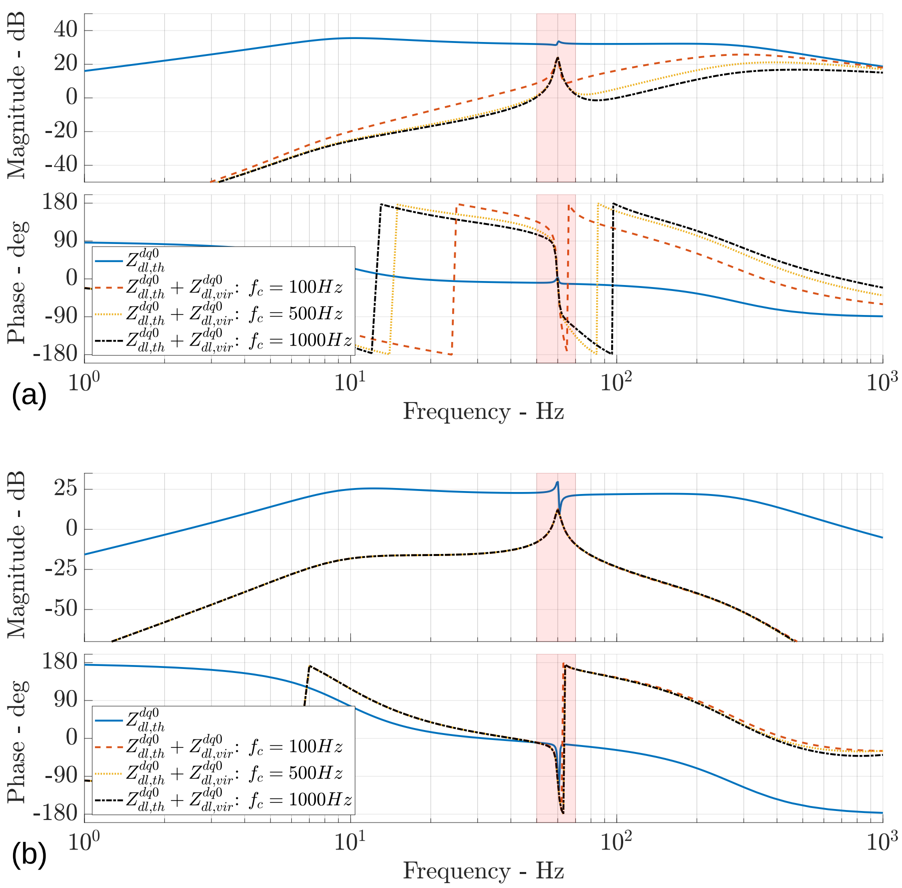

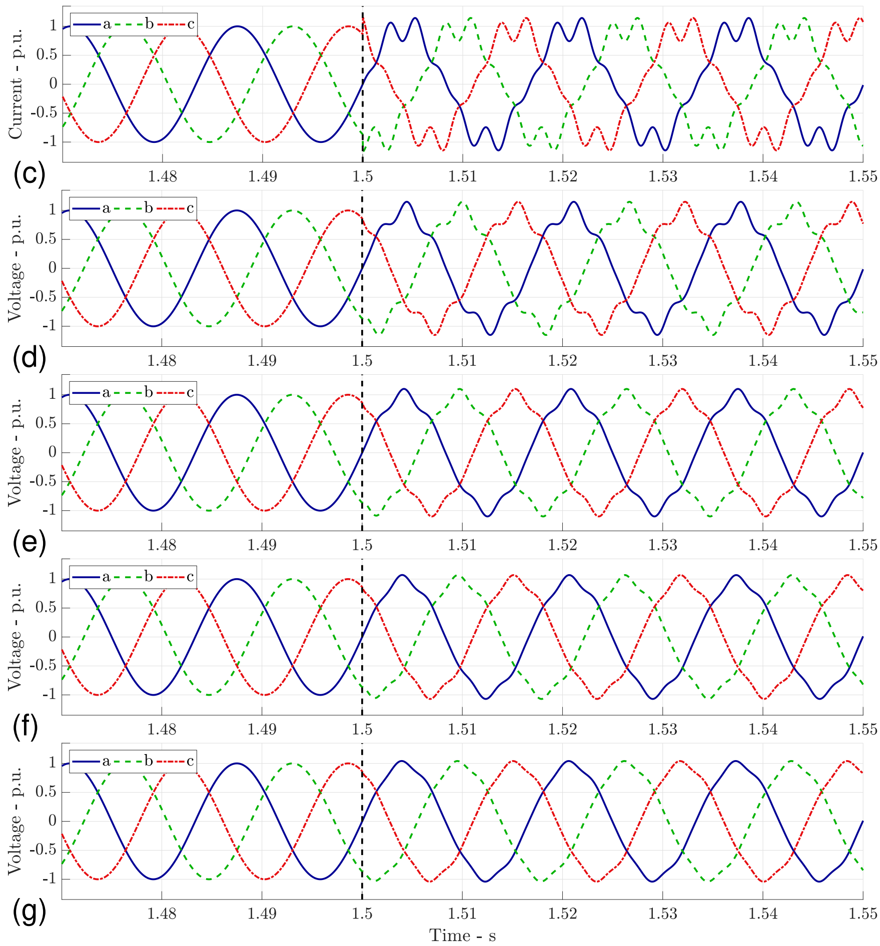

Figure 5.32: Results showing the influence of virtual admittance: SRF double-loop voltage-controlled MMC. Frequency response of the (a) self-related and (b) cross-axis terms; (c) Load currents; (d) produced voltage without virtual admittance, and produced voltage with (e) $100Hz$-bandwidth, (f) $500Hz$-bandwidth and (g) $1000Hz$-bandwidth virtual impedance.

Table 5.8: Summary of the results for the analysis of the use of virtual elements in SRF-controlled MMC. VirA stands for virtual admittance and VirI for virtual impedance.

Control Mode	**-**	THD_v **(%)**	THD_i **(%)**
Current-Controlled	Without VirA	7.1	3.5
	With VirA	7.1	0.5
Single-Loop Voltage-Controlled	Without VirI	11.5	22.8
	With VirI ($fc = 100Hz$)	7.4	22.8
	With VirI ($fc = 500Hz$)	5.4	22.8
	With VirI ($fc = 1000Hz$)	3.5	22.8
Double-Loop Voltage-Controlled	Without VirI	11.5	22.8
	With VirI ($fc = 100Hz$)	7.4	22.8
	With VirI ($fc = 500Hz$)	5.4	22.8
	With VirI ($fc = 1000Hz$)	3.5	22.8

5.3 Applications of the developed models

This section has the objective of presenting some applications for the developed models. In this regard, it was chosen as examples the use of the model for fast time-domain simulations and stability analysis of power-electronic-based systems. In both cases, the results are validating through simulations with the detailed PSCAD model. It is important to mention that, it was considered on the NRF-controlled MMC, yet the SRF model also could be used for the same objective. Besides that, the control actions defined in Section 5.2 are not considered in this part of the thesis.

5.3.1 Step response of the MMC

For showing how the developed model can be used in time-domain simulations, the MMC, initially in steady-state condition, was submitted to step changes. It was considered here only the case were the MMC is under double-loop current/voltage control a the step chages were firstly performed in the ac load current i_o and then in the dc voltage v_{dc}, yet not simultaneously. For obtaining the time-domain step response of the system, is necessary to sum the steady-state value of the variables with the time response indicated by the proposed model. Thus:

$$\begin{aligned} v_o^k &= v_{o_{ss}}^k + \tilde{v}_o^k \\ i_{cir}^k &= i_{cir_{ss}}^k + \tilde{i}_{cir}^k \end{aligned} \tag{5.26}$$

where $v_{o_{ss}}^k$ and $i_{cir_{ss}}^k$ are, respectively, the steady-state values of the ac bus voltage and the MMC circulating current before the perturbation of the system. In this analysis, it was considered that the MMC supply an rated power with unitary-power-factor load. Furthermore, $\tilde{v}_o^k$ and $\tilde{i}_{cir}^k$ are the time-domain changes caused by the perturbations in v_{dc} and i_o and predicted by (4.30) and (4.8), respectively, in frequency domain.

Figure 5.33 shows the results obtained for three different perturbations in i_o^k. Here, it was chosen to present only the results for the phase **a** to optimize the space, but the other phases presented similar behavior. The mentioned perturbations comprised three components, fundamental, fifth- and seventh-order harmonic components, all of which with an amplitude of 0.17 $p.u.$, starting at $t = 3s$. The upper graph of each sub-figure shows how the output current is changed by the considered perturbation. It is possible to notice that the proposed model (straight line), in comparison to the PSCAD/EMTDC model (circle-filled dashed lines), was able to accurately predict the voltage effects imposed by the perturbation in i_o^k.

The same approach was used to analyze the effect of the perturbation in v_{dc}: it was considered three different cases covering the major components the dc vol-

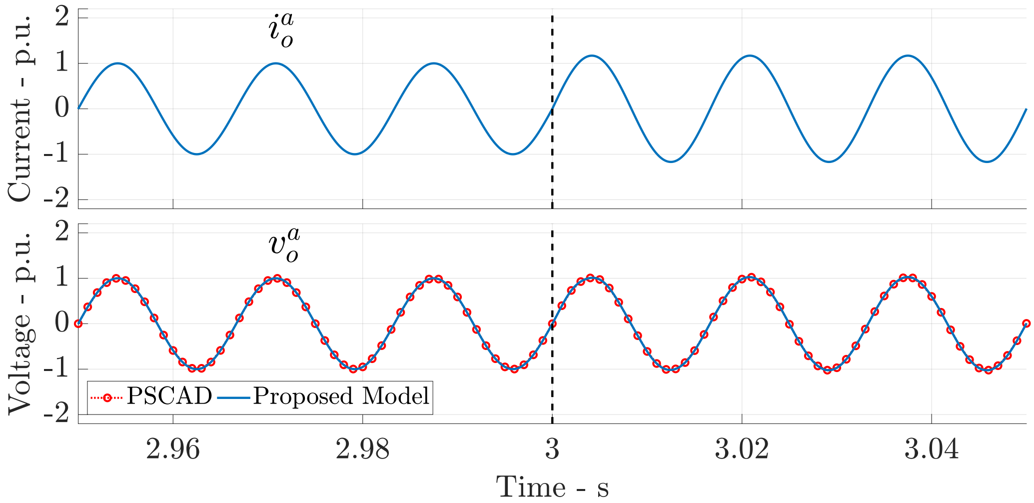

(a) $60Hz$ perturbation

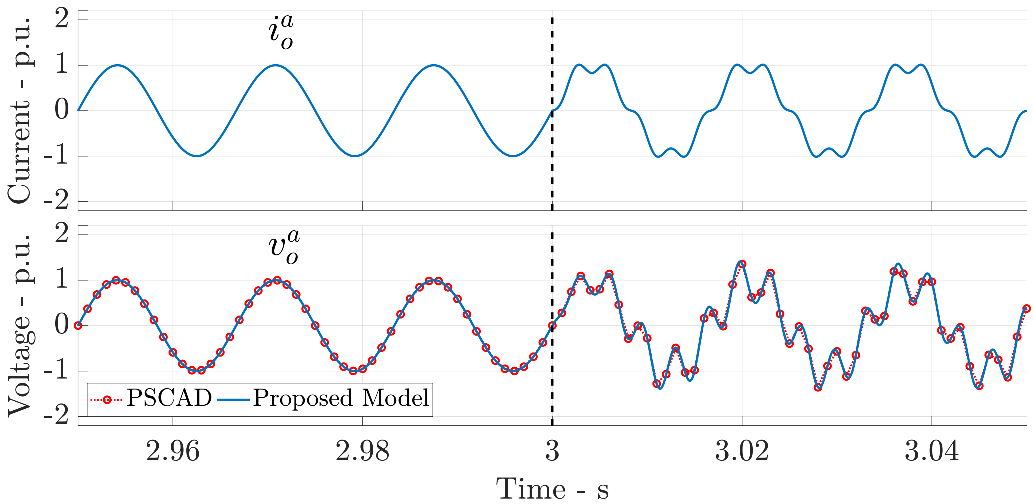

(b) $300Hz$ perturbation

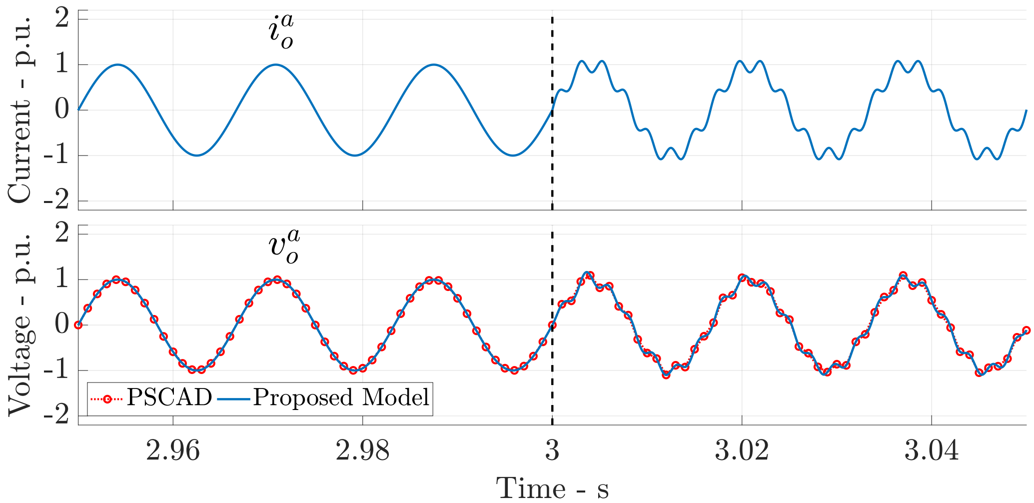

(c) $420Hz$ perturbation

Figure 5.33: Time response to a perturbation in the load current at $t = 3s$. The upper charts represent the load current i_o^a, whereas the lower ones display the voltage v_o^a.

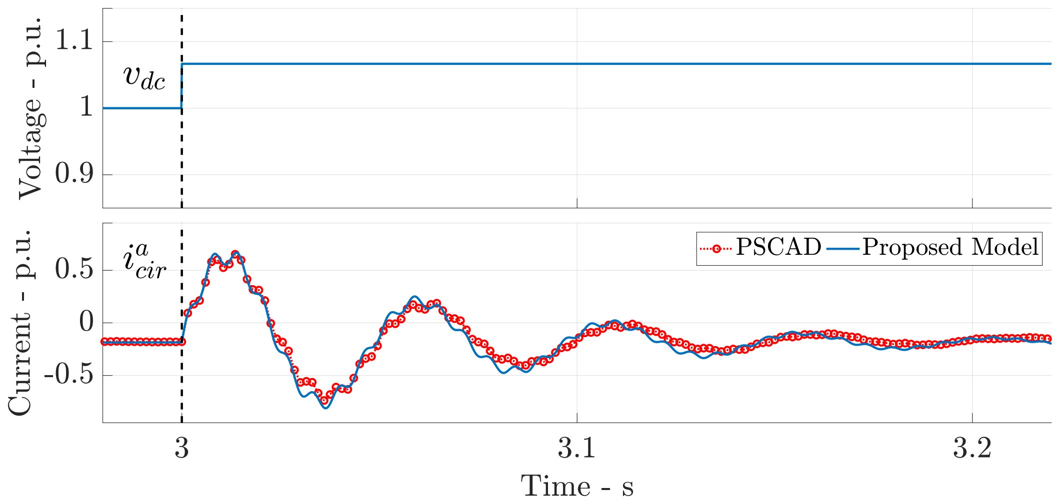

(a) DC perturbation

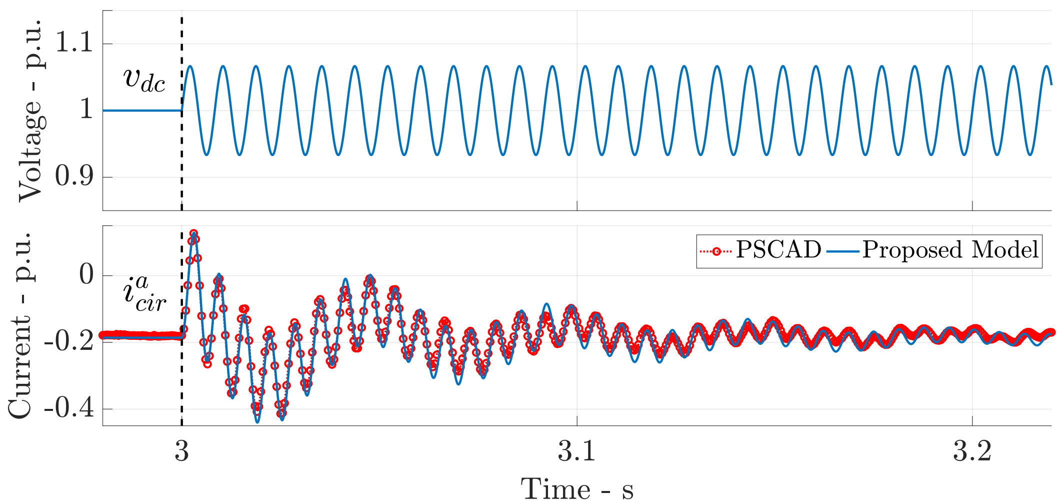

(b) $120Hz$ perturbation

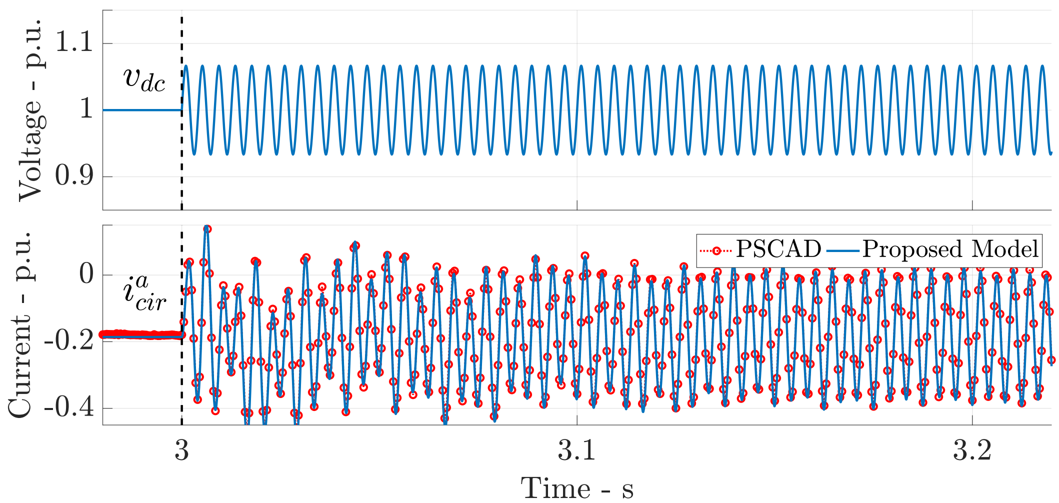

(c) $240Hz$ perturbation

Figure 5.34: Time response to a perturbation in the DC-link voltage v_{dc}. The upper charts represent the DC voltage v_{dc}, whereas the lower ones display the circulating current i_{cir}^{a}.

tage can present. Thus, DC, second- and fourth-order harmonic components, with 0.066 $p.u.$-amplitude, were added to the dc voltage at $t = 3s$. As depicted in Figure 5.34, the change in the circulating current predicted by the proposed analytical model followed the results indicated by the PSCAD/EMTDC simulation with some small differences. These differences, mostly observed in the response for the DC change in Figure 5.34a, concerning high-frequency effects due to the non-linearities which are not included in the model.

5.3.2 Stability analysis of the MMC

Besides using the proposed model to speed up time-domain simulations encompassing grid-forming MMC, it is also possible to use it in stability analysis in systems where the MMC interacts with other converters. For this reason, it is presented in this subsection an example where two MMC interact with each other as in Fi-

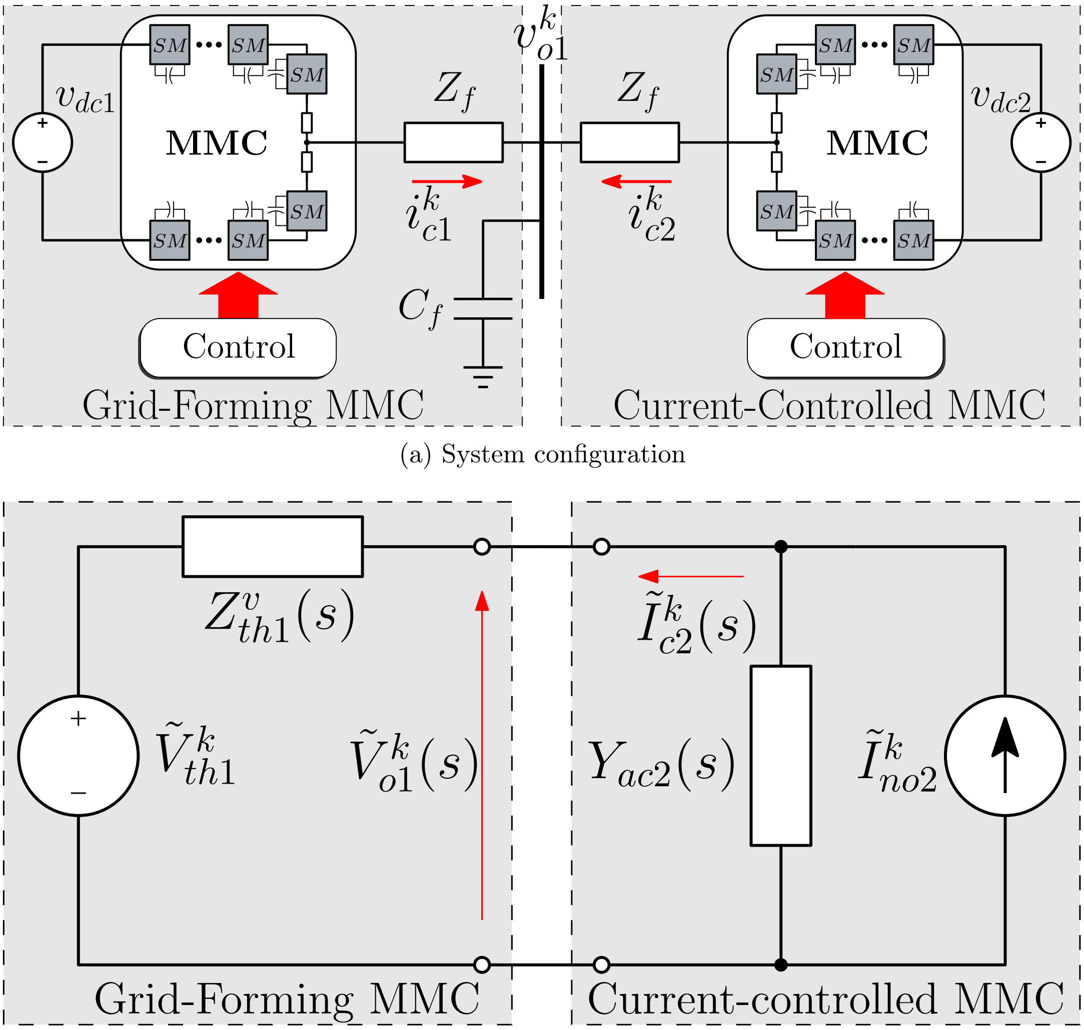

(a) System configuration

(b) Equivalent circuit

Figure 5.35: Grid-forming MMC feeding a current-controlled MMC.

gure 5.35a. The first as a grid-forming converter and the second as a current-controlled converter. The grid-forming converter, for instance, plays the role of the inverter station of an HVDC system whereas the current-controlled represent a renewable, non-dispatchable power plant. Thus, v_{dc1} and v_{dc2} are two independent ideal sources, representing the DC links of each converter. The equivalent circuit which represents this system is depicted in Figure 5.35. Here, the index 1 and 2 are used to distinguish each one of the converters.

According to the impedance-based stability criterion [125], the loop function $\mathcal{L}(s) = Z^{v}_{th1}(s)Y_{ca2}(s)$ is equivalent to the open-loop transfer function which represents the interaction between the voltage- and current-source sides[5]of the system and because of that, can be used to assess its stability. Considering firstly that the control settings of both converters are in accordance with the values considered in

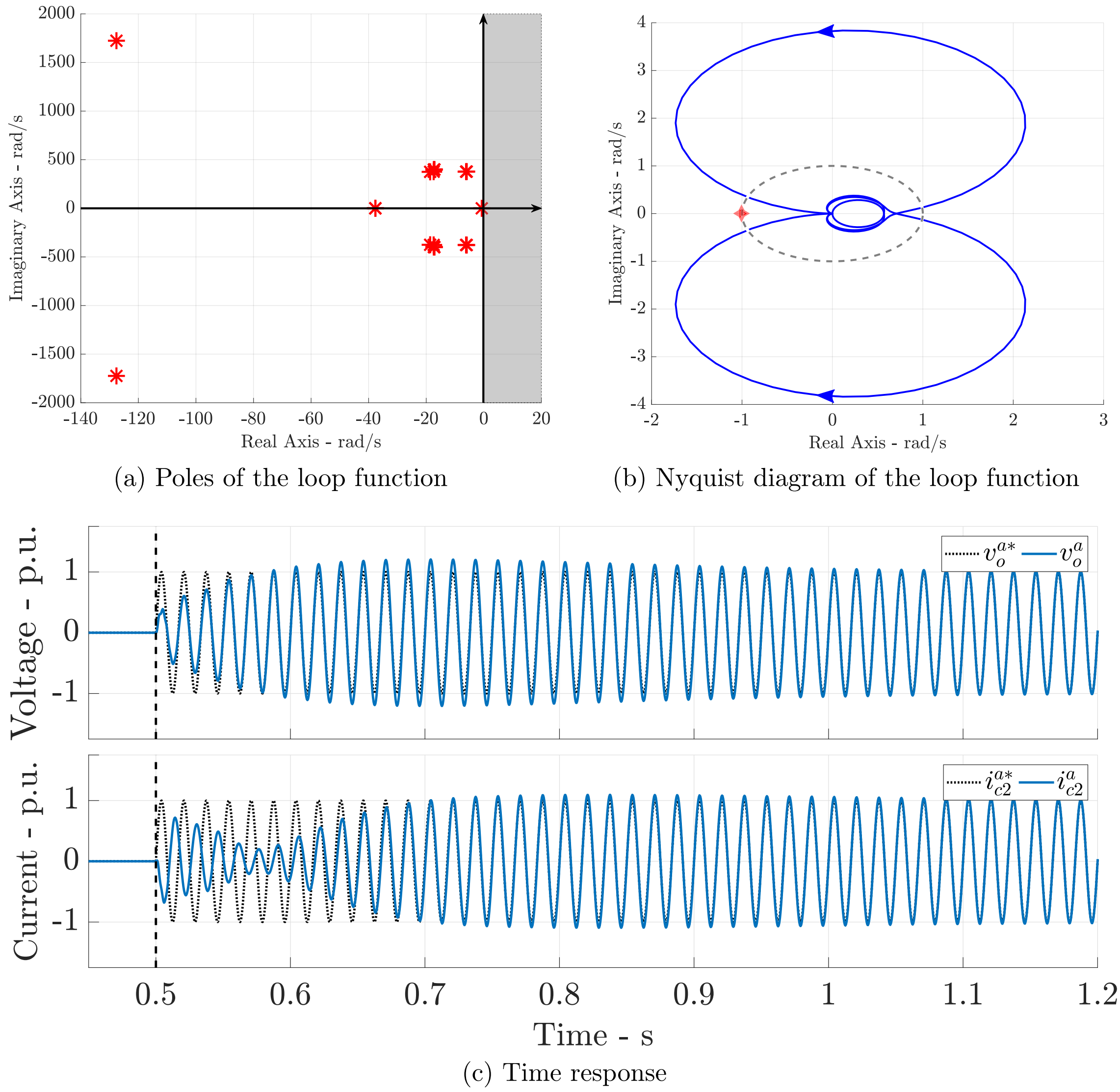

Figure 5.36: Stability evaluation of a system composed by a grid-forming MMC feeding a current-controlled MMC: stable condition.

Chapter 4, whenever applicable, the loop function does not present any right half plane (RHP) pole as shown in Figure 5.36a. Furthermore, the Nyquist curve presented in Figure 5.36b does not encircle the critical point $(-1, 0)$, indicating that the system is stable. This prediction is confirmed by the time-domain simulation results presented in Figure 5.36c, as both the grid voltage v_{o2}^a and the load current i_{c2}^a converge to their references.

It can be observed at the bottom graph of Figure 5.36c that the produced current of the MMC2 (the current-controlled MMC) starts with a 180° lag to its reference. This is caused by the inherent characteristic of current-controlled converters, and to be better understood, considerer the circuits in Figure 5.37. This figure shows that the output current $i_{c2}(t)$ is composed by two components, $i_y(t)$ and $i_i(t)$. The former is the ac voltage response and flows though the equivalent admittance Y_{ac2}, as in the circuit in the left of Figure 5.37. The other component, $i_i(t)$, is the response for the reference current and can be called the desired current to be produced. Thus, it is possible to write the following result:

$$\tilde{I}_{c2}^k(s) = \underbrace{G_i^{cl}(s) I_{c2}^{k*}(s)}_{\tilde{I}_i^k(s)} - \underbrace{Y_{ac2}(s) \tilde{V}_o^k(s)}_{\tilde{I}_y^k(s)}. \tag{5.27}$$

The response to the ac voltage, i.e. $i_y(t)$, must converge to zero due to the action of the resonant controller. However, during a transient period, it presents a fading $60Hz$ component, which caused the 180°-lag observed in the interval that goes from 0.5 to 0.6s in the bottom graph of Figure 5.36c. For better understanding this point, it was obtained the time responses from the Laplace-domain models of $Y_{ac2}(s)$ and $G_i^{cl}(s)$ for sinusoidal inputs as follows:

$$i_y^a(t) = \mathscr{L}^{-1}\{Y_{ac2}(s) V_o^a(s)\}, \tag{5.28}$$

$$i_i^a(t) = \mathscr{L}^{-1}\{G_i^{cl}(s) I_{c2}^{a*}(s)\}, \tag{5.29}$$

where $\mathscr{L}^{-1}$ is the inverse Laplace operator. In this case, $V_o^a(s)$ represents a $60Hz$ rated-amplitude input voltage, and $I_{c2}^{a*}(s)$ a $60Hz$ rated-amplitude reference current. Figure 5.38 presents the results for these testes. In both cases, Figures 5.38a and 5.38b, the upper and bottom graphs present, respectively, the input and response of the circuit. As mentioned, during a transient period $i_y^a(t)$ is different of zero and its peak even overpass $2p.u.$, as can be observed in Figure 5.38a. Here it is important to notice that in the simulated system (which results are presented in Figure 5.36c), this component is not as harmful because instead of step-like, the voltage in the

[5]The grid-forming MMC plays the role of the voltage source, whereas the current-controlled does the current source.

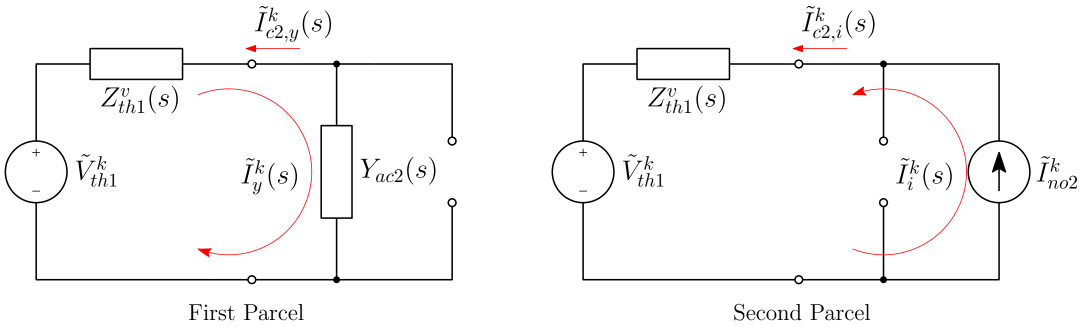

Figure 5.37: Interpretation of the grid for understanding the start up.

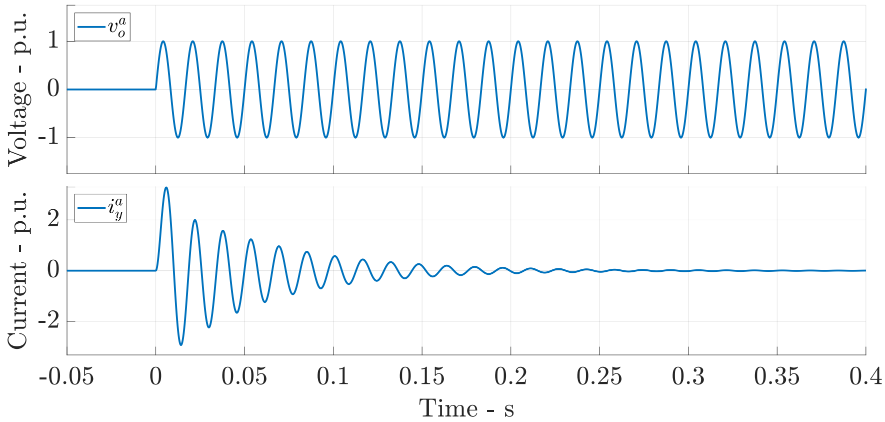

(a) Time response of $Y_{ac2}(s)$ ($i^a_y(t)$)

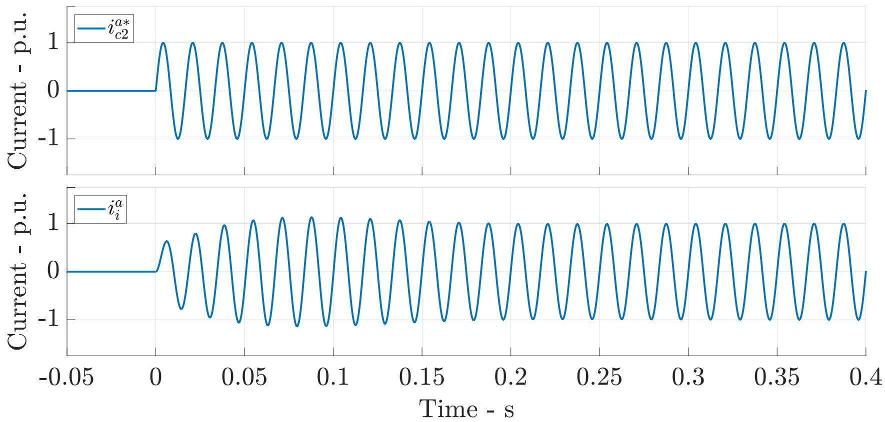

(b) Time response of $G^{cl}_i(s)$ ($i^a_i(t)$)

Figure 5.38: Time responses of $Y_{ac2}(s)$ and $G^{cl}_i(s)$ for rated-amplitude $60Hz$ inputs.

circuit grows gradually. Figure 5.38b, on the other hand, shows the response for the reference current, and it stands out that it is smoother than the response for the voltage.

Now it is necessary to investigate the physical meaning of this transient response for the ac voltage. As previously mentioned, it enforces a 180°-lagged current which, in turn, indicates a transient inversion in the direction of the power flux in the current-controlled MMC. The upper graph of Figure 5.39 highlights this lagging between the produced current and the voltage at the ac bus. As can be observed in the bottom graph, the power inversion raises the equivalent dc voltages v_{dc2}^{pa} and v_{dc2}^{na} of the SMs of the current-controlled MMC.

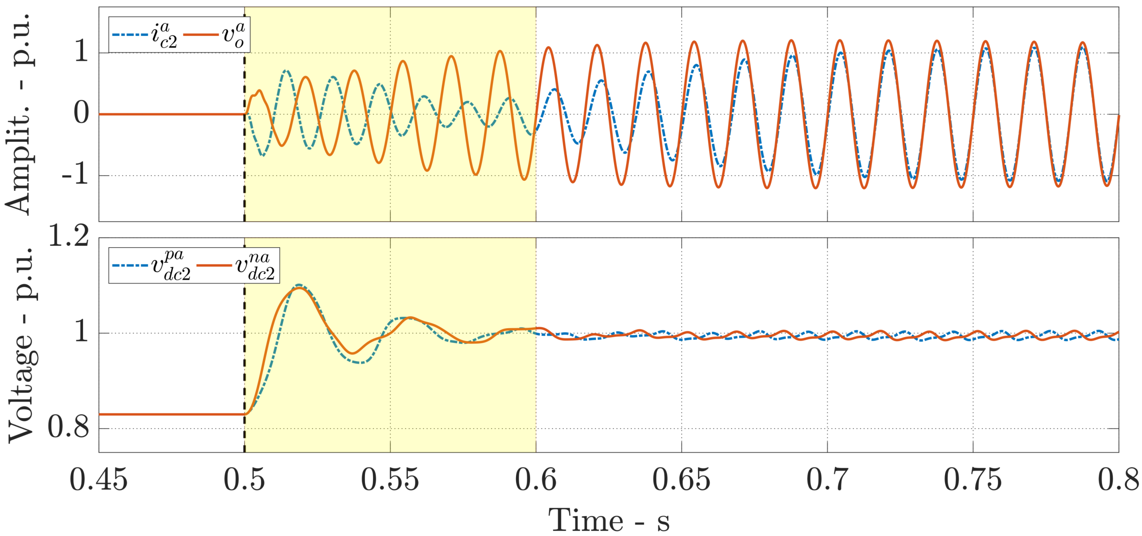

Figure 5.39: Simulation results of the current-controlled MMC.

Just for the sake of comparison, if all the control settings are adjusted to a tenth of their values, the loop function will present RHP poles as in Figure 5.40a. According to the Nyquist stability criterion, the system remains stable if and only if the Nyquist plot encircles the critical point in the counterclockwise direction as many times as the number of RHP poles. This is not observed in Figure 5.40b, indicating that the system is unstable. Once again, the prediction is confirmed by the simulation results in Figure 5.40c. Table 5.9 presents the control settings considered throughout this section.

Table 5.9: Control settings considered during the stability analysis.

MMC		**Proportional Gain**		**Resonant Gain**	
		Stable	**Unstable**	**Stable**	**Unstable**
Grid-Forming MMC	**Voltage Loop**	0.10000	0.01000	1.00000	0.10000
	Current Loop	0.00010	0.00001	0.01000	0.00100
Current-Controlled MMC	**Current Loop**	0.00010	0.00001	0.01000	0.00100

5.4 Partial Conclusions

The first point addressed in this chapter was the effects of the control parameters on the equivalent admittances and impedances of the MMC in different control

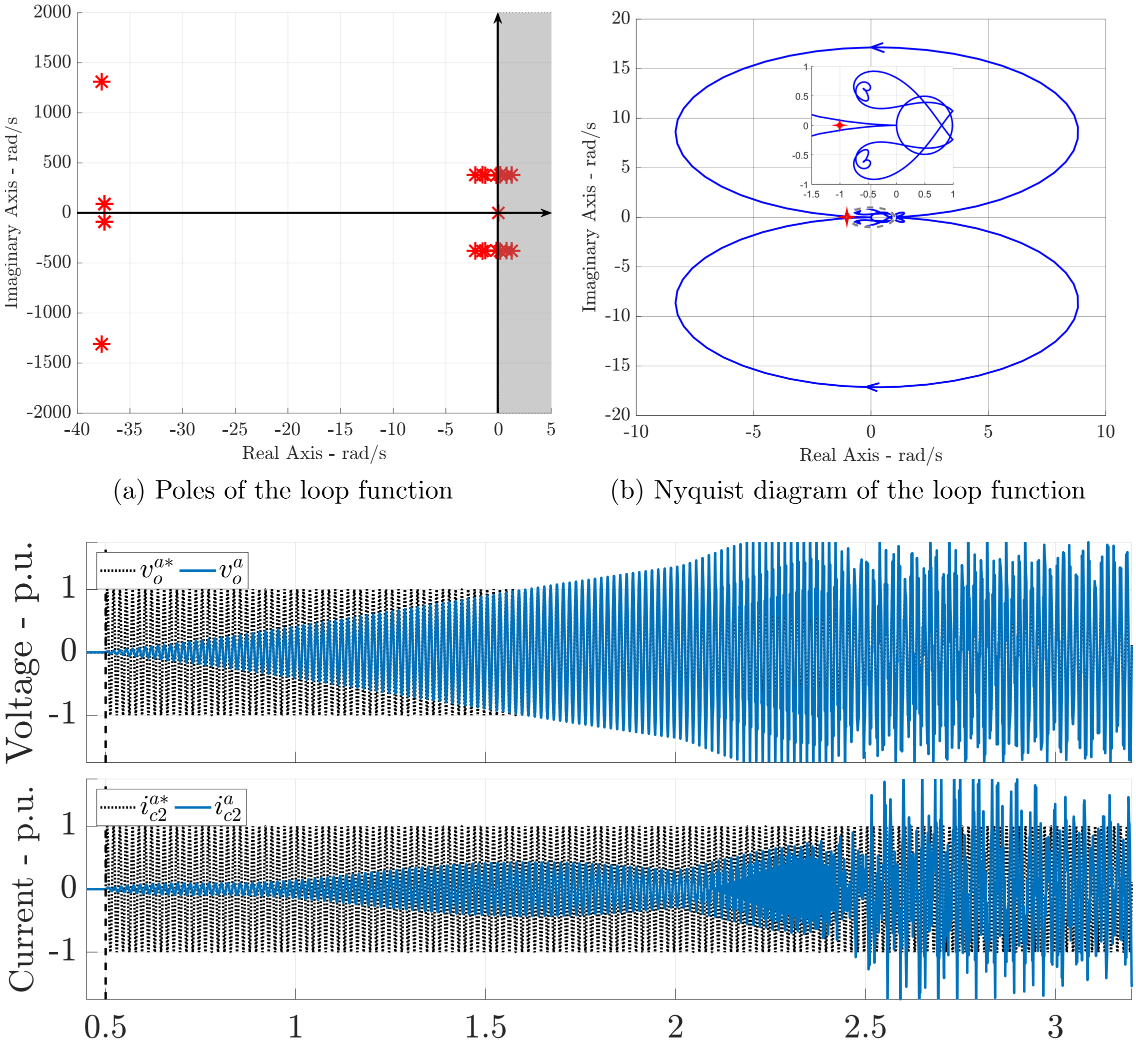

(a) Poles of the loop function

(b) Nyquist diagram of the loop function

(c) Time response

Figure 5.40: Stability evaluation of a system composed by a grid-forming MMC feeding a current-controlled MMC: unstable condition.

modes. At first, it was considered the MMC controlled in NRF and one of the major conclusions is that the proportional gain is considerably more significant than the resonant when it comes to the shape of the admittances and impedances in the frequency domain. In general, it was observed that the greater the proportional gains, the better for the MMC because it reduces the level of the magnitude curves, making the system stronger in face of harmonic disturbances. It was also noticed that the proportional gains affect the position of resonant peaks when the MMC is either single- or double-loop current/voltage control, yet the same is not observed when the MMC is under current control. As for the SRF controlled modes, the analyses returned similar results, i.e., proportional gains stand out as more related to changes of the equivalent impedances/admittances in key frequencies. In most of the cases, the integral only interfered in the magnitude of resonant peaks.

Then, it was shown that the strategy of using multiple resonant loops in NRF produced multiple notches at the frequencies of fifth- and seventh-order harmonic components in the magnitude curve of the equivalent impedance/admittance of the MMC. These notches guaranteed, for instance, that distorted voltages do not affect the produced voltages of the current-controlled MMC. Analogously, they also contributed to making the grid-forming MMC supply non-linear loads without having its produced voltages distorted. In both cases, the simulation results showed that the currents/voltages of MMC presented higher levels of THD when using a single resonant loop. After that, it was analyzed the use of proportional-integral-resonant controllers in SRF. The frequency-domain results indicated the presence of notches in the magnitude curves of the equivalent impedance/admittance of the MMC, likewise, the notches observed in the NRF-controlled MMC. In this case, the notch appears at $360HZ$, which corresponds to the frequency of the fifth- and seventh-order harmonic components in SRF. The simulation results also indicated that the additional resonant loop reduced the harmonic distortion of the produced voltages and currents.

After that, it was derived in the chapter feed-forward control to produce virtual elements (admittance or impedance) with the function of shaping the equivalent impedance to reduce their magnitudes for key frequencies. The effectiveness of the proposed controllers was also demonstrated both in the frequency response of the system and through time-domain simulations. The results pointed out that the low-pass filters used in the feed-forward actions of the voltage-controlled MMC play an important role in the produced virtual impedance. In this context, the greater the cut-off frequency, the better the immunity created by the virtual impedance to harmonic content in the load currents.

It was also shown in this chapter two applications for the proposed models. In the first application, the proposed model for the NRF-controlled double-loop current/voltage-controlled MMC was used in a time-domain simulation. The results pointed out that the proposed model was effective in predicting the dynamics of the MMC. In the second application, the developed models were used to predict the stability of a power-electronics-based system comprising a grid-forming MMC and a current controlled MMC. It was presented two cases, one where the system was stable and another in which the system was unstable. Using the proposed models and the impedance-based stability criterion, it was possible to predict whether the system was stable or unstable.

Chapter 6

Conclusions

This thesis presented a group of linearized models for the MMC in different control modes in Natural and Synchronous Reference Frames. First, the models for the current-controlled, single-loop voltage controlled and double-loop current/voltage controlled were derived, for both reference frames, then they were validated through simulations using PSCAD and PSIM. It is important to mention that, along with the models representing the output variables, it was also derived models for the dynamics of the circulating currents of the MMC. In the sequence, some analyses were carried out to show the influence of control gains in the frequency response of the equivalent admittance and impedance of the MMC. It was also analyzed the effect of using resonant controllers tuned in the frequencies of the major harmonic components in the shape of the equivalent ac admittance/impedance of the MMC in Natural Reference Frame (NRF) and Synchronous Reference Frames (SRF) and, afterward, it was proposed a feed-forward control to provide the MMC with immunity to harmonic content from the system. As a last point presented in the thesis, it was shown typical applications for the developed model, i.e., time-domain simulations and stability analysis of a power-electronic-based system.

It was possible to show that when the MMC is current controlled, it can be represented in the Laplace domain by a current source associated with an admittance (which corresponds to a Norton-equivalent model), both of which influenced by the values of passive elements and control settings alike. For the grid-forming modes, i.e., single-loop voltage controlled and double-loop current/voltage controlled MMC, it was possible to represent the converter by a voltage source behind an equivalent impedance (which corresponds to a Thévenin-equivalent model). As for the current-controlled MMC, the voltage source and equivalent impedance are also dependent on the values of passive elements and control settings. As for the circulation currents, the derived models pointed out a direct relationship with the dc-link voltage. This relationship, indeed, allowed representing the circulating current dynamics through an equivalent admittance. Once more, it is important to mention that the major results for the doubly-loop voltage-controlled MMC were published in [62].

When the MMC is controlled in NRF, there is no coupling between the phases and, consequently, it is possible to use one-dimensional admittances, impedances, and sources to compose the system. When the MMC is controlled in SRF, on the other hand, such approach is not feasible since the frame transformation creates couplings between the direct and quadrature axes. Thus, the admittances, impedances, and sources of the system might be represented by 3×3 matrices and the variables by arrays containing the direct-axis, quadrature-axis, and zero-sequence components.

The results obtained with the proposed models matched those predicted by the non-linear model of the MMC with few small differences. For instance, some differences were observed in the resonant frequencies of the models of the MMC controlled in NRF. In this case, the digital implementation of these controllers in the non-linear model is responsible for this disparity, but it was understood that this raises no great concerns. Some small errors in the predictions of the SRF models were also observed in specific points of the spectrum. In contrast to the differences observed for the NRF models, these were caused by the numeric implementation of the proposed models. The operations with 3×3 matrices led to hundred-order transfer functions, requiring the use of some numeric simplifications, which, in turn, reduced the precision of the model in some points of the spectrum. Once more, it was understood that no great concern must be raised because these errors did not appear in the key frequencies of the system.

It was also highlighted in the thesis that the control settings can modify the resonant peaks present in the equivalent admittances and impedances of the MMC either amplifying, damping or even changing the frequency in which they occur. These results shed light on the importance of the careful adjusting of the control settings, otherwise, the output ac currents and voltages could be severely distorted by background harmonics and by the presence of the non-linear loads in the power grid. Also in this context, the swelling of small oscillating components - components other than the second-order harmonic, which is the only component damped through control - in the circulating currents may or may not occur depending on the control settings.

Still considering the relationship of the control settings with the power quality issue, it was shown that the use of extra resonant loops tuned in the frequency of the major harmonic components of the system contributed to the reduction of the THD of the output currents and voltages. In the frequency domain, these resonant loops produced notches at 300 and $420Hz$ for the control modes implemented in the natural reference frame, and a notch at $360Hz$ for the control modes implemented in the synchronous reference frame. In other words, the resonant loops reduced significantly the magnitude of the admittances and impedances at the frequencies of the fifth- and seventh-order harmonic components.

The proposed feed-forward controllers were also able to reshape the equivalent admittances and impedances of the MMC to provide it with immunity to harmonic components of the grid. On one hand, this approach allowed a broader effect in the frequency domain in comparison to the use of multiple resonant loops, on the other, the reduction of the magnitudes of admittances and impedance at key frequencies were smaller. As presented in the thesis, the feed-forward action creates a virtual admittance in the system when the converter is under current control and a virtual impedance when the MMC is under voltage control. To obtain proper transfer functions for the virtual impedances, for instance, it was necessary the use of low-pass filters which, in turn, undermined the performance of the feed-forward action.

The time-domain simulation using the proposed model for the NRF double-loop current/voltage-controlled MMC showed accurate results when compared to more detailed models. Given that, it is possible to conclude that the proposed models for the different control modes can be employed in transient analysis of MMC-based power grids. One upper point in this regard is the fact that the simulations involving the proposed models are considerably faster than the simulations considering more detailed models, which paves the way for the use in transient analyses of large and complex power systems.

Another potential application of the proposed models is in frequency-domain studies such as small-signal stability analyses of power-electronics-based power systems. The example presented in the last section of the last chapter, for instance, accurately predicted the stability/instability of the chosen cases. In this case, the scenario in which a grid-forming MMC supplies the voltages for a current-controlled MMC is similar to the typically used configuration for the integration of offshore wind power plants to the onshore power grid. The only difference here is that, in real offshore power plants, the current-controlled MMC would be replaced by current-controlled two-level converters associated with step-up transformers. The use of the current-controlled MMC was for no other reason than avoiding inserting other elements in this thesis.

Among the proposed models, those for the double-loop voltage-controlled MMC stand out due to the novelty of this control approach in the context of high power high voltage applications. As mentioned in the introduction, as far as the authors could find, only one paper has considered modeling the MMC with this control approach until 2019 [55], yet the focus of their research considered the power and energy, instead of voltages and currents, as state variables. The approach followed in this thesis [62] allows among other things applying power-electronics popular techniques such as the impedance-based stability criterion [125], as shown in the example analyzed in the previous paragraph. It is understood that the double-loop control approach should become more common in MMC application, especially in the integration of offshore wind power plants to the onshore grid, and for this reason, the models (implemented in Natural and Synchronous Reference Frames) presented in the thesis might be of great relevance for the analyses of the future power grid.

6.1 Further works

Further works include the following topics:

- Investigate computational approaches to mitigate errors cased by the matrix manipulations in SRF models;
- Using the models for fast transient analysis of complex MMC-based power grids;
- Combine the circulating current equivalent admittance with the dc-voltage control loop to derive an analytical model to represent the dc side of the MMC when it is acting as a rectifier converter of an HVDC;
- Use of the proposed models for spotting resonance and stability issues involving the integration of MMC-based HVDC with transmission lines, power plants, FACTS and other elements composing a power grid;
- Development of analytical models for representing MMC-based multiterminal HVDC (MTDC);
- Development of analytical for representing current-source-based modular multilevel converters and modular multilevel matrix converter;
- Development of analytical models for the MMC operating in grid-supporting mode, i.e., under voltage control, but with frequency and voltage droop controllers.

List of References

[1] STRASSER, T., ANDRÉN, F., KATHAN, J., et al. "A Review of Architectures and Concepts for Intelligence in Future Electric Energy Systems", *IEEE Transactions on Industrial Electronics*, v. 62, n. 4, pp. 2424–2438, April 2015. ISSN: 0278-0046. doi:10.1109/TIE.2014.2361486.

[2] OBI, M., BASS, R. "Trends and challenges of grid-connected photovoltaic systems – A review", *Renewable and Sustainable Energy Reviews*, v. 58, pp. 1082 – 1094, 2016. ISSN: 1364-0321. doi:10.1016/j.rser.2015.12.289.

[3] JANA, J., SAHA, H., BHATTACHARYA, K. D. "A review of inverter topologies for single-phase grid-connected photovoltaic systems", *Renewable and Sustainable Energy Reviews*, v. 72, pp. 1256 – 1270, 2017. ISSN: 1364-0321. doi:10.1016/j.rser.2016.10.049.

[4] OBEIDAT, F. "A comprehensive review of future photovoltaic systems", *Solar Energy*, v. 163, pp. 545 – 551, 2018. ISSN: 0038-092X. doi:10.1016/j.solener.2018.01.050.

[5] RABIUL ISLAM, M., MAHFUZ-UR-RAHMAN, A. M., MUTTAQI, K. M., et al. "State-of-the-Art of the Medium-Voltage Power Converter Technologies for Grid Integration of Solar Photovoltaic Power Plants", *IEEE Transactions on Energy Conversion*, v. 34, n. 1, pp. 372–384, March 2019. ISSN: 1558-0059. doi:10.1109/TEC.2018.2878885.

[6] MANSOURI, N., LASHAB, A., SERA, D., et al. "Large Photovoltaic Power Plants Integration: A Review of Challenges and Solutions", *Energies*, v. 12, n. 19, 2019. ISSN: 1996-1073. doi:10.3390/en12193798.

[7] YARAMASU, V., WU, B., SEN, P. C., et al. "High-power wind energy conversion systems: State-of-the-art and emerging technologies", *Proceedings of the IEEE*, v. 103, n. 5, pp. 740–788, May 2015. ISSN: 1558-2256. doi:10.1109/JPROC.2014.2378692.

[8] DE FREITAS, T. R., MENEGÁZ, P. J., SIMONETTI, D. S. "Rectifier topologies for permanent magnet synchronous generator on wind energy conversion

systems: A review", *Renewable and Sustainable Energy Reviews*, v. 54, pp. 1334 – 1344, 2016. ISSN: 1364-0321. doi:10.1016/j.rser.2015.10.112.

[9] BLAABJERG, F., MA, K. "Wind Energy Systems", *Proceedings of the IEEE*, v. 105, n. 11, pp. 2116–2131, Nov 2017. ISSN: 1558-2256. doi:10.1109/JPROC.2017.2695485.

[10] PÁEZ, J. D., FREY, D., MANEIRO, J., et al. "Overview of DC–DC Converters Dedicated to HVdc Grids", *IEEE Transactions on Power Delivery*, v. 34, n. 1, pp. 119–128, Feb 2019. ISSN: 1937-4208. doi:10.1109/TPWRD.2018.2846408.

[11] ALASSI, A., BAÑALES, S., ELLABBAN, O., et al. "HVDC Transmission: Technology Review, Market Trends and Future Outlook", *Renewable and Sustainable Energy Reviews*, v. 112, pp. 530 – 554, 2019. ISSN: 1364-0321. doi:10.1016/j.rser.2019.04.062.

[12] ESLAMI, M., SHAREEF, H., MOHAMED, A., et al. "A survey on flexible AC transmission systems (FACTS) [Analiza urządzeń systemu FACTS]", *Przeglad Elektrotechniczny*, v. 88, n. 1 A, pp. 1–11, 2012. Disponível em: <https://www.scopus.com/inward/record.uri?eid=2-s2.0-84855334055&partnerID=40&md5=bedb5cf288ee017dcee8f291b06a6f7a>.

[13] WATANABE, E. H., DE ARAÚJO LIMA, F. K., DA SILVA DIAS, R. F., et al. "28 - Flexible AC Transmission Systems". In: Rashid, M. H. (Ed.), *Power Electronics Handbook (Fourth Edition)*, fourth edition ed., Butterworth-Heinemann, pp. 885 – 909, Oxford, 2018. ISBN: 978-0-12-811407-0. doi:10.1016/B978-0-12-811407-0.00031-3.

[14] BOSE, B. K. "Power Electronics and Motor Drives Recent Progress and Perspective", *IEEE Transactions on Industrial Electronics*, v. 56, n. 2, pp. 581–588, Feb 2009. ISSN: 1557-9948. doi:10.1109/TIE.2008.2002726.

[15] RONANKI, D., SINGH, S. A., WILLIAMSON, S. S. "Comprehensive Topological Overview of Rolling Stock Architectures and Recent Trends in Electric Railway Traction Systems", *IEEE Transactions on Transportation Electrification*, v. 3, n. 3, pp. 724–738, Sep. 2017. ISSN: 2372-2088. doi:10.1109/TTE.2017.2703583.

[16] KRASTEV, I., TRICOLI, P., HILLMANSEN, S., et al. "Future of Electric Railways: Advanced Electrification Systems with Static Converters for ac

Railways", *IEEE Electrification Magazine*, v. 4, n. 3, pp. 6–14, Sep. 2016. ISSN: 2325-5889. doi:10.1109/MELE.2016.2584998.

[17] VAZQUEZ, S., LUKIC, S. M., GALVAN, E., et al. "Energy Storage Systems for Transport and Grid Applications", *IEEE Transactions on Industrial Electronics*, v. 57, n. 12, pp. 3881–3895, Dec 2010. ISSN: 1557-9948. doi:10.1109/TIE.2010.2076414.

[18] ZHANG, N., SUTANTO, D., MUTTAQI, K. M. "A review of topologies of three-port DC–DC converters for the integration of renewable energy and energy storage system", *Renewable and Sustainable Energy Reviews*, v. 56, pp. 388 – 401, 2016. ISSN: 1364-0321. doi:10.1016/j.rser.2015.11.079.

[19] DRAGIČEVIĆ, T., BLAABJERG, F. "Chapter 9 - Power Electronics for Microgrids: Concepts and Future Trends". In: Mahmoud, M. S. (Ed.), *Microgrid*, Butterworth-Heinemann, pp. 263 – 279, Oxford, 2017. ISBN: 978-0-08-101753-1. doi:10.1016/B978-0-08-101753-1.00009-7.

[20] BAYHAN, S., ABU-RUB, H., LEON, J. I., et al. "Power electronic converters and control techniques in AC microgrids". In: *IECON 2017 - 43rd Annual Conference of the IEEE Industrial Electronics Society*, pp. 6179–6186, Oct 2017. doi:10.1109/IECON.2017.8217073.

[21] DORN, J. "Novel voltage-sourced converters for HVDC and FACTS applications". In: *OSAKA: SYSTEM DEVELOPMENT AND ASSET MANAGEMENT UNDER RESTRUCTURING*, OSAKA, 2007. CIGRE. Disponível em: <`https://e-cigre.org/publication/SYMP_OSA_2007-osaka-system-development-and-asset-management-under-restructuring`>. Accessed in July 14, 2020.

[22] KUMAR, Y. S., PODDAR, G. "Control of Medium-Voltage AC Motor Drive for Wide Speed Range Using Modular Multilevel Converter", *IEEE Transactions on Industrial Electronics*, v. 64, n. 4, pp. 2742–2749, April 2017. ISSN: 0278-0046. doi:10.1109/TIE.2016.2631118.

[23] JUNG, J., LEE, H., SUL, S. "Control Strategy for Improved Dynamic Performance of Variable-Speed Drives With Modular Multilevel Converter", *IEEE Journal of Emerging and Selected Topics in Power Electronics*, v. 3, n. 2, pp. 371–380, June 2015. ISSN: 2168-6777. doi:10.1109/JESTPE.2014.2323955.

[24] NADEMI, H., DAS, A., BURGOS, R., et al. "A New Circuit Performance of Modular Multilevel Inverter Suitable for Photovoltaic Conver-

sion Plants", *IEEE Journal of Emerging and Selected Topics in Power Electronics*, v. 4, n. 2, pp. 393–404, June 2016. ISSN: 2168-6777. doi:10.1109/JESTPE.2015.2509599.

[25] SHAHNAZIAN, F., ADABI, J., POURESMAEIL, E., et al. "Interfacing modular multilevel converters for grid integration of renewable energy sources", *Electric Power Systems Research*, v. 160, pp. 439 – 449, 2018. ISSN: 0378-7796. doi:10.1016/j.epsr.2018.03.014.

[26] LIN, N., DINAVAHI, V. "Behavioral Device-Level Modeling of Modular Multilevel Converters in Real Time for Variable-Speed Drive Applications", *IEEE Journal of Emerging and Selected Topics in Power Electronics*, v. 5, n. 3, pp. 1177–1191, Sept 2017. ISSN: 2168-6777. doi:10.1109/JESTPE.2017.2673818.

[27] OULD-BACHIR, T., SAAD, H., DENNETIÈRE, S., et al. "CPU/FPGA-Based Real-Time Simulation of a Two-Terminal MMC-HVDC System", *IEEE Transactions on Power Delivery*, v. 32, n. 2, pp. 647–655, April 2017. ISSN: 0885-8977. doi:10.1109/TPWRD.2015.2508381.

[28] SHEN, Z., DINAVAHI, V. "Real-Time Device-Level Transient Electrothermal Model for Modular Multilevel Converter on FPGA", *IEEE Transactions on Power Electronics*, v. 31, n. 9, pp. 6155–6168, Sept 2016. ISSN: 0885-8993. doi:10.1109/TPEL.2015.2503281.

[29] LI, W., BÉLANGER, J. "An Equivalent Circuit Method for Modelling and Simulation of Modular Multilevel Converters in Real-Time HIL Test Bench", *IEEE Transactions on Power Delivery*, v. 31, n. 5, pp. 2401–2409, Oct 2016. ISSN: 0885-8977. doi:10.1109/TPWRD.2016.2541461.

[30] ASHOURLOO, M., MIRZAHOSSEINI, R., IRAVANI, R. "Enhanced Model and Real-Time Simulation Architecture for Modular Multilevel Converter", *IEEE Transactions on Power Delivery*, v. 33, n. 1, pp. 466–476, Feb 2018. ISSN: 0885-8977. doi:10.1109/TPWRD.2017.2723540.

[31] ILVES, K., ANTONOPOULOS, A., NORRGA, S., et al. "Steady-State Analysis of Interaction Between Harmonic Components of Arm and Line Quantities of Modular Multilevel Converters", *IEEE Transactions on Power Electronics*, v. 27, n. 1, pp. 57–68, Jan 2012. ISSN: 0885-8993. doi:10.1109/TPEL.2011.2159809.

[32] SHI, X., WANG, Z. ., LIU, B., et al. "Steady-State Modeling of Modular Multilevel Converter Under Unbalanced Grid Conditions", *IEEE Transactions*

on Power Electronics, v. 32, n. 9, pp. 7306–7324, Sept 2017. ISSN: 0885-8993. doi:10.1109/TPEL.2016.2629472.

[33] ZHAO, F., XIAO, G., ZHAO, T. "Accurate Steady-State Mathematical Models of Arm and Line Harmonic Characteristics for Modular Multilevel Converter", *IEEE Transactions on Power Delivery*, v. PP, n. 99, pp. 1–1, 2017. ISSN: 0885-8977. doi:10.1109/TPWRD.2017.2764950.

[34] PERALTA, J., SAAD, H., DENNETIERE, S., et al. "Detailed and Averaged Models for a 401-Level MMC-HVDC System", *IEEE Transactions on Power Delivery*, v. 27, n. 3, pp. 1501–1508, July 2012. ISSN: 0885-8977. doi:10.1109/TPWRD.2012.2188911.

[35] WANG, J., BURGOS, R., BOROYEVICH, D. "Switching-Cycle State-Space Modeling and Control of the Modular Multilevel Converter", *IEEE Journal of Emerging and Selected Topics in Power Electronics*, v. 2, n. 4, pp. 1159–1170, Dec 2014. ISSN: 2168-6777. doi:10.1109/JESTPE.2014.2354393.

[36] HARNEFORS, L., ANTONOPOULOS, A., NORRGA, S., et al. "Dynamic Analysis of Modular Multilevel Converters", *IEEE Transactions on Industrial Electronics*, v. 60, n. 7, pp. 2526–2537, July 2013. ISSN: 0278-0046. doi:10.1109/TIE.2012.2194974.

[37] JAMSHIDIFAR, A., JOVCIC, D. "Small-Signal Dynamic DQ Model of Modular Multilevel Converter for System Studies", *IEEE Transactions on Power Delivery*, v. 31, n. 1, pp. 191–199, Feb 2016. ISSN: 1937-4208. doi:10.1109/TPWRD.2015.2478489.

[38] ZHOU, J. Z., DING, H., FAN, S., et al. "Impact of Short-Circuit Ratio and Phase-Locked-Loop Parameters on the Small-Signal Behavior of a VSC-HVDC Converter", *IEEE Transactions on Power Delivery*, v. 29, n. 5, pp. 2287–2296, Oct 2014. ISSN: 0885-8977. doi:10.1109/TPWRD.2014.2330518.

[39] MEHRASA, M., POURESMAEIL, E., ZABIHI, S., et al. "Dynamic Model, Control and Stability Analysis of MMC in HVDC Transmission Systems", *IEEE Transactions on Power Delivery*, v. 32, n. 3, pp. 1471–1482, June 2017. ISSN: 0885-8977. doi:10.1109/TPWRD.2016.2604295.

[40] LEON, A. E., AMODEO, S. J. "Modeling, control, and reduced-order representation of modular multilevel converters", *Electric Power Sys-*

tems Research, v. 163, pp. 196 – 210, 2018. ISSN: 0378-7796. doi:10.1016/j.epsr.2018.05.024.

[41] HAO, Q., LI, Z., GAO, F., et al. "Reduced-Order Small-Signal Models of Modular Multilevel Converter and MMC-Based HVdc Grid", *IEEE Transactions on Industrial Electronics*, v. 66, n. 3, pp. 2257–2268, March 2019. doi:10.1109/TIE.2018.2869358.

[42] ZHU, S., LIU, P. K., QIN, L., et al. "Reduced-Order Dynamic Model of Modular Multilevel Converter in Long Time-Scale and Its Application in Power System Low-Frequency Oscillation Analysis", *IEEE Transactions on Power Delivery*, pp. 1–1, 2019. doi:10.1109/TPWRD.2019.2900070.

[43] WANG, G., XIAO, H., XIAO, L., et al. "Electromechanical Transient Modeling and Control Strategy of Decentralized Hybrid HVDC Systems", *Energies*, v. 12, n. 15, 2019. ISSN: 1996-1073. doi:10.3390/en12152856.

[44] XIAO, L., LI, Y., XIAO, H., et al. "Electromechanical Transient Modeling of Line Commutated Converter-Modular Multilevel Converter-Based Hybrid Multi-Terminal High Voltage Direct Current Transmission Systems", *Energies*, v. 11, n. 8, 2018. ISSN: 1996-1073. doi:10.3390/en11082102.

[45] TRINH, N. T., ZELLER, M., WUERFLINGER, K., et al. "Generic Model of MMC-VSC-HVDC for Interaction Study With AC Power System", *IEEE Transactions on Power Systems*, v. 31, n. 1, pp. 27–34, Jan 2016. ISSN: 0885-8950. doi:10.1109/TPWRS.2015.2390416.

[46] YANG, H., DONG, Y., LI, W., et al. "Average-Value Model of Modular Multilevel Converters Considering Capacitor Voltage Ripple", *IEEE Transactions on Power Delivery*, v. 32, n. 2, pp. 723–732, April 2017. ISSN: 0885-8977. doi:10.1109/TPWRD.2016.2555983.

[47] SUN, J., LIU, H. "Sequence Impedance Modeling of Modular Multilevel Converters", *IEEE Journal of Emerging and Selected Topics in Power Electronics*, v. 5, n. 4, pp. 1427–1443, Dec 2017. ISSN: 2168-6777. doi:10.1109/JESTPE.2017.2762408.

[48] KHAZAEI, J., BEZA, M., BONGIORNO, M. "Impedance Analysis of Modular Multi-Level Converters Connected to Weak AC Grids", *IEEE Transactions on Power Systems*, v. 33, n. 4, pp. 4015–4025, July 2018. ISSN: 0885-8950. doi:10.1109/TPWRS.2017.2779403.

[49] LIU, Z., MIAO, S., FAN, Z., et al. "Analysis of the performance characteristics and arm current control for modular multilevel converter with asymmetric arm parameters", *International Journal of Electrical Power & Energy Systems*, v. 110, pp. 258 – 270, 2019. ISSN: 0142-0615. doi:10.1016/j.ijepes.2019.03.010.

[50] WANG, J., GAO, S., JI, Z., et al. "Time/frequency domain modelling for grid-connected MMC sub-synchronous/super-synchronous oscillation in PV MVDC power collection and integration system", *IET Renewable Power Generation*, v. 13, n. 1, pp. 57–66, 2019. ISSN: 1752-1416. doi:10.1049/iet-rpg.2018.5041.

[51] MA, Y., LIN, H., WANG, Z. "Equivalent Model of Modular Multilevel Converter Considering Capacitor Voltage Ripples", *IEEE Transactions on Power Delivery*, pp. 1–1, 2019. doi:10.1109/TPWRD.2019.2915820.

[52] BESSEGATO, L., ILVES, K., HARNEFORS, L., et al. "Effects of Control on the AC-Side Admittance of a Modular Multilevel Converter", *IEEE Transactions on Power Electronics*, v. 34, n. 8, pp. 7206–7220, Aug 2019. ISSN: 0885-8993. doi:10.1109/TPEL.2018.2878600.

[53] LYU, J., CAI, X., MOLINAS, M. "Frequency Domain Stability Analysis of MMC-Based HVdc for Wind Farm Integration", *IEEE Journal of Emerging and Selected Topics in Power Electronics*, v. 4, n. 1, pp. 141–151, March 2016. ISSN: 2168-6777. doi:10.1109/JESTPE.2015.2498182.

[54] BEZA, M., BONGIORNO, M., STAMATIOU, G. "Analytical Derivation of the AC-Side Input Admittance of a Modular Multilevel Converter With Open- and Closed-Loop Control Strategies", *IEEE Transactions on Power Delivery*, v. 33, n. 1, pp. 248–256, Feb 2018. ISSN: 0885-8977. doi:10.1109/TPWRD.2017.2701415.

[55] SÁNCHEZ-SÁNCHEZ, E., PRIETO-ARAUJO, E., GOMIS-BELLMUNT, O. "The Role of the Internal Energy in MMCs Operating in Grid-Forming Mode", *IEEE Journal of Emerging and Selected Topics in Power Electronics*, pp. 1–1, 2019. ISSN: 2168-6785. doi:10.1109/JESTPE.2019.2961774.

[56] ROCABERT, J., LUNA, A., BLAABJERG, F., et al. "Control of Power Converters in AC Microgrids", *IEEE Transactions on Power Electronics*, v. 27, n. 11, pp. 4734–4749, Nov 2012. ISSN: 0885-8993. doi:10.1109/TPEL.2012.2199334.

[57] GOMIS-BELLMUNT, O., LIANG, J., EKANAYAKE, J., et al. “Topologies of multiterminal HVDC-VSC transmission for large offshore wind farms”, *Electric Power Systems Research*, v. 81, n. 2, pp. 271 – 281, 2011. ISSN: 0378-7796. doi:https://doi.org/10.1016/j.epsr.2010.09.006. Disponível em: <http://www.sciencedirect.com/science/article/pii/S0378779610002166>.

[58] WANG, L., NGUYEN THI, M. S. “Comparative Stability Analysis of Offshore Wind and Marine-Current Farms Feeding Into a Power Grid Using HVDC Links and HVAC Line”, *IEEE Transactions on Power Delivery*, v. 28, n. 4, pp. 2162–2171, Oct 2013. ISSN: 1937-4208. doi:10.1109/TPWRD.2013.2278039.

[59] LIU, H., SUN, J. “Voltage Stability and Control of Offshore Wind Farms With AC Collection and HVDC Transmission”, *IEEE Journal of Emerging and Selected Topics in Power Electronics*, v. 2, n. 4, pp. 1181–1189, Dec 2014. ISSN: 2168-6785. doi:10.1109/JESTPE.2014.2361290.

[60] VIDAL-ALBALATE, R., BELTRAN, H., ROLÁN, A., et al. “Analysis of the Performance of MMC Under Fault Conditions in HVDC-Based Offshore Wind Farms”, *IEEE Transactions on Power Delivery*, v. 31, n. 2, pp. 839–847, April 2016. ISSN: 0885-8977. doi:10.1109/TPWRD.2015.2468171.

[61] ROUZBEHI, K., ZHANG, W., IGNACIO CANDELA, J., et al. “Unified reference controller for flexible primary control and inertia sharing in multi-terminal voltage source converter-HVDC grids”, *IET Generation, Transmission Distribution*, v. 11, n. 3, pp. 750–758, 2017. ISSN: 1751-8695. doi:10.1049/iet-gtd.2016.0665.

[62] FREITAS, C. M., WATANABE, E. H., MONTEIRO, L. F. C. “A linearized small-signal Thévenin-equivalent model of a voltage-controlled modular multilevel converter”, *Electric Power Systems Research*, v. 182, pp. 106231, 2020. ISSN: 0378-7796. doi:10.1016/j.epsr.2020.106231.

[63] FALCAO, D. M., BORGES, C. L. T., TARANTO, G. N. “High Performance Computing in Electrical Energy Systems Applications”. In: Khaitan, S. K., Gupta, A. (Eds.), *High Performance Computing in Power and Energy Systems*, Springer Berlin Heidelberg, pp. 1–42, Berlin, Heidelberg, 2013. ISBN: 978-3-642-32683-7. doi:10.1007/978-3-642-32683-7_1.

[64] RAILING, B. D., MILLER, J. J., MOREAU, G., et al. “THE DIRECTLINK VSC-BASED HVDC PROJECT AND ITS COMMISSIONING”. In: *Proc. Session 2002 Cigre*. Cigre, 2002. Disponível

em: <https://e-cigre.org/publication/14-108_2002-the-direct-link-vsc-based-hvdc-project-and-its-commissioning>. accessed in July 10th, 2020.

[65] LARSSON, T., PETERSSON, A., EDRIS, A., et al. "Eagle Pass back-to-back tie: a dual purpose application of voltage source converter technology". In: *2001 Power Engineering Society Summer Meeting. Conference Proceedings (Cat. No.01CH37262)*, v. 3, pp. 1686–1691 vol.3, 2001. doi:10.1109/PESS.2001.970329.

[66] KIM, J., MIN, B., SHENDEREY, S. V., et al. "High Voltage Pulsed Power Supply Using IGBT Stacks", *IEEE Transactions on Dielectrics and Electrical Insulation*, v. 14, n. 4, pp. 921–926, 2007. doi:10.1109/TDEI.2007.4286526.

[67] SOONWOOK HONG, VENKATESH CHITTA, TORREY, D. A. "Series connection of IGBT's with active voltage balancing", *IEEE Transactions on Industry Applications*, v. 35, n. 4, pp. 917–923, 1999. doi:10.1109/28.777201.

[68] MASSOUD, A. M., FINNEY, S. J., WILLIAMS, B. W. "Multilevel converters and series connection of IGBT evaluation for high-power, high-voltage applications". In: *Second International Conference on Power Electronics, Machines and Drives (PEMD 2004).*, v. 1, pp. 1–5 Vol.1, 2004. doi:10.1049/cp:20040249.

[69] ROHNER, S., BERNET, S., HILLER, M., et al. "Modulation, Losses, and Semiconductor Requirements of Modular Multilevel Converters", *IEEE Transactions on Industrial Electronics*, v. 57, n. 8, pp. 2633–2642, 2010. doi:10.1109/TIE.2009.2031187.

[70] FRANCOS, P. L., VERDUGO, S. S., ÁLVAREZ, H. F., et al. "INELFE - Europe's first integrated onshore HVDC interconnection". In: *2012 IEEE Power and Energy Society General Meeting*, pp. 1–8, July 2012. doi:10.1109/PESGM.2012.6344799.

[71] ORTHS, A., BIALEK, J., CALLAVIK, M., et al. "Connecting the Dots: Regional Coordination for Offshore Wind and Grid Development", *IEEE Power and Energy Magazine*, v. 11, n. 6, pp. 83–95, Nov 2013. ISSN: 1540-7977. doi:10.1109/MPE.2013.2278044.

[72] ANEEL. "Banco de Informações de Geração". urlhttp://www2.aneel.gov.br/aplicacoes/capacidadebrasil/capacidadebrasil.cfm, fev. 2020. Acessado em: Feb 22, 2017.

[73] ONS. *Boletim Mensal de Geração Eólica*. Relatório técnico, Operador Nacional do Sistema Elétrico, dez. 2019. Disponível em: <`http://www.ons.org.br/AcervoDigitalDocumentosEPublicacoes/Boletim%20Mensal%20de%20Gera%C3%A7%C3%A3o%20Eolica%202019-12.pdf`>. Accessed in July 14, 2020.

[74] GAUDARDE, G. "Neoenergia estuda três complexos eólicos offshore no Ceará, RJ e RS". 2020. Disponível em: <`https://epbr.com.br/eolicas-offshore-novos-projetos-somam-9-gw-de-capacidade-instalada/`>. Accessed: Feb 22, 2020.

[75] EPE. *Roadmap eólica offshore no Brasil*. Relatório técnico, Empresa de Pesquiza Energética, 2020. Disponível em: <`http://www.epe.gov.br/sites-pt/publicacoes-dados-abertos/publicacoes/PublicacoesArquivos/publicacao-456/Roadmap_Eolica_Offshore_EPE_versao_R1.pdf`>. accesced: Feb 22, 2020.

[76] P., H. M., BINA, M. T. "A Transformerless Medium-Voltage STATCOM Topology Based on Extended Modular Multilevel Converters", *IEEE Transactions on Power Electronics*, v. 26, n. 5, pp. 1534–1545, 2011. doi:10.1109/TPEL.2010.2085088.

[77] KONTOS, E., TSOLARIDIS, G., TEODORESCU, R., et al. "High Order Voltage and Current Harmonic Mitigation Using the Modular Multilevel Converter STATCOM", *IEEE Access*, v. 5, pp. 16684–16692, 2017. doi:10.1109/ACCESS.2017.2749119.

[78] LIU, X., LV, J., GAO, C., et al. "A Novel STATCOM Based on Diode-Clamped Modular Multilevel Converters", *IEEE Transactions on Power Electronics*, v. 32, n. 8, pp. 5964–5977, 2017. doi:10.1109/TPEL.2016.2616495.

[79] CUPERTINO, A. F., FARIAS, J. V. M., PEREIRA, H. A., et al. "Comparison of DSCC and SDBC Modular Multilevel Converters for STATCOM Application During Negative Sequence Compensation", *IEEE Transactions on Industrial Electronics*, v. 66, n. 3, pp. 2302–2312, 2019. doi:10.1109/TIE.2018.2811361.

[80] ABB. "SVC Light: The next generation". 2011. Disponível em: <https://library.e.abb.com/public/0cd6a99c795508fcc1256fda003b4cec/SVC%20Light_brochure.pdf>. Accessed in July 11, 2020.

[81] ABB. "A matter of FACTS". 2016. Disponível em: <https://search.abb.com/library/Download.aspx?DocumentID=1JNS018770&LanguageCode=en&DocumentPartId=&Action=Launch>. Accessed in July 11, 2020.

[82] GE GRID SOLUTIONS. "Flexible AC Transmission Systems". 2016. Disponível em: <https://www.gegridsolutions.com/products/brochures/services/facts_gea32010-lr.pdf>. Accessed in July 11, 2020.

[83] GE GRID SOLUTIONS. "Static Synchronous Compensator (STATCOM) Solutions". 2018. Disponível em: <https://www.gegridsolutions.com/products/brochures/powerd_vtf/statcom_gea31986_hr.pdf>. Accessed in July 11, 2020.

[84] SIEMENS. "FACTS: Solutions for industry". 2016. Disponível em: <https://assets.new.siemens.com/siemens/assets/api/uuid:4f6acbb0e2524be50a5f6ac110297efdcf9a9108/version:1490614184/263-160099-db-svc-industry-o2e-161028.pdf>. Accessed in July 11, 2020.

[85] SIEMENS. "Parallel compensation: Comprehensive solutions for safe and reliable grid operation". 2016. Disponível em: <https://assets.new.siemens.com/siemens/assets/api/uuid:d3e2a900-0b9b-4a55-9ccc-08db73063415/version:1541584203/emts-b10018-00-7600.pdf>. Accessed in July 11, 2020.

[86] VATANI, M., HOVD, M., SAEEDIFARD, M. "Control of the Modular Multilevel Converter Based on a Discrete-Time Bilinear Model Using the Sum of Squares Decomposition Method", *IEEE Transactions on Power Delivery*, v. 30, n. 5, pp. 2179–2188, Oct 2015. ISSN: 0885-8977. doi:10.1109/TPWRD.2015.2412151.

[87] KONSTANTINOU, G., ZHANG, J., CEBALLOS, S., et al. "Comparison and evaluation of sub-module configurations in modular multilevel converters". In: *2015 IEEE 11th International Conference on Power Electronics and Drive Systems*, pp. 958–963, June 2015. doi:10.1109/PEDS.2015.7203440.

[88] MESHRAM, P. M., BORGHATE, V. B. "A Simplified Nearest Level Control (NLC) Voltage Balancing Method for Modular Multilevel Converter

(MMC)", *IEEE Transactions on Power Electronics*, v. 30, n. 1, pp. 450–462, Jan 2015. ISSN: 1941-0107. doi:10.1109/TPEL.2014.2317705.

[89] DEBNATH, S., QIN, J., BAHRANI, B., et al. "Operation, Control, and Applications of the Modular Multilevel Converter: A Review", *IEEE Transactions on Power Electronics*, v. 30, n. 1, pp. 37–53, Jan 2015. ISSN: 0885-8993. doi:10.1109/TPEL.2014.2309937.

[90] TU, Q., XU, Z., XU, L. "Reduced Switching-Frequency Modulation and Circulating Current Suppression for Modular Multilevel Converters", *IEEE Transactions on Power Delivery*, v. 26, n. 3, pp. 2009–2017, July 2011. ISSN: 1937-4208. doi:10.1109/TPWRD.2011.2115258.

[91] AKAGI, H., WATANABE, E., AREDES, M. *Instantaneous Power Theory and Applications to Power Conditioning.* IEEE Press Series on Power Engineering. New Jersey, Wiley, 2017. ISBN: 9781118362105. doi:10.1002/9781119307181.

[92] LI, B., XU, Z., SHI, S., et al. "Comparative Study of the Active and Passive Circulating Current Suppression Methods for Modular Multilevel Converters", *IEEE Transactions on Power Electronics*, v. 33, n. 3, pp. 1878–1883, March 2018. ISSN: 0885-8993. doi:10.1109/TPEL.2017.2737541.

[93] KONSTANTINOU, G., POU, J., CEBALLOS, S., et al. "Control of Circulating Currents in Modular Multilevel Converters Through Redundant Voltage Levels", *IEEE Transactions on Power Electronics*, v. 31, n. 11, pp. 7761–7769, Nov 2016. ISSN: 0885-8993. doi:10.1109/TPEL.2015.2512842.

[94] DARUS, R., POU, J., KONSTANTINOU, G., et al. "Controllers for eliminating the ac components in the circulating current of modular multilevel converters", *IET Power Electronics*, v. 9, n. 1, pp. 1–8, 2016. ISSN: 1755-4535. doi:10.1049/iet-pel.2014.0930.

[95] FERREIRA, J. R. B. L. *Sistema HVDC multiterminal com conversores comutados pela linha e conveersores multinível modulares.* Tese de Doutorado, COPPE/UFRJ, 2019. Disponível em: <http://www.pee.ufrj.br/index.php/pt/producao-academica/teses-de-doutorado/2019/2016033350--167/file>.

[96] ANGQUIST, L., ANTONOPOULOS, A., SIEMASZKO, D., et al. "Open-Loop Control of Modular Multilevel Converters Using Estimation of Stored Energy", *IEEE Transactions on Industry Applicati-

ons, v. 47, n. 6, pp. 2516–2524, Nov 2011. ISSN: 0093-9994. doi:10.1109/TIA.2011.2168593.

[97] MAHDAVI, J., EMAADI, A., BELLAR, M. D., et al. "Analysis of power electronic converters using the generalized state-space averaging approach", *IEEE Transactions on Circuits and Systems I: Fundamental Theory and Applications*, v. 44, n. 8, pp. 767–770, Aug 1997. ISSN: 1558-1268. doi:10.1109/81.611275.

[98] DAVOUDI, A., JATSKEVICH, J., RYBEL, T. D. "Numerical state-space average-value modeling of PWM DC-DC converters operating in DCM and CCM", *IEEE Transactions on Power Electronics*, v. 21, n. 4, pp. 1003–1012, July 2006. ISSN: 1941-0107. doi:10.1109/TPEL.2006.876848.

[99] BORDONAU, J., COSAN, M., BOROJEVIC, D., et al. "A state-space model for the comprehensive dynamic analysis of three-level voltage-source inverters". In: *PESC97. Record 28th Annual IEEE Power Electronics Specialists Conference. Formerly Power Conditioning Specialists Conference 1970-71. Power Processing and Electronic Specialists Conference 1972*, v. 2, pp. 942–948 vol.2, June 1997. doi:10.1109/PESC.1997.616837.

[100] KROUTIKOVA, N., A. HERNANDEZ-ARAMBURO, C., GREEN, T. C. "State-space model of grid-connected inverters under current control mode", *IET Electric Power Applications*, v. 1, n. 3, pp. 329–338, May 2007. ISSN: 1751-8679. doi:10.1049/iet-epa:20060276.

[101] LUDOIS, D. C., VENKATARAMANAN, G. "Simplified Terminal Behavioral Model for a Modular Multilevel Converter", *IEEE Transactions on Power Electronics*, v. 29, n. 4, pp. 1622–1631, 2014. doi:10.1109/TPEL.2013.2268856.

[102] LU, X., XIANG, W., LIN, W., et al. "State-space model and PQ operating zone analysis of hybrid MMC", *Electric Power Systems Research*, v. 162, pp. 99 – 108, 2018. ISSN: 0378-7796. doi:10.1016/j.epsr.2018.05.003.

[103] BERGNA-DIAZ, G., FREYTES, J., GUILLAUD, X., et al. "Generalized Voltage-Based State-Space Modeling of Modular Multilevel Converters With Constant Equilibrium in Steady State", *IEEE Journal of Emerging and Selected Topics in Power Electronics*, v. 6, n. 2, pp. 707–725, June 2018. ISSN: 2168-6777. doi:10.1109/JESTPE.2018.2793159.

[104] MARZOUGHI, A., BURGOS, R., BOROYEVICH, D., et al. "Steady-state analysis of voltages and currents in modular multilevel converter based

on average model". In: *2015 IEEE Energy Conversion Congress and Exposition (ECCE)*, pp. 3522–3528, 2015. doi:10.1109/ECCE.2015.7310158.

[105] ZHAO, F., XIAO, G., ZHAO, T. "Accurate Steady-State Mathematical Models of Arm and Line Harmonic Characteristics for Modular Multilevel Converter", *IEEE Transactions on Power Delivery*, v. 33, n. 3, pp. 1308–1318, 2018. doi:10.1109/TPWRD.2017.2764950.

[106] NODA, T., SEMLYEN, A., IRAVANI, R. "Harmonic domain dynamic transfer function of a nonlinear time-periodic network", *IEEE Transactions on Power Delivery*, v. 18, n. 4, pp. 1433–1441, Oct 2003. ISSN: 0885-8977. doi:10.1109/TPWRD.2003.817788.

[107] LYU, J., ZHANG, X., CAI, X., et al. "Harmonic State-Space Based Small-Signal Impedance Modeling of Modular Multilevel Converter with Consideration of Internal Harmonic Dynamics", *IEEE Transactions on Power Electronics*, pp. 1–1, 2018. ISSN: 0885-8993. doi:10.1109/TPEL.2018.2842682.

[108] YUAN, X., MERK, W., STEMMLER, H., et al. "Stationary-frame generalized integrators for current control of active power filters with zero steady-state error for current harmonics of concern under unbalanced and distorted operating conditions", *IEEE Transactions on Industry Applications*, v. 38, n. 2, pp. 523–532, March 2002. ISSN: 0093-9994. doi:10.1109/28.993175.

[109] ZMOOD, D. N., HOLMES, D. G. "Stationary frame current regulation of PWM inverters with zero steady-state error", *IEEE Transactions on Power Electronics*, v. 18, n. 3, pp. 814–822, 2003. doi:10.1109/TPEL.2003.810852.

[110] WANG, J., BURGOS, R., BOROYEVICH, D. "Switching-Cycle State-Space Modeling and Control of the Modular Multilevel Converter", *IEEE Journal of Emerging and Selected Topics in Power Electronics*, v. 2, n. 4, pp. 1159–1170, Dec 2014. ISSN: 2168-6777. doi:10.1109/JESTPE.2014.2354393.

[111] MATHWORKS. "Matlab". 2020. Disponível em: <`https://nl.mathworks.com/products/matlab.html`>. Accessed in August 14th, 2020.

[112] WANG, X., HARNEFORS, L., BLAABJERG, F. "Unified Impedance Model of Grid-Connected Voltage-Source Converters", *IEEE Transac-*

tions on Power Electronics, v. 33, n. 2, pp. 1775–1787, Feb 2018. doi:10.1109/TPEL.2017.2684906.

[113] "GNU Octave". 2020. Disponível em: <https://www.gnu.org/software/octave/>. Accessed in August 14th, 2020.

[114] "Python". 2020. Disponível em: <https://www.python.org/>. Accessed in August 14th, 2020.

[115] FREITAS, C. M. "PhD-Theses Matlab Codes". 2020. Disponível em: <https://github.com/cleitoncmf/PhD-Thesis-Codes>.

[116] MATHWORKS. "inv". 2020. Disponível em: <https://nl.mathworks.com/help/matlab/ref/inv.html>. Accessed in July 20th, 2020.

[117] MATHWORKS. "mtimes, *". 2020. Disponível em: <https://www.mathworks.com/help/matlab/ref/mtimes.html>. Accessed in July 20th, 2020.

[118] BEERTEN, J., DIAZ, G. B., D'ARCO, S., et al. "Comparison of small-signal dynamics in MMC and two-level VSC HVDC transmission schemes". In: *2016 IEEE International Energy Conference (ENERGYCON)*, pp. 1–6, 2016. doi:10.1109/ENERGYCON.2016.7514048.

[119] DE CARVALHO, K. J. S. *COMPORTAMENTO DE CONVERSORES FONTE DE TENSÃO E FILTRO LCL NA PRESENÇA DE HARMÔNICOS NA REDE*. Tese de Doutorado, Universidade Federal do Rio de Janeiro, 2019. Disponível em: <http://www.pee.ufrj.br/index.php/pt/producao-academica/teses-de-doutorado/2019/2016033337--158/file>.

[120] XIAOMING YUAN, MERK, W., STEMMLER, H., et al. "Stationary-frame generalized integrators for current control of active power filters with zero steady-state error for current harmonics of concern under unbalanced and distorted operating conditions", *IEEE Transactions on Industry Applications*, v. 38, n. 2, pp. 523–532, March 2002. ISSN: 1939-9367. doi:10.1109/28.993175.

[121] PEREIRA, L. F. A., FLORES, J. V., BONAN, G., et al. "Multiple Resonant Controllers for Uninterruptible Power Supplies—A Systematic Robust Control Design Approach", *IEEE Transactions on Industrial Electronics*, v. 61, n. 3, pp. 1528–1538, March 2014. ISSN: 1557-9948. doi:10.1109/TIE.2013.2259781.

[122] LISERRE, M., TEODORESCU, R., BLAABJERG, F. “Multiple harmonics control for three-phase grid converter systems with the use of PI-RES current controller in a rotating frame”, *IEEE Transactions on Power Electronics*, v. 21, n. 3, pp. 836–841, May 2006. ISSN: 1941-0107. doi:10.1109/TPEL.2006.875566.

[123] OCTAVE. “minreal”. 2020. Disponível em: <`https://octave.sourceforge.io/control/function/@lti/minreal.html`>.

[124] MATHWORKS. “mineal: Minimal realization or pole-zero cancellation”. `https://la.mathworks.com/help/control/ref/minreal.html`, 2019. Accessed: 2020-02-05.

[125] SUN, J. “Impedance-Based Stability Criterion for Grid-Connected Inverters”, *IEEE Transactions on Power Electronics*, v. 26, n. 11, pp. 3075–3078, Nov 2011. ISSN: 0885-8993. doi:10.1109/TPEL.2011.2136439.

[126] KRAUSE, P., WASYNCZUK, O., SUDHOFF, S. D., et al. “Reference-Frame Theory”. In: *Analysis of Electric Machinery and Drive Systems*, pp. 86–120, New Jersey, Wiley-IEEE Press, 2013. doi:10.1002/9781118524336.ch3.

[127] FREITAS, C. M. “Jupyter notebook for computing the steady-state solution of the modular multilevel converter”. mar. 2020. Disponível em: <`https://mybinder.org/v2/gh/cleitoncmf/Steady-State/108debcfbbbd226ca7150704d3ca877d2bd155d3`>.

Apêndice A

Relationships between natural and synchronous reference frame

This appendix is focused on presenting a brief review of frame transformations and its effects on mathematical models of three-phase systems.

A.1 Definition

To understand how frame transformation work, lets first consider a balanced three-phase in which the bus voltage v and the current i can be represented as follows:

$$\begin{cases} v_a(t) = V_m sin(\omega t) \\ v_b(t) = V_m sin(\omega t - 2\pi/3) \\ v_c(t) = V_m sin(\omega t + 2\pi/3) \end{cases}, \tag{A.1}$$

$$\begin{cases} i_a(t) = I_m sin(\omega t + \phi_i) \\ i_b(t) = I_m sin(\omega t - 2\pi/3 + \phi_i) \\ i_c(t) = I_m sin(\omega t + 2\pi/3 + \phi_i) \end{cases}, \tag{A.2}$$

where V_m and I_m are the amplitudes of voltage and current, ω is the angular frequency of the fundamental component, and ϕ_i is the displacement angle. This set of equations is represented in Natural Reference Frame (NRF), that is, they did not suffer any frame transformation.

To simplify some mathematical manipulations, it is defined the vector $\mathbf{v}^{abc}$ and $\mathbf{i}^{abc}$ containing the three phase components of v and i as follows:

$$\mathbf{v}^{abc}(t) = \begin{bmatrix} v_a \\ v_b \\ v_c \end{bmatrix}, \tag{A.3}$$

$$\mathbf{i}^{abc}(t) = \begin{bmatrix} i_a \\ i_b \\ i_c \end{bmatrix}. \tag{A.4}$$

The frame transformation defined in Section 4.2.1 and its inverse are rewritten here for easier understanding:

$$\mathbf{T}_{dq0} = \frac{2}{3} \begin{bmatrix} \cos(\theta) & \cos\left(\theta - \frac{2\pi}{3}\right) & \cos\left(\theta + \frac{2\pi}{3}\right) \\ \sin(\theta) & \sin\left(\theta - \frac{2\pi}{3}\right) & \sin\left(\theta + \frac{2\pi}{3}\right) \\ \frac{1}{2} & \frac{1}{2} & \frac{1}{2} \end{bmatrix}, \tag{A.5}$$

$$\mathbf{T}_{dq0}^{-1} = \begin{bmatrix} \cos(\theta) & \sin(\theta) & 1 \\ \cos\left(\theta - \frac{2\pi}{3}\right) & \sin\left(\theta - \frac{2\pi}{3}\right) & 1 \\ \cos\left(\theta + \frac{2\pi}{3}\right) & \sin\left(\theta + \frac{2\pi}{3}\right) & 1 \end{bmatrix}. \tag{A.6}$$

In both cases, the angle θ defines the frame transformation to be applied. If θ is constant, we have a static transformation[126]. For instance, the abc to $\alpha\beta 0$ transformation (also known as Clark transformation) is obtained when $\theta = 0$. Here the *static* means that there is no change in the frequencies of the harmonic/sequence components of either $\mathbf{v}^{abc}$ or $\mathbf{i}^{abc}$ due to the transformation. When θ rotates synchronously with the fundamental frequency, that is, $\theta = \omega t$, the transformation in (A.5) changes the variables into a Synchronous Reference Frame (SRF). The major effect is that the positive-sequence fundamental components in $\mathbf{v}^{abc}$ or $\mathbf{i}^{abc}$ are transformed in dc quantities (frequency shift).

For a better understanding of the mathematical approach, here it is presented the relationships between NRF and SRF variables:

$$\mathbf{v}^{dq0}(t) = \mathbf{T}_{dq0}\mathbf{v}^{abc}(t) \Longleftrightarrow \mathbf{v}^{abc}(t) = \mathbf{T}_{dq0}^{-1}\mathbf{v}^{dq0}(t), \tag{A.7}$$

$$\mathbf{i}^{dq0}(t) = \mathbf{T}_{dq0}\mathbf{i}^{abc}(t) \Longleftrightarrow \mathbf{i}^{abc}(t) = \mathbf{T}_{dq0}^{-1}\mathbf{i}^{dq0}(t). \tag{A.8}$$

A.2 Effects of SRF transformations into variables with multiple harmonic/sequence components

The previous section mentioned that the SRF transformation changes fundamental-frequency sinusoidal components into dc quantities. Here, we expand this analysis considering different harmonic/sequence components. Let:

$$\mathbf{i}^{abc}(t) = \mathbf{i}_{+1}^{abc}(t) + \mathbf{i}_{-1}^{abc}(t) + \mathbf{i}_{-5}^{abc}(t) + \mathbf{i}_{+7}^{abc}(t) + \mathbf{i}_{-11}^{abc}(t) + \mathbf{i}_{+13}^{abc}(t), \tag{A.9}$$

where the subscripts + and − indicate positive or negative sequence and the integer following them represents the harmonic order.

Each component of order $\pm h$ in (A.9) is represented by:

$$\mathbf{i}_{+h}^{abc}(t) = \begin{bmatrix} I_{+h}\sin\left(h\omega t + \phi_{+h}\right) \\ I_{+h}\sin\left(h\omega t - 2\pi/3 + \phi_{+h}\right) \\ I_{+h}\sin\left(h\omega t + 2\pi/3 + \phi_{+h}\right) \end{bmatrix} \tag{A.10}$$

$$\mathbf{i}_{-h}^{abc}(t) = \begin{bmatrix} I_{-h}\sin\left(h\omega t + \phi_{-h}\right) \\ I_{-h}\sin\left(h\omega t + 2\pi/3 + \phi_{-h}\right) \\ I_{-h}\sin\left(h\omega t - 2\pi/3 + \phi_{-h}\right) \end{bmatrix} \tag{A.11}$$

In this case, the currents in SRF become:

$$\begin{aligned} i^d(t) = I_{+1}\sin(\phi_{+1}) + I_{-1}\sin(2\omega t + \phi_{-1}) \\ + I_{-5}\sin(6\omega t + \phi_{-5}) + I_{+7}\sin(6\omega t + \phi_{+7}) \\ + I_{-11}\sin(12\omega t + \phi_{-11}) + I_{+13}\sin(12\omega t + \phi_{+13}), \end{aligned} \tag{A.12}$$

$$\begin{aligned} i^q(t) = I_{+1}\cos(\phi_{+1}) - I_{-1}\cos(2\omega t + \phi_{-1}) \\ - I_{-5}\cos(6\omega t + \phi_{-5}) + I_{+7}\cos(6\omega t + \phi_{+7}) \\ - I_{-11}\cos(12\omega t + \phi_{-11}) + I_{+13}\cos(12\omega t + \phi_{+13}), \end{aligned} \tag{A.13}$$

$$i^0(t) = 0. \tag{A.14}$$

As it was already mentioned, the positive-sequence fundamental component was turned into dc quantities $I_{+1}\sin(\phi_{+1})$ and $I_{+1}\cos(\phi_{+1})$. Equations (A.11) and (A.11) also show that negative-sequence fundamental component was shifted into 2ω, being represented in SRF by the terms $I_{-1}\sin(2\omega t+\phi_{-1})$ and $I_{-1}\cos(2\omega t+\phi_{-1})$. The negative-sequence fifth-order and the positive-sequence seventh-order, on the other hand, were shifted into 6ω. Finally, the negative-sequence eleventh-order and positive-sequence thirteenth-order harmonic components were shifted into 12ω.

It is possible to generalize the previous results as follows:

$$i_h^d(t) = \begin{cases} +I_{-h}\sin\left[(h+1)\,\omega t + \phi_{-h}\right], & \text{for negative sequence} \\ +I_{+h}\sin\left[(h-1)\,\omega t + \phi_{+h}\right], & \text{for positive sequence} \end{cases}, \tag{A.15}$$

$$i_h^q(t) = \begin{cases} -I_{-h}\cos\left[(h+1)\,\omega t + \phi_{-h}\right], & \text{for negative sequence} \\ +I_{+h}\cos\left[(h-1)\,\omega t + \phi_{+h}\right], & \text{for positive sequence} \end{cases}, \tag{A.16}$$

In this case, h is the harmonic order ($h = 1$ for the fundamental component), and $(h \pm 1)\omega$ is the frequency in which this component appears in SRF dq axes. It is important to notice that, although the results were presented considering currents, the same is also valid for voltages.

A.3 Effects of generic frame transformations into variables with multiple harmonic/sequence components

In some cases it necessary to use other reference frames for analyzing a system. This is the case, for instance, of the analyzes in Section 4.2.2, where a D-SRF (frame transformation considering $\theta = 2\omega$) transformation is considered. Thus, the effects shown at the end of the previous sections are extended here for generic transformations.

Considering a generic frame transformation where $\theta = \omega_F t$, and $\omega_F = \pm h\omega$ depending on the frame transformation is aligned with the positive/negative sequence of the hth-order harmonic component. In this case, the currents in (A.11) are represented in this new reference frame as follows:

$$i_h^d(t) = \begin{cases} +I_{-h}\sin\left[(h\omega + \omega_F)\,t + \phi_{-h}\right], & \text{for negative sequence} \\ +I_{+h}\sin\left[(h\omega - \omega_F)\,t + \phi_{+h}\right], & \text{for positive sequence} \end{cases}, \tag{A.17}$$

$$i_h^q(t) = \begin{cases} -I_{-h}\cos\left[(h\omega + \omega_F)\,t + \phi_{-h}\right], & \text{for negative sequence} \\ +I_{+h}\cos\left[(h\omega - \omega_F)\,t + \phi_{+h}\right], & \text{for positive sequence} \end{cases}, \tag{A.18}$$

A.4 Applying the transformation into algebraic equations

Lets first consider a generic voltage-across-resistor matrix equation in NRF:

$$\mathbf{v}_r^{abc}(t) = R\,\mathbf{i}_r^{abc}(t) \tag{A.19}$$

where $\mathbf{v}_r^{abc}$ and $\mathbf{i}_r^{abc}$ are the voltage and current vectors, and R is the resistance.

To change (A.19) into SRF, it necessary to substitute the following results in it:

$$\mathbf{v}_r^{abc}(t) = \mathbf{T}_{dq0}^{-1}\ \mathbf{v}_r^{dq0}(t), \tag{A.20}$$

$$\mathbf{i}_r^{abc}(t) = \mathbf{T}_{dq0}^{-1}\ \mathbf{i}_r^{dq0}(t). \tag{A.21}$$

Thus,

$$\mathbf{T}_{dq0}^{-1}\ \mathbf{v}_r^{dq0}(t) = R\ \mathbf{T}_{dq0}^{-1}\ \mathbf{i}_r^{dq0}(t) \tag{A.22}$$

Multiplying both sided by $\mathbf{T}_{dq0}$ on the left side:

$$\mathbf{v}_r^{dq0}(t) = R\ \mathbf{i}_r^{dq0}(t) \tag{A.23}$$

It is possible to observe that the SRF transformation does not change the pattern of the equation. This is valid for any algebraic equation.

A.5 Applying the transformation into differential equations

Let us consider in this time a generic voltage-across-inductor matrix equation in NRF:

$$\mathbf{v}_L^{abc}(t) = L\ \frac{d}{dt}\mathbf{i}_L^{abc}(t) \tag{A.24}$$

where $\mathbf{v}_L^{abc}$ and $\mathbf{i}_L^{abc}$ are the voltage and current vectors, and L is the inductance.

It is necessary, now, to follow the same steps presented in the previous section, i.e:

$$\mathbf{v}_L^{abc}(t) = \mathbf{T}_{dq0}^{-1}\ \mathbf{v}_L^{dq0}(t), \tag{A.25}$$

$$\mathbf{i}_L^{abc}(t) = \mathbf{T}_{dq0}^{-1}\ \mathbf{i}_L^{dq0}(t). \tag{A.26}$$

Making the substitution leads to:

$$\mathbf{T}_{dq0}^{-1}\ \mathbf{v}_L^{dq0}(t) = L\ \frac{d}{dt}\left[\mathbf{T}_{dq0}^{-1}\ \mathbf{i}_L^{dq0}(t)\right] \tag{A.27}$$

Considering the chain rule of calculus, it is possible to obtain the following result:

$$\mathbf{T}_{dq0}^{-1}\ \mathbf{v}_L^{dq0}(t) = L\ \frac{d}{dt}\left[\mathbf{T}_{dq0}^{-1}\right]\mathbf{i}_L^{dq0}(t) + L\ \mathbf{T}_{dq0}^{-1}\frac{d}{dt}\left[\mathbf{i}_L^{dq0}(t)\right] \tag{A.28}$$

Multiplying both sides of the equation by $\mathbf{T}_{dq0}$ leads to:

$$\mathbf{v}_L^{dq0}(t) = L\ \mathbf{\Omega}_c(\theta)\ \mathbf{i}_L^{dq0}(t) + L\ \frac{d}{dt}\left[\mathbf{i}_L^{dq0}(t)\right]. \tag{A.29}$$

$$\mathbf{\Omega}_c(\theta) = \mathbf{T}_{dq0}\frac{d}{dt}\left[\mathbf{T}_{dq0}^{-1}\right] \tag{A.30}$$

Observe in (A.29) that, differently from the algebraic case, the pattern of the differential equation is changed. In this case, the matrix term $\mathbf{\Omega}_c$ represents the coupling between the direct and quadrature axes. For the SRF transformation used in Section 4.2, $\mathbf{\Omega}_c(\theta)$ can be simplified as follows:

$$\mathbf{\Omega} = \mathbf{\Omega}_c(\omega t) = \begin{bmatrix} 0 & -\omega_0 & 0 \\ \omega_0 & 0 & 0 \\ 0 & 0 & 0 \end{bmatrix} \tag{A.31}$$

where ω_0 is the angular frequency of the fundamental component.

Apêndice B

Steady-state results of the Section 3.5

This Appendix presents the results which did not fit in Section 3.5. The first section presents the representation of the linear system used do compute the steady-state result of the MMC, while the second presents part of the results. Due to the size of the mathematical expressions, it was decided to provide a Jupyter notebook containing the python code and any explanation necessary to use it in the following reference [127]. It was wrapped in a Binder environment, which also can be assessed clicking **HERE**, which allows the user to run the code without the need to install anything on your computer.

B.1 Linear system

$$\mathbf{X}_{ss} = \begin{bmatrix} X_{icir} & X_{vdcp} & X_{vdcn} \end{bmatrix}^T, \tag{B.1}$$

$$X_{icir} = \begin{bmatrix} I_{cir_{2s}} & I_{cir_{2c}} & I_{cir_{4s}} & I_{cir_{4c}} \end{bmatrix}, \tag{B.2}$$

$$X_{vdcn} = \begin{bmatrix} V^n_{dc_{1s}} & V^n_{dc_{1c}} & V^n_{dc_{2s}} & V^n_{dc_{2c}} & V^n_{dc_{3s}} & V^n_{dc_{3c}} & V^n_{dc_{4s}} & V^n_{dc_{4c}} \end{bmatrix}, \tag{B.3}$$

$$X_{vdcp} = \begin{bmatrix} V^p_{dc_{1s}} & V^p_{dc_{1c}} & V^p_{dc_{2s}} & V^p_{dc_{2c}} & V^p_{dc_{3s}} & V^p_{dc_{3c}} & V^p_{dc_{4s}} & V^p_{dc_{4c}} \end{bmatrix}. \tag{B.4}$$

$$\mathbf{B}_{ss} = \begin{bmatrix} \mathbf{B}^1_{ss} \\ \mathbf{0}_{4\times 1} \\ \mathbf{B}^2_{ss} \\ \mathbf{0}_{4\times 1} \\ \mathbf{0}_{4\times 1} \end{bmatrix} \tag{B.5}$$

$$\mathbf{0}_{4\times 1} = \begin{bmatrix} 0 \\ 0 \\ 0 \\ 0 \end{bmatrix} \tag{B.6}$$

$$\mathbf{B}_{ss}^{1} = \begin{bmatrix} -\frac{E_0^{s*} I_{cir_0}}{2} + \frac{1}{4} I_{0s} \\ -\frac{E_0^{c*} I_{cir_0}}{2} + \frac{1}{4} I_{0c} \\ -\frac{1}{8} E_0^{c*} I_{0s} - \frac{1}{8} E_0^{s*} I_{0c} \\ -\frac{1}{8} E_0^{c*} I_{0c} + \frac{1}{8} E_0^{s*} I_{0s} \end{bmatrix} \tag{B.7}$$

$$\mathbf{B}_{ss}^{2} = \begin{bmatrix} \frac{E_0^{s*} I_{cir_0}}{2} - \frac{1}{4} I_{0s} \\ \frac{E_0^{c*} I_{cir_0}}{2} - \frac{1}{4} I_{0c} \\ -\frac{1}{8} E_0^{c*} I_{0s} - \frac{1}{8} E_0^{s*} I_{0c} \\ -\frac{1}{8} E_0^{c*} I_{0c} + \frac{1}{8} E_0^{s*} I_{0s} \end{bmatrix} \tag{B.8}$$

$$\mathbf{A}_{ss} = \begin{bmatrix}
E_{c,s} & \mathbf{0}_{2\times 2} & \mathbf{0}_{2\times 2} & \mathbf{0}_{2\times 2} & \mathbf{0}_{2\times 2} & \mathbf{0}_{2\times 2} & \mathbf{M}_{Ceq}^{\omega} & \mathbf{0}_{2\times 2} & \mathbf{0}_{2\times 2} & \mathbf{0}_{2\times 2} \\
-\frac{1}{2}\mathbf{I} & \mathbf{0}_{2\times 2} & \mathbf{0}_{2\times 2} & \mathbf{0}_{2\times 2} & \mathbf{0}_{2\times 2} & \mathbf{0}_{2\times 2} & \mathbf{0}_{2\times 2} & 2\mathbf{M}_{Ceq}^{\omega} & \mathbf{0}_{2\times 2} & \mathbf{0}_{2\times 2} \\
E_{c,s}^{T} & E_{c,s} & \mathbf{0}_{2\times 2} & \mathbf{0}_{2\times 2} & \mathbf{0}_{2\times 2} & \mathbf{0}_{2\times 2} & \mathbf{0}_{2\times 2} & \mathbf{0}_{2\times 2} & 3\mathbf{M}_{Ceq}^{\omega} & \mathbf{0}_{2\times 2} \\
\mathbf{0}_{2\times 2} & -\frac{1}{2}\mathbf{I} & \mathbf{0}_{2\times 2} & \mathbf{0}_{2\times 2} & \mathbf{0}_{2\times 2} & \mathbf{0}_{2\times 2} & \mathbf{0}_{2\times 2} & \mathbf{0}_{2\times 2} & \mathbf{0}_{2\times 2} & 4\mathbf{M}_{Ceq}^{\omega} \\
-E_{c,s} & \mathbf{0}_{2\times 2} & \mathbf{M}_{Ceq}^{\omega} & \mathbf{0}_{2\times 2} & \mathbf{0}_{2\times 2} & \mathbf{0}_{2\times 2} & \mathbf{0}_{2\times 2} & \mathbf{0}_{2\times 2} & \mathbf{0}_{2\times 2} & \mathbf{0}_{2\times 2} \\
-\frac{1}{2}\mathbf{I} & \mathbf{0}_{2\times 2} & \mathbf{0}_{2\times 2} & 2\mathbf{M}_{Ceq}^{\omega} & \mathbf{0}_{2\times 2} & \mathbf{0}_{2\times 2} & \mathbf{0}_{2\times 2} & \mathbf{0}_{2\times 2} & \mathbf{0}_{2\times 2} & \mathbf{0}_{2\times 2} \\
-E_{c,s}^{T} & -E_{c,s} & \mathbf{0}_{2\times 2} & \mathbf{0}_{2\times 2} & 3\mathbf{M}_{Ceq}^{\omega} & \mathbf{0}_{2\times 2} & \mathbf{0}_{2\times 2} & \mathbf{0}_{2\times 2} & \mathbf{0}_{2\times 2} & \mathbf{0}_{2\times 2} \\
\mathbf{0}_{2\times 2} & -\frac{1}{2}\mathbf{I} & \mathbf{0}_{2\times 2} & \mathbf{0}_{2\times 2} & \mathbf{0}_{2\times 2} & 4\mathbf{M}_{Ceq}^{\omega} & \mathbf{0}_{2\times 2} & \mathbf{0}_{2\times 2} & \mathbf{0}_{2\times 2} & \mathbf{0}_{2\times 2} \\
\mathbf{M}_{rl}^{2\omega} & \mathbf{0}_{2\times 2} & \frac{1}{2}E_{c,s}^{T} & \frac{1}{4}\mathbf{I} & \frac{1}{2}E_{c,s} & \mathbf{0}_{2\times 2} & -\frac{1}{2}E_{c,s}^{T} & \frac{1}{4}\mathbf{I} & -\frac{1}{2}E_{c,s} & \mathbf{0}_{2\times 2} \\
\mathbf{0}_{2\times 2} & \mathbf{M}_{rl}^{4\omega} & \mathbf{0}_{2\times 2} & \mathbf{0}_{2\times 2} & \frac{1}{2}E_{c,s}^{T} & \frac{1}{4}\mathbf{I} & \mathbf{0}_{2\times 2} & \mathbf{0}_{2\times 2} & -\frac{1}{2}E_{c,s}^{T} & \frac{1}{4}\mathbf{I}
\end{bmatrix} \tag{B.9}$$

$$\mathbf{0}_{2\times 2} = \begin{bmatrix} 0 & 0 \\ 0 & 0 \end{bmatrix} \tag{B.10}$$

$$\mathbf{E}_{c,s} = \begin{bmatrix} \frac{E_0^{c*}}{4} & -\frac{E_0^{s*}}{4} \\ \frac{E_0^{s*}}{4} & \frac{E_0^{c*}}{4} \end{bmatrix} \tag{B.11}$$

$$\mathbf{M}_{rl}^{2\omega} = \begin{bmatrix} R & -2\omega L \\ 2\omega L & R \end{bmatrix} \tag{B.12}$$

$$\mathbf{M}_{rl}^{4\omega} = \begin{bmatrix} R & -4\omega L \\ 4\omega L & R \end{bmatrix} \tag{B.13}$$

$$\mathbf{M}_{Ceq}^{\omega} = \begin{bmatrix} 0 & -\omega C_{eq} \\ \omega C_{eq} & 0 \end{bmatrix} \tag{B.14}$$

B.2 solution

Considering:

$$\begin{gathered}\Delta_I = 37748736.0C_{eq}^4 L^4 \omega^8 + 11796480.0C_{eq}^4 L^2 R^2 \omega^6 + 589824.0C_{eq}^4 R^4 \omega^4 \\ - 3538944.0C_{eq}^3 (E_0^{c*})^2 L^3 \omega^6 - 294912.0C_{eq}^3 (E_0^{c*})^2 L R^2 \omega^4 - 3538944.0C_{eq}^3 (E_0^{s*})^2 L^3 \omega^6 \\ - 294912.0C_{eq}^3 (E_0^{s*})^2 L R^2 \omega^4 - 5898240.0C_{eq}^3 L^3 \omega^6 - 589824.0C_{eq}^3 L R^2 \omega^4 \\ + 95232.0C_{eq}^2 (E_0^{c*})^4 L^2 \omega^4 + 4864.0C_{eq}^2 (E_0^{c*})^4 R^2 \omega^2 + 190464.0C_{eq}^2 (E_0^{c*})^2 (E_0^{s*})^2 L^2 \omega^4 \\ + 9728.0C_{eq}^2 (E_0^{c*})^2 (E_0^{s*})^2 R^2 \omega^2 + 350208.0C_{eq}^2 (E_0^{c*})^2 L^2 \omega^4 + 13824.0C_{eq}^2 (E_0^{c*})^2 R^2 \omega^2 \\ + 95232.0C_{eq}^2 (E_0^{s*})^4 L^2 \omega^4 + 4864.0C_{eq}^2 (E_0^{s*})^4 R^2 \omega^2 + 350208.0C_{eq}^2 (E_0^{s*})^2 L^2 \omega^4 \\ + 13824.0C_{eq}^2 (E_0^{s*})^2 R^2 \omega^2 + 304128.0C_{eq}^2 L^2 \omega^4 + 11520.0C_{eq}^2 R^2 \omega^2 \\ - 576.0C_{eq} (E_0^{c*})^6 L\omega^2 - 1728.0C_{eq} (E_0^{c*})^4 (E_0^{s*})^2 L\omega^2 - 4416.0C_{eq} (E_0^{c*})^4 L\omega^2 \\ - 1728.0C_{eq} (E_0^{c*})^2 (E_0^{s*})^4 L\omega^2 - 8832.0C_{eq} (E_0^{c*})^2 (E_0^{s*})^2 L\omega^2 - 9216.0C_{eq} (E_0^{c*})^2 L\omega^2 \\ - 576.0C_{eq} (E_0^{s*})^6 L\omega^2 - 4416.0C_{eq} (E_0^{s*})^4 L\omega^2 - 9216.0C_{eq} (E_0^{s*})^2 L\omega^2 \\ - 5760.0C_{eq} L\omega^2 + (E_0^{c*})^8 + 4.0(E_0^{c*})^6 (E_0^{s*})^2 + 12.0(E_0^{c*})^6 \\ + 6.0(E_0^{c*})^4 (E_0^{s*})^4 + 36.0(E_0^{c*})^4 (E_0^{s*})^2 + 48.0(E_0^{c*})^4 + 4.0(E_0^{c*})^2 (E_0^{s*})^6 \\ + 36.0(E_0^{c*})^2 (E_0^{s*})^4 + 96.0(E_0^{c*})^2 (E_0^{s*})^2 + 72.0(E_0^{c*})^2 + (E_0^{s*})^8 \\ + 12.0(E_0^{s*})^6 + 48.0(E_0^{s*})^4 + 72.0(E_0^{s*})^2 + 36.0,\end{gathered} \tag{B.15}$$

The steady-state solution for $I_{cir_{2s}}$ is given by:

$$I_{cir_{2s}} = \frac{1}{\Delta_I} \left[\begin{array}{cccc} A_1^{cir_2} & A_2^{cir_2} & A_3^{cir_2} & A_4^{cir_2} \end{array} \right] \begin{bmatrix} 2.0E_0^{s*} I_{cir_0} - I_{0s} \\ 2.0E_0^{c*} I_{cir_0} - I_{0c} \\ E_0^{c*} I_{0c} - E_0^{s*} I_{0s} \\ E_0^{c*} I_{0s} + E_0^{s*} I_{0c} \end{bmatrix} \tag{B.16}$$

In this case, we have the following results:

$A_1^{cir_2} = 589824.0C_{eq}^3 E_0^{c*} L^2 R\omega^5 + 36864.0C_{eq}^3 E_0^{c*} R^3 \omega^3 - 1179648.0C_{eq}^3 E_0^{s*} L^3 \omega^6 - 73728.0C_{eq}^3 E_0^{s*} L R^2 \omega^4 - 6144.0C_{eq}^2 \left(E_0^{c*}\right)^3 L R\omega^3 + 61440.0C_{eq}^2 \left(E_0^{c*}\right)^2 E_0^{s*} L^2 \omega^4 + 3072.0C_{eq}^2 \left(E_0^{c*}\right)^2 E_0^{s*} R^2 \omega^2 - 6144.0C_{eq}^2 E_0^{c*} \left(E_0^{s*}\right)^2 L R\omega^3 - 18432.0C_{eq}^2 E_0^{c*} L R\omega^3 + 61440.0C_{eq}^2 \left(E_0^{s*}\right)^3 L^2 \omega^4 + 3072.0C_{eq}^2 \left(E_0^{s*}\right)^3 R^2 \omega^2 + 110592.0C_{eq}^2 E_0^{s*} L^2 \omega^4 + 4608.0C_{eq}^2 E_0^{s*} R^2 \omega^2 + 32.0C_{eq} \left(E_0^{c*}\right)^5 R\omega - 480.0C_{eq} \left(E_0^{c*}\right)^4 E_0^{s*} L\omega^2 + 64.0C_{eq} \left(E_0^{c*}\right)^3 \left(E_0^{s*}\right)^2 R\omega + 96.0C_{eq} \left(E_0^{c*}\right)^3 R\omega - 960.0C_{eq} \left(E_0^{c*}\right)^2 \left(E_0^{s*}\right)^3 L\omega^2 - 2496.0C_{eq} \left(E_0^{c*}\right)^2 E_0^{s*} L\omega^2 + 32.0C_{eq} E_0^{c*} \left(E_0^{s*}\right)^4 R\omega + 96.0C_{eq} E_0^{c*} \left(E_0^{s*}\right)^2 R\omega +$

$144.0C_{eq}E_0^{c*}R\omega - 480.0C_{eq}\left(E_0^{s*}\right)^5 L\omega^2 - 2496.0C_{eq}\left(E_0^{s*}\right)^3 L\omega^2 - 2592.0C_{eq}E_0^{s*}L\omega^2 + \left(E_0^{c*}\right)^6 E_0^{s*} + 3.0\left(E_0^{c*}\right)^4\left(E_0^{s*}\right)^3 + 9.0\left(E_0^{c*}\right)^4 E_0^{s*} + 3.0\left(E_0^{c*}\right)^2\left(E_0^{s*}\right)^5 + 18.0\left(E_0^{c*}\right)^2\left(E_0^{s*}\right)^3 + 24.0\left(E_0^{c*}\right)^2 E_0^{s*} + \left(E_0^{s*}\right)^7 + 9.0\left(E_0^{s*}\right)^5 + 24.0\left(E_0^{s*}\right)^3 + 18.0E_0^{s*}$

$A_2^{cir_2} = 1179648.0C_{eq}^3E_0^{c*}L^3\omega^6 + 73728.0C_{eq}^3E_0^{c*}LR^2\omega^4 + 589824.0C_{eq}^3E_0^{s*}L^2R\omega^5 + 36864.0C_{eq}^3E_0^{s*}R^3\omega^3 - 61440.0C_{eq}^2\left(E_0^{c*}\right)^3 L^2\omega^4 - 3072.0C_{eq}^2\left(E_0^{c*}\right)^3 R^2\omega^2 - 6144.0C_{eq}^2\left(E_0^{c*}\right)^2 E_0^{s*}LR\omega^3 - 61440.0C_{eq}^2E_0^{c*}\left(E_0^{s*}\right)^2 L^2\omega^4 - 3072.0C_{eq}^2E_0^{c*}\left(E_0^{s*}\right)^2 R^2\omega^2 - 110592.0C_{eq}^2E_0^{c*}L^2\omega^4 - 4608.0C_{eq}^2E_0^{c*}R^2\omega^2 - 6144.0C_{eq}^2\left(E_0^{s*}\right)^3 LR\omega^3 - 18432.0C_{eq}^2E_0^{s*}LR\omega^3 + 480.0C_{eq}\left(E_0^{c*}\right)^5 L\omega^2 + 32.0C_{eq}\left(E_0^{c*}\right)^4 E_0^{s*}R\omega + 960.0C_{eq}\left(E_0^{c*}\right)^3\left(E_0^{s*}\right)^2 L\omega^2 + 2496.0C_{eq}\left(E_0^{c*}\right)^3 L\omega^2 + 64.0C_{eq}\left(E_0^{c*}\right)^2\left(E_0^{s*}\right)^3 R\omega + 96.0C_{eq}\left(E_0^{c*}\right)^2 E_0^{s*}R\omega + 480.0C_{eq}E_0^{c*}\left(E_0^{s*}\right)^4 L\omega^2 + 2496.0C_{eq}E_0^{c*}\left(E_0^{s*}\right)^2 L\omega^2 + 2592.0C_{eq}E_0^{c*}L\omega^2 + 32.0C_{eq}\left(E_0^{s*}\right)^5 R\omega + 96.0C_{eq}\left(E_0^{s*}\right)^3 R\omega + 144.0C_{eq}E_0^{s*}R\omega - \left(E_0^{c*}\right)^7 - 3.0\left(E_0^{c*}\right)^5\left(E_0^{s*}\right)^2 - 9.0\left(E_0^{c*}\right)^5 - 3.0\left(E_0^{c*}\right)^3\left(E_0^{s*}\right)^4 - 18.0\left(E_0^{c*}\right)^3\left(E_0^{s*}\right)^2 - 24.0\left(E_0^{c*}\right)^3 - E_0^{c*}\left(E_0^{s*}\right)^6 - 9.0E_0^{c*}\left(E_0^{s*}\right)^4 - 24.0E_0^{c*}\left(E_0^{s*}\right)^2 - 18.0E_0^{c*}$

$A_3^{cir_2} = -589824.0C_{eq}^3L^3\omega^6 - 36864.0C_{eq}^3LR^2\omega^4 + 30720.0C_{eq}^2\left(E_0^{c*}\right)^2 L^2\omega^4 + 1536.0C_{eq}^2\left(E_0^{c*}\right)^2 R^2\omega^2 + 30720.0C_{eq}^2\left(E_0^{s*}\right)^2 L^2\omega^4 + 1536.0C_{eq}^2\left(E_0^{s*}\right)^2 R^2\omega^2 + 55296.0C_{eq}^2L^2\omega^4 + 2304.0C_{eq}^2R^2\omega^2 - 240.0C_{eq}\left(E_0^{c*}\right)^4 L\omega^2 - 480.0C_{eq}\left(E_0^{c*}\right)^2\left(E_0^{s*}\right)^2 L\omega^2 - 1248.0C_{eq}\left(E_0^{c*}\right)^2 L\omega^2 - 240.0C_{eq}\left(E_0^{s*}\right)^4 L\omega^2 - 1248.0C_{eq}\left(E_0^{s*}\right)^2 L\omega^2 - 1296.0C_{eq}L\omega^2 + 0.5\left(E_0^{c*}\right)^6 + 1.5\left(E_0^{c*}\right)^4\left(E_0^{s*}\right)^2 + 4.5\left(E_0^{c*}\right)^4 + 1.5\left(E_0^{c*}\right)^2\left(E_0^{s*}\right)^4 + 9.0\left(E_0^{c*}\right)^2\left(E_0^{s*}\right)^2 + 12.0\left(E_0^{c*}\right)^2 + 0.5\left(E_0^{s*}\right)^6 + 4.5\left(E_0^{s*}\right)^4 + 12.0\left(E_0^{s*}\right)^2 + 9.0$

$A_4^{cir_2} = -8.0C_{eq}R\omega\Big[36864.0C_{eq}^2L^2\omega^4 + 2304.0C_{eq}^2R^2\omega^2 - 384.0C_{eq}\left(E_0^{c*}\right)^2 L\omega^2 - 384.0C_{eq}\left(E_0^{s*}\right)^2 L\omega^2 - 1152.0C_{eq}L\omega^2 + 2.0\left(E_0^{c*}\right)^4 + 4.0\left(E_0^{c*}\right)^2\left(E_0^{s*}\right)^2 + 6.0\left(E_0^{c*}\right)^2 + 2.0\left(E_0^{s*}\right)^4 + 6.0\left(E_0^{s*}\right)^2 + 9.0\Big]$

All the constants and variables presented in this result were defined in Section 3.5. The solution for the other components are omitted here due to the space they were required, but the can be visualized running the Jupyter notebook hosted **HERE** [127].

Apêndice C

Methodology used to validate the developed models

This appendix in focused on explaining how the validations of the models were carried out. It is used as example the MMC in natural reference frame, but the idea is easily adapted to the MMC in Synchronous reference frame.

C.1 Validation of the equivalent dc admittance

The equivalent dc admittance, Y_{dc}, models the relationship between the voltage in the dc link, v_{dc}, and the circulating currents, i^k_{cir}. If a harmonic component v_{dch} appears in the dc voltage, a harmonic component i^k_{cirh} is created in the circulating currents. Thus, to validate the model, the dc admittance can be computed using a detailed model (in this case, the non-linear model) by inserting a harmonic component in v_{dch} and observing the effect caused in the circulating currents, as shown in Figure C.1.

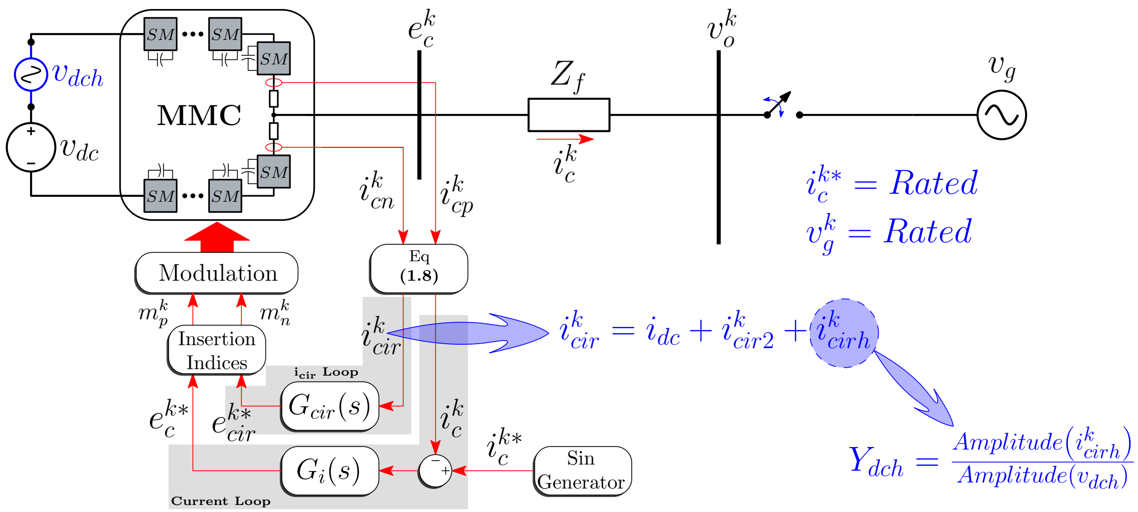

Figure C.1: Strategy for measuring the equivalent dc admittance of the MMC.

In this case, the measured admittance at a given frequency is computed by:

$$Y_{dch} = \frac{Amplitude\,(v_{dch})}{Amplitude\,(i_{cirh})} \tag{C.1}$$

C.2 Validation of the Norton-equivalent admittance

When the MMC is under current control and connected to a power grid, the harmonic content of the voltages can distort the output current. This distortion is caused by the harmonic current which is drawn by the Norton-equivalent admittance of the converter. Thus, this admittance can be measured in a detailed model by adding harmonic components to the grid voltages and measuring the respective harmonic components created in the output current. Figure C.2 presents a diagram illustrating this approach.

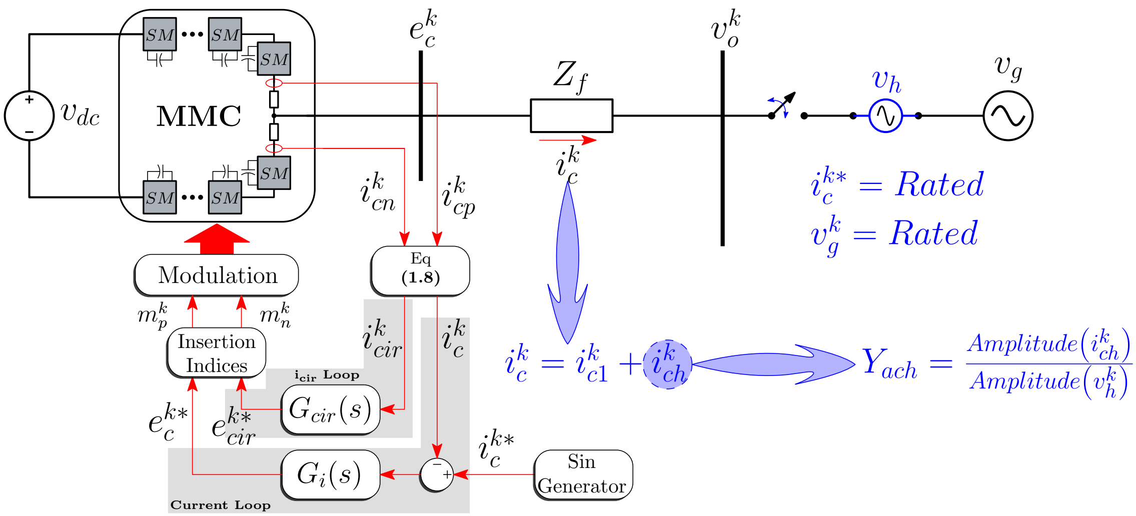

Figure C.2: Strategy for measuring the Norton-equivalent admittance of the MMC.

In this case, the measured admittance at a given frequency is computed by:

$$Y_{ach} = \frac{Amplitude\,(i_{ch})}{Amplitude\,(v_{oh})} \tag{C.2}$$

C.3 Validation of the Closed-loop current gain

The closed-loop current gain measures the relationship between the reference currents and the produced currents. For measuring it, harmonic components i_{ch}^{k*} are inserted in the reference signals and the effects on the output currents are measured. Since the voltages are kept without distortion, the components i_{ch}^{k} are caused directly by i_{ch}^{k*}. Figure C.3 presents an illustrative diagram for this procedure.

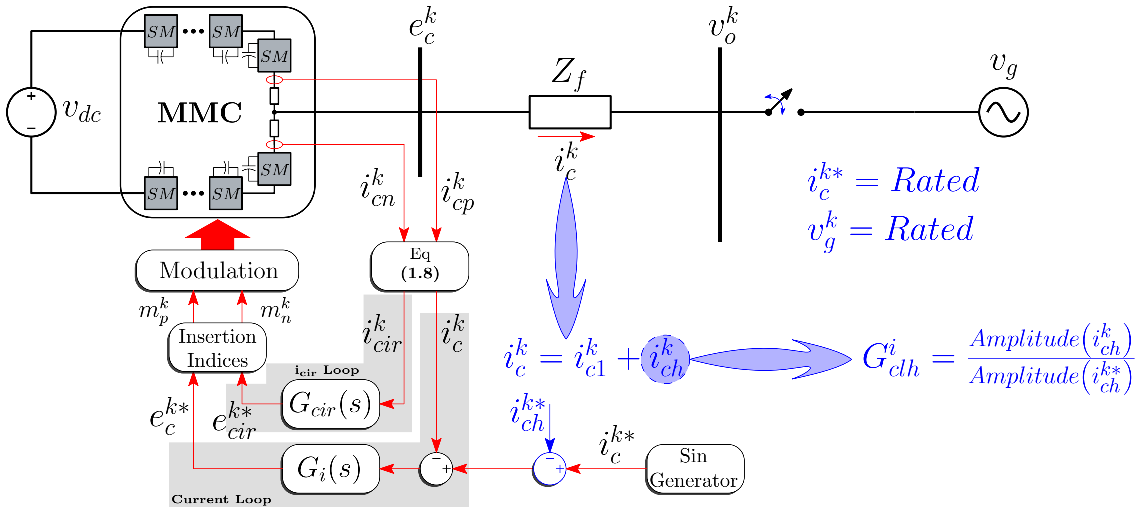

Figure C.3: Strategy for measuring the closed-loop current gain of the MMC.

In this case, the measured closed-loop gain at a given frequency is computed by:

$$G_{clh}^{i} = \frac{Amplitude\,(i_{ch})}{Amplitude\,(i_{ch}^{*})} \tag{C.3}$$

C.4 Validation of the Thevenin-equivalent impedance

To measure the Thévenin-equivalent impedance of the MMC, a harmonic component i_{oh}^k is added to the load currents and the corresponding harmonic voltage v_{oh} is observed. The Figure C.4 illustrated this process. Bear in mind that, despite the fact the figure considers the single-loop voltage-controlled MMC, the approach also used for the double-loop current/voltage-controlled MMC.

In this case, the measured closed-loop gain at a given frequency is computed by:

$$Z_{thh} = \frac{Amplitude\,(v_{oh})}{Amplitude\,(i_{oh}^{*})} \tag{C.4}$$

C.5 Validation of the Closed-loop voltage gain

Thevenin gain measures the relationship between the reference voltage and the output voltage. Thus, it can be measured by adding a harmonic component v_{oh}^* in the reference signals and observing the corresponding component in the voltage. Figure C.5 illustrates the process.

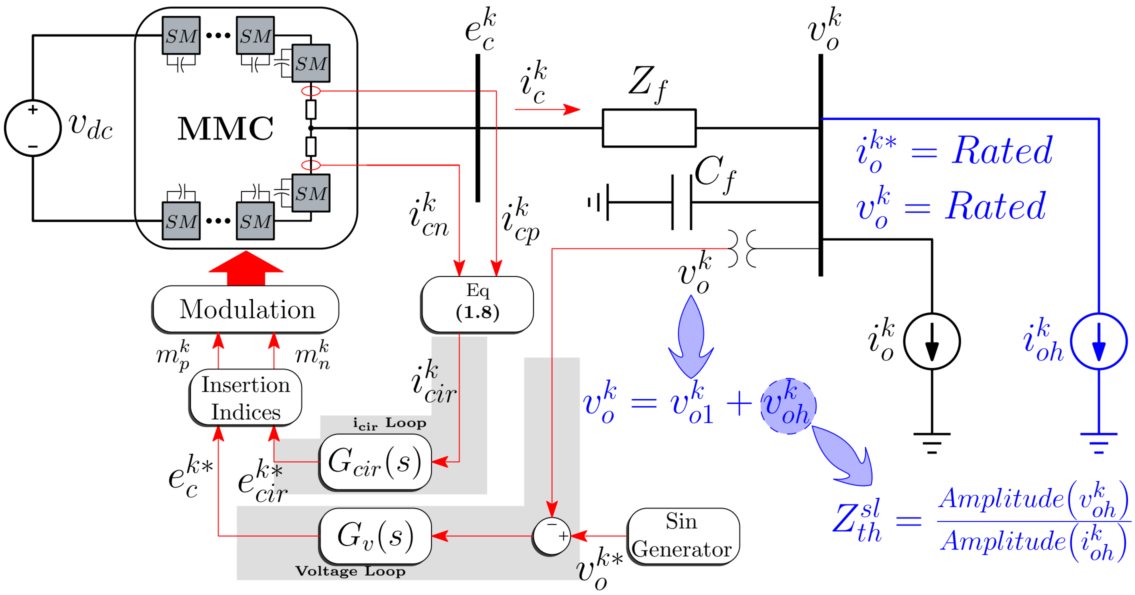

Figure C.4: Strategy for measuring the Thévenin-equivalent impedance of the MMC.

In this case, the measured Thévenin gain at a given frequency is computed by:

$$Z_{thh} = \frac{Amplitude\,(v_{oh})}{Amplitude\,(v_{oh}^*)} \tag{C.5}$$

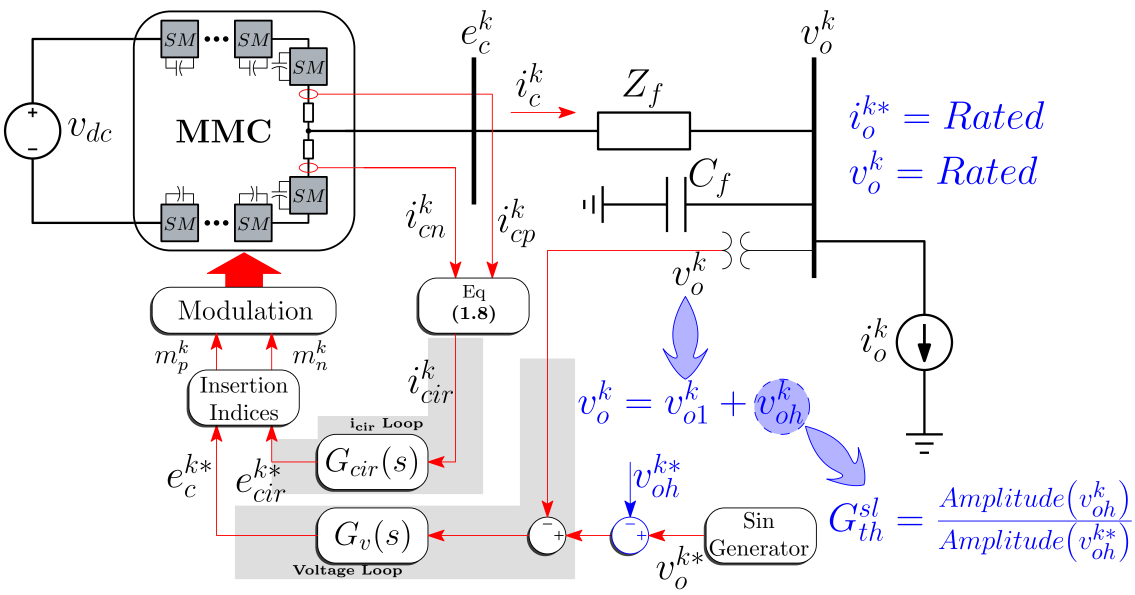

Figure C.5: Strategy for measuring the Thévenin gain of the MMC.

Apêndice D

Step by Step obtaining of the feed-forward terms to produce the virtual impedances

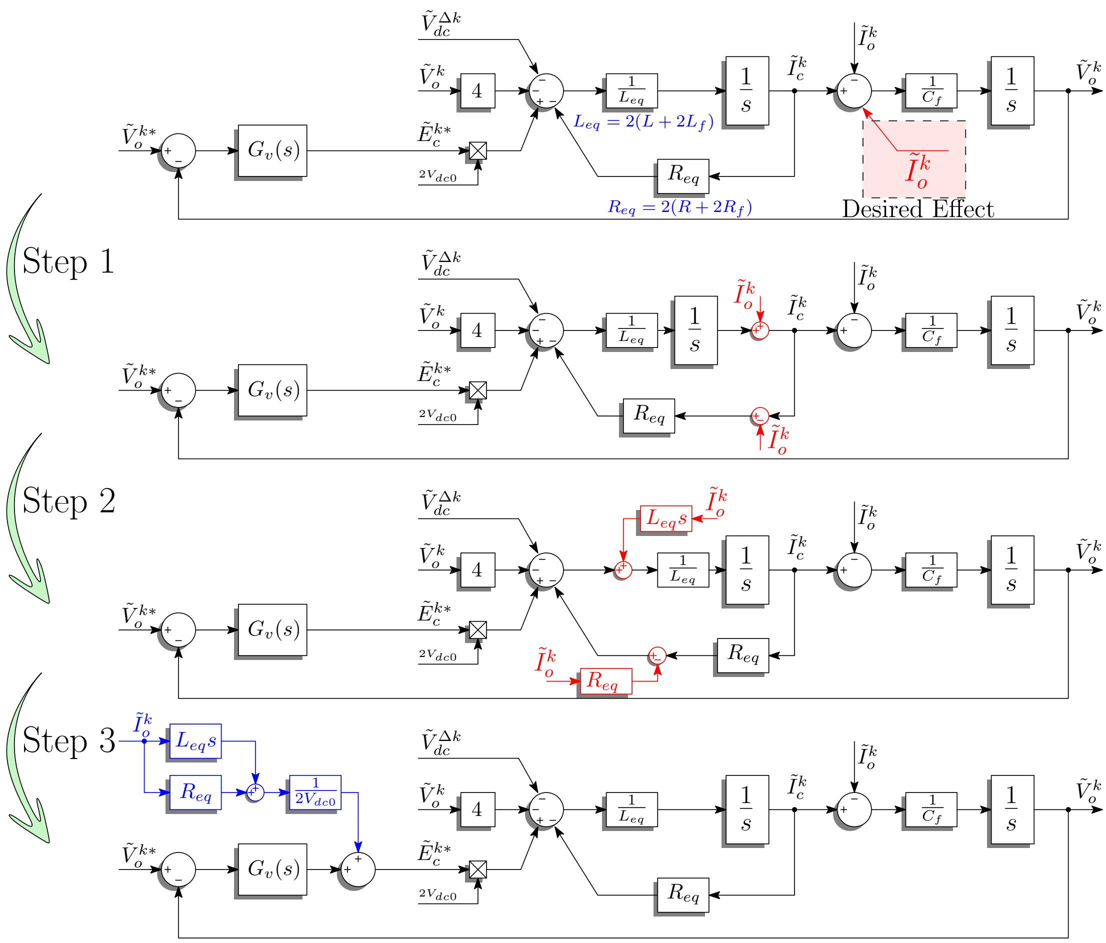

Figure D.1: Step-by-step obtaining the feed-forward term for generating the virtual impedance of the NRF single-loop voltage-controlled MMC.

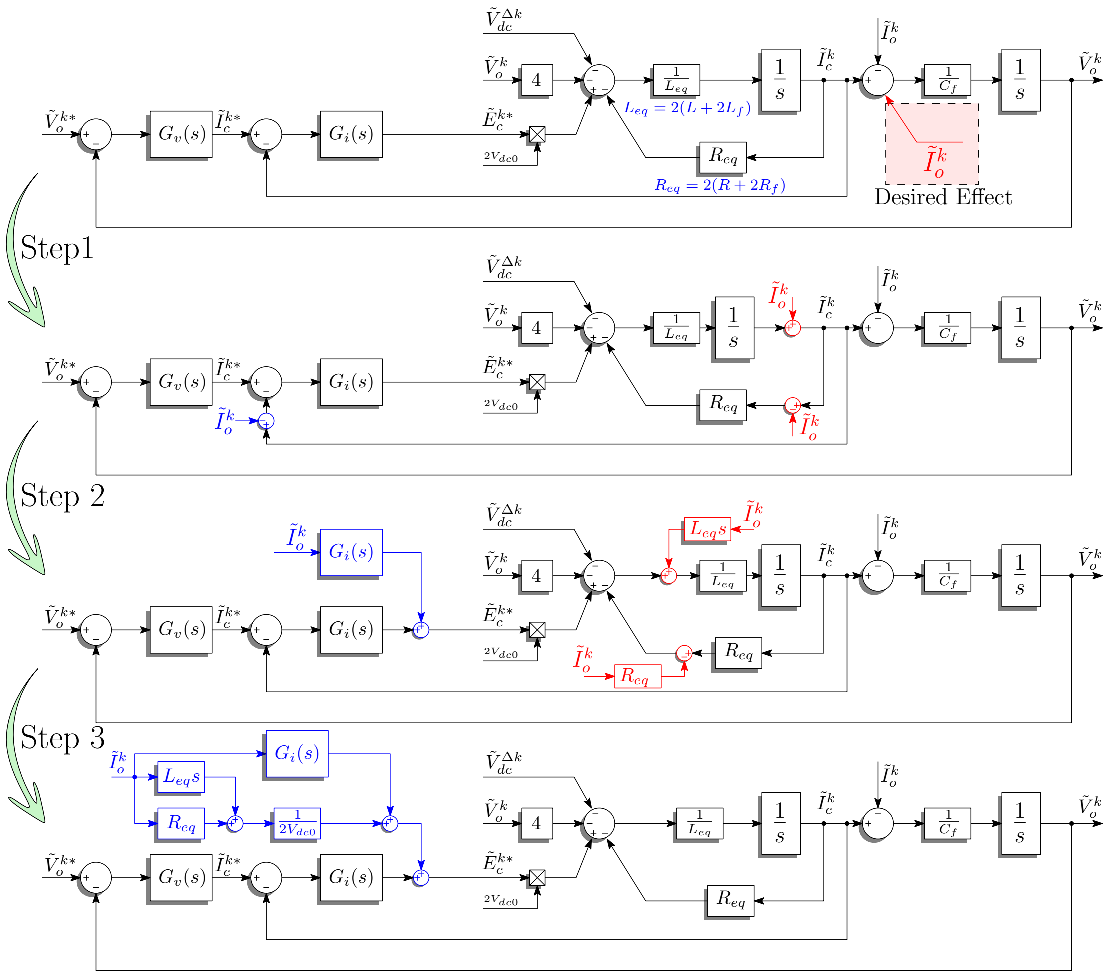

Figure D.2: Step-by-step obtaining the feed-forward term for generating the virtual impedance of the NRF double-loop voltage-controlled MMC.

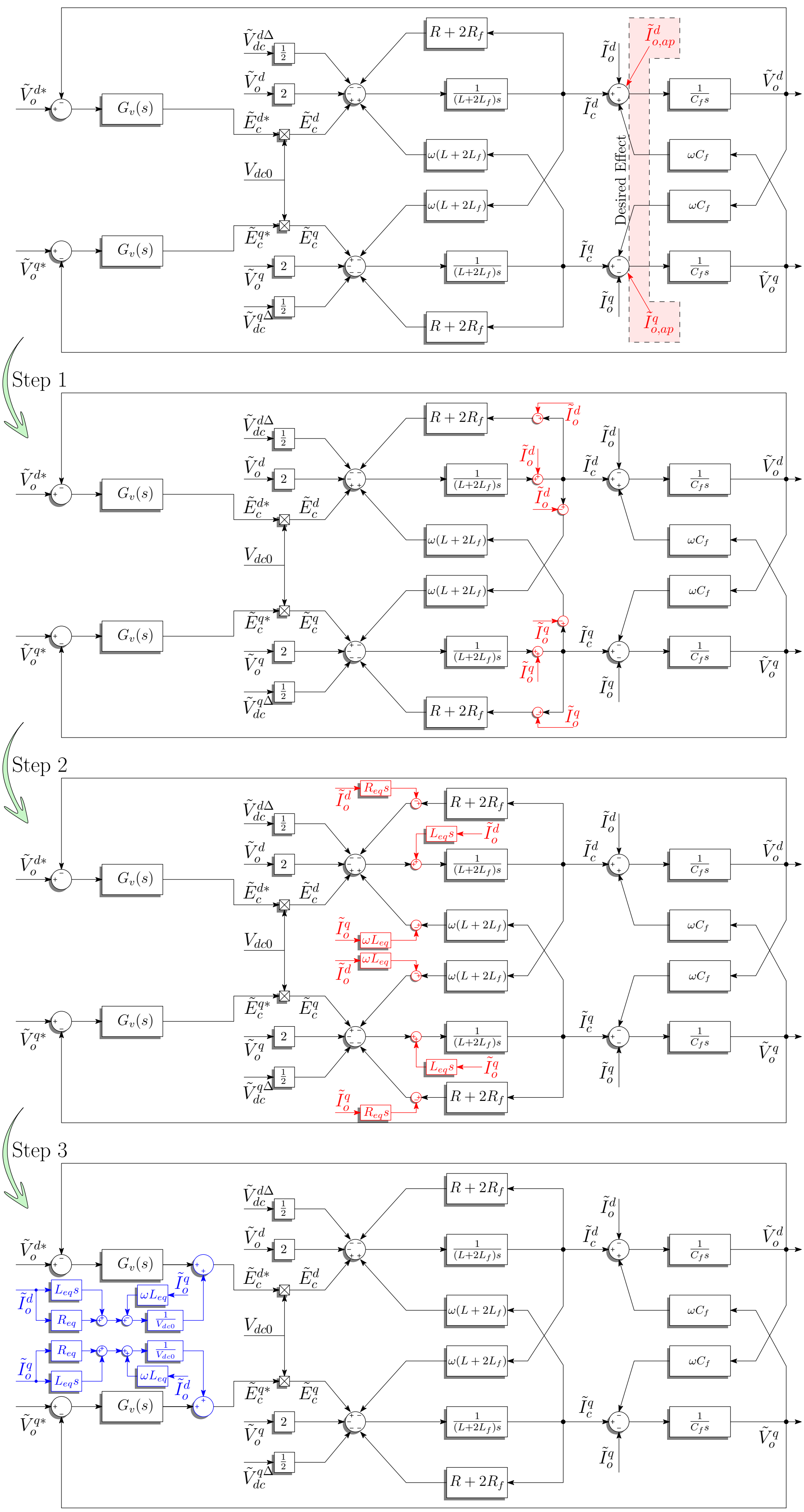

Figure D.3: Step-by-step obtaining the feed-forward term for generating the virtual impedance of the SRF single-loop voltage-controlled MMC.

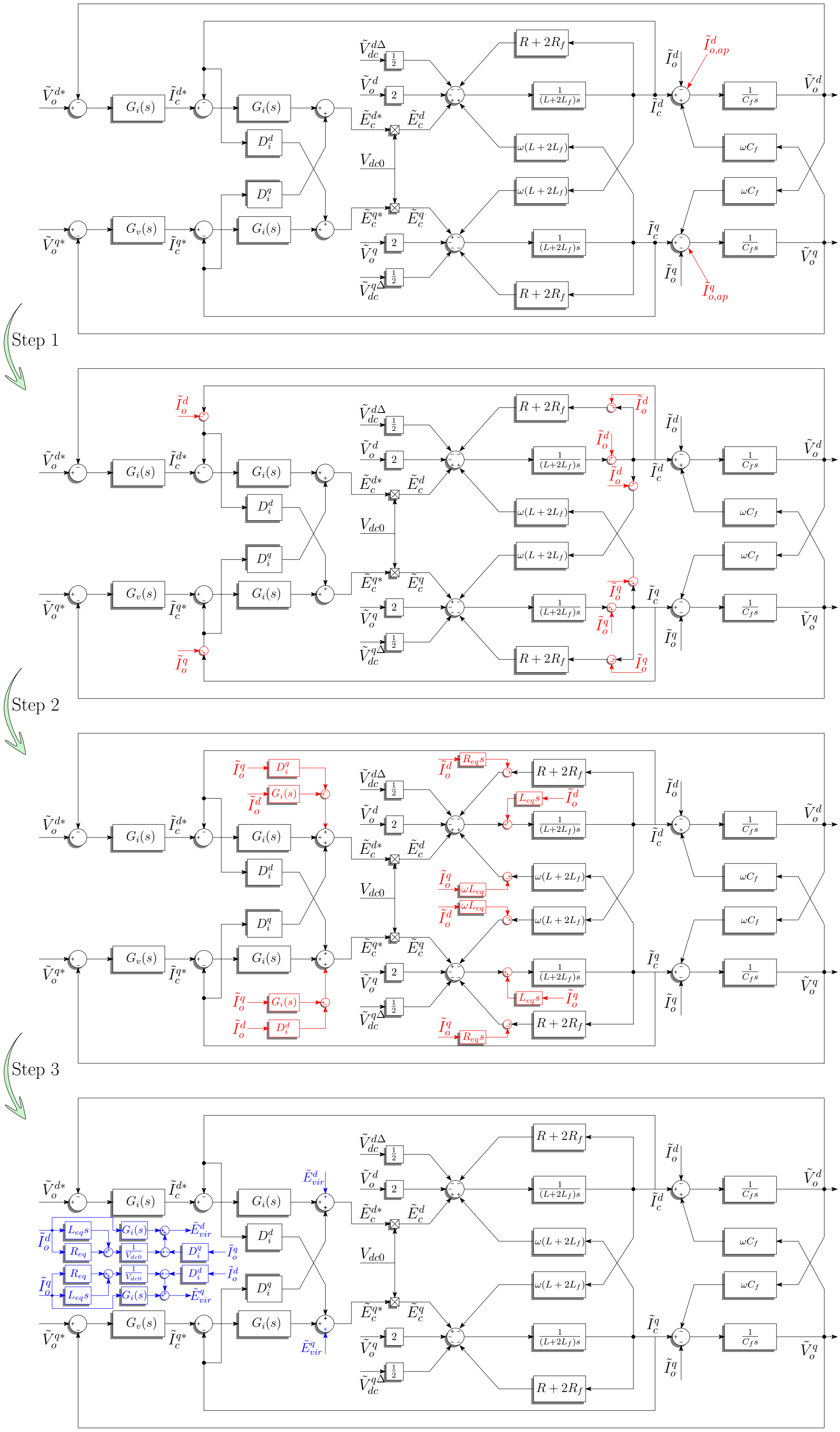

Figure D.4: Step-by-step obtaining the feed-forward term for generating the virtual impedance of the SRF double-loop voltage-controlled MMC.